DISS. ETH NO. 28894

ANALYSIS OF CORTICAL CONNECTOMES

A thesis submitted to attain the degree of
DOCTOR OF SCIENCES
(Dr. sc. ETH Zurich)

presented by
ALESSANDRO MOTTA
MSc in Life Sciences and Technologies (EPFL)

born on 24th of September 1991

accepted on the recommendation of
Prof. Dr. Mehmet Fatih Yanik (internal supervisor)
Prof. Dr. Moritz Helmstaedter (external supervisor)
Prof. Dr. Richard Hahnloser (co-examiner)
Prof. Dr. Fritjof Helmchen (co-examiner)

2023

Acknowledgements

Much of this thesis is the result of collaborative efforts. By necessity, the emphasis is on my personal contributions. But many of the joys and ideas of the last years came from tackling and discussing interesting problems together. Never has this been more painfully clear than over the last weeks of sitting alone and writing this thesis. All the more do I now want to thank the following people.

First, I would like to thank Moritz Helmstaedter. From the first day in September 2015, when I have joined the Department of Connectomics as an internship student, I felt that my ideas and contributions were being valued. Together with the incredible team of people that he has assembled, this resulted in an immensely stimulating atmosphere. Now, when thinking back over the last years, my memories are defined by a few periods of very intense working, thinking, and discussing. It was in these periods of staring into the shadows that, I feel, I have learnt the most—both about science and myself. Thank you for your mentorship and support throughout!

I would also like to thank Prof. Dr. Mehmet Fatih Yanik for accepting me as an external doctoral student, and Prof Dr. Richard Hahnloser and Prof. Dr. Fritjof Helmchen for agreeing to co-examine this thesis. My thanks also go to Prof. Dr. Julijana Gjorgjieva, who supported this work as a member of the thesis advisory committee, and to Dr. Wolfger von der Behrens.

Thanks to Ali Karimi, David Laubender, and Sahil Loomba for providing feedback on an early draft of this thesis. The works in this thesis did also profit from the support of Christian Guggenberger, Klaus Reuter, Mykola Petrov, Alexis Huxley, Manuel Panea, and Timoteo Colnaghi of the Max Planck Computing and Data Facility. Thank you to Norman Rzepka, Tom Herold, Tom Bocklisch, Johannes Frohnhofen, Florian Meinel and Daniel Werner of scalable minds GmbH for developing and supporting the webKnossos ecosystem. The collaboration with Meike Sievers and Martin Schmidt, and with Georg Wiese, Valentin Pinkau, Jonathan Striebel, Daniel Werner, and Florian Meinel of scalable minds GmbH on the development of voxelytics was great fun.

Many thanks also to all the former and current members of the Department of Connectomics. In particular, I would like to thank Manuel Berning, who stoically answered the many questions of this annoying little internship student; Jakob Straehle, for interesting scientific discussions and a masterclass in storytelling; Benedikt Staffler, Kevin Boergens, Emmanuel Klinger, Florian Drawitsch, and Philip Laserstein. I am also very grateful to Sahil Loomba, Jakob Straehle, Vijayan Gangadharan, Natalie Heike, Abdelrahman Khalifa, and Niansheng Ju for letting me contribute to their work. It was fun to explore some more wild ideas together with many internship students, including Elias Eulig, Martin Schmidt, Yagmur Yener, Hamza Kebiri, Donal Naylor, Sam Clothier, Ali Hadian, and Saksham Pruthi. That Martin and Yagmur have decided to stay on as PhD students and to continue working with me makes me very happy.

A special ‘thank you’ to Meike Sievers, with whom I have had the great pleasures of working, discussing, dancing, skiing and mountain-biking (but not yet running!) over the last years. Thank you for reassuring me when I was losing hope, and thank you for ceaselessly playing the ‘good cop’ to my ‘bad cop’. I will miss all of this.

Finally, I would like to thank my parents, Maja and Cristoforo, for giving me the freedom to follow my interests out into the world, while always warmly welcoming me back home. And thank you to my sisters, Valentina and Sara, for their constant reminders of not taking life too seriously.

Table of contents

Summary

The brain is arguably the most complex organ in the human body. The network consisting of 86 billion neurons, each connected to thousands of other neurons through long and thin neurites and through synaptic contacts, is thought to implement most of our cognitive abilities. While individual neurons have been studied in considerable detail, their synaptic connectivity remains largely unknown.

The reverse engineering of synapse-resolution circuit diagrams (so-called "connectomes") has recently become possible due to progress in three-dimensional electron microscopy. Since 2015, the size of synapse-resolution electron microscopy volumes from the mammalian cerebral cortex has increased by more than four orders of magnitude. This progress comes with a great many opportunities and challenges. This cumulative thesis consists of four chapters, each corresponding to a previously published journal article, concerned with these analysis opportunities and challenges.

Chapter 1 provides a review of the electron microscopy and data analysis techniques used in connectomics. At the hypothetical example of the connectomic reconstruction of a whole human brain, the progress and remaining challenges of electron microscopy-based connectomics are illustrated. In particular, the accuracy and computational cost of existing reconstruction methods based on artificial intelligence are identified as principal limiting factors.

Chapter 2 describes the dense connectomic reconstruction of an electron microscopy volume of roughly 500,000μm^3 from layer 4 of mouse primary somatosensory cortex and the analysis of the around 2.7 meters of neurites and 400,000 synapses contained therein. The unprecedented size of this reconstruction was enabled by efficient semi-automated reconstruction methods presented in this chapter. The resulting subcellular connectome was subjected to various analyses. In particular, the connectome was used to derive upper bounds on the circuit fraction that is consistent with saturated Hebbian plasticity.

Chapter 3 presents a method for the analysis of neuron-to-neuron connectomes of local cortical circuits, the reconstruction of which has recently become possible. Specifically, it is demonstrated by simulation that summary statistics derived from the connectome of a local cortical circuit are sufficient for Bayesian selection among seven competing models. Furthermore, it is shown that "weighted" connectomes with information about connection strengths are sufficient to distinguish between artificial recurrent neural networks with biologically plausible connectivity that differ only in the task that they were trained on.

Finally, chapter 4 reports a connectomic comparison of mouse and human cerebral cortex. A combination of efficient automated and manual analysis methods was used to analyze nine electron microscopy volumes from mouse, macaque and human cortical layers 2/3. In particular, these data were used to infer the relative contributions of excitatory and inhibitory synaptic inputs onto pyramidal neurons. The increased interneuron population in human compared to mouse cerebral cortex was found to be associated not with a corresponding increase in inhibitory synapses onto pyramidal neurons, but rather with an increase in interneuron-to-interneuron connectivity.

Zusammenfassung

Das Gehirn ist das wohl komplexeste Organ des menschlichen Körpers. Das Netzwerk aus rund 86 Milliarden Neuronen, von denen jedes mit tausenden anderen Neuronen durch lange und dünne Neuriten und durch synaptische Kontake verbunden ist, implementiert die meisten unserer kognitiven Fähigkeiten. Während Neurone in Einzelheit bereits im Detail studiert wurden, ist deren synaptische Konnektivität noch immer grösstenteils unbekannt.

Das Reverse Engineering von solchen synaptischen Schaltplänen (auch «Konnektome» genannt) wurde in den letzten Jahren durch Forschritte in dreidimensionaler Elektronenmikroskopie ermöglicht. Seit 2015 haben Elektronenmikroskopievolumen von der Grosshirnrinde von Säugetieren in ihrem Volumen um mehr als vier Grössenordnungen zugenommen. Dieser Fortschritt bringt viele neue Möglichkeiten, aber auch viele Herausforderungen. Diese kumulative Doktorarbeit besteht aus vier Kapiteln (jedes einem bereits veröffentlichten Fachartikel entsprechend), die sich mit diesen Analysemöglichkeiten und –herausforderungen beschäftigen.

Kapitel 1 gibt einen Überblick über die in Connectomics eingesetzten Techniken der Elektronenmikroskopie und Datenanalyse. Am hypothetischen Beispiel der konnektomischen Rekonstruktion eines ganzen menschlichen Gehirns werden die Fortschritte und verbleibenden Herausforderungen von Connectomics illustriert. Insbesondere werden die Fehlerraten und Rechenkosten der bestehenden, auf künstlicher Intelligenz basierenden Rekonstruktionsmethoden als limitierende Faktoren identifiziert.

Kapitel 2 beschreibt die dichte konnektomische Rekonstruktion eines Elektronenmikroskopie-volumens von etwa 500 000 μm^3 aus Schicht 4 des primären somatosensorischen Kortex der Maus und die Analyse der rund 2,7 m an Neuriten und 400 000 Synapsen darin. Die Grösse dieser Rekonstruktion wurde ermöglicht durch effiziente halbautomatische Rekonstruktionsmethoden, die in diesem Kapitel beschrieben werden. Das daraus resultierende subzelluläre Konnektom wurde verschiedenen Analysen unterzogen. Zum Beispiel wurde das Konnektom verwendet, um Obergrenzen für den mit saturierter Hebb'schen Plastizität kompatiblen Schaltkreisanteil zu bestimmen.

In Kapitel 3 wird eine Methode zur Analyse von Neuron-zu-Neuron-Konnektomen eines lokalen kortikalen Schaltkreises vorgestellt. Durch Simulation wird gezeigt, dass von dem Konnektom eines lokalen kortikalen Schaltkreises abgeleitete Statistiken ausreichen für die Bayes'sche Auswahl zwischen sieben alternativen Schaltkreismodellen. Darüber hinaus wird gezeigt, dass «gewichtete» Konnektome mit Information über Verbindungsstärken ausreichen zur Unterscheidung zwischen künstlichen rekurrenten neuronalen Netzen mit biologisch plausibler Verbindungsdichte, die sich nur unterscheiden durch die Aufgabe, für die sie trainiert wurden.

Schliesslich wird in Kapitel 4 ein konnektomischer Vergleich zwischen der Grosshirnrinde von Mäusen und Menschen vorgestellt. Mit einer Kombination effizienter automatischer und manueller Analysemethoden wurden neun Elektronenmikroskopievolumen aus kortikaler Schicht 2/3 von Maus, Makak und Mensch analysiert. Diese Daten wurden verwendet, um die relativen Beiträge errengender und hemmender Synapsen auf Pyramidalneuronen abzuleiten. Die erhöhte Interneuronenpopulation in der menschlichen Grosshirnrinde im Vergleich zur Maus ist nicht einhergehend mit einer entsprechenden Zunahme an synaptischer Hemmung auf Pyramidenneuronen, sondern mit einer Erweiterung des Interneuron-zu-Interneuron-Netzwerks.

Introduction

The human brain consists of an estimated 86 billion neurons, each receiving and transmitting signals from and to other neurons through thousands of synapses. This high degree of connectivity is possible because of the specialized morphology of these cells: Neurons extend centimeter-to-meter long and micrometer-to-nanometer thin and branching neurites that support the flow and transformation of signals. Together, this results in a network of unique size and complexity, physically implemented in the extremely dense brain tissue, folded and packed in the human skull.

It is thought that these neuronal circuits and the circuits of the neocortex, in particular, are at the core of our ability to learn, to think logically and abstractly, to be creative, and to navigate complex and changing physical and social environments. These are often considered hallmarks of intelligence. Understanding the biological underpinnings of intelligence is thus among the biggest ambitions of neuroscience.

The following section will briefly introduce the concept of psychometric "general intelligence" and will provide a summary of experimental evidence from human and non-human studies. This evidence indicates promising approaches to studying the neurobiology of intelligence. Being able to reproduce intelligence *in silico* is arguably a necessary but insufficient condition to an understanding of biological intelligence. While insufficient, artificial intelligence still contributes to our understanding of the neurobiology of intelligence: through artificial intelligence-based methods in neurobiological research and by indicating open research questions through its failures. These aspects will be briefly discussed in the subsequent section.

Intelligence in humans and non-human animals

Intelligence is commonly defined as involving "the ability to reason, plan, solve problems, think abstractly, comprehend complex ideas, learn quickly and learn from experience (Gottfredson 1997)" and has been studied for more than 100 years, both in humans and non-human animals. Understanding the biological underpinnings of intelligence is among the biggest ambitions of neuroscience.

Cognitive tests in humans indicate that task performance across many different cognitive domains is positively correlated. For example, humans that perform well on linguistic tests also tend to perform well on other tasks, such as spatial thinking. This positive correlation was termed "*g*-factor", with "*g*" standing for "general intelligence" (Spearman 1927), and was found to explain ~40% of inter-individual variability in task performance (Carroll 1993).

In non-human animals, early empirical research focused on the ability to learn associations between a situation and a response through trial and error (Thorndike 1911) or through reward and punishment (Pavlov 1927, Skinner 1938). Animal behavior was thought of as a combination of innate and learned sensory-motor reflexes (Watson 1913). However, evidence for psychometric "general intelligence" was also found in non-human animals (for a comprehensive review, see (Burkart et al. 2017)). In mice, tests of "general cognitive abilities" across a battery of tasks (including fear conditioning, odor discrimination, and spatial navigation) revealed that individual performance across all tasks was correlated and that a single factor explained 30% to 40% of the inter-individual variability (Matzel et al. 2003). In macaques, ~50% of inter-individual variability in task performance was explained by a single factor that declined with age (Herndon et al. 1997). In the cleaner fish, no evidence for psychometric "general intelligence" was found (Aellen et al. 2022) despite evidence for fish being able to recognize themselves in a mirror (Kohda et al. 2022) or to count (Triki and Bshary 2018).

This evidence from human and non-human animals indicates a number of promising approaches to studying the neurobiology of psychometric “general intelligence”: First, psychometric differences across individuals of the same species can be directly correlated with neurobiological differences. A second approach consists of correlating inter-species differences in psychometric intelligence with neurobiological differences. Finally, the correlated performance across many different tasks is suggestive of a general, brain-wide biological mechanism. Thus, a third approach consists of identifying neurobiological features that are similar across brain areas within individuals, but that are variable across individuals.

To date, studies of the neurobiology of intelligence (for a review, see (Goriounova and Mansvelder 2019)) are mostly based on the former two approaches: Structural and functional brain imaging in humans found psychometric intelligence to be associated with brain volume (Pietschnig et al. 2015), cortical thickness (Narr et al. 2007), and low metabolic rate (Haier et al. 1988) across a large and distributed network of cortical areas and white matter (for a review, see (Jung and Haier 2007)). However, brain size and neuron count cannot fully explain intelligence; macroscopic brain structure and psychometric intelligence in humans are only moderately correlated (e.g., (Narr et al. 2007)), and wales have been reported to have larger brains and more neocortical neurons than humans (Mortensen et al. 2014).

This indicates that differences in psychometric intelligence might rather be associated with differences in neuronal physiology or connectivity. Indeed, recent comparative studies have reported human-specific molecular (e.g., (Bakken et al. 2021)), morphological (e.g., (Mohan et al. 2015)), and electrophysiological (e.g., (Gidon et al. 2020)) neuronal features. Inter-species differences in synaptic connectivity have been reported in terms of volumetric synapse density and synapse size (DeFelipe et al. 2002), but remain largely unknown. This is despite evidence for strong inheritability of psychometric intelligence and for its association with genes related to nervous system development and to synapse structure and function (Savage et al. 2018).

Comprehensive mapping of neuronal morphologies and synaptic connectivity could provide some of these missing data. As indicated above, connectomic comparisons across species, individuals, and brain areas could help to identify pertinent circuit structures, even in the absence of psychometric measurements. While reliant on large amounts of data, such “connectomic screening” has become plausible due to recent developments in volume electron microscopy and artificial intelligence-based analysis methods.

Neurobiology has and continues to inspire the development of artificial intelligence (AI). Vice versa, AI contributes to neurobiology by providing data analysis tools and hypotheses (Fukushima 1980, Helmstaedter 2015, Hassabis et al. 2017, Richards et al. 2019, Kudithipudi et al. 2022). The following section will give a brief overview of how AI is used in the field of connectomics and how limitations in today’s AI may indicate interesting directions for neurobiological research.

“Intelligence” of artificial neural networks

Over the last decade, AI has made tremendous progress. This progress was enabled primarily by three factors: the adoption of deep neural network, the availability of unprecedented computational power in form of graphics processing units (GPUs), and the dramatically increasing amount of digital information for training. Deep learning systems, in form of convolutional neural networks (LeCun et al. 1989, LeCun et al. 1998), first substantially exceeded alternative machine learning approaches on computer vision problems, such as image recognition (Ciresan et al. 2011, Krizhevsky et al. 2012).

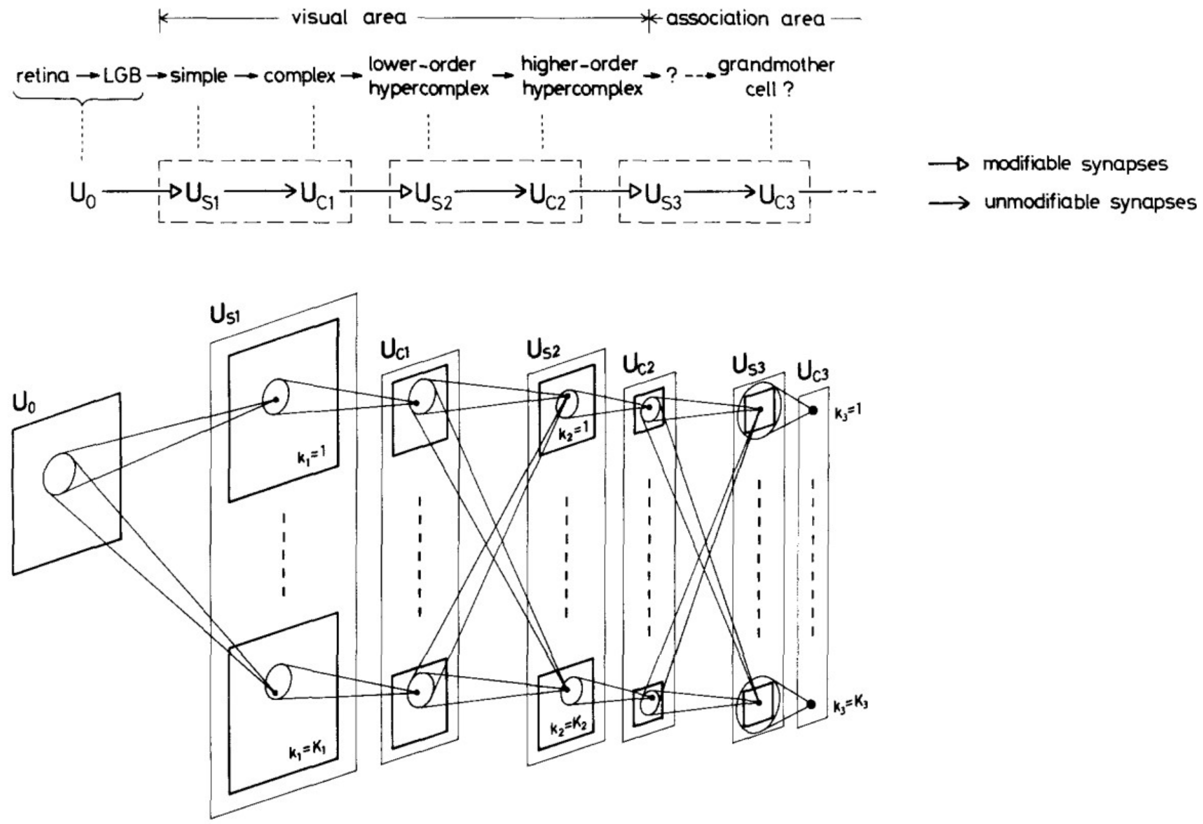

Figure I-1 Architecture of the neocognitron (Fukushima 1980), a neurobiologically inspired artificial neural network for shift invariant pattern recognition. Top: Correspondence between the layers of artificial neural networks (U_0, U_{S1}, U_{C1}, etc.) and the hierarchical model of cat visual cortex proposed by Hubel and Wiesel (1959), Hubel and Wiesel (1962). Bottom: Spatial representation of the artificial neurons and their connectivity. Note that each neuron receives inputs only from a small set of neuron in the previous layer that represent a finite patch of the visual field. Modified and reproduced with permission from Springer Nature.

The architecture of these convolutional neural networks (CNNs) was based on the neocognitron (Figure I-1; (Fukushima 1980)), which was largely inspired by the research of Hubel and Wiesel (1962) in the cat visual cortex. This biologically-inspired architecture was combined with pragmatic algorithmic decision, such as weight sharing, and error backpropagation (Rumelhart et al. 1986) for training by gradient descent.

The majority of AI systems in connectomics are still backpropagation-trained CNNs (Berning et al. 2015, Dorkenwald et al. 2017, Lee et al. 2017, Januszewski et al. 2018, Heinrich et al. 2021, Sheridan et al. 2022, Schmidt et al. 2022). Some have been claimed to achieve “superhuman” performance (Lee et al. 2017). The combination of deep neural networks and training by backpropagation has also achieved impressive results on other tasks, such as speech recognition (Hinton et al. 2012), playing of video games (Mnih et al. 2015), and the prediction of protein structures (Jumper et al. 2021). The combination of deep neural networks with “big data” and “big compute” enabled AI systems that outperform humans in tasks ranging from playing Go (Silver et al. 2016) to the detection of skin cancer (Esteva et al. 2017).

This is despite substantial differences between biological and artificial neural networks (ANNs). For example, an artificial neuron can establish both positive (“excitatory”) as well as negative (“inhibitory”) connections onto postsynaptic neurons. In contrast, most neurons in the mammalian cerebral cortex are thought to be either excitatory or inhibitory (Dale's principle; (Eccles et al. 1976, Strata and Harvey 1999), but see also (Granger et al. 2017)). Another substantial difference is energy efficiency: While biological neurons are on average only weakly coupled and thus asynchronously and typically only sparsely active, artificial neural networks are simulated by iteratively updating all neurons in lockstep (but see also (Tavanaei et al. 2019, Gallego et al. 2022)). Computation and memory is intermixed in biological neural networks, but artificial neural networks are typically simulated on computers with von Neumann architectures (but see (Zhang et al. 2020)). This architecture is characterized—and today often "bottlenecked" (Backus 1978)—by the separation of data from computation.

To identify potential neurobiological mechanisms of intelligent behavior, it might thus be more informative to consider problems that have remained unsolved in AI. Examples can be found by considering how artificial neural networks learn. ANNs are typically trained in a supervised manner by error backpropagation (Rumelhart et al. 1986). This requires enormous amounts and repeated presentation of training data. Even when ANNs perform well on both the training and test data, they are often "fooled" by minimally perturbed training samples (Szegedy et al. 2013). Such adversarial attacks indicate that today's ANNs do not truly "understand" the task that they were trained on (Goodfellow et al. 2014). Thus, error backpropagation is controversial as a potential biological learning mechanism (Zador 2019, Lillicrap et al. 2020).

Learning multiple tasks remains challenging for ANNs. Today, multi-task ANNs are typically obtained by simultaneously training on all tasks (Ruder 2017). When the different tasks are trained sequentially, later tasks were found to cause "catastrophic forgetting" of earlier tasks (French 1999, Goodfellow et al. 2013, Parisi et al. 2019). In contrast, humans continue to learn new skills and knowledge throughout life, and they often do so by generalizing from previous experiences. Notably, learning new skills also improves previously learned skills. This ability to expand specific into general knowledge is not yet found in today's AI. Humans learn while performing tasks, while in AI the training and inference phases are strictly separated. For an extensive comparison of human and machine learning, see (Lake et al. 2017).

In summary, artificial intelligence has made tremendous progress over the last decade with the adoption of artificial "deep" neural networks. These networks are inspired at least partially by neuroscientific research and the neurosciences profit from progress in AI to automatically analyze the increasing amounts of data. However, there are still limitations in the architecture and learning mechanisms of artificial neural networks that make ANNs lag behind human cognitive performance: ANNs lack general features of human intelligence, such as the ability for lifelong learning across many domains. And the poor generalization performance results in fragility, even on domain-specific tasks. This indicates that much can still be learned by studying the mechanisms of computation and learning in the biological neuronal circuits of the cerebral cortex.

Chapter 1 discusses the use of AI in connectomics and the improvements in accuracy and computational efficiency that would be required for the automated reconstruction of a whole human brain at nanometer resolution. A key analysis challenge in connectomics is the reconstruction of connectomes from three-dimensional electron microscopy (3D EM) image volumes. Because this analysis step reduces giga- and increasingly frequently petabyte-scale image volumes to much smaller data structures describing synaptic connectivity, it is often the computationally most expensive step. This is in essence a computer vision problem, which makes it particularly amendable for convolutional neural networks.

Chapter 2 describes a first attempt to quantify in a mammalian cortical circuit the fraction of connections potentially “learned” by Hebbian synaptic plasticity (Hebb 1949). More precisely, this analysis indicates that only a minority—less than a quarter—of connections in layer 4 of mouse primary somatosensory cortex is consistent with saturated Hebbian plasticity. Such quantifications of circuit plasticity may contribute to the understanding of the tradeoff between learning speed and memory stability in biological intelligence. This tradeoff will be subject of the discussion.

The following section will give a brief historical account of the neurobiological study of brain functions and their biological implementation. The discoveries that the brain is organized into functionally specialized areas and that these consist of separate, but interconnected nerve cells—the neurons—were crucial. This enabled the study of brain functions by characterizing neurons and their connectivity in well-defined regions using light microscopy and electrodes.

Towards a mechanistic understanding of brain functions

In the neurobiological study of cognitive processes, one of the first and most fundamental findings was the functional specialization of the brain. In the second half of the 19th century, Broca and Wernicke correlated the cognitive impairments of their patients with the locations of lesions in the patients’ brains (Broca 1861, Wernicke 1874). Their findings indicated that speech was linked to two regions of the cerebral cortex: Broca’s area in the left frontal lobe for speech production (Broca 1861), and Wernicke’s area in the left temporal lobe for speech comprehension (Wernicke 1874). An alternative approach to studying the local specialization of the brain was pursued by Fritsch and Hitzig (Fritsch and Hitzig 1870). They made use of Galvani’s observation that the leg of a frog reacts to electrical stimulation (Galvani 1791). Fritsch and Hitzig used electrodes to locally stimulate the cerebral cortex of dogs. They observed that stimulations in a particular area of the cerebral cortex could induce muscle contractions on the contralateral side and that the relationship between the stimulated location and the contracted muscles appeared to be consistent across dogs. Together, these experiments provided first evidence for the electrical excitability of the cerebral cortex, for motor cortex, and for the somatotopic organization of parts of the cerebral cortex.

These observations of functional cortical specializations beg the question: What is the cerebral cortex made of? And what are the differences between cortical areas with different functional specializations?

Cellular organization of the cerebral cortex

In the middle of the 19th century, it was still in question whether the cell theory (Schleiden 1838, Schwann 1839) applies to the brain as well. The relationship between cell bodies and the much thinner fibers in nervous tissue was unclear, largely because of inadequate microscopy techniques. A big step forward was taken by the development of a novel staining technique by Golgi (Golgi 1883), which only stains a small subset of neurons. Ramón y Cajal adopted and adapted this staining method and used it in his extensive anatomical studies of, e.g., the bird cerebellum, the retina, and the mammalian cerebral cortex (Ramón y Cajal 1891, Cajal 1899).

These experiments revealed a large diversity in neuronal morphologies (Figure I-2). However, Ramón y Cajal also recognized shared features across neurons: He recognized, for example, that there were two different types of branches emerging from the cell body of each neuron: Most branches—termed “dendrites”—were of large diameter, spatially restricted to the surround of the cell body and often stubbed with spines. But one branch—the “axon”—was thinner, of more complex morphology, spine-free and much longer (despite incomplete staining).

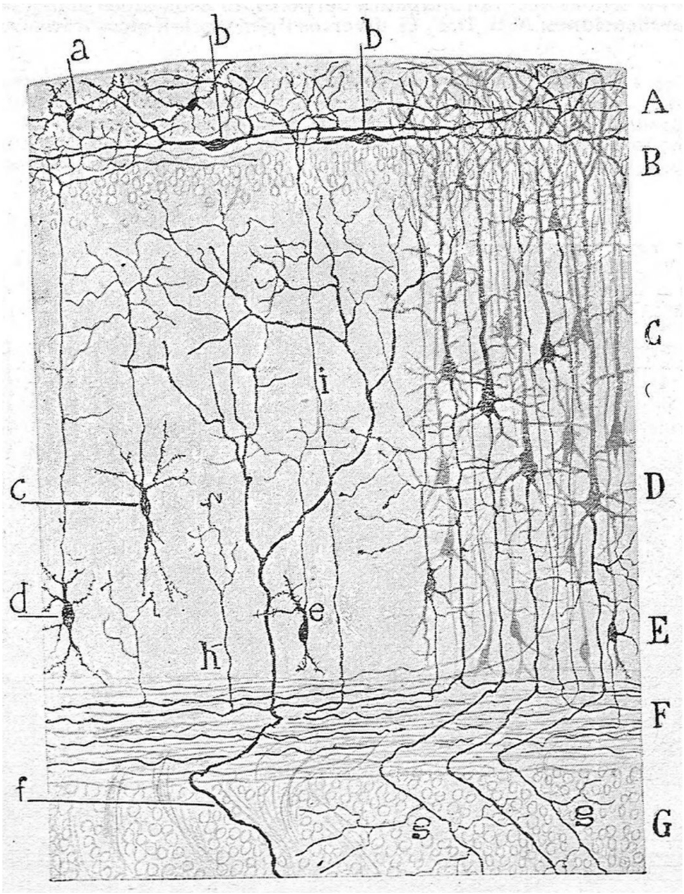

Figure I-2 Summary of the cellular organization of the mammalian cerebral cortex (from rabbits, mice, etc.) drawn by Ramón y Cajal (1923). Note the structures at different spatial scales: the subdivision of the cerebral cortex into five layers (A–E; F: white matter; G: striatum) based on the distribution of cell bodies, the axonal and dendritic morphology of neurons, and subcortical afferents (f) and efferents (g).Types of pyramidal (right) and non-pyramidal (left) neurons were defined based on the morphology of axons (e.g., neurons with ascending axons (c–e)) and dendrites, including the rate of spines.

Based on the morphology of these branches, Ramón y Cajal hypothesized that the branches serve different functions, namely those of collecting and distributing signals. This was based on the thinking that dendritic spines are the sites of synaptic connections. Golgi had previous noticed these dendritic protrusions, but considered them to be an artifact of the staining technique. However, by providing evidence for spines from multiple staining techniques, Ramón y Cajal substantially contributed towards the gradual acceptance of dendritic spines and, ultimately, of the neuron doctrine (Waldeyer-Hartz 1891).

Based on the extensive description of neuron morphologies in the mammalian cerebral cortex, Ramón y Cajal, and later his student Lorente de Nó (Lorente de Nó 1922, Lorente de Nó 1949), separated neurons into distinct cell types. Most importantly, these included various types of pyramidal neurons and interneurons, which were identified based on the characteristic cell body shape and the short axon, respectively, and further subdivided based on the cell body location and the distribution of the axonal and dendritic arbors across cortical layers (Brodmann 1909). From the morphology of interneuron axons, Lorente de Nó inferred potential cell type-specific functions. Furthermore, the vertical orientation of interneuron axons led him to suggest that the cerebral cortex consists of repeated, identical, and vertically aligned units of neurons.

Circuit inference using electrodes and light microscopy

Evidence for functional "cortical columns" was obtained by electrophysiological recordings from the cat somatosensory (Mountcastle 1957) and visual cortex (Hubel and Wiesel 1962). In the latter study, the receptive field properties of neurons were characterized based on extracellular recordings. As the recording electrode was advanced through the visual cortex, changes in receptive field properties were observed. By correlating the receptive field properties with estimated electrode positions, it was noted that neurons aligned along the cortical axis often responded most strongly to stimuli in the same eye and of similar orientation. However, marked shifts in preferred orientations were observed when the electrode was oblique to the cortical axis. Based on these observations, it was concluded that cat visual cortex was composed of discrete columns in which neurons have common receptive field properties. These columns were estimated to span from the pial surface of the cortex to white matter and to measure ~500µm in diameter. (However, the notion of discrete cortical columns in cat visual cortex has since been questioned. For example, neuronal orientation preferences have been described as being arranged in a pinwheel-like pattern (Bonhoeffer and Grinvald 1991). In this arrangement, changes in orientation preferences are mostly continuous. Despite such observations, the notion of functional cortical columns in visual cortex held on. In the visual cortex, "columnar organization" is now typically understood to mean "shared functional properties of neurons along the cortical axis." In this one-dimensional definition of "columns", little importance is given to the implied cylindrical volume with finite radius and well-defined boundary. Furthermore, in the rodent visual cortex, receptive fields appear to be incompatible even with the one-dimensional column definition (Ohki et al. 2005).)

In the same study (Hubel and Wiesel 1962), receptive fields were separated into two categories: "Simple" receptive fields were described as relatively small and could be decomposed into excitatory and inhibitory regions which interacted linearly. "Complex" receptive fields were described as "far more intricate and elaborate" and were defined primarily by exclusion. The distribution of neurons with simple and complex receptive fields was found to differ across layers: Simple cells were found most frequently in layers 3, 4, and 6; and complex cells most frequently in layers 2 and 3. The authors (Hubel and Wiesel 1962) argued that simple and complex cells implement two sequential transformations of the inputs from visual thalamus: Afferents from visual thalamus converge onto cortical neurons as to produce simple receptive fields. And axons of simple cells converge onto other neurons to produce complex receptive fields.

To identify potential synaptic connections implementing these signal transformations, Gilbert and Wiesel (1979) combined intracellular recordings with intracellular injection of horseradish peroxidase (HRP, (LaVail and LaVail 1972)). Compared to the Golgi technique, HRP stained the axonal arbor much more completely. Thus, the simple and complex cells identified by intracellular recordings could be correlated with detailed morphological cell types. Because physical contact is a necessary condition for two neurons to be connected, the morphological reconstructions from multiple experiments could be combined to infer potential synaptic connectivity based on spatial overlap (Figure I-3).

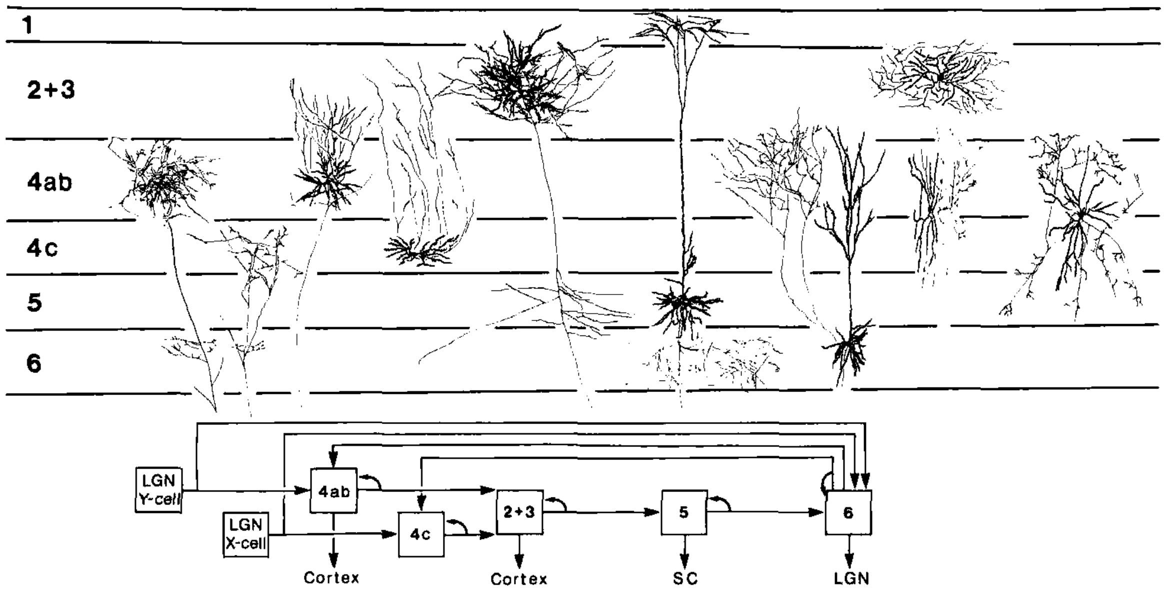

Figure I-3 Schematic diagram (bottom) of the neuronal circuit in cat visual cortex inferred by Gilbert and Wiesel (1979) from the layer-wise distribution of neurons and of their axonal plexus (top). Neurons with cell bodies in, say, layer 2/3 were assumed to be innervated by neurons with axonal plexus in that layer (e.g., layer 4ab and 4c neurons). Note the combination of feed-forward connectivity across layers (from LGN to layers 4, 2+3, 5, and ultimately 6) with recurrent connectivity within layers and from layer 6 back to layer 4. Reproduced from Gilbert and Wiesel (1983) with permission from Elsevier.

Gilbert and Wiesel (1979) assumed that neurons innervated a random subset of the neurons whose cell bodies are located in the layer of densest axonal projections. Based on this assumption, they have inferred that thalamocortical axons innervated the spiny stellate neurons in cortical layer 4 and to a lesser degree the pyramidal neurons in layer 6. This was consistent with the previously observed high proportions of simple cells in these layers. It was also in line with the hypothesis of simple receptive fields being the result of combined thalamocortical innervations. The neurons in layer 4 were hypothesized to innervate the pyramidal neurons in superficial layers 2 and 3, which, in turn, were hypothesized to innervate pyramidal neurons in layer 5. Layer 6 pyramidal neurons, so it was inferred, received synaptic inputs from layer 5 and sent outputs back to layer 4. They hypothesized that this translaminar connectivity was complemented by recurrent connections within layers. Together, these synaptic connections would amount to a "canonical" circuit structure that was repeated across functional cortical columns.

Geometrically inferred potential neural circuits are insightful in that they provide "upper bounds" / necessary conditions on the true synaptic connections. A major limitation of the inferences by Gilbert and Wiesel is the use of somata as model of synaptic input domains: Pyramidal neurons in layer 5, for example, have apical dendrites that span and may receive synaptic inputs across layers 1–5. Reducing complex axonal arbors to the cortical layer of their main plexus is similarly problematic. These limitations were addressed in more recent geometrical circuit inferences (Binzegger et al. 2004, Egger et al. 2014, Markram et al. 2015). Taking into account the complexity of axonal and dendritic arbors provides more accurate estimates of the number of physical contacts and thus of the potential synapses. However, the relationship between physical contacts and actual synaptic contacts, which is central to geometric circuit inferences, is largely inaccessible in light-microscopic neuron reconstructions. The following questions are of particular importance: What fraction of physical contacts is synaptic? And is this fraction constant across the various types of neurons and synapses?

Arguably the “gold standard” method for addressing these questions is electron microscopy. The development of this technique and its applications to the study of individual chemical synapses and of neuronal circuits will be briefly summarized in the following section. These studies were highly informative about the ultrastructural organization of neurons, their synapses, and their organization in the neuropil, but also immensely laborious. Ultimately, this motivated the recent development in electron microscopy techniques that have enabled connectomics and the works in this thesis.

Electron microscopy

The neuron doctrine, according to Ramón y Cajal (1911), states that the brain consists of physically separate cells—the neurons—that are interconnected via specialized contacts between axons on one hand, and somata and dendritic spines on the other hand. Sherrington (Foster and Sherrington 1897) introduced the term “synapse” to refer to these specialized contacts.

Chemical synapses

While the concept of synapses dates back to the end of the 19th century, confirmation thereof—that is, of the physical separation of the interconnected neurons at synapses—required a microscopy technique with sufficient spatial resolution to resolve ~10nm thick cell membranes. The development of the electron microscope (EM; (Knoll and Ruska 1932)) and of techniques for fixation, staining, plastic embedding and thin sectioning of biological tissue (Newman et al. 1943, Pease and Baker 1948, Geren and McCulloch 1951, Palade 1952) finally allowed for the microscopic identification of synapses (de Robertis and Bennett 1955, Palay 1956).

Synapses were characterized as appositions of pre- and postsynaptic membranes that showed “thickenings and increased densities (Gray 1959)”. The presynaptic terminal was identified by the presence of synaptic vesicles of around 30–50nm diameter, which were hypothesized to contain neurotransmitter molecules and to underlie the electrophysiologically inferred quantal release (Fatt and Katz 1952). Evidence for neurotransmitter content in synaptic vesicles was later provided by “fractionation” of nervous tissue, isolation of “synaptosomes” and of the synaptic vesicles therein. The synaptic vesicle fractions were found to be enriched in neurotransmitter molecules (Whittaker et al. 1963, de Robertis et al. 1963). EM also revealed that presynaptic terminals often contained mitochondria.

Gray (1959) provided an influential ultrastructural characterization of synapses in the cerebral cortex (Figure I-4). Synapses were found on cell bodies, dendritic trunks and dendritic spines. These synapses differed in ultrastructure and were subdivided into two types: Synapses onto dendritic spines and a subset of synapses onto dendritic trunks showed thickenings that were noticeably more pronounced along the post- than presynaptic membrane. Overall, the thickened apposition in these synapses made up a large fraction of the total contact site. These are the characteristics of synapses of “type 1” (Figure I-4, top). In contrast, the thickening was found to be only a minor fraction of the total contact in synapses onto cell bodies and in a subset of synapses onto dendritic trunks. Also, the thickening was equally pronounced along the pre- and postsynaptic membranes. These synapses were designated as “type 2” (Figure I-4, bottom). Later, Colonnier (1968) proposed a closely related classification of cortical synapses into “asymmetric” or “symmetric” synapses.

In aldehyde-fixed samples it was found that symmetric—but not asymmetric—synapses were associated in the presynaptic terminal with elongated, non-spherical synaptic vesicles. It had been suggested that asymmetric synapses with spherical vesicles and symmetric synapses with elongated vesicles correspond to excitatory and inhibitory, respectively (Uchizono 1965). This was based on the observations that synapses onto somata and distal dendrites of cerebellar Purkinje cells contained elongated and spherical vesicles, respectively, and that electrophysiological recordings suggested

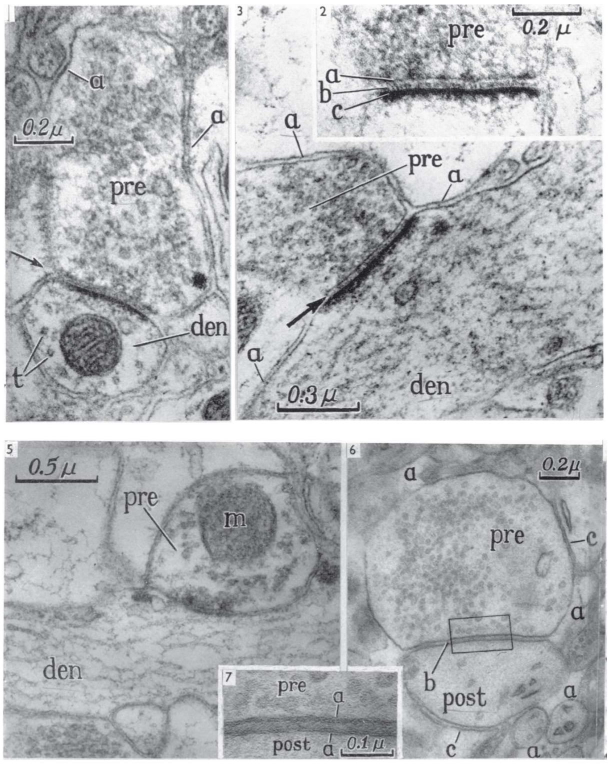

Figure I-4 Synaptic ultrastructure in the rat cerebral cortex revealed by transmission electron microscopy (Gray 1959). Presynaptic (pre) terminals contain synaptic vesicles and occasionally mitochondria (m). Dendrites (den; containing microtubules and occasionally mitochondria) and spine heads (top right and bottom right) are the most common postsynaptic targets. Synaptic contact (insets top right and bottom center) show thickened apposed membranes with clear separation by extracellular space. Two types of cortical synapses were defined based on the patterns of membrane thickening (Gray 1959, Colonnier 1968): asymmetric (likely excitatory) synapses with a prominent postsynaptic density (top), and symmetric (likely inhibitory) synapses with little difference in the pre- and postsynaptic thickening. Note also that symmetric synapses typically only correspond to a minor fraction of the total axo-dendritic contact (e.g., bottom left). Modified and reproduced with permission from Blackwell Publishing Ltd.

strong inhibitory, respectively excitatory connections onto these compartments (Uchizono 1965). The classification of asymmetric and symmetric cortical synapses as excitatory and inhibitory, respectively, was later corroborated by EM images of synapses with immuno-labelling for GABA (Beaulieu et al. 1992).

Degeneration studies of Peters et al. and White et al.

The high resolution of the electron microscope came at the cost of a limited field of view. Typically, the field of view was sufficiently large to classify synapses as asymmetric or symmetric and to distinguish between synapses onto somata, dendritic trunks, or dendritic spines. However, the field of view was typically too small to identify the pre- or postsynaptic cell types.

This problem was partially addressed by the axon degeneration method (Colonnier 1964, Alksne et al. 1966): Colonnier (1964) had observed that lesioning of long-range connections to the cerebral cortex resulted in ultrastructural degenerations, such as accumulation of electron-dense material, in the affected axons. This was exploited by Jones (1968), who lesioned the thalamus to degenerate and thereby identify thalamocortical axons in electron micrographs of the cat somatosensory cortex. In this first study of identified synapses and of the corresponding postsynaptic targets, thalamocortical synapses were found primarily on dendritic spines and shafts in layer 4, but also in adjacent parts of layers 3 and 5.

Among the most influential studies of thalamocortical synapses by axon degeneration are those of Peters and colleagues (Peters and Feldman 1976). Lesions in the lateral geniculate nucleus (LGN) were used to study the postsynaptic targets of thalamocortical synapses in the rat visual cortex. Synapses were found onto dendritic spines (83%), dendritic shafts (15%) and somata (2%), with the latter two targets likely belonging to inhibitory interneurons. This was compared to the overall distribution of asymmetric synapses onto dendritic spines (86%) and dendritic shafts (14%). Because of the similarity in postsynaptic targets, it was noted that thalamocortical terminals "appeared to be disposed randomly, forming no discernible patterns" and it was hypothesized that "every component in layer IV capable of forming an asymmetric synapse is a potential recipient for a thalamocortical axon terminal (Peters and Feldman 1976)". A generalization of this hypothesis later became known as "Peters' rule" (Braitenberg and Schüz 1998).

However, this experimental approach was insufficient to identify the types of neurons postsynaptic to degenerated axon terminals. Because of the thin diameter of spine necks and the large section thickness, even in serial section electron microscopy it was difficult to trace innervated spine heads back to the corresponding dendrites. Inference of the postsynaptic cell type from the local dendritic geometry was an additional challenge. Thus, it remained unclear whether thalamocortical synapses were, in fact, randomly distributed onto spiny dendrites in layer 4 or whether thalamocortical synapses were differentially distributed over the dendrites of the various spiny cell types.

Identification of the postsynaptic neurons became possible by combining axon degeneration with Golgi impregnation of postsynaptic neurons (Blackstad 1975, Fairén et al. 1977, Peters et al. 1977). In one method, the silver chromate of the Golgi stain was chemically replaced by gold deposits, which were then visible under both light and electron microscopes (Fairén et al. 1977).

White et al. made extensive use of this method (or retrograde HRP labeling for projection-based definition of postsynaptic cell types (LaVail and LaVail 1972, Somogyi et al. 1979)) to study thalamocortical connections in layer 4 of mouse primary somatosensory cortex. The following targets were found postsynaptic to identified thalamocortical synapses: spiny stellate (White 1978) and pyramidal neurons in layers 4 (White and Hersch 1981), pyramidal neurons in layers 3 (White 1978), 5 (White 1978) and 6 (Hersch and White 1981), and many interneuron cell types (e.g., (White and Rock 1981)). Many of the same connections were found by similar studies in the visual cortex of rats and cats (for an overview, see (White and Keller 1989)).

Quantitative analyses of these connections indicated that different cell types receive thalamocortical synapses at different rates (White and Keller 1989): The average distance between identified thalamocortical synapses was roughly 5µm along the dendrites of a layer 4 spiny stellate neuron, but around 2µm along the dendrites of a layer 4 bitufted interneuron. The fraction of asymmetric synapses along the dendrite with identified thalamocortical presynaptic terminals was found to be around 13% for the spiny stellate neuron, 20% for the bitufted interneuron, and only 4% for a multipolar interneuron. This is despite identified thalamocortical axons contributing an estimated 20% of the asymmetric synapses in the surrounding neuropil (White and Rock 1981).

Based on these data, White and Keller (1989) proposed "rule 3. Neuronal types receive characteristic patterns of synaptic connections; the actual numbers, proportions, and spatial distribution of the synapses formed by each neuronal type occur within a range of values." with the corollary that "different extrinsic and intrinsic synaptic pathways form specific proportions of their synapses with different postsynaptic elements (spines vs. dendritic shafts, one cell type vs. another)."

In summary, the combination of EM images with high resolution, but small field of view for ultrastructural identification and characterization of synaptic contacts with degeneration and Golgi staining for the identification of pre- and postsynaptic cell types provided valuable insights about the "first" cortical synapses in sensory processing. However, this method also has a number of limitations: Degeneration is heterogeneous across axons, brain regions, and species. This makes absolute quantifications difficult. Furthermore, mechanically-induced lesions are large compared to neurons. As a result, this experimental approach was most suitable to study the synapses in long-range connections. Local cortical connections, in contrast, were more difficult to study. Light and electron microscopy-compatible labeling techniques were too coarse, and the distances between a synapse and the cell bodies of the pre- and postsynaptic neurons—often hundreds of micrometers or millimeters—too large for serial section transmission electron microscopy (ssTEM) at that time. However, a smaller nervous system could be studied using only ssTEM.

Connectome of Caenorhabditis elegans

In 1986, Brenner and colleagues published a comprehensive reconstruction of the hermaphrodite nervous systems of C. elegans (White et al. 1986). For this, worms were fixed with osmium tetroxide, dehydrated, and embedded in epoxy before being cut into approximately 50nm thick sections for ssTEM. Section ribbons were manually picked up, collected on grids, and stained for TEM. Tissue sections were then imaged by TEM microscopes onto film.

For circuit reconstruction, neurons and their synaptic connectivity were marked by Rotring pens directly onto the photographs from approximately 8000 serial sections. Groups of processes were assigned arbitrary labels, which were then copied manually onto each photograph in which the processes were visible. At the same time, a list of synapses between labeled processes was compiled. To reduce human errors (the dominant source of errors), redundancy was used: Synapses were annotated once for each of the involved processes and these annotations were checked for consistency; processes that reached no or multiple cell bodies were corrected; and reconstructions that violated the bilateral symmetry of the nervous system were double-checked. These checks were focused on parts of processes with inconsistent "synaptic behavior" before falling back to an exhaustive search of the reconstructions.

The resulting neuronal connectivity map ("connectome") comprised 302 neurons, 5000 chemical synapses, and 2000 neuromuscular and 600 gap junctions in the hermaphrodite. The ventral cord, in which only every third section was imaged, was later found to miss gap junctions and was completed (Varshney et al. 2011). The value of such a whole-organism connectome is being questioned (Bargmann and Marder 2013), but it has also been claimed that the C. elegans connectome "has profoundly influenced subsequent studies of the function of neural circuits in this species (Briggman and Denk 2006)". Despite these successes, no further whole-organism or other large-scale connectomes were pursued in the following decades. (Connectomes of both sexes of adult C. elegans were published only recently (Cook et al. 2019).)

Reason for this was partly the large amount of labor involved in preparing, imaging and then manually annotating the series of thousands of tissue sections. (Though computer-aided reconstruction methods had been explored (Levinthal and Ware 1972, White 1974).) Furthermore, the manual handling of the 50nm thick tissue sections was prone to errors. Sections could get contaminated by debris, deformed, or break. Even few problematic sections were prohibitive to the faithful reconstruction of processes through the image series and thus of the connectome. While thicker sections could alleviate these problems, the poor depth resolution even in 50nm thin sections was (after human errors) the second most common source of reconstruction errors.

Recent developments in volume electron microscopy techniques have at least partially addressed these issues. In the following section, three connectomic volume EM techniques and their tradeoffs in terms of automation, reliability, image quality and acquisition speed will be discussed. Of these, serial section transmission electron microscopy (ssTEM) and a combination of automated tape-collecting microtomy and multi-beam scanning electron microscopy (ATUM-multiSEM) have recently been used to image volumes on the order of $(1\text{mm})^3$ from the mammalian cerebral cortex. However, analysis of these petabyte-scale EM volumes is currently limited by the speed and accuracy of neuron reconstructions. Manual, automated, and hybrid reconstruction methods will be briefly surveyed at the end of the following section.

Modern volume electron microscopy

Serial block-face scanning electron microscopy (SBEM)

To address the limitations of manual section handling, serial block-face scanning electron microscopy (SBEM; (Denk and Horstmann 2004)) has been proposed. Instead of manually cutting and collecting tissue sections prior to image acquisition, SBEM alternates between imaging and automated, diamond knife-based ablation of the surface of a tissue block. Because imaging is performed on the tissue block surface, consecutive images are pre-aligned and mostly devoid of physical deformations (though electron beam deflections caused by the accumulation and deposition of charged debris is a problem; see also chapter 1).

For the same reason, SBEM is incompatible with transmission electron microscopy. Furthermore, the lack of surface structure after diamond knife-based ablation results in poor contrast by secondary electron detection. Instead, images are generated by the detection of backscattered electrons from a scanning electron beam. This has a number of implications. Because of the relatively low rate of detected backscattered electrons, comparably high electron doses are required. This comes at the risk of degenerated image resolution through charge accumulation and through degradation of the plastic embedding, which negatively affects cutting quality. The risk of charge accumulation was partially addressed by providing neutralizing charges in form of gas molecules or atoms in the microscopy chamber that get ionized by (a small fraction of) the electron beam. Thus, SBEM was typically carried out in low vacuum. The required electron doses (and with it the image quality and acquisition speed) were further improved by the development of high-contrast staining (e.g., (Hua et al. 2015)).

Together, this results in a 3D-EM technique that reliably produces image volumes on the order of $(100\mu\text{m})^3$ at voxel sizes of around $12\times12\times25\text{nm}^3$ at effective image acquisition rates of up to ~6MHz (e.g., (Briggman et al. 2011, Helmstaedter et al. 2013, Wanner et al. 2016, Kornfeld et al. 2017, Schmidt et al. 2017, Svara et al. 2018, Motta et al. 2019, Karimi et al. 2020, Gour et al. 2021, Loomba et al. 2022)). However, even under these highly idealized conditions it would take more than 600 years to image the 450mm^3 of a whole mouse brain. And a volume of $(1\text{mm})^3$ for the study of local circuits in the mouse cerebral cortex would still take more than 1.5 years.

The effective imaging rate is limited by time spent on cutting and stage movements for image tiling. To overcome the issue of low imaging speed in SBEM and the practical issues arising from the tight coupling image acquisition with diamond knife-based ablation, alternative approaches have been developed (Figure I-5).

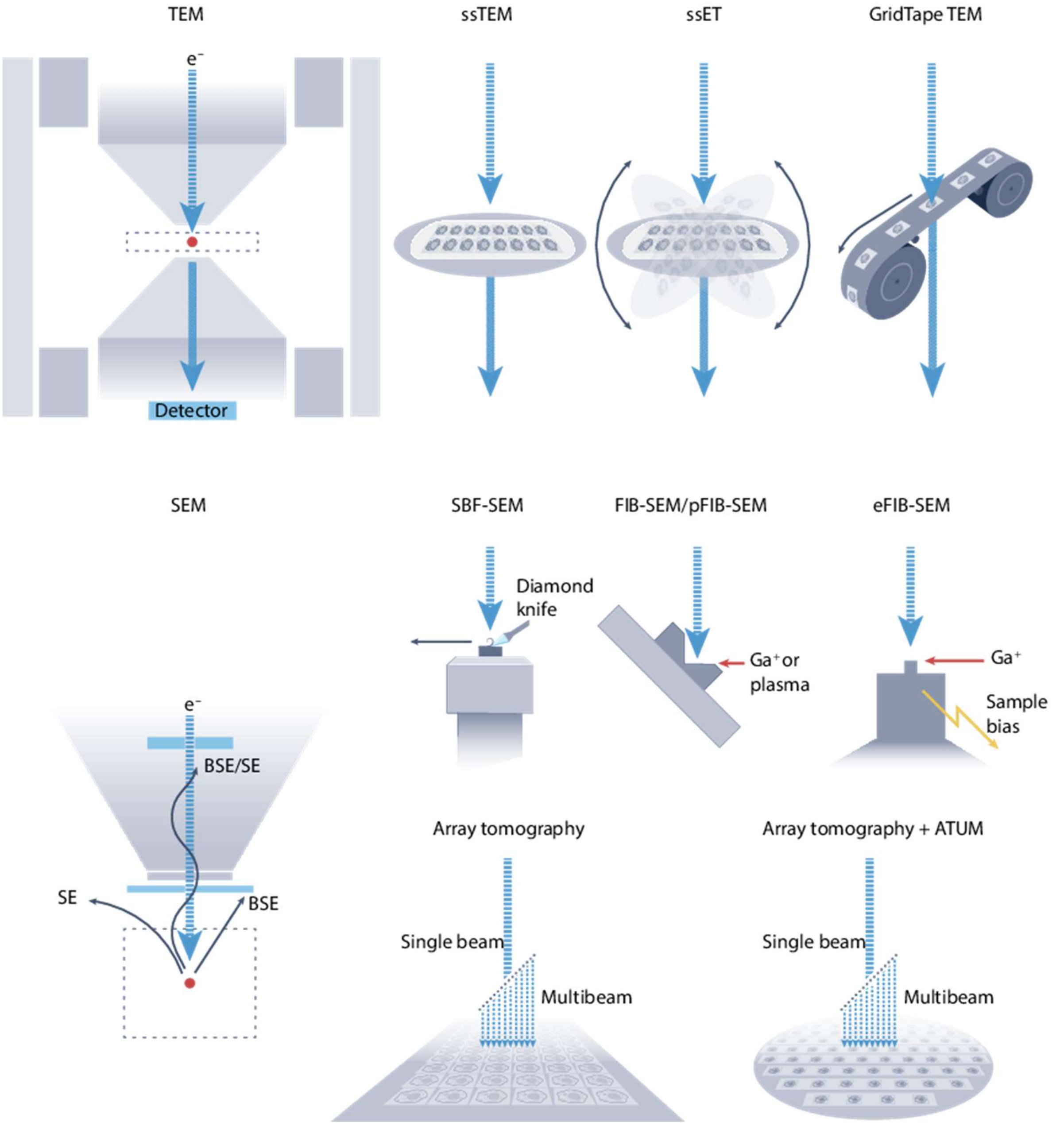

Figure I-5 Overview of modern volumetric transmission (TEM; top) and scanning (SEM; bottom) electron microscopy methods used in connectomics. The high spatial resolution of TEM enabled the first visualization of synapses (Palade and Palay 1954). Serial section TEM (ssTEM) was used for the three-dimensional reconstruction of the C. elegans nervous system (White et al. 1986) and is still used in large-scale connectomic efforts (Zheng et al. 2018, MICrONS consortium et al. 2021). Serial section tilt electron tomography (ET) enables virtual re-sectioning, which was used, for example, in a detailed analysis of the structure-function relationship in cortical synapses (Holler et al. 2021). GridTape TEM (Graham et al. 2019) was used for automated TEM imaging of motor control circuits in the Drosophila nerve cord (Phelps et al. 2021). Serial block-face SEM (SBF-SEM / SBEM; (Denk and Horstmann 2004)) was used, for example, to study the neural circuits of the retina (Briggman et al. 2011) and in the works in chapters 2 and 4. Focused ion beam SEM (FIB-SEM; (Knott et al. 2008)) was used in an enhanced variant (eFIB-SEM; (Xu et al. 2017)) to image and reconstruct a substantial portion of the Drosophila central brain at high and isotropic resolution (Scheffer et al. 2020). Multi-beam SEM (multiSEM; (Eberle et al. 2015)) imaging of section series automatically collected on wafers (Templier 2019) is a promising approach for imaging of very large tissue volumes at high speed and quality. Automated tape-collecting ultramicrotomy (ATUM; (Schalek et al. 2011, Hayworth et al. 2014)) has been used in combination with multiSEM to image large tissue volumes from mouse (Sievers) and human cerebral cortex (chapter 4 and (Shapson-Coe et al. 2021)). Reproduced from Peddie et al. (2022) with permission from Springer Nature.

Serial section transmission electron microscopy (ssTEM)

Transmission electron microscopy offers high in-plane resolution, non-destructive imaging, and high image acquisition speed. The tissue sample is typically cut into ~50nm thick sections, which are then placed in electron-transparent slots in a sample holder. The manual and error-prone handling of tissue sections is increasingly being replaced by robot-assisted (Lee et al. 2018) and fully-automated (Graham et al. 2019, Phelps et al. 2021) methods. Image acquisition speed was optimized by using an array of CCD (Bock et al. 2011) or CMOS (Zheng et al. 2018) sensors, or a combination of a custom scintillator with a large-format CMOS sensor (Yin et al. 2020). This increased the field of view and thus the interval between time-intensive stage movements.

ssTEM was used to image the complete brain of an adult Drosophila melanogaster (Zheng et al. 2018). More recently, ssTEM was used to acquire a volume of nearly 1mm^3 from functionally characterized primary and higher-order visual cortices of mouse (MICrONS consortium et al. 2021). In the latter case, image acquisition was further sped up by parallelization across five ssTEM setups, each with nominal effective imaging speed of 100MHz (Yin et al. 2020, MICrONS consortium et al. 2021). Across the entire experiment, acquisition of roughly 1mm^3 at 4×4×40 nm^3 nominal voxel size took 6 months, corresponding to a throughput of ~26MB/s per microscope (Yin et al. 2020).

Despite the increasingly automated tissue sectioning and section handling, large-scale ssTEM volumes typically suffer from high rates of image defects, such as knife marks, cracks and folds (MICrONS consortium et al. 2021, Macrina et al. 2021). These defects correspond to complex deformation or loss of tissue, both of which complicate the alignment of the two-dimensional images into a continuous three-dimensional image volume. Together, the defects and resulting alignment issues are the primary limiting factors in the automated circuit reconstructions from large-scale ssTEM volumes. It has been noted that “robust handling of image defects is crucial for real-world accuracy, and is where human experts outshine AI (Lee et al. 2019)”. Thus, circuit reconstructions in the ssTEM volumes of the whole fly brain or of mouse visual cortex are typically done manually (e.g., (Bates et al. 2020)) or semi-automatically (Dorkenwald et al. 2022).

Automated tape-collecting ultramicrotomy (ATUM) for multi-beam scanning electron microscopy (multiSEM)

Around the same time that SBEM was developed, Hayworth, Schalek et al. worked on an alternative approach to address the issue of manual section handling in ssTEM (Hayworth et al. 2006, Schalek et al. 2011, Hayworth et al. 2014). The goal was to automate the cutting and collecting of tissue sections onto a substrate suitable for imaging by SEM (Schalek et al. 2011, Hayworth et al. 2014). In this approach, tissue sections are cut by a standard ultramicrotome and automatically collected from a water boat onto tape. Within 24 hours, 1000 to 10,000 sections can be automatically collected on tape. Because of the lack of manual handling, this method allows for the collection of long series of large and thin tissue sections of high quality.

For imaging by SEM, the tape is then cut into strips and mounted onto an electrically conductive substrate, typically a silicon wafer. To avoid charge accumulation, the tape is “connected” to the wafer by applying a conductive paint along the tape edge. These steps are performed manually and have the risk of contaminating or damaging the sections. Furthermore, this approach has stringent requirements for the tape: For the collection of tissue sections from the water boat, the tape must be hydrophilic, which is achieved by plasma treatment (Kubota et al. 2018). Furthermore, the tape must be electrically conductive (to avoid charge accumulation during imaging) and free of electron contrast.

ATUM decouples tissue sectioning from SEM imaging. As a result, it is possible to prepare section series, image them at low resolution using light or electron microscopy, and perform the resourceintensive high-resolution EM imaging only if quality checks are met. This substantially reduces the complexity and risk of large-volume EM experiments compared to SBEM. Using multiple ATUM setups, multiple samples or even multiple blocks from the same sample (Hayworth et al. 2015) could be cut in parallel.

As a further consequence of decoupling the sectioning from imaging, a larger fraction of microscope time is spent imaging. This overhead reduction is particularly important for microscopes with high image acquisition speeds, such as the recently developed multi-beam scanning electron microscopes (multiSEM; (Eberle et al. 2015)). To reduce the overhead from exchanging sample holders, it is also important to maximize the density of tissue sections per silicon wafer. Using ATUM, for example, around 220 sections of $(1.3\text{mm})^2$ were fit onto a $(100\text{mm})^2$ wafer (Sievers unpublished). Recently, an alternative approach has been proposed that uses magnetic force to automatically collect sections onto a silicon wafer (Templier 2019). By collecting 203 sections of 0.8mm×1.4mm onto a roughly $(40\text{mm})^2$ wafer, this method has demonstrated nearly 4-fold higher packing density.

ATUM combined with single-beam SEM was used to generate image volumes from the mouse visual cortex ($40\times40\times50\mu\text{m}^3$ at $3\times3\times29\text{nm}^3$ voxel size and an average effective imaging rate of 0.5MHz; (Kasthuri et al. 2015)) and thalamus ($400\times600\times280\mu\text{m}^3$ at $4\times4\times30\text{nm}^3$ voxel size and average effective imaging rate of ~12MHz; (Morgan et al. 2016)) and the cerebellum ($190\times120\times49\mu\text{m}^3$ and $190\times120\times75\mu\text{m}^3$ at $4\times4\times30\text{nm}^3$ voxel size and 5MHz brutto imaging rate; (Wilson et al. 2019)). Multi-beam SEM imaging of ATUM samples was used to acquire EM volumes from mouse primary somatosensory cortex ($1.3\times1.3\times0.25\text{mm}^3$ at $4\times4\times35\text{nm}^3$ voxel size and 240MHz effective imaging rate; (Sievers unpublished)) and from human temporal cortex (around $4.2\text{mm}^2\times0.175\text{mm}$ at $4\times4\times(30\text{–}40)\text{nm}^3$ voxel size and 125–190MHz effective imaging rate, (Shapson-Coe et al. 2021)) and ($1.1\times1.1\times0.082\text{mm}^3$ at $4\times4\times(35\text{–}40)\text{nm}^3$ voxel size and ~1.2GHz brutto imaging rate; (Loomba et al. 2022)), both on a 61 beam Zeiss multiSEM.

Circuit reconstructions from volumetric electron micrographs

Semi-automated computer-assisted circuit reconstruction has been explored already in the 1970ies (Levinthal and Ware 1972, White 1974). Since then, automated and semi-automated methods for circuit reconstruction from volume EM have improved dramatically. However, due to improvements in EM techniques, the image volumes and the average length of the neurites contained in these image volumes have increased as well. Thus, the observation from 1972 that "with current techniques of embedding, cutting, staining and preparing of micrographs … the difficulty in obtaining three dimensional information does not lie primarily in the preparation of the photographs of many serial sections but rather in making use of the photographs in such a way that useful information can be obtained (Levinthal and Ware 1972)" remains highly relevant.

Circuit reconstruction evolved from fully manual volume reconstructions (e.g., (Fiala 2005, Morgan et al. 2016)) to fully manual neurite center-line ("skeleton") reconstructions (e.g., (Briggman et al. 2011, Wanner et al. 2016, Eichler et al. 2017)) to overlapping fully manual skeleton reconstruction with automatically generated volume over-segmentations (Helmstaedter et al. 2013).

The latter approach was enabled by the adoption of machine learning-based methods for the automated detection of cell membranes, which serve as boundaries for image segmentation algorithms. These methods include random forest classifiers (Andres et al. 2008, Kaynig et al. 2010), learned probabilistic ridge detection (Mishchenko et al. 2010), and convolutional neural networks (CNNs; (Jain et al. 2007, Turaga et al. 2009, Berning et al. 2015, Lee et al. 2017, Sheridan et al. 2022)). Today, most automated circuit reconstruction workflows use CNNs for the detection of cell membranes, with the output serving as "elevation map" for volume segmentation by watershed transform (but see (Januszewski et al. 2018, Meirovitch et al. 2019) for alternative approaches). Each resulting segment is typically contained in a single neurite, but each neurite is still split into many segments. To reduce the number of split errors per neurite, volume segments are typically "agglomerated" by machine learning-based methods (Andres et al. 2008, Jain et al. 2011, Nunez-Iglesias et al. 2013, Parag et al. 2015, Lee et al. 2017, Motta et al. 2019).

As a result of these improvements, the circuit reconstruction approaches gradually shifted from manual reconstructions augmented by automation (e.g., (Helmstaedter et al. 2013)) to (a combination of manual and) exhaustively proofread automated reconstructions (e.g., (Mishchenko et al. 2010, Kim et al. 2014, Kasthuri et al. 2015)). As error rates decreased further, exhaustive proofreading became inefficient. Thus, reconstruction speed was optimized by "focusing" manual inspection and correction efforts onto automatically detected locations of reconstruction errors (Plaza et al. 2012, Takemura et al. 2015, Motta et al. 2019). Likely error locations are identified based on implausible local morphology (Meirovitch et al. 2016, Rolnick et al. 2017, Zung et al. 2017, Motta et al. 2019) or transitions in neurite types (Li et al. 2020).

In chapter 2, automated reconstructions in combination with focused error corrections were used to obtain a dense circuit reconstruction from a SBEM volume from layer 4 of mouse primary somatosensory cortex. This reconstruction was ~300 times larger and obtained ~20-times more efficiently than previous dense reconstructions from the mammalian cerebral cortex.

In collaboration with Meike Sievers, Martin Schmidt, and scalable minds, the automated reconstruction methods were later substantially improved in terms of accessibility, computational efficiency, and reconstruction quality for a petabyte-scale ATUM-multiSEM dataset from mouse primary somatosensory cortex (Sievers unpublished). The most notable changes are the adoption of improved CNN architectures and training procedures (Lee et al. 2017) and the use of biologically-informed global constraints to prevent merge errors during agglomeration. When applied to the SBEM volume from layer 4 of mouse primary somatosensory cortex, these changes increased the expected run length (ERL) from ~8µm (Motta et al. 2019) to ~130µm. Together with a synapse detection method specifically developed for SBEM, these methods were used in the connectomic reconstruction and comparison of cortical layer 2/3 of mouse (n=5 SBEM volumes), macaque (n=2), and human (n=2) in chapter 4.

Subcellular connectomic analyses

With the recent methodological improvements, the acquisition of EM volumes on the order of $(100\mu m)^3$ has become routine. However, these volumes are still orders of magnitudes smaller than the volumes necessary for reconstruction of cortical connectomes between identified pre- and postsynaptic neurons in mouse (Figure I-6). Despite this limitation, $(100\mu m)^3$ volumes of mouse cerebral cortex are rich in information: They contain roughly hundred neuronal somata, meters of neurites, and millions of synapses (Braitenberg and Schüz 1998). Individual neurites and their synaptic connections can be reconstructed over tens to a few hundred micrometers. The analysis potential of these volumes also comes with unique challenges: Because most neurites cannot be followed to the corresponding soma, established electrophysiological, molecular or even morphological neuron classifications are unavailable for them. Instead, neurites must be characterized based on their ultrastructure (e.g., size and distribution of mitochondria), their detailed local morphology (e.g., spine density, inter-bouton distance, bouton volume) or their synaptic connectivity.

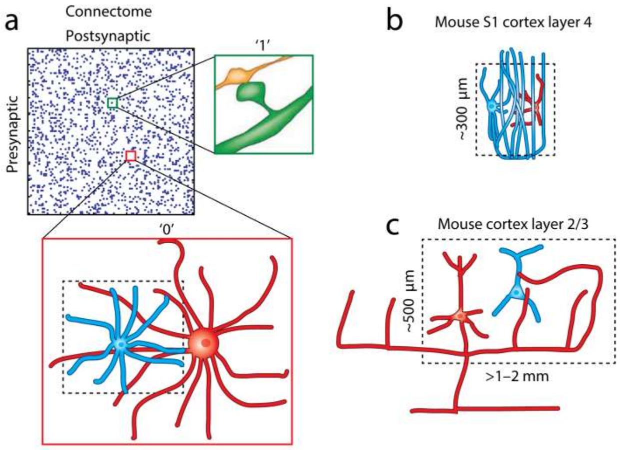

Figure I-6 Intralaminar neuron-to-neuron connectomes in mouse primary somatosensory (S1) cortex and their minimal circuit volumes. EM volumes smaller than the minimal circuit volume can be used for subcellular connectomic analyses (see chapters 2 and 4). **(a)** In its most simple form, a neuron-to-neuron connectome is represented by a binary adjacency matrix. Matrix entries indicate the presence ('1') or absence ('0') of synaptic connections (right) between pre- and postsynaptic neurons. To measure the absence of a connection (bottom), the dendrites of the postsynaptic neuron must be reconstructed completely. The presynaptic axon must be reconstructed from the soma to all terminals plausibly in contact with the postsynaptic neuron. The smallest volume containing both of these reconstructions is called 'minimal circuit volume'. **(b,c)** The minimal circuit volumes for neuron-to-neuron connectomes of the intralaminar, recurrent connectivity in mouse S1 is (b) approximately (300µm)^3 in layer 4 and (c) approximately (1–2mm)^2×0.5mm in layer 2/3. Modified and reproduced from Helmstaedter (2013) with permission from Springer Nature.

Even at this subcellular level, morphologies and connectivity of neurites in mammalian cerebral cortex were found to be highly structured, non-random, and informative about cortical organization. The following sections will discuss how subcellular connectomes can be used (i) to quantify the degree to which the synaptic outputs of axons can be predicted from proximity to postsynaptic targets, (ii) to make inferences about synaptic strengths and plasticity mechanisms, (iii) for the definition axons with evidence for non-random innervation of subcellular targets, and (iv) to compare the relative contributions of excitatory and inhibitory neurons to the synaptic inputs onto the dendritic trees across cell types and species.

Testing the geometric predictability of synaptic connectivity (Peters' rule)

In their studies of thalamocortical synaptic connectivity (see "Degeneration studies of Peters et al. and White et al."), Peters and Feldman (Peters and Feldman 1976, Peters 1979) argued that thalamocortical axon terminals in layer 4 innervated all available postsynaptic elements in proportion to their availability. As a corollary, all dendrites in layer 4 are supposed to be innervated by thalamocortical axons at equal rate. Braitenberg and Schüz (1998) later generalized these suppositions to all connections in the cerebral cortex and termed this generalization "Peters' rule".

The idea that synaptic connectivity could be inferred from proximity between neurons was at the core of efforts to understand or simulate the brain (Binzegger et al. 2004, Egger et al. 2014, Markram et al. 2015, Reimann et al. 2015). It is hypothesized that statistical connectivity inferred from overlaps between light-microscopic reconstructions of neuron morphologies (potentially from multiple experiments) provides a sufficient description of neuronal circuits. In this context, the complete connectivity maps by EM-based connectomics are of limited value (da Costa and Martin 2013). Thus, testing Peter's rule beyond thalamocortical connections (see "Degeneration studies of Peters et al. and White et al.") was a highly relevant research question for early connectomic studies.

Mishchenko et al. (2010) used ssTEM to image four neuropil volumes from the stratum radiatum of rat hippocampus, spanning a total of ~670µm^3. They asked whether the density of input synapses along micrometer-long fragments of spiny dendrites could be predicted from the number of axons around them. Because only a small fraction of these axons established synapses onto that dendrite, they introduced a distance-dependent contact-to-synapse conversion fraction. However, even with this distance-dependent model, the dendritic synapse density was poorly predicted. This was interpreted as evidence for changes in the conversion factor along or across dendrites. Instead, Mishchenko et al. (2010) found that local dendritic synapse density could be predicted based on the average circumference of the dendritic trunk.

Kasthuri et al. (2015) used ATUM-SEM to image a volume of 80,000µm^3 from layer 5 of mouse somatosensory cortex. For their reconstructions they followed the approach of Mishchenko et al. (2010): Using semi-automated methods, they densely reconstructed three cylinders, each ~600µm^3 in size and centered onto an apical dendrite. When accounting for overlaps, the total reconstructed volume amounted to ~1500µm^3. For their analyses, Kasthuri et al. (2015) started with the observation that approximately 14–17% of excitatory connections onto the spine heads of the central apical dendrites consisted of multiple synapses. In the following, they asked whether these multi-synaptic connections could be the result of random synaptic connections following Peters' rule.

First, they quantified for each excitatory axon that enters the cylindrical volume around an apical dendrite the path length within this volume. This path length was found to be only weakly correlated with the number of synapses an axon established onto the central apical dendrite. Similarly, the number of physical contacts (both synaptic and non-synaptic) between an axon and the spines of the central apical dendrite was found to be essentially uncorrelated with the number of synapses.

Second, they directly addressed the question whether the observed multi-synaptic connections could be the result of random synaptic connectivity. Specifically, they asked whether the observed synaptic contacts were a random subset of all physical contacts between excitatory axons and the spines of the central apical dendrite. To test this, they considered a random subset of physical contacts as synaptic contacts while keeping constant the total number of synapses per axon and per spine. They found that the observed number of multi-synaptic connections far exceeded expectation based on random connectivity. Similarly, they reported that the number of synapses that an excitatory axon established on a segment of the central apical dendrite was correlated with the number of additional synapses onto the same dendrite beyond that segment.

In conclusion, the detailed subcellular morphology and synaptic connectivity of neurites in small electron microscopy volumes provided evidence for non-random local excitatory connectivity in the mammalian brain. In rat hippocampus, poor predictability of the synapse density along a dendrite based the number of surrounding axon fragments was found (Mishchenko et al. 2010). In mouse somatosensory cortex, the probability of synapses onto a particular apical dendrite was found to be inhomogeneous across excitatory axons (Kasthuri et al. 2015).

However, due to the small image volumes, these studies were limited to testing Peters' rule at short length scales. The above-mentioned analyses were limited to radii of at most 1µm (Mishchenko et al. 2010) and ~5µm (Kasthuri et al. 2015), respectively. Therefore, these studies were unable to directly quantify the geometric predictability of synaptic connections from light-microscopic reconstructions of neuron morphologies. The alignment of morphological reconstructions from multiple light-microscopic experiments is typically on the order of a few tens of micrometers. Thus, a direct treatment of this question became possible only with EM volumes in which even the smallest dimension is a few tens of micrometers in length. The first such EM volume from the mammalian cerebral cortex and quantitative tests of various formulations of Peters' rule are described in chapter 2.

Because of the limited extent of previous EM volumes (Mishchenko et al. 2010, Kasthuri et al. 2015), each axon fragment was short and established only a small number of synapses within the reconstructed image volume. Thus, only little information was available for sub-classification of excitatory axons. As a result, it could not be excluded that the observed non-random connectivity was, in fact, the result of two or more subtypes of excitatory axons with different target-preferences, but random synaptic targeting. In chapter 2, this issue could be partially addressed because the reconstructed excitatory axons were sufficiently long that morphological and connectomic features were descriptive enough for a separation of thalamocortical and corticocortical axons.

Interneurons make up only 8%–25% of the neuron in the rodent cerebral cortex (see chapter 4) and small fractions of the total axonal and dendritic path lengths. Thus, the small volumes of previous studies contained only few fragments of inhibitory axons and dendrites. Furthermore, it was reported that the few identified inhibitory axon fragments established, on average, fewer synapses than excitatory axon fragments (Kasthuri et al. 2015). As a result, previous studies were unable to test the geometric predictability of synaptic connections originating from inhibitory axons or terminating onto interneuron dendrites. The results of such an analysis are reported in chapter 2.

Inferences about synaptic strength and plasticity

The flow of signals and thus also the computations in neural networks not only depend on the non-random structure in the presence or absence of synaptic connections, but also on the strength of these connections. In general, connection strengths are highly variable. For example, paired electrophysiological recordings from spiny neurons in layer 4 of rat primary somatosensory cortex indicate that connections strengths, as measured by the average evoked excitatory postsynaptic potentials (EPSPs), range from 0.3mV to 9.6mV (Feldmeyer et al. 1999). The distribution of connection strengths even within homogeneous neuron populations is positively skewed and approximately log-normal (Buzsáki and Mizuseki 2014). The range of EPSP amplitudes is even larger when considering differences across cell types: Across 36 different excitatory connections in mouse primary somatosensory cortex, EPSP amplitudes were found to range from 0.04mV to 7.79mV (Lefort et al. 2009). Ideally, a connectome would thus contain information not only about the presence and absence of connections, but also about connection strengths.

Connection strength is the result of many factors: To first approximation, connection strength scales linearly with the number of synapses. Direct measurements of the number of synapses in a connection is possible in large EM volumes that cover at least the minimal circuit volume (Helmstaedter 2013). And alternative approach consists of light-microscopic neuron reconstructions followed by inspection of putative synaptic contacts in many targeted small EM volumes (e.g., (Markram et al. 1997, Holler et al. 2021)). However, due to the intracellular stain, accurate classification of contacts as synaptic or non-synaptic is non-trivial.

Notably, this approximation assumes that all synapses contribute equally to the total connection strength. Experimental evidence suggests, however, that even individual synapses differ in strength (Matsuzaki et al. 2001). It is thought that synapse strength depends on three factors: the probability that a synaptic vesicle fuses and releases neurotransmitter molecules into the synaptic cleft in response to the local increase in Ca^{2+} concentration that is caused by the depolarization of an action potential; the number of synaptic vesicle release sites; and the average postsynaptic response caused by the release of a single synaptic vesicle. (The average postsynaptic response is itself the result of many factors, such as the number of neurotransmitter molecules per synaptic vesicle, the probability of a neurotransmitter molecule binding to a receptor on the postsynaptic site, the permeability and binding kinetics of these receptors, the ion concentrations and membrane potential in the postsynaptic terminal, etc.)

Structural correlates of synaptic strength

Can the strength of individual synapses be inferred from ultrastructural information contained in EM volumes? One line of evidence comes from EM studies using immuno-labelling for synaptic receptors. For example, strong and significant correlations were observed between synapse size (PSD or active zone) and the number of AMPA receptor-specific immuno-particles (Nusser et al. 1998, Takumi et al. 1999, Kharazia and Weinberg 1999). In excitatory synapses, PSD area was found to be strongly correlated presynaptically with the active zone area and with the number of docked vesicles (Schikorski and Stevens 1997) and postsynaptically with spine head volume (Harris and Stevens 1989, Holtmaat et al. 2005, Arellano et al. 2007, Bopp et al. 2017). Spine head volume, in turn, was found to correlate with the amplitude of excitatory postsynaptic currents (EPSCs) evoked by two-photon-based glutamate uncaging (Matsuzaki et al. 2001) and with the volume of the presynaptic bouton (Knott et al. 2006).

Together, these studies indicate strong correlations between PSD area and quantities that are related to the three-factor model of synaptic strength. A direct measurement of the relationship between total PSD area and EPSP amplitude across synaptic connections was reported only recently (Holler et al. 2021).

In conclusion, these studies indicate that EM-based connectomes of the mammalian cerebral cortex are not limited to binary connectivity matrices, but that structural measurements such as the total PSD area allow the connectome to be augmented with information about connection strengths.

Synaptic long-term potentiation (LTP)

Importantly, the strength of a synapse is generally not static, but may change over time.

Almost 50 years ago, Bliss and Lømo (1973) studied the synaptic connections from axons of the perforant pathway onto granule cells in the dentate gyrus. They found that brief high-frequency stimulations of perforant pathway axons (at 10–20Hz for 10–15s or at 100Hz for 3–4s) using an extracellular electrode reliably (>80%) and rapidly (within seconds) induced long-lasting (30min to 10h) potentiation of the connection by >40%. This study established simultaneous extracellular stimulation of perforant pathway axons and recording of the evoked field potential in granule cells of the dentate gyrus as the model system for long-term potentiation (LTP). Subsequent studies in rabbit and rat indicated that, depending on the stimulation protocol, potentiation may last from hours to many weeks (Abraham 2003).

Since then, hippocampal LTP by extracellular stimulation has been studied extensively (for a review, see (Bliss and Collingridge 1993)). Most excitatory connections in the hippocampus were found to be capable of LTP, and most forms of LTP were found to depend on the activation of postsynaptic NMDA receptors (for a review, see (Malenka 1994)). However, pharmacological activation of NMDA receptors alone was found to be insufficient for LTP induction (Kauer et al. 1988). Instead, the combined activation of NMDA receptors by glutamate released from the presynaptic terminal with simultaneous postsynaptic depolarization (Gustafsson et al. 1987) is necessary to open the NMDA receptors' ion channels and to eject from it the magnesium block, which then allows for the influx of Ca^{2+} (Ascher and Nowak 1988). The mechanism by which Ca^{2+} contributes to the expression of LTP is still under investigation, but Ca^{2+}/calmodulin-dependent protein kinase II (CaMKII) is likely to play a central role (Herring and Nicoll 2016). CaMKII-mediated phosphorylation of AMPA receptor subunits seems to enhance their trafficking to and insertion into the PSD as well as to increase the conductance of the corresponding channels. There is also evidence for CaMKII-mediated modification of PSD proteins, which affects the number of synaptic AMPA receptors through regulation of their rates of endo- and exocytosis and of displacement along the cell membrane. LTP induction was found to correlate with the transport of AMPA receptor into the postsynaptic terminal (Shi et al. 1999) as well as with the polymerization of actin filaments in spine heads (see (Kim and Lisman 1999)).

The latter two could be mechanisms that result in an increase in synapse area and spine head volume, respectively. In fact, already shortly after the discovery of LTP, electron microscopy studies by Van Harreveld and Fifková described stimulation-induced ultrastructural changes (Van Harreveld and Fifková 1975, Fifková and Van Harreveld 1977). In the region of the molecular layer that contains the likely stimulated synapses from perforant pathway axons onto granule cells, a substantial increase in total spine head volume was observed. This change was detected two minutes after stimulation and persisted for at least 23h. The increase was largest (+38%) within the first hour after stimulation, but remained large (+23%) for up to 23h. Interestingly, the total size of axonal boutons and the density of synaptic vesicles transiently decreased within the first hour. In contrast, the total spine head volume remained unchanged in the region of the molecular layer that contains the likely unstimulated synapses from commissural pathway axons onto granule cells. Together, these observations indicate a strong correlation between lasting changes in connection strength and spine head size, and that these changes are specific to the stimulated connections. Furthermore, the mechanisms underlying LTP are likely to be multiple and of varying time courses.

Desmond and Levy conducted similar experiments (e.g., (Desmond and Levy 1983, Desmond and Levy 1988)). In the latter study, synapses were quantified in terms of axon-spine interface (ASI) area, which encompasses both the PSD and non-PSD areas. After stimulation, a substantial increase in the total ASI area per unit neuropil volume was found. This effect was driven primarily by and was significant only for “concave” (large), but not for other (smaller) spine synapses. Furthermore, the increase in total ASI area was due to proportional increases in total PSD and total non-PSD areas.

Structural plasticity and circuit remodeling

To what degree this increase in total synapse size per unit neuron volume was caused by an enlargement of existing synapses or by the addition of new synapses was disputed. By interpreting polyribosomes and multi-synaptic axonal boutons as markers of synaptogenesis, the reduction in these markers post-stimulus was interpreted as evidence for a strengthening of existing synapses (Desmond and Levy 1990). However, other studies reported an increase in the density of synapses onto dendritic shafts (Lee et al. 1980), shafts and stubby spines of likely interneuron dendrites (Chang and Greenough 1984), or spines of spiny dendrites (Trommald et al. 1996) after stimulation.

Even if the synapse density remained constant, could it be that this is the result of balanced removal of existing and addition of new synaptic connections? In fact, it has been argued that LTP may correspond to a balanced redistribution of synaptic strength, without changing the overall synapse densities or sizes (Sorra and Harris 1998).

Monitoring of dendrites for growth or retraction of their spines across time became feasible with the development of two-photon (2P) fluorescence microscopy (Denk et al. 1990, Denk and Svoboda 1997). For a review of 2P-based studies of plasticity-related spine dynamics, see (Yuste and Bonhoeffer 2001).

Using this method, extracellular high-frequency stimulation in organotypic slice cultures of developing rat hippocampus was found to initiate a spatiotemporal window of tens of minutes and restricted to tens of micrometers around the electrode in which the density and length filopodia on individual pyramidal neuron dendrites substantially increased (Maletic-Savatic et al. 1999). Within an hour, roughly a quarter of these filopodia developed a “bulbous”, spine head-like morphology. A similar experiment found that new protrusions emerged in, but only rarely outside of, the dendritic region of long-term potentiated synaptic connections (Engert and Bonhoeffer 1999). When LTP induction failed or was blocked by an NMDA receptor-antagonist, no generation of new, but only a loss of existing spines was found.

In vivo, filopodia and spines on dendrites of pyramidal neurons in layer 2/3 of developing rat barrel cortex were found to be motile, changing in length by roughly 0.2–0.6μm within 10min (Lendvai et al. 2000). Sensory deprivation during the critical period by whisker trimming reduced this motility by ~40%, but did not change the density of filopodia and spines. To study the relationship between the motility of spines and their synaptic innervation, *in vivo* 2P time-lapse imaging of pyramidal neuron dendrites in layer 1 of adult mouse barrel cortex was combined with ssTEM (Knott et al. 2006). Asymmetric synapses were reported on all spines that persisted for ≥4 days, but only on about a third of “younger” spines. Consistent with previous reports (Toni et al. 1999), the axonal boutons presynaptic to these young spines were mostly multi-synaptic (67% vs. 14% on average across random boutons) and thus likely pre-existing. Thus, LTP induction *in vivo* appears to be associated with increased but balanced rates of spine removal and spine generation. Newly generated spines are synaptically innervated within days, corresponding to a change of the binary connectome.

However, most of the data discussed so far were obtained by spatially unspecific manipulation of neuronal activity, such as extracellular stimulation of afferents or sensory deprivation. Targeted stimulation and monitoring of identified spines was achieved by exploiting the 2P approach not only for imaging, but also for photolysis of caged glutamate (Matsuzaki et al. 2001). More than 90% of stimulated spines, but less than 10% of spines adjacent along the same dendrite, were found to rapidly (within less than 5 minutes) double to triple in volume (Matsuzaki et al. 2004). This enlargement was transient in ~95% of initially large spines. In initially small spines, the enlargement decayed to ~75% within tens of minutes, but then persisted for at least 100 minutes. When combined with whole-cell recordings from the postsynaptic neurons, strong correlations were found—both in the few minutes after stimulation as well as after tens of minutes—between spine volume and the evoked excitatory postsynaptic currents. A similar study reported that, while being synapse specific, the induction of LTP reduced for around ten minutes the threshold for LTP induction on spines less than ~10μm away on the same dendrite (Harvey and Svoboda 2007), thus supporting the formation of synapse clusters. Recently, it has been suggested that potentiation of such clustered synapses during motor learning induces the generation of new spines and that the survival of these spines depends on the correlation of the synaptic input with the clustered input (Hedrick et al. 2022).

Bidirectional Hebbian plasticity

In 1949, Hebb stated the following postulate about the neural mechanism of associative learning: “When an axon of cell A is near enough to excite a cell B and repeatedly or persistently takes part in firing it, some growth process or metabolic change takes place in one or both cells such that A’s efficiency, as one of the cells firing B, is increased. (Hebb 1949)” In other words, the synaptic connection from neuron A onto neuron B increases in strength if neuron A is repeatedly and causally involved in the generation of action potentials in neuron B. Importantly, the strength change in connection A→B depends only on the activities of neurons A and B, but not of any other neuron C. Synaptic LTP, as described above, is thus widely considered to be a neurobiological mechanism of homosynaptic Hebbian plasticity.

However, this model is clearly too simplistic: Following Hebb’s postulate, synaptic connections only ever increase in strength. Even more problematic is the positive feedback loop arising from the fact that strengthening of a synaptic connection increases the probability of this connection causing a postsynaptic action potential and thus to further increase in strength. To address this concern, a number of potential mechanisms have been proposed (for a review, see (Abbott and Nelson 2000)). These include global exponential decay of synaptic strength (Nass and Cooper 1975), renormalization of input synapse strengths per neuron (von der Malsburg 1973), and neuron-specific activity-dependent plasticity thresholds (Bienenstock et al. 1982). Experimental evidence for these mechanisms comes, for example, from studies of synaptic scaling during sleep (de Vivo et al. 2017) and of activity-dependent homeostatic plasticity (Turrigiano et al. 1998) during development (Turrigiano and Nelson 2004) or in response to sensory stimulation/deprivation (Knott et al. 2002, Mrsic-Flogel et al. 2007).

Only shortly after the first reports of LTP, it has been observed that changing the order of pre- and postsynaptic stimulation of the same synaptic connections could instead induce long-term depression (LTD) (Levy and Steward 1983). Since then, the precise spike timing dependence of LTP and LTD in synaptic plasticity have been studied extensively (e.g., (Markram et al. 1997, Bi and Poo 1998, Egger et al. 1999); for a review, see (Markram et al. 2012)). Thus, the term "Hebbian plasticity" is now commonly used to refer to bidirectional homosynaptic plasticity. Induction of LTD by low-frequency stimulation in hippocampal synapses was found to be accompanied by a reduction in AMPA-, but not NMDA-receptors and corresponding postsynaptic current (Carroll et al. 1999). LTD induction was also found to be associated with spine head shrinkage (Okamoto et al. 2004, Zhou et al. 2004, Oh et al. 2013) and retraction (Nägerl et al. 2004).

Together, these studies indicate that the efficacy of hippocampal and cortical synaptic connection may increase or decrease in an activity-dependent manner. Both LTP and LTD are accompanied by ultrastructural changes at the level of individual synapses, such as the expansion or shrinkage of spine heads; and by larger structural changes, such as the growth or retraction of spines. The densities and sizes of dendritic spines—though not the changes thereof—are directly observable in electron microscopy. EM-based comparisons of stimulated and unstimulated nervous contributed to the understanding of synaptic plasticity.

Intriguingly, even a single EM volume of unstimulated nervous tissue allows inferences about synaptic plasticity mechanism. For example, Hebbian learning by spike timing dependent plasticity (STDP) is a homosynaptic process. Thus, to first approximation, all synapses in a multi-synaptic connection (i.e., from the same axon onto the same dendrite) are expected to follow the same changes in efficacy and thus also in structure. As a consequence, two synapses from the same axon onto the same dendrite are expected to be more similar than two synapses from two separate, functionally less correlated axons onto the same dendrite. Indeed, EM-based studies have reported that the synapses in multi-synaptic connections are unexpectedly similar in size (Sorra and Harris 1993, Kasthuri et al. 2015, Bartol et al. 2015, Bloss et al. 2018, Motta et al. 2019, Dorkenwald et al. 2021), thereby providing purely structural observations compatible with and suggestive of homosynaptic plasticity.

The first report of unexpected size similarity in multi-synaptic connections was based on six pairs of synapses, each from a multi-synaptic axonal bouton onto spines of the same dendrite (Sorra and Harris 1993). Later, ten bisynaptic connections in CA1 of rat hippocampus were used to estimate the precision of homosynaptic size modulation and the range of synaptic sizes to infer a storage capacity of 4.7 bits per synapse (Bartol et al. 2015). As EM volumes grow in size, increasingly more detailed predictions of homosynaptic plasticity can be tested (see Discussion).

In an analysis described in chapter 2, more than 5000 bisynaptic connections were used not only to provide evidence for Hebbian plasticity in layer 4 of the mouse cerebral cortex, but also to quantify the fraction of the circuit that is consistent with saturated Hebbian plasticity. To date, synaptic plasticity has been studied primarily in tissue subjected to artificial electrical, chemical or sensory stimulation. As a result, it is still unclear at what rates LTP and LTD occur *in vivo* under naturalistic sensory inputs. Furthermore, it has been reported that spines are highly dynamic *in vivo* and that spine head volumes fluctuate substantially even in the absence of pre- or postsynaptic activity (for a review, see (Shimizu et al. 2021)). Thus, even if LTP and LTD occur at high rates, the stability of the corresponding synaptic changes is unclear. As exemplified by the various pathway-specific critical periods during cortical development, the capacities for LTP and LTD are also likely to be experience- and cell type-dependent. Connection-specific analyses have first been attempted in chapter 2, but are facilitated as EM volumes approach the minimal circuit volume (Dorkenwald et al. 2021).

In summary, the weighted connectome that can be extracted from an EM volume provides a snapshot of the dynamic processes that shape synaptic connectivity. Thus, a static connectomic snapshot of nervous tissue can be used for inferences about inherently dynamic processes, such as synaptic plasticity. This has been exemplified in chapter 2 by the analysis of bisynaptic connections for evidence of Hebbian plasticity, which is possibly even in subcellular connectomes. Recent progress in EM methods made the reconstruction of such connectomes routine, thus enabling a quantitative comparison of synaptic plasticity across cell types, brain regions, and species. The same data can be used to make inferences about other forms of synaptic plasticity, such as heterosynaptic or homeostatic plasticity. Implicitly, these synaptic mechanisms also make predictions about higher-order synaptic connectivity patterns. Studying these will become possible within the near future.

Quantification of subcellular target specificities of interneurons

While pyramidal neurons are the principal cell type of the cerebral cortex, the repertoire of potential computation in cortical circuits is considerably expanded by inhibitory interneurons. In the mouse cerebral cortex, for example, inhibitory interneurons form 8%–25% of all neurons (see chapter 4) and ~10% of the synapses in the neuropil (Braitenberg and Schüz 1998).

Inhibitory interneurons can be found in all layers of the cerebral cortex, including layer 1. As implied by the name, the axons and typically “smooth” (i.e., spine-free or sparsely-spiny) dendrites of interneurons are typically more localized than in pyramidal neurons, thus suggesting a role primarily in local computations. (Historically, spiny stellate neurons have been described as excitatory interneurons. While this characterization is justifiable based on the localization of the axonal and dendritic arbors to layer 4, the term “interneuron” will be used to refer exclusively to inhibitory interneurons in the following.) The primary neurotransmitter released by cortical interneurons is GABA, which mostly has a hyperpolarizing and thus inhibitory effect on postsynaptic neurons. This effect is mediated primarily by GABA_A and GABA_B receptors, which react to GABA by opening channels selective for chloride and potassium ions with reversal potentials around and below the typical neuronal resting potential, respectively.

Based on the inhibitory effect, various functional roles have been suggested for interneurons. These include the dynamic counterbalance of excitation to maintain a stable activity level across the local circuit. In the absence of inhibition, the recurrent excitatory network is at risk of runaway excitation. Such epileptiform hyperactivity is likely neurotoxic and has low dynamic range and thus also low capacity for information coding and processing. Another potential functional role of interneurons is the contribution to oscillatory activity. Oscillations may serve as reference signal for phase-based information coding or as basis for reliable information transfer by increasing the temporal coincidence of excitatory synaptic release. These functions could be implemented even by unstructured and random inhibitory connectivity. However, a more complex functional role in the precise spatiotemporal control of neuronal dynamics even at the subcellular level is suggested by the large diversity of interneurons (Kubota et al. 2016).

Already Ramón y Cajal and Lorente de Nó have described cortical interneurons (which were identified by their short axons in Golgi-stained tissue) and divided them into separate morphological cell types. Later, interneuron subtypes were further refined as methods for electrophysiological, molecular, functional, developmental, etc. characterizations became available and were improved. The definition of interneuron subtypes is still an area of ongoing research (Ascoli et al. 2008, Yuste et al. 2020).

Correlated electrophysiological, light- and electron-microscopic studies revealed that neuronal cell types in the cerebral cortex differed in the subcellular postsynaptic targets. In mouse cerebral cortex, excitatory synapses are presynaptic primarily to dendritic spines of excitatory neurons or to dendritic shafts of interneurons (Braitenberg and Schüz 1998). Inhibitory synapses, in contrast, are presynaptic mostly to multi-synaptic spines (Jones and Powell 1969), dendritic shafts, somata or axon initial segments (Somogyi et al. 1982) of excitatory neurons, and to interneurons (Braitenberg and Schüz 1998, Kubota et al. 2016). These subcellular postsynaptic targets are innervated in an interneuron subtype-specific manner (for a review, see (Kubota et al. 2016)). For example, somata and proximal dendrites of excitatory neurons are primarily innervated by parvalbumin- or cholecystokinin-positive "basket" interneurons. Distal (apical) dendrites of excitatory are innervated mostly by somatostatin-positive interneurons, and the axo-axonal synapses onto excitatory axon initial segments were thought to originate almost exclusively from "chandelier" interneurons (but see (Gour et al. 2021, Schneider-Mizell et al. 2021)).

The synapses onto the different targets are likely to underlie different functions. Inhibitory synapses onto multi-synaptic spines were found to induce small inhibitory postsynaptic potentials (IPSP) in the soma of the postsynaptic neuron (Kubota et al. 2015), but strong inhibitory and shunting effects in the spine head and its local surround. Thus, inhibitory spine synapses have the potential for synapse-specific suppression of excitatory inputs and plasticity mechanisms (Chiu et al. 2013). In contrast, synapses onto the soma or onto the axon initial segment (Somogyi et al. 1982) are positioned ideally to suppress the initiation of action potentials. However, the local postsynaptic membrane potential is the result of non-linear integration of all synaptic inputs onto that neuron (e.g., (Branco et al. 2010)). The strong and temporally precise control over action potential initiation of synapses onto the axon initial segment thus comes at the cost of unspecific inhibitory-excitatory interactions.

These subcellular target specificities are thought to be the result of concurrent attractive and repulsive mechanisms (for a review, see (Sanes and Zipursky 2020)). The precision of these mechanisms, of the resulting synapse distributions, and ultimately of the notion of cell type-specific connectivity is still unclear. EM-based connectomics is well-suited for an unbiased analysis of interneuron axons and of their subcellular target properties. In chapter 2, mathematical models are proposed for the connectomic identification of excitatory and inhibitory axons and of axon subpopulations with statistically significant evidence for subcellular target preference. Using these purely connectivity-based methods, inhibitory axon subpopulations with preferential innervation of smooth (likely interneuron) dendrites, proximal and distal dendrites and somata of excitatory neurons were identified. Notably, no evidence for axon initial segment-specific interneuron axons was found in mouse primary somatosensory cortex layer 4.

As with the analysis of structural correlates of Hebbian plasticity, these analyses of axonal target specificity are suitable for connectomic screening subcellular connectomes. Synaptic adhesion molecules and thus likely also in specificity mechanisms are thought to be altered in neurological disorders. Connectomic comparisons of healthy and diseased tissue from animal models and humans are thus of interest.

Excitation-inhibition balance across cell types and species

The features of cortical architecture described in the previous sections—the ultrastructure of excitatory and inhibitory neurons, the poor geometric predictability and plasticity of synaptic connections, and the preferential innervation of specific postsynaptic targets—have been studied primarily in non-human animals. In particular, the primary animal models over the last decades have been rodents.

Rodents are attractive model systems because of the availability of genetic tools. This allowed, for example, for the introduction of human disease-associated genetic mutations or for genetically targeted expression of fluorescence proteins, calcium-sensitive fluorescence proteins, or light-sensitive ion channels. Together, these tools were used to study the neurobiology of human diseases in mice. However, insights from mouse models of neurodegenerative diseases have so far failed to translate into effective treatments for humans (Dawson et al. 2018).

Arguably, for mice to become an effective model system of human neurodegenerative diseases, it might be necessary—but insufficient—to understand the relationship between mouse and human brains under healthy conditions. In particular, how much variability is there within and across healthy mouse brains? How much variability is there within and across human brains? And what are the common features and differences between healthy mouse and human brains? Addressing these questions might also shed light on the neural mechanisms underlying the substantial differences in cognitive abilities.

The cerebral cortex is a particularly attractive subject in this regard. The cortical sheath expanded 600–800-fold in area from mouse to human (Mota and Herculano-Houzel 2015). In the lissencephalic mouse brain, ~98% of the cortical sheath is exposed at the surface, whereas the majority of the human cortical sheath (55%–65%) is folded into gyri. Gyration allows for a supra-linear expansion of the cortical sheath relative to brain surface and increases the potential connectivity by separating neuronal distance along the cortical sheath from the neuronal distance in Euclidean space (for a review, see (Striedter et al. 2015)). The cortical sheath not only expanded in surface area, but also ~3-fold in thickness (DeFelipe et al. 2002). This is accompanied by a ~1000-fold increase in number of neurons: from 5 million (Herculano-Houzel et al. 2013) to 16 billion (Azevedo et al. 2009).

The relationship between number of neurons and cognitive abilities remains unclear. For example, normal aging-related cognitive decline is thought to be associated not with a substantial loss of cortical neurons, but rather with changes in synaptic connectivity (Morrison and Baxter 2012). This begs the question how the cerebral cortices of mice and humans differ in terms of connectivity. For example, does the ~3-fold increase in cortical sheath thickness and the corresponding increase in the extent of pyramidal neuron dendrites (Mohan et al. 2015) results in a 3-fold increase in synaptic inputs per neuron?

The relative contribution of excitation and inhibition to the total synaptic input per neuron is another key determinant of neuronal dynamics and computations. Thus, it is notable that the proportions of glutamatergic and GABAergic cell types were found to differ substantially across species (e.g., (Bakken et al. 2021)). For example, the fraction of GABAergic interneurons was found to double in a recent study from ~16% in mice to ~33% in human (Bakken et al. 2021). Does this imply a corresponding increase in inhibitory synapses in the cortical neuropil?

Comparative electron microscopy is well-suited suited to address this question. For example, a study based on two-dimensional TEM images compared the synaptic composition of cortical neuropil in mouse and human (DeFelipe et al. 2002). The average volumetric synapse density was found to be ~2.7 times lower in human than in mouse (~1.1μm^{-3} vs. ~2.9μm^{-3}), but average synapse size was found to be 20%–30% larger. The fraction of symmetric (likely inhibitory) synapses was reported to be slightly lower in human than in mouse cortex (11% vs. 16%) and very similar when restricted to cortical layers 2 and 3 (~11%).

How do volumetric fractions of interneurons and inhibitory synapses relate to the excitatory and inhibitory synaptic inputs onto excitatory neurons? In general, these relationships are non-linear. For example, even if the interneuron fraction remained constant from mouse to human, the proportion of inhibitory input synapses onto excitatory neurons could have changed due to a change in the average target specificity of interneurons. To assess the synaptic inputs onto excitatory neurons, the volumetric fractions of interneurons and inhibitory synapses are thus insufficient.

These considerations are further complicated by the fact that many of the existing data about the ultrastructure of the human cerebral cortex were obtained from diseased tissue. Most human cortical tissue was obtained post-mortem or in form of access tissue from surgeries for the treatment of drug-resistant epilepsy (e.g., (DeFelipe et al. 2002, Shapson-Coe et al. 2021)). Both of these conditions—through the decay of nervous tissue post-mortem or as consequence of pharmacological treatment—are unlikely to reflect human cortical circuits under healthy physiological conditions.

Thus, even basic, low-order statistics of synaptic connectivity in the human cerebral cortex are unclear. Chapter 4 provides measurements of the average synaptic connectivity within and across excitatory and inhibitory neurons in layer 2/3 of mouse and human cerebral cortex. The fraction of inhibitory synaptic inputs onto excitatory neurons was found to have increased modestly and sublinearly with the fraction of interneurons. This is the consequence of a shift in the average inhibitory target specificity towards interneurons. Together with the increased fraction of interneurons, this shift in average inhibitory target specificities resulted in a substantial expansion of potentially disinhibitory interneuron-to-interneuron connectivity.

In conclusion, even electron microscopy volumes on the order of $(100\mu m)^3$, which are too small to follow pre- or postsynaptic neurites of a synapse to the corresponding somata and which are thus limited to subcellular connectomic analyses, can provide valuable insights about the organization of the mammalian cerebral cortex. However, recent improvements in sample preparation and electron microscopy methods made it possible to image $1mm^3$-sized volumes of cortical tissue at nanometer resolution (Shapson-Coe et al. 2021, MICrONS consortium et al. 2021, Sievers unpublished), thus exceeding the minimal resolution and volume requirements for the reconstruction of neuron-to-neuron connectomes of local cortical circuits (Helmstaedter 2013). Hence, it is becoming plausible to realize one of the promises of dense circuit mapping: the experimental testing of neural network models of brain function based on their structural implications (Seung 2009).

The following section will introduce a widely used approach for the analysis of neuron-to-neuron connectivity, namely that of identifying overrepresented network motifs. The mathematical tools necessary for the identification of such network motifs will be briefly introduced. However, these small network motifs are only indirectly linked to circuit function and it will be argued that more complex analysis approaches are necessary for the structural disambiguation of most network models. One such approach will be presented in chapter 3.

Analysis of neuron-to-neuron connectomes

The neuron-to-neuron connectivity in cortical circuits has been studied using a range of techniques (for a review, see (Luo et al. 2018)). These include, for example, connectivity inferences from overlap between light-microscopic reconstructions of individual—potentially electrophysiologically (Gilbert and Wiesel 1983) or genetically identified (Livet et al. 2007)—neurons; monosynaptic transsynaptic tracing using modified rabies virus (Wickersham et al. 2007); optical stimulation and activity measurement by use of genetically encoded light-gated ion channels and calcium indicators (Petreanu et al. 2007); and multi-electrode recordings. Intracellular multi-electrode recordings in slice preparations have been used to probe the connectivity in small networks of up to six neurons (Mason et al. 1991, Markram et al. 1997, Feldmeyer et al. 1999, Thomson et al. 2002, Song et al. 2005, Lefort et al. 2009).

Already early pair-wise connectivity measurements in homogeneous neuron populations in the cerebral cortex indicated that the excitatory neural network might be non-random in structure. However, to claim that the measured network is in fact non-randomly structured, it must be verified that the observed connectivity is unlikely to have occurred by chance in a random network. Thus, it is necessary to build mathematical models of random networks.

Mathematically, neural networks (or connectomes) are most commonly represented by directed edge-weighted graphs. A graph is defined by a set of vertices (representing the neurons) and a set of weighted directed edges (representing synaptic connections) between these vertices. The foundation of graph theory was laid in 1736 by Leonhard Euler while working on the problem of the “seven bridges of Königsberg”. Initially, the study of graphs was based on the tools of combinatorics. In contrast, the idea of random graphs (i.e., graphs as random discrete objects) was introduced and systematized only the late 1950ies (Gilbert 1959, Erdős and Rényi 1959). In this framework, a graph is a random instance (i.e., a randomly drawn element) from a probabilistic graph model (i.e., a distribution over graphs).

For example, the Erdős-Rényi (ER) model (Erdős and Rényi 1959), $G(n,M)$, corresponds to uniform random sampling from the set of all graphs that consist of exactly n vertices and M edges. The $G(n,p)$ variant of the ER model (Gilbert 1959) corresponds graphs with n vertices that are constructed by randomly and independently connecting each vertex pair with probability p. Both of these models trivially extend to directed graphs. In the context of a connectome, the $G(n,p)$ model corresponds to a network of n neurons, where each combination of pre- and postsynaptic neuron pair is connected independently with probability p. Graph models also allow inference from a graph instance about the model parameters. For example, a measured connectome could be used to infer the maximum likelihood estimate of the pairwise connection probability p between neurons.

Dual-electrode recordings from thick tufted pyramidal neurons in L5 of rat somatosensory cortex indicated that only 10% of cell pairs were synaptic connected in at least one direction (Markram et al. 1997). Under the $G(n,p)$ ER model, the maximum likelihood probability for directed connections is $p = 1\text{-}(1\text{-}10\%)^{1/2} = {\sim}5.1\%$. This model would predict that $p^2/[1\text{-}(1\text{-}p)^2] = {\sim}2.6\%$ of connected neuron pairs should be connected reciprocally. However, the experimentally measured fraction of reciprocal connections more than ten times larger (Markram et al. 1997). Thus, this particular neural network is more structured than predicted by the ER model.

This approach of testing higher-order connectivity predictions (the reciprocal connections) from lower-order statistics (the pairwise connectivity) against experimental data has been generalized and used to study networks of three or four neurons (Milo et al. 2002, Song et al. 2005). Among triplets of thick tufted pyramidal neurons in layer 5 of rat visual cortex, this analysis indicated an overrepresentation of reciprocal connections between all pairs of neurons (Song et al. 2005). Such overrepresented connection patterns have been termed “network motifs” (Milo et al. 2002). Furthermore, the probability of reciprocal connectivity between pairs of neurons was found to increase with connection strength. Based on these observations, the authors suggested that “the network may be viewed as a skeleton of stronger connections in a sea of weaker ones (Song et al. 2005)”.

This illustrates two key challenges of circuit mapping by multi-electrode recordings: First, the proposed “skeleton” consists of a small fraction of connections within a sparsely connected network. The probability of finding these skeletal connections by random sampling of neurons is small. In a dense, weighted connectome, however, they are trivial to identify. Second, it is unclear how the absolute frequency and relative overrepresentation of small networks patterns related to circuit function. Analyses of other networks, such as the web link or social networks, revealed non-random features relative to the ER model (e.g., the average path length between all pairs of nodes as measure of “small-world”-ness (Watts and Strogatz 1998)) that have been proposed as summary statistics of entire neural networks. While addressing the limitations of small network patterns, the relationship between these features and neural network functions remains unclear.

Instead of inferring functional properties from the prevalence of small network motifs, it might be worth considering network models with specific functional properties and structural implications. For example, synfire chains have been proposed as network model for the sequential propagation of neuronal activity over periods that were thought to exceed the timescales of individual neurons (Amari 1972, Abeles 1982, Diesmann et al. 1999). Temporally precise, sequential activation of neurons has been reported, for example, in the cerebral cortex of behaving monkeys (Abeles et al. 1993) and in slice preparations from mouse visual cortex (Mao et al. 2001) and has been inferred from repeated patterns of synchronized synaptic inputs in slices from mouse visual cortex and *in vivo* in the cat visual cortex (Ikegaya et al. 2004). Synfire chains have been proposed as mechanism to represent and learn the hierarchical composition of cognitive concepts (Bienenstock 1995). In its simplest form, synfire chains consist of ordered “pools” of neurons, where all neurons in one pool innervate all neurons in the next pool. Thus, the synfire chain model is a functional model with connectomically testable structural implications.

However, the structural implications are less clear in other functional network models. SORN (self-organizing recurrent neural networks; (Lazar et al. 2009)), for example, is a network model of stable cortical dynamics based on multiple synaptic plasticity mechanisms. Arguably the most extreme functional network models are backpropagation-trained recurrent neural networks (RNNs) whose connectivity is defined almost exclusively by the objective function. Thus, it is unclear how informative connectomic data truly is for the falsification of neural network models.

In chapter 3, a method for connectome-based model selection is proposed. And a set of seven structural and functional models of local cortical circuits with biologically plausible and meaningful parameterizations is presented. The key question addressed in chapter 3 is the following: Given a measured connectome of a local cortical circuits and the set of seven circuit models, is it possible to infer which model explains the connectome best? In particular, is it possible to infer from a connectome the posterior probabilities of the various models? It is shown that six relatively simple connectome summary statistics are sufficient for accurate separation of these models. This holds even in the presence of considerable reconstruction errors, which makes model selection plausible even from fully automated but imperfect reconstructions of petabyte-scale EM volumes.

Are such large-scale EM volumes even necessary for model selection? Or could a smaller EM volume of only part of the local circuit be sufficient? In small EM volumes, neurons and their axons and dendrites are heavily truncated (see “Subcellular connectomic analyses”). Even the synaptic connections between neurons with their soma in the image volume are mostly located outside the image volume. While sufficient for the subcellular connectomic analyses described above, small EM volumes are insufficient for model selection. As a result, the first neuron-to-neuron connectomes that were made possible by recent technological improvements in connectomics have opened the possibility of completely new and fundamentally different connectomic analyses.

Outline of thesis

The remainder of this thesis is organized into four chapters and a discussion. Chapter 1 is a review of electron microscopy and data analysis methods used in connectomics. At the hypothetical example of the dense connectomic reconstruction of a whole human brain, the artificial intelligence-based reconstruction methods are identified as primary limiting factors. Chapter 2 presents the dense connectomic reconstruction of a SBEM volume from layer 4 of mouse primary somatosensory cortex, which was used, for example, to derive upper bounds on the circuit fraction that are consistent with saturated Hebbian plasticity. Chapter 3 proposes a method for Bayesian model selection from summary statistics of neuron-to-neuron connectomes. Simulations are used to validate this method and to illustrate that weighted neuron-to-neuron connectome might be sufficient to dinstinguish between network models that are defined only by their function. Chapter 4 presents a connectomic comparison of nine SBEM volumes from mouse, macaque, and human cerebral cortex, which indicates that the increase in interneurons from mouse to human is accompanied only by a moderate increase in inhibitory synaptic input onto pyramidal neurons, but by a substantial increase of interneuron-to-interneuron connectivity. Finally, the discussion summarizes recent analyses of connectomic correlates of synaptic plasticity and proposes higher-order circuit predictions for future analyses.

Chapter 1. Big data in nanoscale connectomics, and the greed for training labels

Alessandro Motta, Meike Sievers (née Schurr), Benedikt Staffler, Moritz Helmstaedter.
Current Opinion in Neurobiology (2019). DOI: 10.1016/j.conb.2019.03.012

Contributions: Review scientific data acquisition (Figure 1-1a) and analysis methods (Figure 1-1b). Estimation of image acquisition, automated image processing, and manual proofreading costs for connectomic reconstruction of whole human brain (Figure 1-2).

The neurosciences have developed methods that outpace most other biomedical fields in terms of acquired bytes. We review how the information content and analysis challenge of such data indicates that electron microscopy (EM)-based connectomics is an especially hard problem. Here, as in many other current machine learning applications, the need for excessive amounts of labelled data while utilizing only a small fraction of available raw image data for algorithm training illustrates the still fundamental gap between artificial and biological intelligence. Substantial improvements of label and energy efficiency in machine learning may be required to address the formidable challenge of acquiring the nanoscale connectome of a human brain.

In the biomedical sciences, the amounts of measured data become large when they are acquired over multiple dimensions: Human genomes, for example, are each small (about 20 GB) by today's standards, but genomics entered the 'big data' field when entire genomes could be acquired over several time points and over many single cells in a human patient (genomics is expected to generate about 40 exabytes (EB, 10^{18} bytes) by 2025 (Stephens et al. 2015), Figure 1-1a). In microscopy, 2D-to-4D data acquisition is routine and microscopy techniques are leading today in the amount of biomedical scientific data they produce.

In the following, we will first review current data rates in neuroscientific imaging and compare them to other 'big data'-generating biomedical methods; we will then discuss the effective compressibility of the data, asking whether in fact, big data in connectomics (Sporns et al. 2005) can be considered 'small data' (Engert 2014) since it could in principle be turned into information-rich compressed representations. Finally, we discuss how deep learning-based analysis in connectomics improved in terms of accuracy (leading to claims of 'superhuman performance' (Lee et al. 2017, Januszewski et al. 2018)), while still being many orders of magnitude away from the ability to analyze a human connectome. As in many other applications, machine learning in connectomics has not been able to overcome the label burden that is abundant in today's artificial intelligence (AI). Understanding how the biological computers in our (and some other animals') heads are able to extract information from massive amounts of unlabeled data, requiring only minimal labelled input at low computational cost, may be a key challenge of neuroscience, and could become a key contribution of neuroscience to AI research in the future (Helmstaedter 2015, Botvinick et al. 2017, Hassabis et al. 2017, Lake et al. 2017, Lake et al. 2017).

Data rates and volumes

Imaging the brain at low resolution to obtain whole-brain structural and functional information using (functional) magnetic resonance imaging ((f)MRI), and diffusion tensor imaging (DTI) are routine research and clinical techniques in humans. Data amounts for a single MRI scan are on the scale of 50 MB (structural MRI at 0.7 mm isotropic voxel size on a 3 T scanner, ~1.8 MB/s) to 2.6 GB (for fMRI

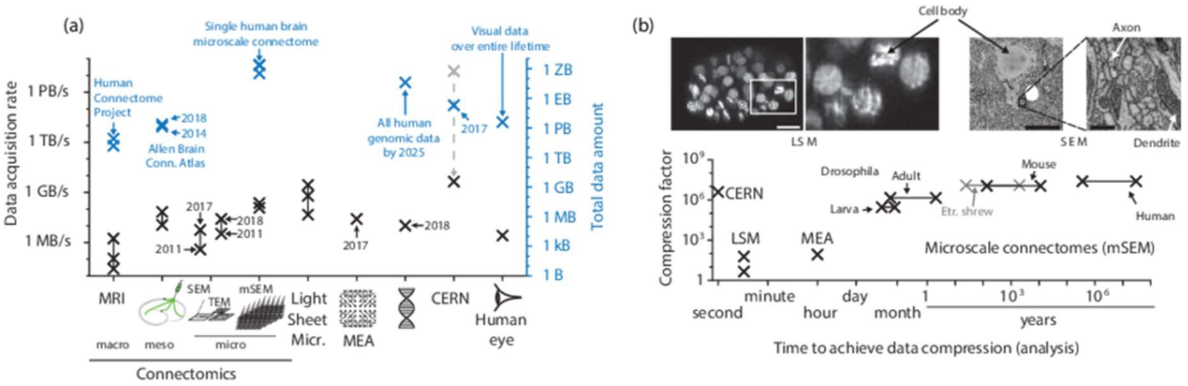

Figure 1-1 Data rates and information content in connectomics and other scientific methods. **(a)** Overview of raw data acquisition rates (black crosses) and total data amounts (blue) for connectomic and other techniques. Macroscale connectomics (macro): data from Human Connectome Project (Van Essen et al. 2013); Mesoscale connectomics (meso, (Bohland et al. 2009)): data from Allen Brain Atlas (Kuan et al. 2015, Oh et al. 2014, Harris et al. 2019), range indicates data rate for 1–6 microscopes; Microscale connectomics (micro): data from (Schmidt et al. 2017, Briggman et al. 2011, Bock et al. 2011, Zheng et al. 2018, Eberle et al. 2015) and M.S., unpublished data; Light sheet microscopy (LSM) for cell tracking in animal development (Keller et al. 2010, Chhetri et al. 2015) and whole-brain activity measurements (Dunn et al. 2016), data from (Amat et al. 2015, Liu and Keller 2016); Multi-electrode array (MEA) recordings; data from (Shein-Idelson et al. 2017, Jun et al. 2017); Genomics: data from (Stephens et al. 2015) and specification of Illumina NovaSeq 6000 (https://www.illumina.com/systems/sequencing-platforms/novaseq/specifications.html); CERN: data from http://cds.cern.ch/record/2299292 and http://cds.cern.ch/record/1997399, gray indicates immediate data rejection yielding a 6-order of magnitude data rate reduction; Human eye: estimate based on 1.2 million ganglion cells per eye (Harman et al. 2000, Curcio and Allen 1990), 1 B/s per ganglion cell axon (Koch et al. 2006), and 70 years median life time at 16 waking hours per day. See appendix A1 for details of the calculations. **(b)** Relation between eventual data compressibility and time to achieve the required analysis for various big-data producing methods. Note that 3D EM techniques for connectomics in large (mammalian) brains stand out because of the enormous analysis times. Inset illustrates why imaging of cells using LSM, while generating higher data rates, is immediately and substantially compressible, which connectomic data are not (sample images from (Liu and Keller 2016) as adapted from (Wu et al. 2013), with permission, and (Berning et al. 2015)). Note further that first whole-brain 3D EM connectomic datasets (Zheng et al. 2018, Ohyama et al. 2015, Hildebrand et al. 2017) and analyses (Li et al. 2019) are available. Scale bars, 10 µm (LSM and SEM, left); 0.5 µm (SEM, right).

at 1.6 mm isotropic voxel size on a 7 T scanner, 0.02–0.1 MB/s, see appendix A1), thus all the imaging datasets from 1113 participants acquired in the 'Human Connectome Project' (Van Essen et al. 2013) comprise a total of 81 TB (Figure 1-1a).

At the other end of the resolution spectrum, imaging mammalian brain tissue at a scale sufficient to identify chemical synapses and to reconstruct even the thinnest neuronal processes (axons, dendrites and their spines) for mapping synaptic neuronal networks in the mammalian gray matter using 3D EM generates 0.3–2.1 PB per cubic millimeter of brain tissue (at voxel size of 11 × 11 × 30 nm^3 (Schmidt et al. 2017) to 4 × 4 × 30 nm^3 (Morgan et al. 2016), see also (Lichtman et al. 2014)). Thus, even a single human brain imaged in such detail would comprise 0.5–3.1 zettabytes (ZB, 10^{21} bytes) (Figure 1-1a), about 10–100 times more than the total amount of genomic data expected world-wide by 2025 (Stephens et al. 2015).

But is it at all realistic to image such large volumes using today's 3D-EM technology? The effective imaging rates of 3D single-beam scanning EM (SEM) setups has improved by about 200-fold over the last 15 years from ~0.03 to 0.5 million voxel per second (MVx/s) (Briggman et al. 2011, Denk and Horstmann 2004, Kasthuri et al. 2015) via ~1–2 MVx/s (Morgan et al. 2016, Wanner et al. 2016, Svara et al. 2018, Kornfeld et al. 2017) to ~6 MVx/s ((Schmidt et al. 2017), accounting for the voxel size, this yields a volume throughput of 23 Gnm^3/s) or 12 MVx/s ((Morgan et al. 2016), 0.6 Gnm^3/s). Similarly, the effective imaging rate of transmission electron microscopy (TEM) setups has accelerated from ~1–5 MVx/s (Bock et al. 2011, Lee et al. 2016) to 11 MVx/s ((Zheng et al. 2018), this corresponds to ~0.6–7 Gnm^3/s, with automated grid exchange (Zheng et al. 2018) up to 21 Gnm^3/s). In both the serial block-face SEM imaging (SBEM) and serial-section transmission electron microscopy (ssTEM) approaches, improvements in effective imaging rate were achieved primarily by reducing the overhead times of moving the sample under the electron beam—by either continuous imaging along one dimension in SBEM (Schmidt et al. 2017) or by minimizing the stage movement and settling times in ssTEM (Zheng et al. 2018). Effective imaging rates in focused ion-beam million SBEM (FIB-SEM) (Knott et al. 2008) setups have improved from ~0.035 MVx/s (Korogod et al. 2015) to ~0.6 MVx/s (scanning rate 1.25 MHz, (Xu et al. 2017, Takemura et al. 2017), i.e. ~0.3Gnm^3/s). The development of the multi-beam SEM (mSEM, Zeiss, (Eberle et al. 2015)) has drastically increased the imaging rate on a single EM setup, yielding today effective imaging rates of 190 MHz (at 10 MHz imaging rate per electron beam, 106 Gnm^3/s) or 230 MHz (at 20 MHz imaging rate per electron beam, 129 Gnm^3/s), both on a 61-beam mSEM. Still, the time required to move the sample under the beam is limiting these setups from yielding the nominal imaging rates of 1.2–1.8 GHz per microscope (with 61 or 91 beams).

Thus, imaging even one single human brain at nanoscale connectomic resolution would currently require about 0.5–3.9 million electron beam years at an effective imaging speed of 20 MVx/s per beam (200–1500 electron beam years for a mouse brain; 30–260 electron beam years for the smallest mammalian brain, that of the Etruscan shrew (Mikula 2016); ranges given correspond to voxel sizes of $11 \times 11 \times 30$ nm^3 to $4 \times 4 \times 30$ nm^3), thus about one million single-beam EM setups (or about 10,000 mSEM setups) to obtain the image data for one human brain within a couple of years. This optimistic estimate assumes that imaging of a large brain can be parallelized by using approaches to separate tissue cutting from tissue imaging (most notably the hot knife approach, (Hayworth et al. 2015)), which currently also requires that such large brains can be stained and resin-embedded in one piece (see (Mikula 2016) for detailed discussion). While in SBEM and ssTEM or ssSEM (Hayworth et al. 2006) approaches (see (Briggman and Bock 2012) for a review) tissue cutting is not a critical time-consuming step (and neither is milling in FIB-SEM (Xu et al. 2017)), the combined error rates from cutting and imaging can become increasingly burdensome for long-term imaging when tissue removal and block-face imaging are tightly integrated. Soberingly, in all current 3D-EM approaches, obtaining long tissue series in the 3rd dimension at tolerable loss and error rate is still the key challenge, and current published datasets have not yet exceeded an extent of 280 μm in the smallest imaged dimension (Schmidt et al. 2017, Morgan et al. 2016, Zheng et al. 2018).

Compressibility of raw data

While thus enormous amounts of bytes can be generated by the most advanced imaging techniques in the neurosciences (see Figure 1-1a for several additional examples including light-sheet microscopy (LSM) and large-scale multi-electrode recording), their relevant scientific content can often be represented in a much more condensed form (Engert 2014). For the imaging of cell bodies and their developmental migration using LSM at nominally more than 2 GB/s, for example, the imaged volumes contain a large fraction of 'background' voxels which are not needed for further processing (Figure 1-1b). Up to 60-fold initial compression of the data are, therefore, possible immediately (Amat et al. 2015), with real-time cell segmentation and tracking algorithms (Stegmaier et al. 2016) reducing the scientifically relevant data further to a few kB/s. Importantly, this analysis result can be achieved within a few days of computer processing (Figure 1-1b). Similarly, for large-scale functional recordings of calcium transients in thousands of neuronal cell bodies (Ahrens et al. 2012, Ahrens et al. 2013, Tang et al. 2018), the initially very large datasets can be highly compressed once the underlying sequences of action potentials have been extracted for each neuron. In these data, the 3D-locality of the relevant information (cell bodies), the locally high volumetric and temporal correlation of the signal and the effectively low-dimensional underlying phenomenon (cell body locations over time; action potentials over time) enable the efficient conversion of initially large datasets to much more condensed representations (Figure 1-1b, note that additional information may be contained in the fluorescence transients in the surrounding neuropil). The disposal of a majority of acquired data is actually well-known from large-scale particle accelerators, where hardware-based and software-based filters reduce the captured sensory data by more than six orders of magnitude to about 4.5 GB/s (Figure 1-1b), yielding about 12 PB of storage per month of experiments at CERN (http://cds.cern.ch/record/2299292).

A consideration of data compressibility for high-resolution connectomic imaging at EM level illustrates the fundamentally different nature of this data: Information is highly anisotropic and dense (Figure 1-1b). At any location along an axon, there is a 2D plane in which the axon is a very local object; but along a 3rd (convoluted) dimension, the axon is often as extended as the entire brain. As a result, in some part of the 3D image data centimeters away, the very same neuron may give rise again to a nanoscale local axonal cross section (Figure 1-1b). Additionally, the image information about one thin neuronal process is locally independent of that of the directly neighboring one at sometimes less than 100 nm distance, which can be another thin axon, or a very large dendrite, Figure 1-1b. Therefore, compression at the image level is far from obvious, and can hardly be lossless. While the compression factor in high resolution connectomics could be enormous (compression would go from zettabytes of image data to 10–100 terabytes for a binary connectome encoding which neuron connects to which other neuron in a human brain), the time to obtain such a compression would today be at least several decades (Figure 1-1b, see below). To complicate the situation, it is by no means clear yet which representation of connectomic data is sufficient for a given nervous system. As an example, not only the positioning of synapses along dendrites of neurons but also along their axons has been described as a relevant anatomic feature in birds (Kornfeld et al. 2017, Carr and Konishi 1990, Carr and Konishi 1988) and recently also in mammals (Schmidt et al. 2017). Having condensed a connectomic EM dataset to 'just' the underlying connectivity matrix would have lost this relevant structural feature of neuronal networks in these species (see also (Mitra 2014)). Obviously, much more information is contained in the 3D-EM data (detailed features of synapses; glial cells; interaction with blood vessels to name a few).

Taken together, we argue that while in principle, also big data in connectomics could be viewed as highly compressible ((Engert 2014), afterall one major goal of connectomics is a binary connectivity matrix between ideally all neurons in an animal's brain), it is practically no, and the key big data challenge in connectomics remains not that of analyzing connectomes, but of obtaining them efficiently.

Image analysis

Even assuming the imaging of a human connectome was feasible, how far are we away today from being able to analyze the resulting large amounts of 3D image data? Image analysis in connectomics has evolved from fully manual volume labeling of neurites at about 100–200 human work hours/mm path length ((Fiala 2005), see (Helmstaedter et al. 2008) for estimates) to neurite skeletonization at about 5–10 hours/mm (Wanner et al. 2016, Helmstaedter et al. 2011, Eichler et al. 2017, Berning et al. 2015). Recent methodological claims indicate reduction to about 0.5–1 hour/mm or less (Januszewski et al. 2018, Boergens et al. 2017, Kornfeld and Denk 2018), although these methods have not yet been shown to enable actual dense connectomic reconstruction at these rates (see, however, (Motta et al. 2019)). In most cases the reduction of human work load was enabled by parallel computer-based image analysis (Lee et al. 2017, Januszewski et al. 2018, Takemura et al. 2017, Berning et al. 2015, Helmstaedter et al. 2013, Takemura et al. 2013, Meirovitch et al. 2016, Funke et al. 2019, Mishchenko et al. 2010, Kim et al. 2014, Bae et al. 2018, Plaza 2016, Kaynig et al. 2015, Beier et al. 2017, Becker et al. 2012). Thus, with reduced human work hour investment, resource consumption by automated methods has increased.

If one uses today's best estimates of data analysis rates, the analysis of a human connectome would require 10^{13} human work hours and 6×10^{14} compute core hours. Taking a hypothetical substantial investment of one billion EUR spent over five years, these numbers allow us to compare how much improvement is still required for EM imaging, EM data analysis (accuracy, so far leveraged by human involvement) and compute efficiency (Figure 1-2a) to make the acquisition of a nanoscale human connectome even plausible. The amount of human work hours spent would have to be reduced by at least five orders of magnitude. This could be achieved by reducing the number of locations at which human workers are requested to provide annotations; plausibly by improving accuracy of automated methods by a factor of 10^5 (notably this is already compared to the most optimistic current analysis claims, (Januszewski et al. 2018, Boergens et al. 2017, Kornfeld and Denk 2018), which so far yield remaining error rates of analysis that are about 1000-fold higher than needed for human neurons; also this would still imply to recruit 20 million work hours over 5 years, corresponding to 20,000 full-time employees. This indicates that rather, an improvement of 7–10 orders of magnitude may be required). While currently, the resource consumption from computing is about one order of magnitude less severe than that from human work hour investments (Figure 1-2a), four orders of magnitude of improvements of resource consumption efficiency for the computational methods are required, as well (Figure 1-2a, see also (Lichtman et al. 2014)). EM techniques, to the contrary, would have to operate at about 1500–5000 EUR per electron beam (operated at an optimistic 20 MVx/s effective scanning speed per beam), thus roughly 10–50-fold improvements are needed compared to today's setups.

How could the concomitant improvement of at least five orders of magnitude in automated analysis accuracy and four orders of magnitude in computational efficiency be plausibly obtained? Deep learning has made dramatic improvements over the last decade, leading experts to proclaim that almost any problem will soon be solved by artificial neural networks. The increase in accuracy, however, has come at the cost of increased computational resource consumption (compared e.g. LeNet (LeCun et al. 1998), AlexNet (Krizhevsky et al. 2012), GoogLeNet (Szegedy et al. 2015)), even if methods have been proposed to make deep learning approaches more resource efficient (Zhang et al. 2016, Rastegari et al. 2016, He and Sun 2015). Potentially, combination of low-cost but inaccurate with expensive high-accuracy approaches could improve the situation (Lichtman et al. 2014, Meirovitch et al. 2016).

For a different possible approach to this challenge, contrast the training approaches in current machine learning as used in connectomics (Figure 1-2b) with the label and energy efficiency of a human infant's brain that is learning to call a tree a tree: 1–2.4 million retinal ganglion cells (i.e. about 1.1–2.6 MB/s data rate, comparable to standard single-beam SEMs in connectomics, Figure 1-1a) yield about 70 TB of visual input by the age of 1.5 years, of which one can estimate for an urban-raised child about 4% to have been trees in various forms and shapes (see appendix A1 for details of these estimates). Together with an estimated few dozen explicit labels of 'tree', infant tree detection is usually successful thereafter. If one compares to the detection of synapses or neurites (Figure 1-2b) in connectomics, where 10^7–10^8 labels are usually used for current state-of-the-art performance, which are then presented 100–1000 times each, then it becomes clear that today's AI in connectomics is still driven by labels. Furthermore, the core of the learning technique (stochastic gradient descent) has stayed essentially unchanged; Progress was made in terms of prediction accuracy, while training only changed insofar that multiple graphics processing units (GPUs) can now be used to process ever-increasing training data volumes in parallel. And notably, no unsupervised learning approach has so

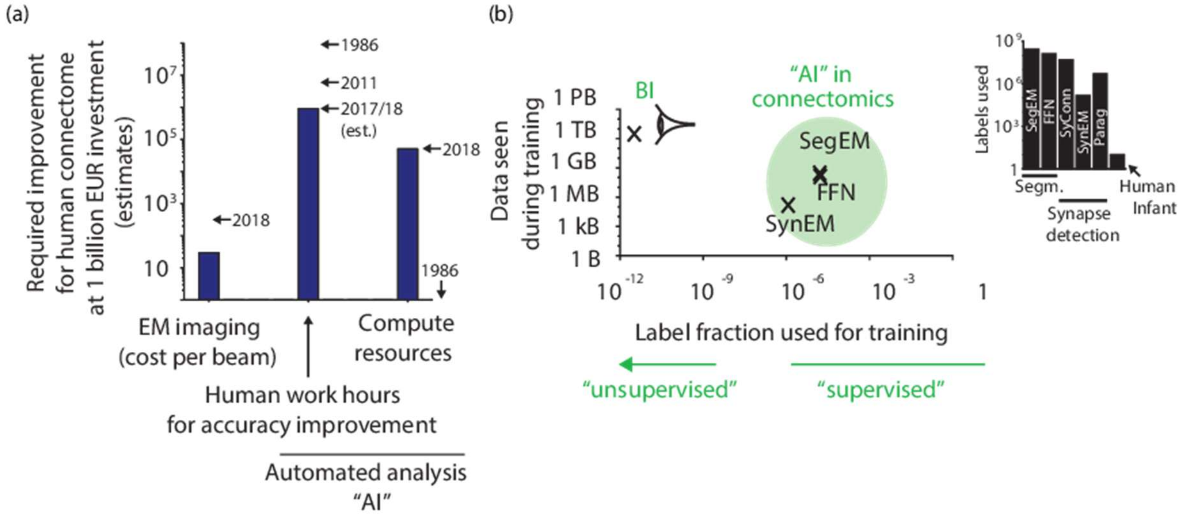

Figure 1-2 Comparison of imaging and data analysis resources for obtaining a human nanoscale connectome; and comparison of the need for labels in artificial and human 'intelligence'. **(a)** Estimates of required improvements of 3D-EM imaging and connectomic data analysis if the goals is to image a human brain microscale connectome investing 1 billion EUR over 5 years for each of the 3 categories (imaging, human annotation, compute resources). Note that while 'only' 5 orders of magnitude improvements of automated analysis accuracy are required, these have to go along with increased computational efficiency of 4 orders of magnitude. Automated analysis improvements over the last decade have yielded about 2 orders of magnitude in accuracy (compare (Helmstaedter 2013)), but at substantial increase in computational cost; however, human annotation cost still exceeds computational cost by about an order of magnitude (cf. (Lichtman et al. 2014) for a focus on the computational cost). Note further that when automated reconstruction accuracy approaches a level at which entire neurons are on average error-free (i.e. error rates below one per 1–10cm for human neurons), human annotation may become entirely dispensable. **(b)** Difference of required label rate and total raw data amount between artificial intelligence (AI) approaches used in connectomics today and estimates for human infant learning to identify trees from visual inputs. Note that while massive data repetition in AI methods shifts exposed data amounts, label fraction stays unchanged. Inset shows total amount of labels used in current connectomic analysis approaches for segmentation and synapse detection: SegEM (Berning et al. 2015); Flood-filling networks (FFN) (Januszewski et al. 2018); SyConn (Dorkenwald et al. 2017); SynEM (Staffler et al. 2017); Parag (Parag et al. 2018).

far gained any substantial traction: While different unsupervised algorithms have been developed for example, for layer-wise pre-training (Hinton et al. 2006), auto-encoders (Bengio 2009, Kingma and Welling 2013), adversarial training (Goodfellow et al. 2014); and semi-supervised methods have been explored (Kingma et al. 2014, Rasmus et al. 2015), none of these has yet resulted in an order-of-magnitude improvement over the performance achieved by supervised learning for a large variety of tasks (see also (Goodfellow et al. 2016), p. 489).

Facing the challenge to speed up connectomic data analysis by at least five orders of magnitude while at the same time reducing the computational cost by four orders of magnitude for the mapping of a human connectome, we think one has to ask whether the current supervised machine learning approaches will be able to provide the order-of-magnitude advance in both accuracy and efficiency every about five years that is needed to see this happen in the lifetime of today's PhD students. Human brains operate at extremely low computational cost, and the accuracy of an attentive, focused human is sufficient to solve probably all segmentation problems in well-aligned 3D image data in connectomics. And they achieve this with minimal labels. This not to say that current progress in connectomic is strictly limited by available labels (compare for example SegEM (Berning et al. 2015) to flood filling networks (Januszewski et al. 2018)—about the same amount of labels, but six-fold improvement of inter-error distances). But it is plausible to ask whether it is maybe inefficient (or wasteful) not to make use of the fact that raw data are available in vast amounts (the equivalent of the visual input of a two-year old can be generated within five days on a mSEM). We may find out that learning with extremely low label rates (that could be higher-order labels (Silver et al. 2017)) is required to accelerate progress in connectomic analysis.

In any case, this comparison may point to the fact that with all current optimism about 'artificial intelligence', it is primarily the availability of massive label amounts (via user agreement, for example https://policies.google.com/privacy or via substantial resource investments into human work, connectomics) that rescues accuracy in current machine learning approaches to a certain degree. Far-reaching progress, in artificial intelligence as in connectomics, may only be possible when we understand and emulate the way biological computers, such as mammalian brains, implement efficient data-driven, not label-driven learning. Connectomic insights may contribute for this to happen (Helmstaedter 2015, Lake et al. 2017, Lake et al. 2017, Schmidt et al. 2017, Motta et al. 2019, Bartol et al. 2015, de Vivo et al. 2017).

Conflict of interest statement

Nothing declared.

Acknowledgements

We thank Mike Hemberger for discussions, Kevin Boergens and Helene Schmidt for comments on the manuscript. Data for Figure 1-1a were provided in part by the Human Connectome Project, WU-Minn Consortium (Principal Investigators: David Van Essen and Kamil Ugurbil; 1U54MH091657) funded by the 16 N.I.H. Institutes and Centers that support the NIH Blueprint for Neuroscience Research; and by the McDonnell Center for Systems Neuroscience at Washington University.

Chapter 2. Dense connectomic reconstruction in layer 4 of somatosensory cortex

Alessandro Motta*, Manuel Berning*, Kevin M. Boergens*, Benedikt Staffler*, Marcel Beining, Sahil Loomba, Philipp Hennig, Heiko Wissler, Moritz Helmstaedter.
Science (2019). DOI: 10.1126/science.aay3134
* authors **contributed equally** to this work

Contributions: Development of automated methods (Figure 2-2A) for neurite type classification (TypeEM; Figure 2-2C), and spine head detection and attachment (Figure 2-2D). Contributions to the semi-automated reconstruction of axons, in particular to the resolution of merge errors (Figure 2-2H). Development of statistical methods for connectome analysis, specifically for the definition of axon classes with subcellular target specificities (Figure 2-4), for the quantification of the contributions of neurite geometry and postsynaptic membrane distribution to axonal targeting (Figure 2-5), for the detection of thalamocortical axons and the analysis of subcellular distribution of their output synapses on postsynaptic neurons (Figure 2-6), and for estimation of the circuit fractions that are consistent with homosynaptic plasticity mechanisms (Figure 2-7). Writing of manuscript with MH and with contributions by all authors.

Research article summary

Introduction

The brain of mammals consists of an enormously dense network of neuronal wires: the axons and dendrites of nerve cells. Their packing density is so high that light-based imaging methods have so far only been able to resolve a very small fraction of nerve cells and their interaction sites, the synapses, in mammalian cortex. Recent advances in three-dimensional (3D) electron microscopy allow researchers to image every nerve cell and all chemical synapses in a given piece of brain tissue, opening up the possibility of mapping neuronal networks densely, not just sparsely. Although there have been substantial advances in imaging speed, the analysis of such 3D image data is still the limiting step. Therefore, dense reconstructions of cortical tissue have thus far been limited to femtoliter-scale volumes, keeping the systematic analysis of axons, neuronal cell bodies and their dendrites of different types, and the dense connectome between them out of reach.

Rationale

Image analysis has made decisive progress using artificial intelligence-based methods, but the resulting reconstructions of dense nerve tissue are still too error-prone to be scientifically meaningful as is. To address this, human data analysis has been integrated into the generation of connectomes and it is the efficiency of this human-machine data analysis that now determines progress in connectomics. We therefore focused on efficiency gains by: (i) improving the automated segmentation quality, (ii) analyzing the automated segmentation for locations of likely errors and directing the human work to these locations only, and (iii) optimizing human data interaction by helping annotators to immediately understand the problem to be solved, allowing fast, in-browser parallel data flight, and by minimizing latency between annotator queries. With this, close to 100 student annotators solved hundreds of thousands of reconstruction problems within just 29 s each, including all preparation and transition time.

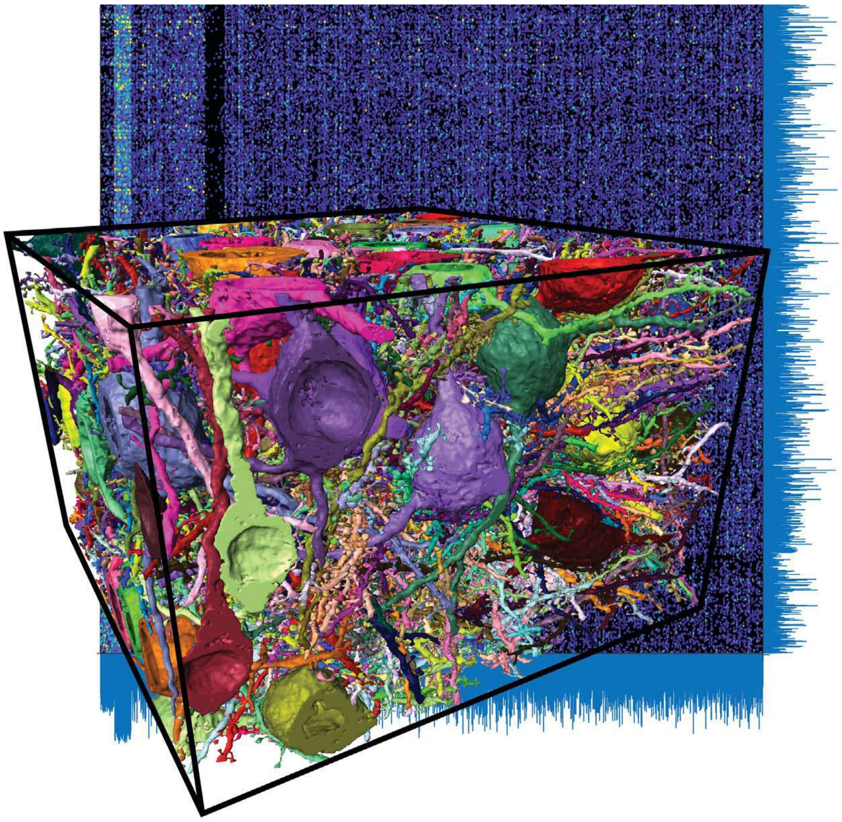

Dense reconstruction of ~500,000 cubic micrometers of cortical tissue yielding 2.7 m of neuronal cables (~3% shown, front) implementing a connectome of ~400,000 synapses between 34,221 axons and 11,400 postsynaptic processes (fraction shown, back). These data were used for connectomic cell-type definition, geometrical circuit analysis, and measurement of the possible plastic fraction (the “learnedness”) of the circuit.

Results

We reconstructed 2.7 m of neuronal wires densely in layer 4 of mouse somatosensory cortex within on ~4000 invested human work hours, yielding a reconstruction ~300 times larger than previous dense cortical reconstructions at ~20-fold increased efficiency, a leap for the dense reconstruction of connectomes. The resulting connectome between 6979 presynaptic and 3719 postsynaptic neurites with at least 10 synapses each, comprising 153,171 synapses total, was then analyzed for the dense circuit structure in the cerebral cortex. We found that connectomic data alone allowed the definition of inhibitory axon types that showed established principles of synaptic specificity for subcellular postsynaptic compartments, but that at scales beyond ~5 μm, geometric predictability of the circuit structure was low and coarser models of random wiring needed to be rejected for dense cortical neuropil. A gradient of thalamocortical synapse density along the cortical axis yielded an enhanced variability of synaptic input composition at the level of single L4 cell dendrites. Finally, we quantified connectomic imprints consistent with Hebbian synaptic weight adaptation, obtaining upper bounds for the fraction of the circuit that could have undergone long-term potentiation.

Conclusion

By leveraging human-machine interaction for connectomic analysis of neuronal tissue, we acquired the largest connectome from the cerebral cortex to date. Using these data for connectomic cell-type definition and the mapping of upper bounds for the learned circuit fraction, we establish an approach for connectomic phenotyping of local dense neuronal circuitry in the mammalian cortex, opening the possibility for the connectomic screening of nervous tissue from various cortices, layers, species, developmental stages, sensory experience, and disease conditions.

Research article

The dense circuit structure of mammalian cerebral cortex is still unknown. With developments in three-dimensional electron microscopy, the imaging of sizable volumes of neuropil has become possible, but dense reconstruction of connectomes is the limiting step. We reconstructed a volume of ~500,000 cubic micrometers from layer 4 of mouse barrel cortex, ~300 times larger than previous dense reconstructions from the mammalian cerebral cortex. The connectomic data allowed the extraction of inhibitory and excitatory neuron subtypes that were not predictable from geometric information. We quantified connectomic imprints consistent with Hebbian synaptic weight adaptation, with yielded upper bounds for the fraction of the circuit consistent with saturated long-term potentiation. These data establish an approach for the locally dense connectomic phenotyping of neuronal circuits in the mammalian cortex.

The cerebral cortex of mammals houses an enormously complex intercellular interaction network implemented with neuronal processes that are long and thin, branching, and extremely densely packed. Early estimates indicated that 4 km of axons and 400 m of dendrites are compressed into a cubic millimeter of cortical tissue (Braitenberg and Schüz 1998). This high packing density of cellular processes has made the locally dense mapping of neuronal network in the cerebral cortex challenging.

So far, reconstructions of cortical tissue have been either sparse (Lübke et al. 2003, da Costa and Martin 2009, Bock et al. 2011, Lee et al. 2016, Schmidt et al. 2017, Han et al. 2018) or restricted to small volumes of up to 1500 μm^3 (Mishchenko et al. 2010, Kasthuri et al. 2015, Calì et al. 2018). Consequently, the detailed network architecture of the cerebral cortex is unknown. Particular open questions are to what degree local neuronal circuits are explainable by geometric rules alone (Braitenberg and Schüz 1998, Lübke et al. 2003, Peters 1979, Binzegger et al. 2004, Markram et al. 2015) and on which spatial scales cortical connectivity is only explainable by innervation preferences beyond such geometric models (Lee et al. 2016, Mishchenko et al. 2010, Kasthuri et al. 2015, White et al. 1984, Shepherd et al. 2005). Similarly, although numerous cortical neuronal cell types have been described based on protein expression, morphology, and electrophysiological characteristics (Ascoli et al. 2008), and these have been shown to have particular target patterns (Kubota et al. 2016), the inverse question—whether, at the level of dense cortical circuit, axons represent a continuum of synaptic preference or a set of distinct innervation paradigms that would allow for a purely connectomic cell type definition [as has been successful in the retina (Helmstaedter et al. 2013, Kim et al. 2014)]—is still open. Next, at the level of synaptic input to the primary dendrites of cortical excitatory cells, it is not known whether the typically three to 10 primary dendrites of a cortical neuron that leave the cell body homogeneously sample the available excitatory and inhibitory synaptic inputs or if there is an enhanced heterogeneity of synaptic input position, making it possible to exploit the numerous mechanisms that have been discussed for the nonlinear integration of local synaptic inputs (Major et al. 2013, Jia et al. 2014, Lavzin et al. 2012, Branco et al. 2010). Finally, whereas the change of synaptic weights in response to electrical and sensory stimulation has been widely studied (Fifková and Van Harreveld 1977, Markram et al. 1997, Egger et al. 1999, Matsuzaki et al. 2004, Sáez and Friedlander 2009) and connectomic data consistent with LTP have been described (Bartol et al. 2015, Sorra and Harris 1993), the fraction of a given cortical circuit that is plausibly shaped by processes related to Hebbian learning under undisturbed conditions is still unknown.

We used dense connectomic reconstruction to quantitatively address these questions about the formational principles of a dense cortical circuit.

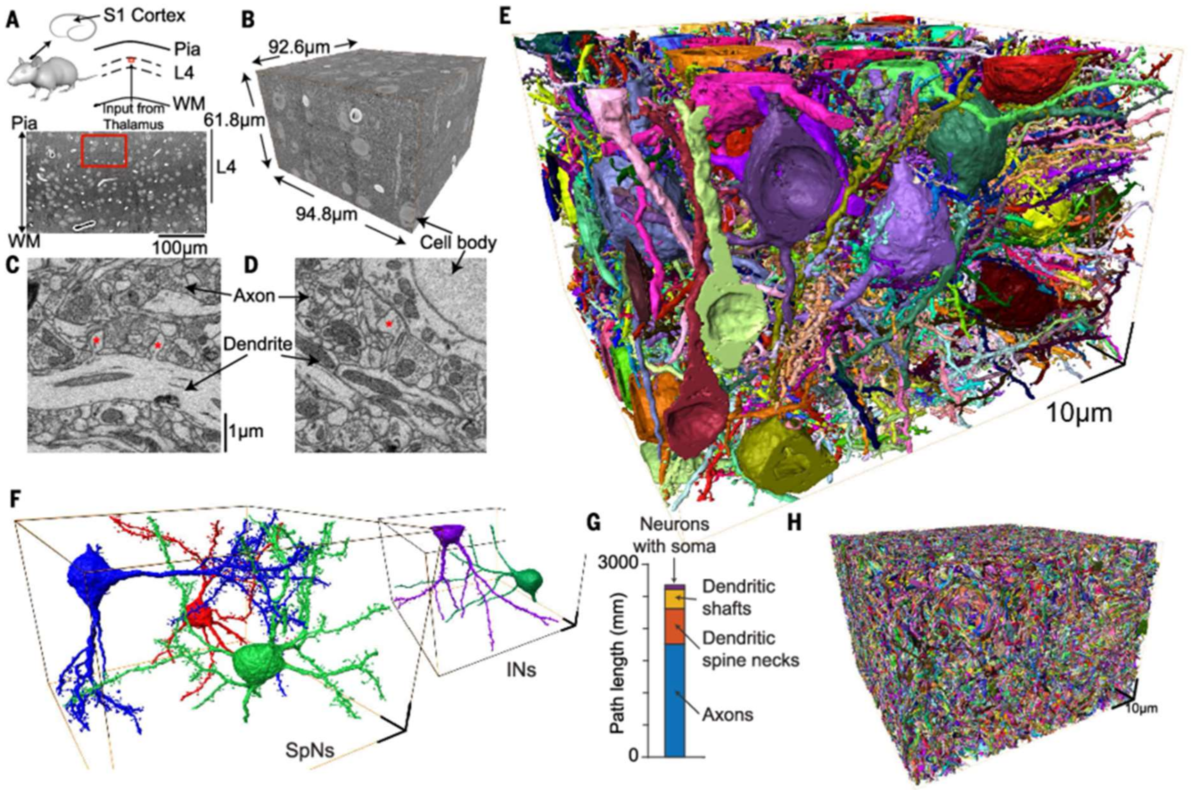

Figure 2-1 Dense connectomic reconstruction of cortical neuropil from layer 4 of mouse primary somatosensory cortex. (**A** to **D**) Location [(A), red] of the 3D EM dataset (B). WM, white matter. High-resolution example images are shown in (C) and (D). Asterisks indicate examples of dendritic spines. Direct links to data browser webKnossos are as follows: https://wklink.org/9276 (B), https://wklink.org/7101 (C), and https://wklink.org/8906 (D). (**E**) Reconstruction of *n* = 89 neurons with a cell body and dendrites in the dataset. (**F**) Three spiny neurons (SpNs) and two INs (see movie A2-1). (**G**) Quantification of circuit components in the dense reconstruction. Most of the circuit path length (total: 2.69 m) is contributed by nonproximal axons (1.79 m, 66.6%), spine necks (0.55 m, 20.5%), and dendritic shafts (0.28 m, 10.3%) not connected to any cell body in the volume. (**H**) Display of all 34,221 reconstructed axons contained in the dataset. Scale bars in (D) are as in (C); scale bar in (F) is 10 µm.

Results

We acquired a three-dimensional (3D) EM dataset from upper layer 4 of primary somatosensory cortex of a 28-day-old mouse (Figure 2-1, A to D, likely located within a barrel, see Materials and Methods in appendix A1) using serial block-face electron microscopy [SBEM (Denk and Horstmann 2004); dataset size: 61.8 × 94.8 × 92.6 µm^3; voxel size: 11.24 × 11.24 × 28 nm^3]. For dense reconstruction (Figure 2-1, E to H), we 3D aligned the images and applied a sequences of automated analyses [SegEM (Berning et al. 2015), SynEM (Staffler et al. 2017), ConnectEM, and TypeEM; Figure 2-2, Materials and Methods in appendix A2 and Table A2-2], followed by focused manual annotation (FocusEM). We reconstructed 89 neurons that had their cell body in the dataset (Figure 2-1, E and F). These neurons constituted only 2.6% of the total path length (69 mm; Figure 2-1G). To reconstruct axons, which constitute most of the wiring in the dense circuit (1.79 m, 66.6%, Figure 2-1H), we applied a scalable distributed annotation strategy that identified locations of uncertainty in the automated reconstruction, which were then resolved by targeted manual annotation. To reduce the required manual annotation time, it was critical to obtain an automated reconstruction with low error rates, to use efficient algorithms for identifying locations for focused manual inspection (queries), and to minimize the time spent per user query. For this (Figure 2-2A), we developed artificial intelligence-based algorithms that evaluated the EM image data and convolutional neural network (CNN)-filtered

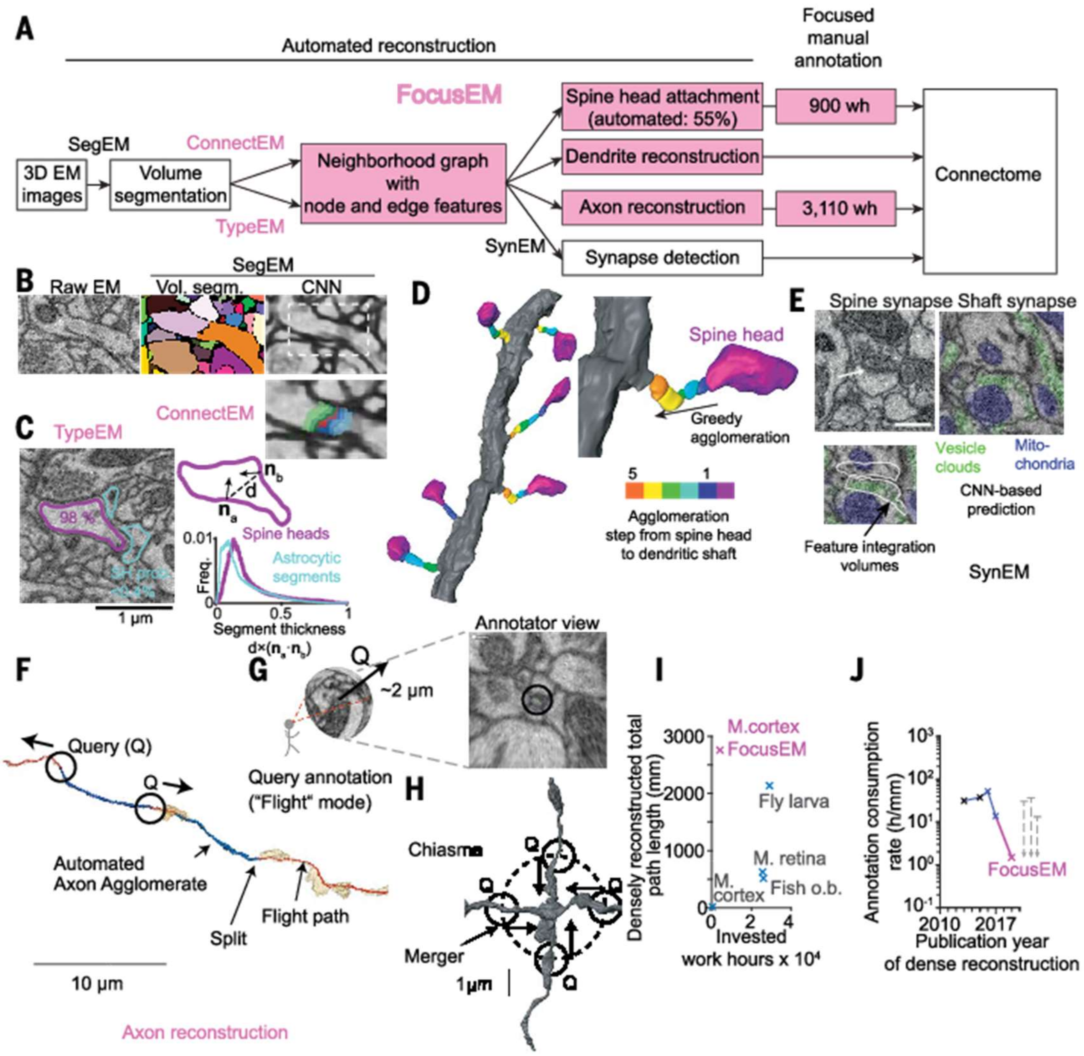

Figure 2-2 Methods for the efficient dense connectomic reconstruction. (**A**) Simplified diagram of reconstruction steps [figure A2-1, detailed in (B) to (H)]. wh, annotation work hours. (**B**) ConnectEM classifier for combining neurite pieces from the CNN-based volume segmentation (Berning et al. 2015): at junctions of volume segments (bottom right), raw data, CNN, and shape features were evaluated. (**C**). TypeEM classifier for assigning cellular identity to volume segments: the probability of axons, dendrites, spine heads, and glial processes was evaluated. Shown is an illustration of spine head (purple) and astrocyte (cyan) classification; one of the 985 features is illustrated (segment thickness). Numbers indicate the probability of the segment being a spine head. Precision and recall of spine head detection were 92.6 and 94.4%, respectively. (**D**) Process for automatically attaching spine heads to the dendritic shaft by stepwise agglomeration of volume segments along the highest-probability transition between neighboring segments [according to the ConnectEM score (B)]. An example of six neighboring spine heads that were all automatically attached is shown. In total, 58.9% of spine heads were automatically attached (A). (**E**) Automated detection of spine and shaft synapses [here, vesicle clouds (green) and mitochondria (blue) were detected and used as additional features for the SynEM (Staffler et al. 2017) classifier]. (**F** to **H**) Focused annotation strategy for directing human annotation queries (Q) to ending locations of the automatically reconstructed axon pieces [(F), blue], oriented along the axon's main axis [traced in webKnossos using flight mode (G (Boergens et al. 2017)), yielding flight paths of 5.5 ± 8.8 µm length (21.3 ± 36.1 s per ending annotation, n = 242,271, movie A2-1)]. Neurite mergers (H) were detected as "chiasmatic" configurations, and queries (Q) directed from the exits of the chiasma toward its center were used to determine correct neurite continuities (figure A2-1). (**I** and **J**) Quantification of circuit size and invested work hours for dense circuit reconstructions in connectomics and resulting order-of-magnitude improvement provided by FocusEM compared with previous dense reconstructions (m). Fish o.b., zebrafish olfactory bulb (Wanner et al. 2016); M. retina, mouse retina IPL (Helmstaedter et al. 2013); Fly larva, mushroom body in larval stage of *D. melanogaster* (Eichler et al. 2017); M. cortex, mouse somatosensory cortex [(Kasthuri et al. 2015) and this study (magenta)]. Only completed dense reconstructions were included in the comparison.

versions of the image data in the surrounding of interjunctions between segmented pieces of neurites (Figure 2-2B). Together with classifiers that computed the probability of volume segments belonging to an axon, a dendrite, a spine head, or a glial process (using, among others, shape features; Figure 2-2C), this allowed us to automatically connect parts of dendrites, attach spine heads to dendritic shafts (by a greedy stepwise agglomeration initiated at the spine head, Figure 2-2D; 58.9% of spine heads unaffected by the dataset boundary were automatically attached) and reconstruct parts of axons. Similarly, synapses were automatically detected by evaluating pre- and postsynaptic volumes at neurite interfaces [Figure 2-2E and Figures A2-2 to A2-5 (Staffler et al. 2017); for shaft synapses, additional CNN-based classifiers for vesicle clouds and mitochondria were used]. To manually correct remaining errors in axons (Figure 2-2, F to H), we detected ending locations of automatically reconstructed axon pieces (Figure 2-2F) and directed user queries to these locations. For this, we used an egocentric 3D image display mode ["flight mode," Figure 2-2G (Boergens et al. 2017)] and oriented the user annotation along the axis of the neurite for which a local annotation ("query") was requested (Movie A2-2). Together with data preloading, this yielded a low-latency, targeted neurite annotation in which individual user queries took 29.4 s to resolve (traveled path length per query: 5.49 μm). These queries could be easily distributed among 87 annotators. Similarly, we detected locations of likely mergers between axons (Figure 2-2H, "chiasmata") and directed user queries to reconnect these chiasma exits along actual axons. Using this scalable annotation architecture, we obtained a dense reconstruction of 2.69 m of neuronal processes (Figure 2-1, G and H) with a total investment of 3981 human work hours, ~10 times faster than a recent dense reconstruction in the fly larval brain (Eichler et al. 2017) (Figure 2-2, I and J), ~20 times faster than the previous dense reconstruction in the mammalian retina (Helmstaedter et al. 2013), and ~25 times faster than the previous dense reconstruction in mammalian cortex (Kasthuri et al. 2015) (Figure 2-2, I and J). To quantify remaining reconstruction error rates in this dense neuropil reconstruction, we measured the remaining errors in a set of 10 randomly chosen axons and found 12.8 errors per millimeter of path length (of these, there were 8.7 continuity errors per millimeter; see Materials and Methods in appendix A2). This is indistinguishable from the error rates previously found in fast human annotations (Helmstaedter et al. 2013, Boergens et al. 2017, Helmstaedter et al. 2011).

We obtained a connectome (Figure 2-3) between 34,221 presynaptic axonal processes and 11,400 postsynaptic processes [6979 × 3719 connectivity matrix (Figure 2-3E) when restricted to those pre- and postsynaptic neurites that established at least 10 synapses]. Among the postsynaptic processes, we classified n = 169 apical dendrites (ADs) that traversed the dataset along the cortical axis without connection to one of the neuronal cell bodies in the dataset (Figure 2-2A), 246 smooth dendrites (SDs, Figure 2-2B), 80 somata, 116 axon initial segments (AIS; Figure 2-2C), and 89 proximal dendrite (PD) trees connected to a soma in the dataset (Movie A2-1; note that some of these neurons also had ADs that were classified as PDs and not included in the AD definition above; see Materials and Methods, and Tables A2-1 and A2-2).

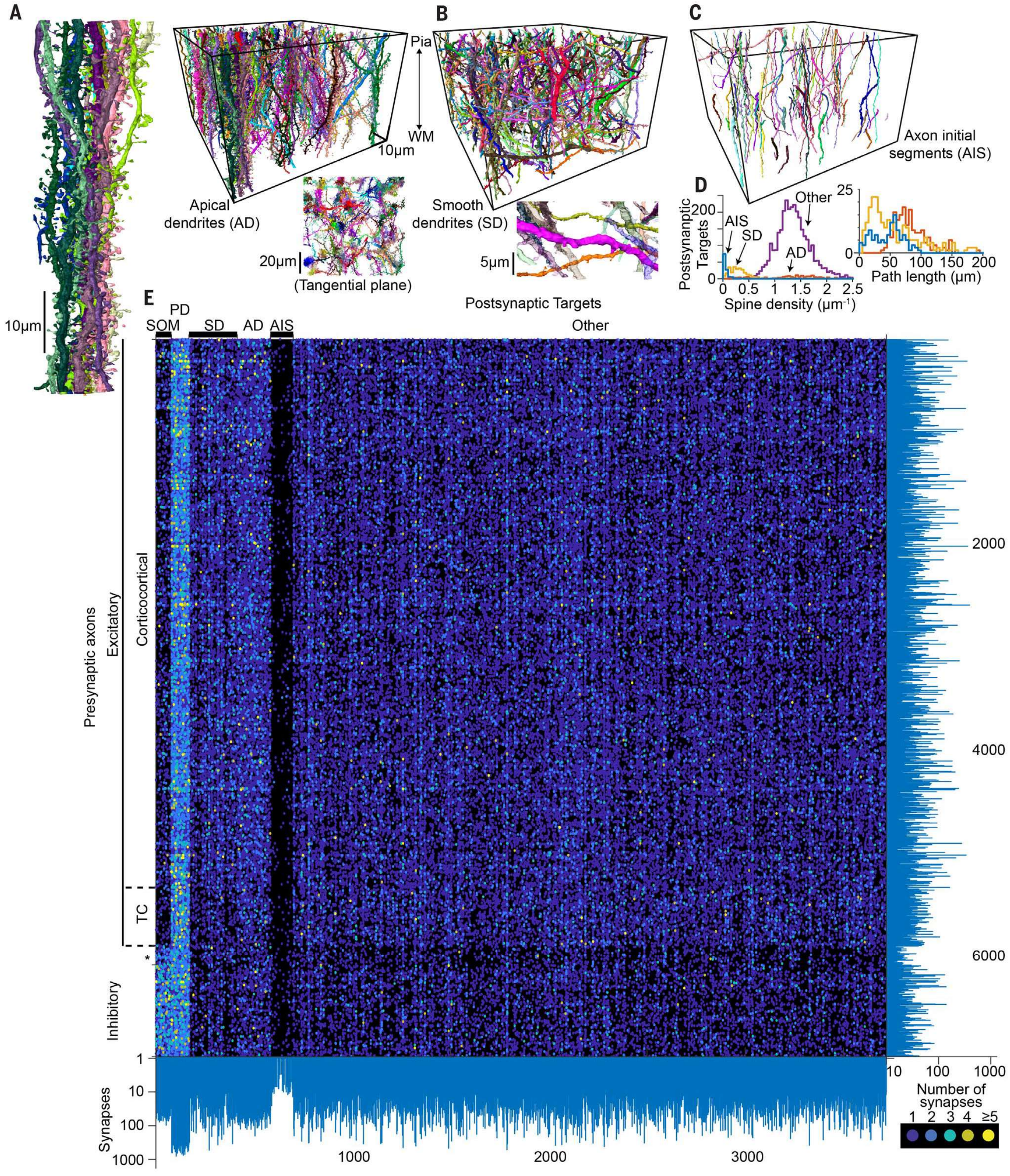

Figure 2-3 Postsynaptic target classes and dense cortical connectome. (**A** to **D**) Display of all ADs [(A), magnified one AD bundle (left) and top view in tangential plane illustrating AD bundles], SDs [(B), magnification inset illustrating low rate of spines], AISs (C), and their respective path length and spine density distributions (D). Note that spine density is underestimated by ~20% (table A2-1). (**E**) Display of connectome between all axons (*n* = 6979) and postsynaptic targets (*n* = 3719) in the volume with at least 10 synapses each, establishing a total of 153,171 synapses (of 388,554 synapses detected in the volume). For the definition of postsynaptic target classes, see (A) to (D); for the definition of presynaptic axon classes, see figure 2-4 and figure A2-6. AISs with fewer than 10 input synapses are also shown. SOM, neuronal somata. Note that some of these PD dendrites are L4 ADs not included in the AD definition above. Asterisks indicate remaining unassigned axons.

Connectomic definition of axon types

We investigated whether, based solely on connectomic information (Figure 2-3), we could extract the rules of subcellular innervation preference described for inhibitory axons in the mammalian cortex (Kubota et al. 2016) and if such synaptic target preference could also be found for excitatory axons. We first measured the preference of each axon for innervating dendritic spine heads versus dendritic shafts and other targets (Figure 2-4, A and B) because, in the mammalian cortex, most axons of inhibitory interneurons (INs) preferentially innervate the dendrites' shafts or neuronal somata (Kubota et al. 2016) and most excitatory glutamatergic axons preferentially innervate the spine heads of dendrites (Braitenberg and Schüz 1998). The fraction of primary spine synapses per axon (out of all synapses of that axon) accordingly allowed the identification of spine-preferring, likely excitatory axons with at least 50% primary spine innervations ($n = 5894$ axons) and shaft-preferring, likely inhibitory axons with <20% primary spine innervations ($n = 893$ axons, or 13.2% of all axons; for exceptions to this rule and control measurements, see appendix A2 and Tables A2-1 and A2-2).

We then determined for each of the subcellular synaptic target classes defined above (Figures 2-3 and 2-4C) the per-synapse innervation probability that would best explain whether and inhibitory axon establishes at least one synapse onto each of these targets. These inhibitory "single-hit" binomial innervation probabilities were 4.2% (somata), 17.8% (PD), 4.9% (SD), 3.3% (AD), and 0.5% (AIS) (Figure 2-4D). We then computed the expected distribution of synapses per axon made onto each target class assuming the double-hit, triple-hit, etc., innervation probabilities are the same as the probability to establish at least one synapse onto that target. When comparing these target distributions with the measured distributions of synapses per axon onto each target class (Figure 2-4E), we found that inhibitory axons established enhanced preference for somata ($p = 2.4 \times 10^{-34}$, $n = 893$, one-sided Kolmogorov-Smirnov test), PDs ($p = 6.0 \times 10^{-77}$), ADs ($p = 2.5 \times 10^{-4}$), and to a lesser degree for SDs ($p = 1.7 \times 10^{-3}$, Table A2-1), but no enhanced preference for AISs in L4 ($p = 0.648$). AISs were synaptically innervated by 0.172 input synapses per micrometer of AIS length, but these innervations were not made by axons with an enhanced preference for AISs, unlike in supragranular and infragranular layers (Taniguchi et al. 2013).

When performing the same analysis for excitatory axons (Figure 2-4F), we found clear target preference for ADs ($p = 2.5 \times 10^{-34}$, Figure 2-4F), SDs ($p = 7.6 \times 10^{-25}$), and PDs ($p = 1.3 \times 10^{-169}$). By contrast, thalamocortical (TC) axons [detected using the criteria reported in (Bopp et al. 2017); see figure A2-6, and Materials and Methods] indicated a target preference for PDs ($p = 2.5 \times 10^{-31}$), but not for ADs ($p = 0.019$) or SDs ($p = 0.723$). To determine the fraction of inhibitory and excitatory axons that had an unexpected high synaptic preference for one (or multiple) of the subcellular target classes, we applied the false detection rate criterion used for the determination of significantly expressed genes [q value (Storey and Tibshirani 2003); see materials and methods] and obtained lower bounds on the fractions of axons in the tissue that preferentially innervate the various subcellular target classes (Figure 2-4G; at 58.0% of inhibitory and 24.4% of excitatory axons). Inhibitory axons (Figure 2-4H), but not excitatory axons (Figure 2-4I), showed higher-order innervation preferences, indicating that at the level of the dense cortical circuit, synaptic target preferences established by axons were not a continuum but allowed cell-type classification without the need for measurements of neuronal morphology, electrical activity, protein expression, or transcription levels.

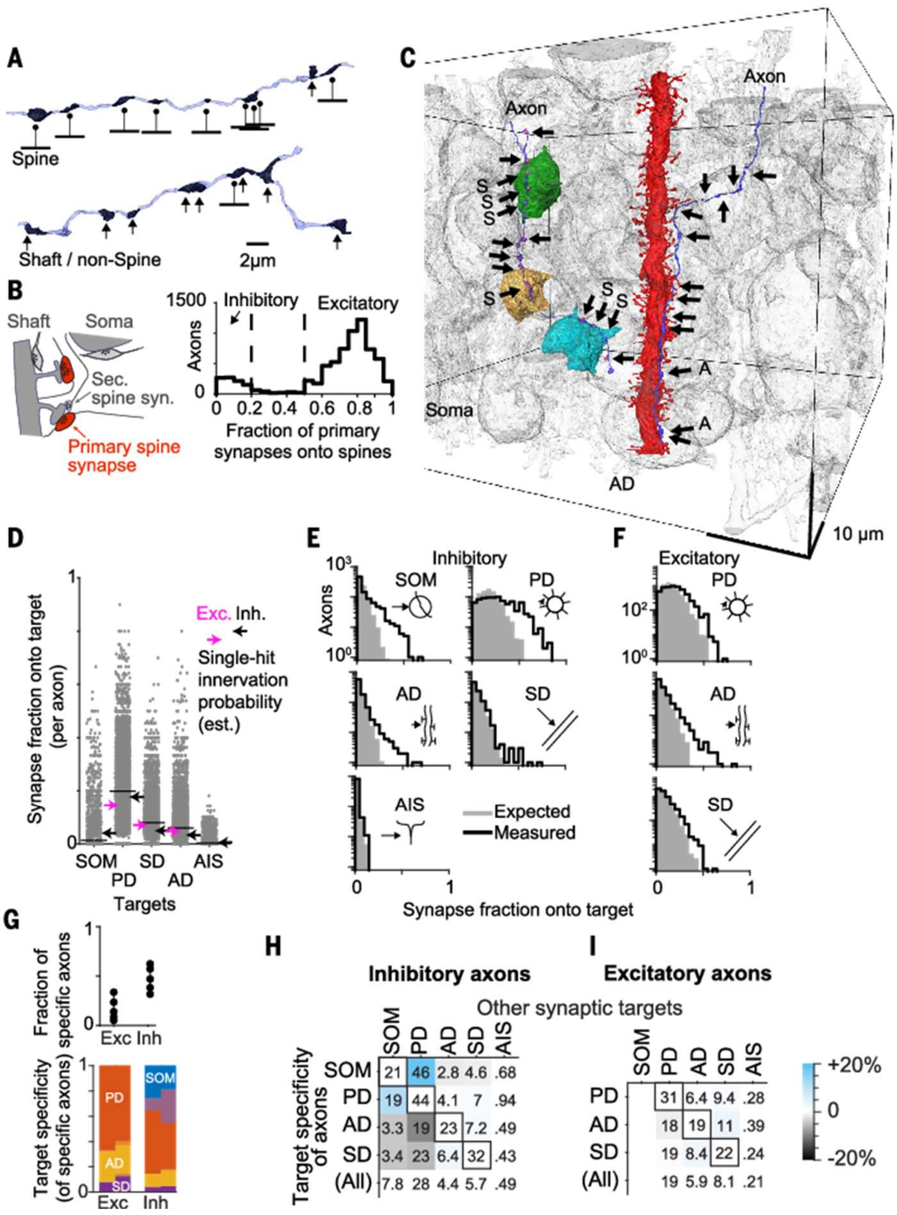

Figure 2-4 Connectomic definition of axon classes. (**A**) Example axons with high (top) and low (bottom) fraction of output synapses made onto dendritic spines. (**B**) Distribution of spine-targeting fraction over all *n* = 6,979 axons; dashed lines indicate thresholds applied to distinguish non-spine preferring, likely inhibitory axons (<20% spine innervation, *n* = 893, 12.8% of all axons) from spine-preferring, mostly excitatory axons (>50% spine innervation, *n* = 5,894, 84.5%). Diagram shows the definition of primary spine innervations. (**C** to **I**) Connectomic definition of axon classes by preferential synaptic innervation of subcellular targets. (C) Two sample axons innervating three somata [left, *n* = 6 synapses onto somata (S) of 14 total, arrows] and an AD (right, *n* = 2 synapses onto AD of 13 total), respectively. All other cell bodies and ADs are shown in gray. (D) Fraction of synapses onto somata, PDs, ADs, SDs, and AISs for all axons. Binomial probabilities are shown over axons to establish at least one synapse onto the respective target (arrows: magenta, excitatory; black, inhibitory). Black lines indicate the average over axons. (E) Comparison of predicted synapse fraction onto target classes per inhibitory axon on the basis of the binomial probability to innervate the target at least once [gray shading; see arrows in (D)] and measured distribution of synapse fractions onto targets (black lines). (F) Same as (E) but for excitatory axons. (G) Fraction of target-preferring excitatory (Exc.) and inhibitory (Inh.) axons identified using the false detection rate criterion [*q* = 5 to 30% (Storey and Tibshirani 2003)]. Colored bars indicate the distribution for *q* = 5% (left) and *q* = 30% (right). Mixed colors indicate axons specific for both somata and PDs. [(H) and (I)] Second-order innervation preference by target-specific axons; numbers indicate fractional innervation by remaining synapses per axon; colors indicate underfrequent (black) or overfrequent (blue) innervation. Diagonal entries are the fraction of synapses onto the same target (black boxes).

Geometric sources of synaptic innervations

Could these local connectivity rules have been derived solely from the geometry of axons and dendrites? We first quantified the overall relation between the spatial distribution of axons and dendrites and the establishment of synapses between them (Figure 2-5). One paradigm, originally proposed by Peters (Peters 1979), states that TC axons entering a certain cortical tissue volume would sample the available cortical dendrites for synaptic innervation according to their relative prevalence in the tissue (Braitenberg and Schüz 1998). This model (Figure 2-5A) predicted the TC innervation of most cortical dendrites rather well, with the exception of smooth dendrites [an exception reported by White et al. (White et al. 1984)] and the enhanced TC innervation of PDs of layer 4 cells (Jia et al. 2014). When applied to cortical excitatory and inhibitory axons (Figure 2-5A), we found that this model predicted excitatory innervation of most spiny dendrites rather well, but again failed to predict innervation of SDs and the proximal bias of inhibitory synapses. Because this model [which has been most widely used for circuit inference (Lübke et al. 2003, Binzegger et al. 2004)] implicitly accounts for the density of synapses along the presynaptic axons, it was capable of capturing the increased synapse density of TC axons (Figure 2-5A). A simpler variant of Peters model (Braitenberg and Schüz 1998, Shepherd et al. 2005) (Figure 2-5B), which uses the density of pre- and postsynaptic path length as basis for the synaptic innervation prediction, failed at predicting the TC innervation but captured the corticocortical innervation of spiny dendrites (Figure 2-5B). We then analyzed whether a Peters model normalized for postsynaptic synapse density (Figure 2-5C) would better capture synaptic innervation and found that, in fact, the dendritic model was a far better predictor of synaptic innervation (compare Figure 2-5, C and B). This indicated that SDs and Ads sampled synaptic input according to the relative path length of the presynaptic axon (Figure 2-5C). We then investigated whether a Peters model account for pre- *and* postsynaptic synapse densities would improve the innervation prediction (Figure 2-5D). In this model, both the output and the input of cortical excitatory neurites were properly predicted, but the suppressed innervation of SDs and Ads by TC axons and the proximal bias of inhibitory axons was not. Notably, none of the Peters models could account for this proximal bias of inhibitory synapses [Figure 2-5D; for other failures of Peters predictions, see, e.g., (da Costa and Martin 2009, Schmidt et al. 2017, Mishchenko et al. 2010, Kasthuri et al. 2015)].

More recently, the Peters has been investigated for the close proximity between axons and dendrites on the scale of a few micrometers (Mishchenko et al. 2010, Kasthuri et al. 2015) and concluded poor (Mishchenko et al. 2010) or absent (Kasthuri et al. 2015) geometric predictability of synaptic innervation. We used our larger dense reconstruction to investigate the geometric prediction over a substantially broader spatial scale from 1 to ~30 µm and accounted for inhibitory axons, excitatory axons, and postsynaptic target types (Figure 2-5, E to H). We measured whether the postsynaptic membrane surface available within a certain radius r_{pred} around a given axon (Figure 2-5E) would be a predictor of synaptic innervation for that given axon. We measured the available membrane surface belonging to the five subcellular target classes around all 6979 axons (Figure 2-5F) and used a linear multinomial regression model to predict synaptic innervation from these data (Figure 2-5G). Then, we computed the coefficient of determination (R^2) reporting the fraction of axonal synaptic innervation variance that could be explained purely based on the geometrical information (Figure 2-5H; for details, see materials and methods). In fact, for small spatial scales of 1 to 5 µm, the membrane surface available around an axon was a rather good predictor of synaptic innervation from excitatory axons (range, 16 to 90%, Figure 2-5H; less so for inhibitory axons: range, 23 to 79%).

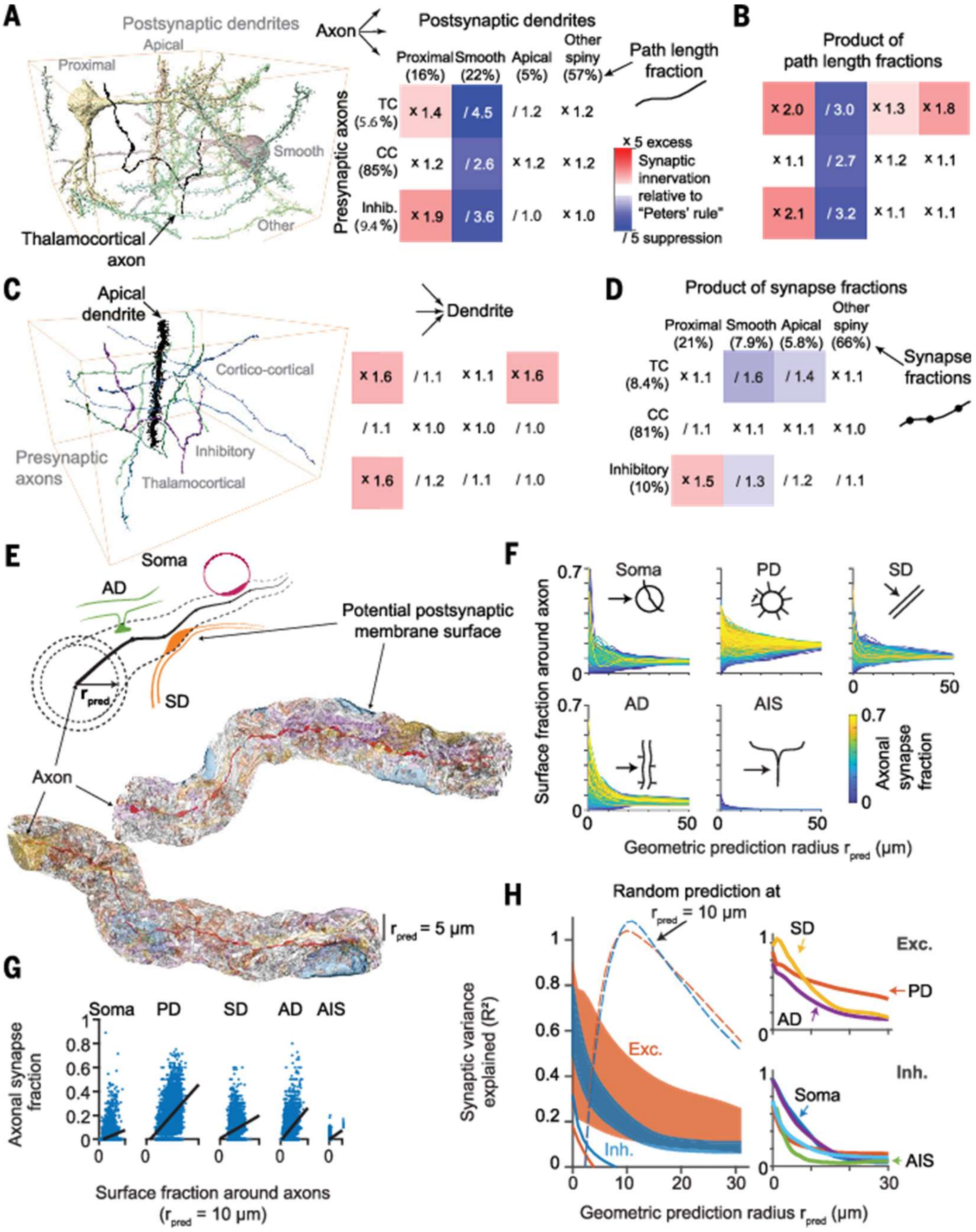

Figure 2-5 Contribution of neurite geometry and membrane availability to cortical wiring. (**A** to **D**) Quantitative test of various formulations of Peters' rule: comparison of actual synaptic innervation to the prediction of synaptic innervation on the basis of the availability of postsynaptic path length in the dataset (A), the product of pre- and postsynaptic path length (B), the sampling of presynaptic partners by their relative prevalence (C), and the product of pre- and postsynaptic synapse density (D). Log likelihood ratios were as follows: -1.1×10^3 (A), -11×10^3 (C), and -12×10^3 (D), all compared with the simple model in (B); $p < 10^{-14}$ (corrected for degrees of freedom). (**E** to **H**) Prediction of single-axon synaptic target preference by distance-dependent postsynaptic surface sampling. (E) Diagram of the surface area of the various subcellular postsynaptic target classes (colors) within a distance r_{pred} from a given axon (black) and example surfaces around two axons within a prediction radius $r_{\mathrm{pred}} = 5$ µm. (F) Surface fraction of target classes around all $n = 6979$ axons in dependence of r_{pred} around axons. Colors indicate the fraction of synapses of a given axon actually innervating the respective target. (G) Relationship between the surface fraction around all axons and synaptic innervation by these axons for each target ($r_{\mathrm{pred}} = 10$ µm). Black lines indicate linear regression for geometrical innervation prediction. (H) R^2 reporting the fraction of synaptic innervation variance [over all axons; see (G)] explained by a multivariate linear innervation model using the available postsynaptic surface area around axons [shaded areas: red, excitatory axons (Exc.); blue, inhibitory axons (Inh.)]; lower end of shades indicates prediction; upper ends indicate correction by the variance contributed by the multinomial sampling of targets along axons; solid lines represent direct prediction of innervation from surface fraction. Dashed lines indicate modeled prediction for a purely geometric forward model at $r_{\mathrm{pred}} = 10$ µm. Insets (right) show sampling-corrected predictive power of excitatory (top) and inhibitory (bottom) axons for the innervation of target classes.

Would this imply that axonal and dendritic proximity at the single-axon level can be used to infer synaptic connectivity in the cortex (Markram et al. 2015)? We found that for the spatial alignment scales that can be achieved in light-microscopy-based neuron reconstructions from multiple animals (10 to 20 µm), predictability dropped substantially (Figure 2-5H), making circuit inference by an emulation of growth processes based on light-microscopically aligned data (Markram et al. 2015, Reimann et al. 2015) implausible.

Subcellular synapse placement

We used our dense reconstruction to study the spatial distribution of synapses along somata and dendrites in the cortical neuropil. The density of TC synapses had a substantial dependence on cortex depth (Figure 2-6, A to D): the absolute density of TC synapses in the volume increased by ~93% over 50 µm cortex depth (Figure 2-6, A and B); the TC excitatory synapse fraction TC/(TC+CC) (where CC is corticocortical) increased by 82.6%, corresponding to an absolute increase in the TC synapse fraction of 5.8% per 50 µm cortex depth (Figure 2-6D). This gradient was consistent with light-microscopic analyses of TC synapses indicating a decrease of TC synapse density from lower to upper L4 (Oberlaender et al. 2012). Neither the inhibitory nor the corticocortical excitatory synapse densities showed a comparable spatial profile (Figure 2-6C).

How is the synaptic TC gradient mapped onto the dendrites of L4 neurons along the cortex axis (Figure 2-6, E to G)? One possibility is that the TC synapse gradient is used to enhance the variability of synaptic input composition between different primary dendrites of the L4 neurons such that a neuron’s dendrites pointing upward toward the pia would sample relatively less TC input than dendrites pointing toward the white matter. Alternatively, mechanisms to establish synaptic target preference (such as those reported in Figure 2-4) could be used to counterbalance this synaptic gradient and equilibrate the synaptic input fractions on the differently oriented dendrites. Our analysis showed that, in fact, even at the level of single primary dendrites, TC input fractions were 1.28-fold higher for dendrites pointing upward toward the cortical surface versus downward toward the white matter (Figure 2-6, F and G; TC input fractions of each dendrite were corrected for the entire neuron’s TC input fraction; for this analysis, see materials and methods). We then investigated whether this differential composition of the excitatory inputs is accompanied by different compositions of the inhibitory input synapses (Figure 2-6, H to L). We found that the fraction of TC input to a neuron’s dendrites was anti-correlated to the fraction of inhibitory synapses that originated from AD-preferring inhibitory axons (Figures 2-6I and 2-4), both at the level of the input to L4 neurons and at the level of single primary dendrites of L4 neurons (Figure 2-6, I and J). The effect was absent for all other synapse classes, most notably the soma-preferring inhibitory axons (Figure 2-6K; see discussion).

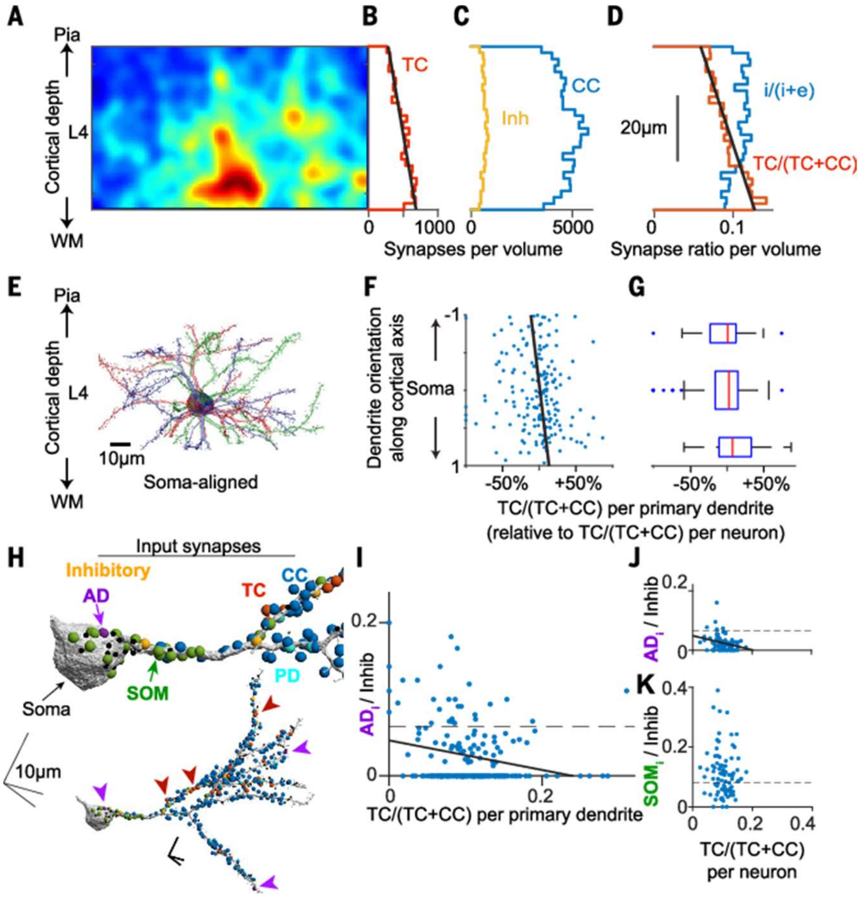

Figure 2-6 Gradient of TC synapse density in L4 and ensuing variability of synaptic input composition in L4 neurons. (**A** to **D**) Distribution of TC synapses within the L4 dataset (A): gradient along the cortical axis (B), which is absent for inhibitory (yellow) or CC (blue) synapses (C). (D) Resulting gradient of TC synapse fraction [increase by 83% from 7.0 to 12.8% (+5.8%) within 50 µm along the cortical axis; line fit, $p < 1.1 \times 10^{-12}$, $n = 134{,}537$ synapses]. (**E** to **G**) Analysis of the variability of TC input onto the primary dendrites of neurons possibly resulting from the TC synapse gradient (D): example reconstructions (E) aligned to the somata; (F) fraction of excitatory input synapses originating from TC axons evaluated for each primary dendrite, plotted according to the direction of the dendrite relative to cortical axis (-1, aligned toward pia; +1, aligned toward WM). TC input fraction [TC/(TC+CC)] of each dendrite compared with the TC input fraction of its entire parent neuron (ratio shown). (G) Summary analysis of relation between dendrite direction and relative TC input fraction showing that the TC input fraction is determined by the dendrites' orientation relative to the cortex (1.28-fold higher relative TC fraction for downward- than upward-pointing dendrites, $n = 183$, $p = 0.026$, two-sided t test for dendrites with a normalized absolute projection >0.5; bars correspond to ranges -1 to -0.5; -0.5 to 0.5; and 0.5 to 1). (**H** to **K**) Enhanced TC synaptic input (red spheres) is correlated to reduced inhibitory input from AD-preferring inhibitory axons (purple spheres and arrows in H) at the level of single dendrites ($r = -0.24$, $p = 0.0095$, $n = 183$, Pearson's correlation after Bonferroni's correction) and for neurons [(J), $r = -0.27$, $p = 0.01$, $n = 84$], but not soma-preferring inhibitory axons [green in (H) and (K), $r = 0.08$, $p = 0.49$, $n = 84$].

Connectomic mapping of the plasticity-consistent circuit fraction

The concept of Hebbian plasticity, thought to be at the core of experience-dependent changes of synaptic weights in the brain, makes predictions about the temporal evolution of synaptic weights in multiple synaptic contacts between the same pre- and postsynaptic neurons (AADD joint synapses; Figure 2-7, A and B): Because Hebbian synaptic plasticity is dependent on the electrical activity of the pre- and postsynaptic neurons, which in a first approximation can be assumed to be similar at joint synapses, long-term potentiation (LTP) predicts joint synapses to become stronger and relatively more similar in weight (especially if synaptic weight saturates) and long-term depression (LTD) predicts joint synapses to become weaker and relatively more dissimilar in weight (but more similar if synaptic weights saturate; Figure 2-7A). Models of LTP and LTD thus make particular predictions about the temporal evolution of joint synaptic weights, and the mapping of synaptic weights and synaptic weight similarity in the connectome allows the quantification of upper bounds on the fraction of the circuit that can have undergone such particular patterns of weight change before the connectomic experiment (we denote those synapse pairs for which such patterns of weight change occurred to a sufficient degree as "having undergone LTP/LTD"; see discussion).

We set out to leverage our large connectomic dataset (n = 5290 excitatory joint synaptic pairs onto spines; Figure 2-7C) to map the relation between synaptic size and synaptic size similarity in joint synapse pairs [Figure 2-7E; for visualization, the figure reports relative synaptic size *dis*similarity on the x-axis; for the utilization of the axon-spine interface area (Figure 2-7D) as an indicator of synaptic weight (Cheetham et al. 2014, de Vivo et al. 2017)]. These data would allow us to determine upper bounds on the plasticity-consistent fraction of the circuit beyond the previous finding that in joint synapse pairs, synaptic size is more similar than for randomly shuffled synapse pairs (Kasthuri et al. 2015, Bartol et al. 2015, Sorra and Harris 1993, Bloss et al. 2018).

Synaptic size similarity in joint synapse pairs showed a broad distribution (Figure 2-7E). When comparing this distribution with the synaptic size and synaptic size similarity distribution obtained from a random assignment of the same synapses onto "random pairs" (Figure 2-7F and Figure A2-7, C and D), we observed that the population of oversimilar synapse pairs (Figure 2-7F) was split into a region of oversimilar and large synapses (mean synaptic size 0.23 to 1.19 μm^2; 16 to 20% of all joint synapse pairs are found in this region; the above-random synapse pairs constitute 3.6 to 3.9% of all joint synapse pairs; see figure A2-7, C and D, and the Materials and Methods for details of the region definition and statistics), and oversimilar and small synapses (mean synaptic size 0.06 to 0.2 μm^2; 15 to 19% of all joint synapse pairs were found in this region; 3.0 to 3.4% of all joint synapse pairs were above random in this region). With this information, we obtained upper bounds on the fraction of the circuit that can have undergone LTP and LTD with weight saturation (compare Figure 2-7, F and A).

To what degree was the observed synaptic weight similarity a result of subtypes of neurons establishing differently sized synapses? Although the quantification of the upper bounds of the plasticity-consistent circuit fraction would remain unaffected, we could use this more detailed analysis to understand whether the plasticity-consistent circuit fractions were specific to types of neuronal connections.

First, we considered the possibility that certain presynaptic cell types made consistently larger or consistently smaller synapses (Figure 2-7G). In this case, the distribution of synaptic weight similarity for same-axon different-dendrite (AADs) synapse pairs would also show a bias toward more similarly size synapses. However, we found no such evidence (Figure 2-7H), excluding cell-type-specific synapse size of either presynaptic (axonal) or postsynaptic (dendritic) origin as the cause of the observed oversimilar synapse pairs.

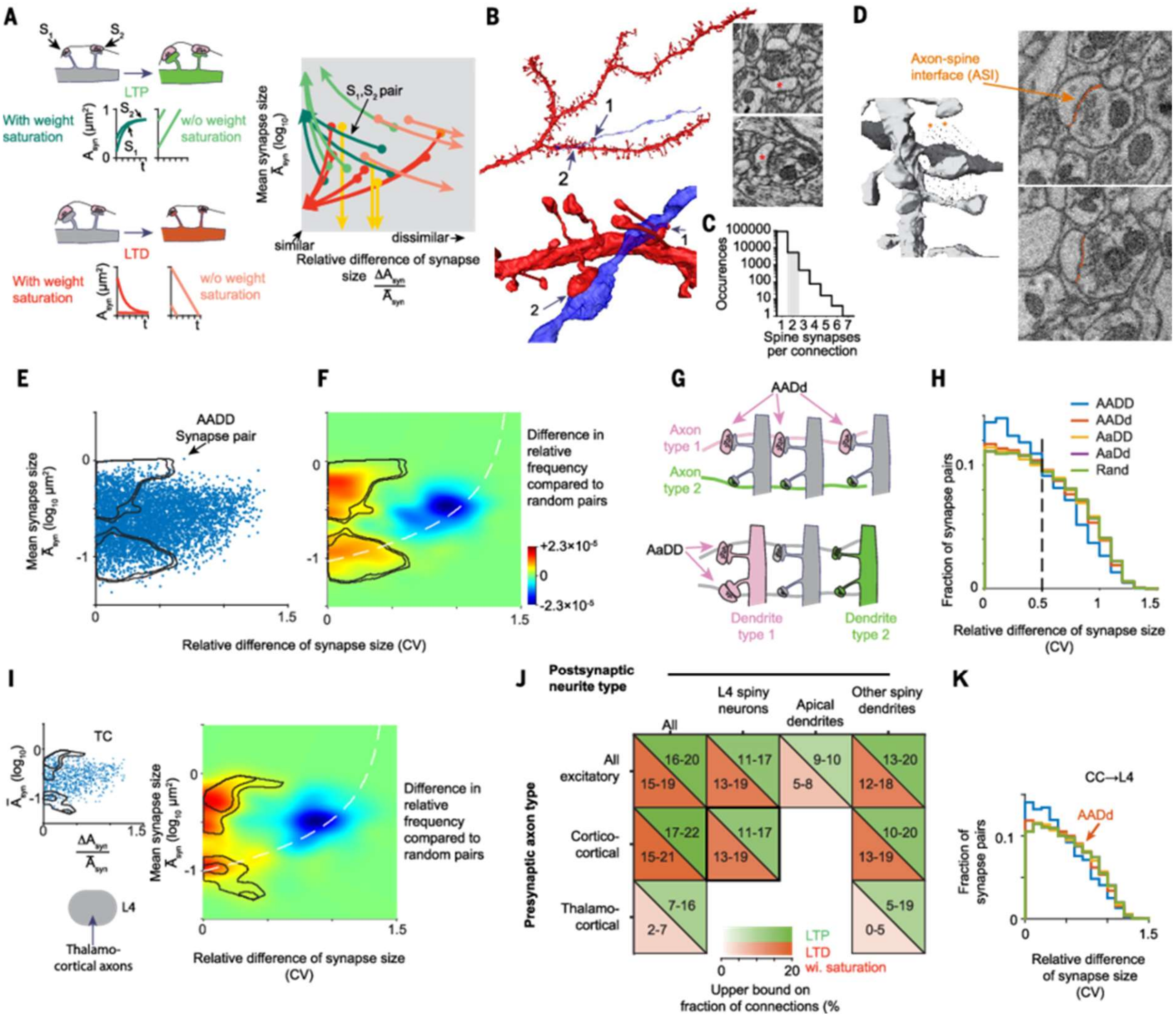

Presynaptic axon type	All	L4 spiny neurons	Apical dendrites	Other spiny dendrites
All excitatory	16-20 15-19	11-17 13-19	9-10 5-8	13-20 12-18
Cortico-cortical	17-22 15-21	11-17 13-19		10-20 13-19
Thalamo-cortical	7-16 2-7			5-19 0-5

Figure 2-7 Connectomic mapping of the plasticity-consistent circuit fraction. (**A**) Hebbian LTP makes predictions about the temporal evolution of synaptic size and size similarity in AADD synapse pairs (green; insets show example model trajectories of synapse pairs exposed to LTP with and without weight saturation), yielding a region in the size-similarity plane (right) where synaptic pairs that have undergone LTP are predicted to be found (colors in right panel as in temporal plots on the left). For Hebbian LTD, pairs of synapses behave accordingly only if synaptic size saturates at low values (red). Arrows indicate trajectories of synapse pairs with randomly drawn initial size that undergone LTP with (dark green) or without (light green) weight saturation; LTD with (red) and without (pink and yellow indicate linear and exponential decay, respectively) weight saturation. (**B**) Example AADD synapse pair (arrows) onto dendritic spines between the same axon (blue) and same dendrite (red). Direct links to datasets are as follows: https://wklink.org/3356 (synapse 1) and https://wklink.org/6145 (synapse 2). (**C**) Frequency of joint synapse pairs in the dataset (n = 5290 spine synapse pairs, shaded, analyzed here). (**D**) ASI as a representative measure of synapse weight (Cheetham et al. 2014, de Vivo et al. 2017), dataset link https://wklink.org/5780 (**E**) Distribution of mean synaptic size and synaptic size similarity for all pairs of AADD synapses from excitatory axons; each dot corresponds to one synapse pair. Isolines indicate statistical regions defined in (F). (**F**) Map of the relation between synaptic size and synaptic size similarity in AADD pairs, reported as the difference of (E) to random synapse pairs (figure A2-7, C and D). Isolines indicate significance levels (p = 0.05 and 0.005 for outer and inner isolines, respectively) outlining overfrequency of synapse pairs that are similar in size and large (upper area) and similar in size and small (lower area). (**G** and **H**) Analysis of AADd and AaDD synapse pairs that would indicate a contribution of cell-type-dependent connection size differences. No oversimilarity can be found in these cases (H). (**I**) Analysis as in (E) and (F) but for TC connections. Note upper bound of 16% of connections consistent with stabilized LTP. (**J**) Summary of fraction of synapse pairs that resided in the regions identified in (F) and (I) as upper bounds (for the interaction between the two upper bounds, see Materials and Methods in appendix A2). Numbers indicate the ranges for different significant thresholds [see (F) and (I) and figure A2-7, C and D]. (**K**) Analysis as in (G) and (H) but for CC-to-L4 neuron connections only, refuting subtypes of CC connections as the source of the observed oversimilarity (see figure A2-7, A and B). Image width is 2 µm in (B) and (D).

Next, we separated those connections established by TC axons from those made by the remaining excitatory (i.e., CC) axons (Figure 2-7I and figure A2-7, A and B). We found an excess of oversimilar synapse pairs in the TC connections as well, with 7 to 16% of pairs found in a region of overly similar and large synapses (i.e., an upper bound of 16% on LTP). The region of overly similar and small synapse pairs, however, only comprised 2 to 7% of joint synapse pairs. This remaining number of overly similar small synapse pairs could in fact be induced by the overly similar large synapse pairs (see Materials and Methods in appendix A2). At 28 days of age, ~3 weeks after the proposed critical period during which LTP can be induced in TC connections (Crair and Malenka 1995, Li et al. 2013), a fraction of up to 16% of joint synapse pairs was still consistent with previous episodes of LTP that led to stabilized potentiated synapse pairs at dendritic spines (Grutzendler et al. 2002, Trachtenberg et al. 2002), but 84% were not.

Repeating these analyses for other combinations of pre- and postsynaptic neurite types (Figure 2-7J), we found upper bounds for LTP and LTD of ~10 to 20%. For each of these subtype-specific connections, we could then again analyze whether any purely presynaptic or purely postsynaptic subtype within the already type-selected connections (corresponding to squares in the table of Figure 2-7J) could be the cause of the observed synapse similarity. For example, the connections from corticocortical axons onto spiny L4 neurons (Feldmeyer et al. 1999) showed no evidence for presynaptic axonal subtypes yielding oversimilar synapses (Figure 2-7K; for additional controls of these findings, see appendix A2; figure A2-7, A and B; and table A2-1).

Together, these results provide a first quantitative upper bound on the fraction of the circuit consistent with previous episodes of saturated Hebbian synaptic plasticity leading to strengthening or weakening of synapses (a "connectomic fingerprint" of the maximum possible plasticity fraction of the circuit) and excluded obvious cell-type-based connection strength differences as the origin of these observations. Because these results were obtained from brains of untrained animals and were not the result of electrical or other simulation ("plasticity induction"), these data may represent an unbiased screening of upper bounds of plasticity traces in local cortical circuits, for which the dense connectomic mapping was essential.

Discussion

Using FocusEM, we obtained the first dense circuit reconstruction from the mammalian cerebral cortex at a scale that allowed the analysis of axonal patterns of subcellular innervation, ~300 times larger than previous dense reconstructions from cortex (Kasthuri et al. 2015). Inhibitory axon types preferentially innervating certain postsynaptic subcellular compartments could be defined solely on the basis of connectomic information (Figures 2-3 and 2-4). In addition to inhibitory axons, a fraction of excitatory axons also exhibited such subcellular innervation preferences (Figure 2-4). The geometrical arrangement of axons and dendrites explained only a moderate fraction of synaptic innervation, revoking coarse random models of cortical wiring (Figure 2-5). A substantial TC synapse gradient in L4 gave rise to an enhanced heterogeneity of synaptic input composition at the level of single cortical dendrites (Figure 2-6), which was accompanied by a reduced innervation from AD-preferring inhibitory inputs. The consistency of synapse size between pairs of axons and dendrites signified fractions of the circuit consistent with saturated synaptic plasticity, placing an upper bound on the "learned" fraction of the circuit (Figure 2-7). FocusEM allowed the dense mapping of circuits in the cerebral cortex at a throughput that enables connectomic screening.

Synaptic input composition along L4 dendrites

Our finding of a covariation of enhanced TC input to L4 excitatory cells with reduced direct inhibitory input from AD-preferring INs (Figure 2-6, H to K) could be interpreted in the context of a disinhibitory circuit described previously (Pfeffer et al. 2013, Yu et al. 2019). Taking into account the preferential targeting of ADs and of soma-preferring parvalbumin (PV)-positive INs by somatostatin (SST)-positive INs, this could imply that SST-IN-based disinhibition can enhance TC input by silencing perisomatic PV inputs recruited by feedforward inhibition (Porter et al. 2001) and concomitantly reducing the direct inhibitory component from SST INs. In any case, this finding of per-dendrite input variation points to a circuit configuration in which TC input variability is enhanced between neurons of the same excitatory type in cortical layer 4, and furthermore provides evidence for a per-dendrite synaptic input composition of enhanced heterogeneity.

Connectomic traces of plasticity

We interpreted the joint synapse data (Figure 2-7) in terms of upper bounds of synapse pairs that could have undergone certain models of plasticity. Although this analysis detects those synapse pairs that were exposed to saturating plasticity (i.e., the possible plasticity event led to a final weight state of both synapses), an alternative interpretation is a dynamic circuit in which at any given point in time, only a fraction of synapses has expressed saturated plasticity, whereas other (or all) synapses are in the process of undergoing plastic changes. We expect that more elaborate plasticity models of entire circuits will also make testable predictions that are accessible by connectomic snapshot experiments as shown here.

Outlook

The presented methods and results open the path to the connectomic screening of nervous tissue from various cortices, layers, species, developmental stages, sensory experiences, and disease conditions. The fact that even a small piece of mammalian cortical neuropil contains a high density of relevant information so rich as to allow the extraction of possible connectomic signatures of the "learnedness" of the circuit makes this approach a promising endeavor for the study of the structural setup of mammalian nervous systems.

Materials and Methods

Animal experiments

A wild-type (C57BL/6) male mouse was transcardially perfused at postnatal day 28 under isoflurane anesthesia using a solution of 2.5% paraformaldehyde and 1.25% glutaraldehyde (pH 7.4) following the protocol in (Briggman et al. 2011). All procedures followed the animal experiment regulations of the Max Planck Society and were approved by the local animal welfare authorities (Regierungspräsidien Oberbayern and Darmstadt).

Tissue sampling and staining

The brain was removed from the skull after 48 hours of fixation and sliced coronally using a vibratome. Two samples were extracted using a 1-mm biopsy punch (Integra Miltex, Plainsboro, NJ) from a 1-mm-thick slice 5 mm from the front of the brain targeted to layer 4 in the somatosensory cortex of the right hemisphere. The corresponding tissue from the left hemisphere was further sliced into 70-µm-thick slices followed by cytochrome oxidase staining, indicating the location of the coronal slice to be in barrel cortex.

Next, the extracted tissue was stained as described previously (Briggman et al. 2011). Briefly, the tissue was immersed in a reduced osmium tetroxide solution (2% OsO_4, 0.15 M CB, 2.5 M KFeCN), followed by a 1% thiocarbohydrazide step and a 2% OsO_4 step for amplification. After an overnight wash, the sample was further incubated with 1.5% uranyl acetate solution and a 0.02 M lead(II) nitrate solution. The sample was dehydrated with propylene oxide and EtOH embedded in Epon Hard (Serva Electrophoresis GmbH, Germany), and hardened for 48 hours at 60°C.

3D electron microscopy experiment

The embedded sample was placed on an aluminum stub and trimmed such that the tissue was directly exposed on all four side of the sample. The sides of the sample were covered with gold in a sputter coater (Leica Microsystems, Wetzlar, Germany). Then, the sample was placed into an SBEM setup [(Denk and Horstmann 2004), Magellan scanning electron microscope, FEI Company, Hillsboro, OR, equipped with a custom-built microtome courtesy of W. Denk]. The sample was oriented so that the radial cortex axis was in the cutting plane. The transition between L4 and L5A was identified in overview electron microscopy (EM) images by the sudden drop in soma density between the two layers (Figure 2-1C). A region of size 96 × 64 μm^2 within L4 was selected for imaging using a 3 × 3 image mosaic, a pixel size of 11.24 × 11.24 nm^2, an image acquisition rate of 10 MHz, a nominal beam current of 3.2 nA (thus a nominal electron dose of 15.8 e^-/nm^2), an acceleration voltage of 2.5 kV, and a nominal cutting thickness of 28 nm. The effective data rate, including overhead time spent during motor movements for cutting and tiling, was 0.9 MB/s. A total of 3420 image planes were acquired, yielding 194 GB of data.

Image alignment

After 3D EM dataset acquisition, all images were inspected manually and marked for imaging artifacts caused by debris present on the sample surface during imaging. Images with debris artifacts were replaced by the images at the same mosaic position from the previous or subsequent plane. First, rigid translation-only alignment was performed based on the procedures in (Briggman et al. 2011). The following modifications were applied. When shift vectors were obtained that yielded offsets of >100 pixels, these errors were iteratively corrected by manually reducing the weight of the corresponding entry in the least-squares relaxation by a factor of up to 1000 until the highest remaining residual error was <10 pixels. Shift calculations of subsequent images in cutting direction was found to be the most reliable measurement and was therefore weighted 3-fold in the weighted least-squares relaxation. The resulting shift vectors were applied (shift by integer voxel numbers) and the 3D image data were written in KNOSSOS format (Boergens et al. 2017, Helmstaedter et al. 2011). For further improvements, subimage alignment was applied (see Materials and Methods in appendix A2).

Methods description for software code

All routines described in the following are available as software at https://gitlab.mpcdf.mpg.de/connectomics/L4dense, which is the relevant reference for the exact sequence of processing steps applied. The following descriptions and the more detailed ones in the Materials and Methods in appendix A2 are aimed at pointing to the key algorithmic steps rather than enumerating all detailed computations.

Workflow for dense circuit reconstruction

The workflow for volume reconstruction of the acquired 3D EM volume (Figure 2-2 and figure A2-1) was as follows. We first detected blood vessels and cell bodies using automated heuristics, and then processed the remaining image volume using machine-learning-based image segmentation [CNN and watershed as described in SegEM (Berning et al. 2015)]. The result of this processing was 15 million volume segments correspond to pieces of axons, dendrites, and somata (volume: 0.0295 ± 0.3846 μm^3, mean ± SD). We then constructed the neighborhood graph between all these volume segments and computed the properties of interfaces between directly adjacent volume segments. On the basis of these features, we trained a connectivity classifier (ConnectEM; Figure 2-2, A and B) to determine whether two segments should be connected (along an axon or a dendrite or glial cell) or if they should be disconnected. Using the SynEM classifier (Staffler et al. 2017), we determined whether an interface between two disconnected processes corresponds to a chemical synapse and, if so, which was the presynaptic and which was the postsynaptic neurite segment (see below for more details). We furthermore trained a set of classifiers (TypeEM; Figure 2-2C) to compute for each volume segment the probability of being part of an axon, a dendrite, a spine head, or a glia cell (precision and recall were 91.8 and 92.9% for axons, 95.3 and 90.7% for dendrites, 97.2 and 85.9% for astrocytes, and 92.6 and 94.4% for spine heads, respectively; see table A2-2).

Cell body-based neuron reconstruction

We next reconstructed those neurons that had their cell bodies in the tissue volume (Figure 2-1, E and F, cell gallery in Movie A2-1; n = 125 cell bodies; of these, 97 were neuronal and of these 97, 89 were reconstructed with dendrites in the dataset). For this, we used a set of simple growth rules for automatically connecting neurite pieces on the basis of the segment-to-segment neighborhood graph and the connectivity and neurite type classifiers (Figure A2-1, "automated agglomeration"; see Materials and Methods in appendix A2). As a result, we obtained fully automated reconstructions of the neuron's soma and dendritic processes. With a minimum additional manual correction investment of 9.7 hours for 89 cells (54.5 mm dendritic and 2.1 mm axonal path length), the dendritic shafts of these neurons could be reconstructed without merge errors, but there were 37 remaining split errors, at 87.3% dendritic length recall (table A2-2). This reconstruction efficiency compares favorably to recent reports of automated segmentation of neurons in 3D EM data from the bird brain obtained at ~2-fold higher imaging resolution (Januszewski et al. 2018), which reports soma-based neuron reconstruction at an error rate of beyond 100 errors per 66 mm dendritic shafts at lower (68%) dendritic length recall with similar resource investment (see Materials and Methods in appendix A2).

In addition to the dendritic shafts, the dendritic spines constitute a major fraction of the dendritic path length in cortical neuropil (Figure 2-1G). Using out spine head classifier (part of the TypeEM classifiers; Figure 2-2C), we found 415,797 spine heads in the tissue volume, which is a density of 0.784 per μm^3 (0.98 per μm^3 neuropil, when excluding somata and blood vessels). To connect these to the corresponding dendritic shafts, we trained a spine neck continuity algorithm that was able to automatically attach 58.9% of these spines (evaluated in the center of the dataset at least 10 µm from the dataset border), yielding a dendritic spine density of 0.672 per µm dendritic shaft length [comparable to spine densities in the bird brain (Kornfeld et al. 2017)]. However, in the mammalian cerebral cortex, the density of spines along dendrites is even higher (at least 1 per µm dendritic shaft length). The remaining spine heads were then attached to their dendritic shafts by seeding manual reconstructions at the spine heads and asking annotators to continue along the spine necks to the dendritic shafts. This annotations was performed in the "orthogonal mode" configuration of webKnossos (Boergens et al. 2017), in which the annotator viewed three orthogonal image planes to decide where to continue the respective spine neck [as in KNOSSOS (Helmstaedter et al. 2011)]. The annotation of all remaining spine necks consumed an additional 900 hours of human work for the attachment of 98,221 spines, resulting in a final overall spine density of 0.959 per µm dendritic shaft length.

Dense tissue reconstruction

The reconstruction of neurons starting from their cell bodies, however, was not the main challenge. Rather, the remaining processes, axons and dendrites not connected to a cell body within the dataset and densely packed in the tissue constitute ~97% of the total neuronal path length in this volume of cortex (Figure 2-1G). To reconstruct this vast majority of neurites (Figure 2-1H), we first used out connectivity and neurite type classifiers (ConnectEM and TypeEM, respectively; Figure 2-2) to combine neurite pieces into larger dendritic and axonal agglomerates ("automated agglomeration", figure A2-1, and Materials and Methods in appendix A2). Then, we took those agglomerates that had a length of at least 5 µm (n = 74,074 axon agglomerates), detected their endings that were not at the dataset border, and directed focused human annotators to these endings ("queries", Figure 2-2, F and G).

For human annotation, we used an egocentric directed 3D image data view ("flight mode" in webKnossos), which we had previously found to provide maximized human reconstruction speed along axons and dendrites in the cortex (Boergens et al. 2017). Here, however, instead of asking human annotators to reconstruct entire dendrites or axons, we only queried their judgement at the endings of automatically reconstructed neurite parts. To make these queries efficient, we made three additions to webKnossos: (i) we oriented the user along the estimated direction of the neurite at its ending, reducing the time the user needs to orient within the 3D brain tissue; (ii) we dynamically stopped the user's flight along the axon or dendrite whenever another of the already reconstructed neurite agglomerates had been reached; and (iii) we preloaded the next query while the user was annotating (Figure 2-2, F and G). Movie A2-2 illustrates this annotation process for cases of splits and mergers, respectively. Note that the user was able to switch quickly to the next query and, based on its 3D orientation, spent little time orienting in the tissue at the new location. With this, the average user interaction time as 21.3 ± 36.1 s per query, corresponding to an average of 5.5 ± 8.8 μm traveled per query. In total, 242,271 axon-ending queries consumed 1978 paid-out work hours (i.e., including all overheads, 29.4 s per query).

However, we had to account for a second kind of reconstruction error, so-called mergers, which can originate from the original segmentation, the agglomeration procedure, or erroneous flight paths from human queries (Figure 2-2H). To detect such mergers, we started with the notion that most of these merger locations will yield a peculiar geometrical arrangement of a 4-fold neurite intersection once all neurite breaks have been corrected (Figure 2-2H, "chiasma"). Because such chiasmatic configurations occur rarely in branching neurites, we directed human focused annotation to these locations. First, we automatically detected these chiasmatic locations using a simple heuristic to detect locations at which axon-centered spheres intersected more than three times with the axon [Figure 2-2H, n = 55,161 chiasmata; for approaches to detect such locations by machine learning, see (Rolnick et al. 2017, Zung et al. 2017)]. Then, we positioned the user queries at a certain distance from the chiasma locations pointing inward (Figure 2-2H) and used a set of case distinctions to query a given chiasma until its configuration had been resolved (see Materials and Methods in appendix A2 for details). Chiasma annotation consumed an additional 1132 work hours [note that the detection of endings and chiasmata was iterated eight times for axons (see Materials and Methods in appendix A2) and that, in a final step, we also detected and queried 3-fold neurite configurations to remove remaining mergers].

Synapse detection, types of postsynaptic targets, and connectome reconstruction

Given the reconstructed pre- and postsynaptic neurites in the tissue volume, we then went on to extract their connectome. For this, we used SynEM (Staffler et al. 2017) to detect synapses between the axonal presynaptic processes and the postsynaptic neurites (Figure 2-2E).

We trained a dedicated interface classifier for nonspine synapses using training data containing only shaft and soma synapses (Figures A2-2 to A2-5; see Materials and Methods in appendix A2). This classifier also used four additional texture filters compared with SynEM in (Staffler et al. 2017), which originated from the voxelwise predictions of a multiclass CNN trained on synaptic junctions, vesicle clouds, mitochondria, and a background class (Figure 2-2E).

Because we were interested in analyzing the subcellular specificity of neuronal innervation, we had to also classify which of the postsynaptic membranes belonged to cell bodies; to classify spiny dendrites as belonging to excitatory cells and smooth dendrites as belonging to INs; and to detect AISs and those dendrites that were likely ADs of neurons located in deeper cortical layers. We developed semiautomated heuristics to detect these subcellular compartments (Figure 2-3, A to D; see Materials and Methods in appendix A2 for details).

Definition of excitatory and inhibitory axons

We used the fraction of primary spine synapses per axon (out of all synapses of that axon, only axons with at least 5 µm path length and at least 10 synapses were analyzed), which had a peak at ~80% (Figure 2-4, A and B), to identify spine-preferring, likely excitatory axons with at least 50% primary spine innervations. Similarly, we identified shaft-preferring, likely inhibitory axons with <20% primary spine innervations. Together, this yielded 6449 axons with clear shaft or spine preferences. For the remaining $n = 528$ axons with primary spine innervations >20% and <50%, we first wanted to exclude remaining mergers between excitatory and inhibitory axons (that would yield intermediate spine innervations rates) and split these axons at possible merger locations (at least 3-fold intersections). Of these, 338 now had at least 10 synapses and spine innervation rates <20% or >50%. The remaining $n = 192$ axons (2.75% of all axons with at least 10 synapses) were not included in the following analyses. This together yielded $n = 5894$ excitatory and $n = 893$ inhibitory axons in our data. For additional controls, see Materials and Methods in appendix A2.

TC axons were defined following parameters described previously (Bopp et al. 2017) (see Materials and Methods in appendix A2).

Analysis of subcellular synaptic target preferences

First, we assumed that all synapses of a given axon class have the same probability to innervate a particular postsynaptic target class (as above). We then inferred this single-hit innervation rate for all combinations of presynaptic axon classes and postsynaptic target classes by determining the probability that best explains whether an axon innervated the target class under a binomial model. The optimized binomial model was then used together with the measured number of synapses of each axon to calculate the expected distribution of target innervation rates. A one-sided Kolmogorov-Smirnov test was used to search for the existence of a subpopulation with an increased target innervation rate. To identify those axons that innervated a given target class beyond chance (Figure 2-4G), we computed the probability $p_{meas,i,k}^{(t)}$ of finding at least the measured fraction of synapses onto target t for each axon i from axon class k. The p values were also calculated for the expected distribution of target innervation rates and combined with $p_{meas,i,k}^{(t)}$ to estimate the p-value threshold $\hat{p}_k^{(t)}$ at which the false discovery rate q (Storey and Tibshirani 2003) crosses 20%. Eighty percent of the axons with $p_{meas,i,k}^{(t)} < \hat{p}_k^{(t)}$ innervate target t with a rate above the single-hit innervation probability and are thus considered to be t preferring.

For the analysis of second-order innervation preference (Figure 2-4, H and I), we reported the fraction of synapses onto target τ by t-preferring axons of class k after removal of synapses onto t. This innervation rate was compared against the fraction of synapses onto target τ by all axons of class k.

Geometrical predictability analysis

Peters' rule (Braitenberg and Schüz 1998) stipulates that synapses between classes of axons and dendrites are established in proportion to the prevalence of these classes. One variant of Peters' rule considered (Figure 2-5B) makes the prediction that the fraction of synapses from axon class A onto target class T is the product of p_A and q_T, where p_A is the proportion of axonal path length made up by class A, and q_T is the proportion of dendritic path length (excluding spines) made up by class T. The measured synapse fractions were compared against the predictions by calculating the ratio of observed to predicted synapse fractions.

Other formations evaluate these predictions independently for each axon class (Figure 2-5A) or each dendrite class (Figure 2-5C).

Finally, to assess the effect of incorporating explicit knowledge about the synapse densities of different axon and dendrite classes, a fourth variant of Peters' rule (Figure 2-5D was considered in which the predicted synapse fraction from axon class A onto target class T is the product of p'_A and q'_T, the overall fractions of synapses originating from A and innervating T, respectively.

How much additional information about the neuropil composition around an axon helps to predict its postsynaptic targets was assessed as follows. For each axon, we determined the total surface area of the target classes that were contained within the cylinder of radius r_{pred} around the axon (Figure 2-5E) and compared it with the actually innervated target fraction of each axon (Figure 2-5, E and F). We then analyzed the correlation between the availability of the target surfaces and the established synapses on these target classes (Figure 2-5G).

We then computed R^2 using the following model. For all axons of a given type, we used the fraction of target innervations and fractional surface availabilities in a surround of radius r_{pred} to find the optimal multivariate linear regression parameters. To estimate best-case geometric predictability, we then calculated R^2 as 1 minus the ratio between the squared residuals of the regression and the synaptic variance on the same axons used for parameter optimization. Here, we corrected for the variance introduced by the finite number of synapses per axon: we used the axons' fractional surface availabilities within r_{pred} and absolute synapse numbers to calculate the expected binomial variance and subtracted it from the square residuals.

This analysis made several assumptions that were in favor of a geometrical explanation of synaptic innervation [there, the conclusion about a minimal predictability (Figure 2-5H) are still upper-bound estimates]. It was assumed that the number of synapses for a given axon was already known; in most settings, only average synapse rates are known for a given circuit. It also assumed that a precise knowledge of the axonal trajectory and the surrounding target surface fractions were available; again, this is usually only available as an average on the scale of r_{pred} of several tens of micrometers.

To relax the assumption of complete knowledge about target availabilities, we repeated the above R^2 analysis for a model in which the predicted fractional innervation of a target is the fractional surface availability of that target.

The computational routine used can be found at https://gitlab.mpcdf.mpg.de/connectomics/L4dense in +connectEM/+Connectome/plotGeometricPredictability.m.

Synapse-size consistency analysis

To determine the consistency of primary spine synapses between a given axon-dendrite pair, we calculated the axon-spine interface area (ASI) (Cheetham et al. 2014, de Vivo et al. 2017) of a synapse as the total contact area between the corresponding axon and spine head agglomerates. For axon-dendrite pairs connected by exactly two primary spine synapses, we then calculated the coefficient of variation (CV) of the ASI areas by CV = $2^{1/2}(\text{ASI}_1 - \text{ASI}_2)/(\text{ASI}_1 + \text{ASI}_2)$., where ASI_1 and ASI_2 are the larger and smaller of the two ASI areas, respectively. To avoid false same-axon same-dendrite (AADD) pairs caused by remaining merge errors in the axon reconstruction, this analysis was performed only after splitting axons at their branch points. The measured distribution of CV values was compared against the CV values obtained by randomly drawing pairs from all AADD synapses and against the CV values of observed AADd synapse pairs and pairs from different axons onto the same dendrite (AaDD) and from different axons onto different dendrites (AaDd; Figure 2-7H). To test whether AADD primary spine synapse pairs are more similar in size than pairs in the control conditions, a one-sided Kolmogorov-Smirnov test was used. We calculated the decimal logarithm of the average ASI area (in square micrometers) and the CV of the ASI areas of each synapse pair to map the size-similarity (Figure 7, F and I). The kernel density estimate of the observed distribution was compared against the distribution expected from random pairs (5000 Monte Carlo samples; figure A2-7C) to identify statistically significantly overrepresented regions. Contour lines show the intersection of the significance regions for p-value thresholds of 0.5% and 5% (Figure 2-7, E, F, I, and figure A2-7, C and D), with the convex hull around the set of all data points. The fraction of data points contained within a contour was used as the upper bound on the fraction of connections consistent with saturated Hebbian plasticity (Figure 2-7J).

Statistical methods

The following statistical tests were performed (in order of presentation in the figures):

The existence of axon subpopulations with unexpectedly high synapse rate onto a given target class was tested using the one-sided Kolmogorov-Smirnov test (Figure 2-4, E and F). Axons belonging to a given target-preference class were identified on the bases of the false detection rate criterion [$q = 20\%$ (Storey and Tibshirani 2003)] (Figure 2-4G).

The degree to which synaptic variance is explainable by geometry-based models was evaluated using R^2 (Figure 2-5H). Binomial variance was corrected for by subtracting the surface fraction-based expected binomial variance from the squared residuals.

F tests were used to evaluate synaptic gradients as function of cortical depth (Figure. 2-6, B and D) or dendritic orientation (Figure 2-6, F and G). For correlation of the TC input fraction with other synaptic input fractions along dendrites, the inhibitory input fraction and seven target-preferential inhibitory and excitatory synapse types were tested. AD-preferring inhibitory synapses were the only ones with significant and substantial correlation (Pearson's correlation after Bonferroni's correction for $n = 8$ multiple tests). The correlation was also significant at the soma level (Pearson's correlation). Both correlations were also significant using Spearman's rank correlation.

The four variants of Peters' rule (Figure 2-5, A to D) were compared using a likelihood-ratio test based on the following multinomial model. It was assumed that the pre- and postsynaptic classes of each synapse in the connectome were sampled either after the path-length fractions of these classes (p_A and q_T) or after the product of the path length and a class-specific likelihood-maximizing relative synapse density. Wilks' theorem was used to compute the corresponding p values.

To test whether the axon-spine interface areas of a given spine-synapse pair configuration were more similar than randomly sampled pairs, a one-sided Kolmogorov-Smirnov test was used (Figure 2-7, H and K).

Acknowledgements

We thank Y. Hua and K. M. Harris for discussions; A. Gour, Y. Hua, P. Laserstein, and H. Schmidt for discussing unpublished observations; B. Cowgill for experimental contributions; E. Eulig, R. Hesse, C. Schramm, and M. Zecevic for code contributions; C. Guggenberger for compute infrastructure; Scalable Minds for implementation of the fast-swapping user queries in webKnossos; and annotators (see appendix A2) for reconstruction work.

Funding: Funding was provided by the Max Planck Society. **Author contributions:** M.H. conceived, initiated, and supervised the project; K.M.B. performed experiments; P.H. provided analysis methods; A.M., M.B., K.M.B., and B.S. developed and performed analyses with contributions by all authors; and A.M. and M.H. wrote the manuscript with contributions by all authors. **Competing interests:** The authors declare no competing financial interests. **Data and materials availability:** The raw EM data are available for browsing at https://wklink.org/9276 (see data links in the figure legends). All data and code are publicly available at https://L4dense2019.brain.mpg.de and in updated form at

https://gitlab.mpcdf.mpg.de/connectomics/L4dense. Less than 2% of the 3D EM image dataset using the initial image alignment were previously published (Berning et al. 2015, Staffler et al. 2017, Boergens et al. 2017, Hua et al. 2015).

Chapter 3. Cellular connectomes as arbiters of local circuit models in the cerebral cortex

Emmanuel Klinger, **Alessandro Motta**, Carsten Marr, Fabian J. Theis, Moritz Helmstaedter.
Nature Communications (2021). DOI: 10.1038/s41467-021-22856-z

Contributions: Development of simulation methods to assess the effects of partial imaging and dense reconstruction of a circuit subvolume (figures 3-5e,f) and of incomplete hypothesis spaces on Bayesian model selection (figure 3-6a). Development of method consisting of the iterative training and sparsification of artificial recurrent neural networks for the synthesis of connectomes with biologically plausible and almost exclusively task-defined connectivity (figure 3-7). Analysis of connectomic separability of task-defined binary and weighted connectomes (figures 3-7). Writing of manuscript with EK and MH and input from all authors.

With the availability of cellular-resolution connectivity maps, connectomes, from the mammalian nervous system, it is in question how informative such massive connectomic data can be for the distinction of local circuit models in the mammalian cerebral cortex. Here, we investigated whether cellular-resolution connectomic data can in principle allow model discrimination for local circuit modules in layer 4 of mouse primary somatosensory cortex. We used approximate Bayesian model selection based on a set of simple connectome statistics to compute the posterior probability over proposed models given a to-be-measured connectome. We find that the distinction of the investigated local cortical models is faithfully possibly based on purely structural connectomic data with an accuracy of more than 90%, and that such distinction is stable against substantial errors in the connectome measurement. Furthermore, mapping a fraction of only 10% of the local connectome is sufficient for connectome-based model distinction under realistic experimental constraints. Together, these results show for a concrete local circuit example that connectomic data allows model selection in the cerebral cortex and define the experimental strategy for obtaining such connectomic data.

In molecular biology, the use of structural (x-ray crystallographic or single-particle electron microscopic) data for the distinction between kinetic models of protein function constitutes the gold standard (e.g., (Doyle et al. 1998, Nogales 2016)). In Neuroscience, however, the question whether structural data of neuronal circuits is informative for computational interpretations is still heavily disputed (Bargmann and Marder 2013, Morgan and Lichtman 2013, Denk et al. 2012, Jonas and Kording 2017), with the extreme positions that cellular connectomic measurements are likely uninterpretable (Jonas and Kording 2017) or indispensable (Denk et al. 2012). In fact, structural circuit data has been decisive in resolving competing models for the computation of directional selectivity in the mouse retina (Briggman et al. 2011).

For the mammalian cerebral cortex, the situation can be considered more complicated: it can be argued that it is not even known which computation a given cortical area or local circuit module carries out. In this situation, hypotheses about the potentially relevant computations and about their concrete implementations are to be explored simultaneously. To complicate the investigation further, the relation between a given computation and its possible implementations is not unique. Take, for example pattern distinction (of tactile or visual inputs) as a possible computation in layer 4 of sensory cortex. This computation can be carried out by multi-layer perceptrons (Rosenblatt 1962), but also by random pools of connected neurons in an "echo state network" (Jaeger and Haas 2004) (Figure 3-1a,

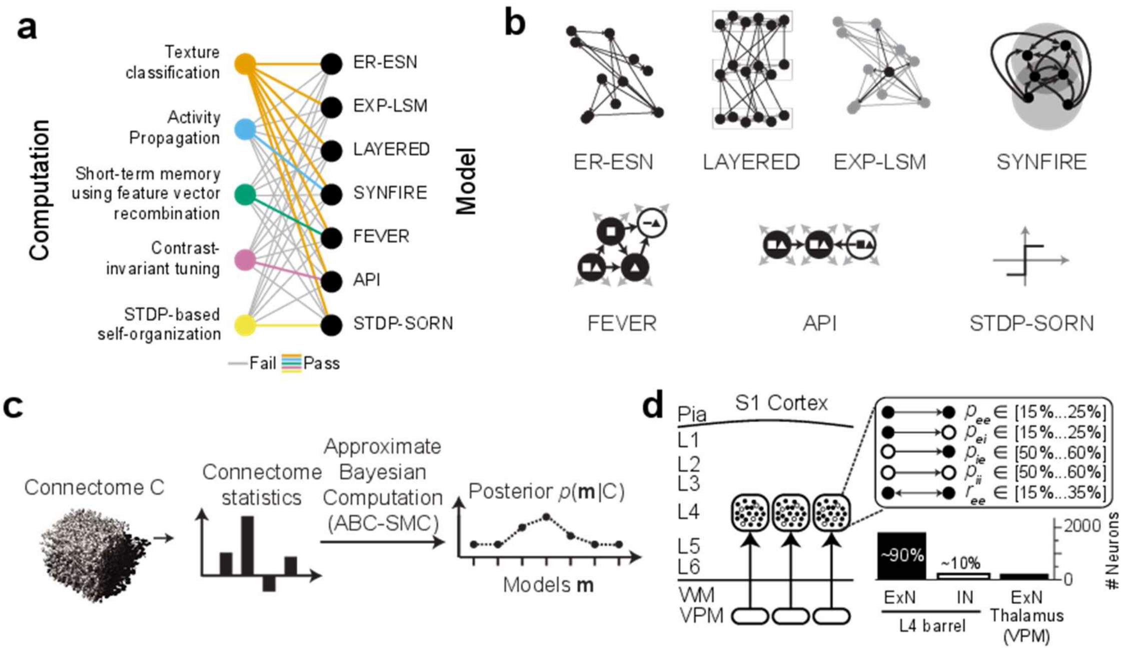

Figure 3-1 Relationship between models and possible computations in cortical circuits, and proposed strategy for connectomic model distinction in local circuit modules of the cerebral cortex. **(a)** Relationship between computations suggested for local cortical circuits (left) and possible circuit-level implementations (right). Colored lines indicate successful performance in the tested computation; gray lines indicate failure to perform the computation (see Figure A3-1 for details). **(b)** Enumeration of candidate models possibly implemented in a barrel-circuit module. See text for details. **(c)** Flowchart of connectomic model selection approach to obtain the posterior $p(\mathbf{m}|\mathrm{C})$ over hypothesized models m given a connectome C. ABC-SMC: approximate Bayesian computation using sequential Monte-Carlo sampling. **(d)** Sketch of mouse primary somatosensory cortex with presumed circuit modules ("barrels") in cortical input layer 4 (L4). Currently known constraints of pairwise connectivity and cell prevalence of excitatory (ExN) and inhibitory (IN) neurons (p_{ee}: pairwise excitatory-excitatory connectivity (Feldmeyer et al. 1999, Gibson et al. 1999, Lübke et al. 2000, Beierlein et al. 2003, Lefort et al. 2009), p_{ei}: pairwise excitatory-inhibitory connectivity (Gibson et al. 1999, Beierlein et al. 2003), p_{ii}: pairwise inhibitory-inhibitory connectivity (Gibson et al. 1999, Gibson et al. 2005), p_{ie}: pairwise inhibitory-excitatory connectivity (Gibson et al. 1999, Beierlein et al. 2003, Koelbl et al. 2015), r_{ee}: pairwise excitatory-excitatory reciprocity (Feldmeyer et al. 1999, Gibson et al. 1999, Beierlein et al. 2003)).

Figure A3-1a-g) and similarly by networks configured as "synfire chains" (Abeles 1982) (Figure 3-1a). If one considers different computational tasks, however, such as the maintenance of sensory representations over time scales of seconds (short-term memory), or the stimulus tuning of sensory representations, then the relation between the computation and its implementation becomes more distinct (Figure 3-1a). Specifically, a network implementation of antiphase inhibition for stimulus tuning (Troyer et al. 1998) is not capable of performing the short-term memory task (Figure A3-1k,l), and a network proposed for a short-term memory task (FEVER (Druckmann and Chklovskii 2012)), fails to perform stimulus tuning (Figure 3-1a, Figure A3-1-3). Together, this illustrates that while it is impossible to uniquely equate computations with their possible circuit-level implementations, the ability to discriminate between proposed models would allow to narrow down the hypothesis space both about computations and their circuit-level implementations in the cortex.

With this background, the question whether purely structural connectomic data is sufficiently informative to discriminate between several possible previously proposed models and thus a range of possible cortical computations is of interest.

Here we asked whether for a concrete cortical circuit module, the "barrel" of a cortical column in mouse somatosensory cortex, the measurement of the local connectome can in principle serve as an arbiter for a set of possibly implemented local cortical models and their associated computations.

We developed and tested a model selection approach (using Approximate Bayesian Computation with Sequential Monte-Carlo Sampling, ABC-SMC (Beaumont et al. 2002, Sisson et al. 2007, Toni et al. 2009), Figure 3-1c) on the main models proposed so far for local cortical circuits (Figure 3-1b) ranging from pairwise random Erdős–Rényi (ER (Erdős and Rényi 1959)) to highly structured "deep" layered networks used in machine learning (Schmidhuber 1992, El Hihi and Bengio 1996). We found that connectomic data alone is in principle sufficient for the discrimination between these investigated models, using a surprisingly simple set of connectome statistics. The model discrimination is stable against substantial measurement noise, and only partly mapped connectomes have already high discriminative power.

Results

To develop our approach we focus on a cortical module in mouse somatosensory cortex, a "barrel" in layer 4 (L4), a main input layer to the sensory cortex (Binzegger et al. 2005). The spatial extent of this module (roughly d_b = 300µm along each dimension) makes it a realistic goal of experimentally mapped dense connectomes using state-of-the-art 3D electron microscopy (Denk and Horstmann 2004, Kasthuri et al. 2015) and circuit reconstruction approaches (Boergens et al. 2017, Berning et al. 2015 , Januszewski et al. 2018, Motta et al. 2019). A barrel is composed of about 2,000 neurons (Meyer et al. 2011, Feldmeyer 2012). Of these about 90% are excitatory, and about 10% inhibitory (Meyer et al. 2011, Feldmeyer 2012) (Figure 3-1d), which establish a total of about 3 million chemical synapses within L4. The ensuing average pairwise synaptic connectivity within a barrel has been estimated based on data from paired whole-cell recordings (Feldmeyer et al. 1999, Gibson et al. 1999, Lübke et al. 2000, Beierlein et al. 2003, Gibson et al. 2005, Koelbl et al. 2015): excitatory neurons connect to about 15-25% of the other intra-barrel neurons; inhibitory neurons connect to about 50-60% of the other intra-barrel neurons (Figure 3-1d). Moreover, the probability of a connection to be reciprocated ranges between 15% and 35% (Feldmeyer et al. 1999, Lefort et al. 2009, Feldmeyer 2012, Gibson et al. 1999, Beierlein et al. 2003). Whether intracortical connections in L4 follow only such pairwise connection statistics or establish higher-order circuit structure is not known (Helmstaedter et al. 2008, Markram et al. 2015, Egger et al. 2014, Kasthuri et al. 2015). Furthermore, it is not understood whether the effect of layer 4 circuits is primarily the amplification of incoming thalamocortical signals (Feldmeyer et al. 1999, Lien and Scanziani 2013), or whether proper intracortical computations commence within L4 (Ahissar and Kleinfeld 2003, Prigg et al. 2002, Bruno and Simons 2002). A L4 circuit module is therefore an appropriate target for model selection in local cortical circuits.

The simplest model of local cortical circuits assumes pairwise random connectivity between neurons, independent of their relative spatial distance in the cortex (Erdős–Rényi (Erdős and Rényi 1959), Figure 3-2a-c). This model has been proposed as Echo State Network (ESN (Jaeger 2001, Jaeger and Haas 2004)). As a slight modification, random networks with a pairwise connectivity dependent on the distance between the neurons' cell bodies are the basis of liquid state machines (LSMs (Maass et al. 2002, Probst et al. 2012), Figure 3-2a-c). At the other extreme, highly structured layered networks are successfully used in machine learning and were originally inspired by neuronal architecture (multi-layer perceptrons (Rosenblatt 1962), Figure 3-2d-g). Furthermore, embedded synfire chains have been studied (SYN (Abeles 1982, Trengove et al. 2013), Figure 3-2h-j), which can be considered an intermediate between random and layered connectivity. In addition to these rather general model classes, particular suggestions of models for concrete cortical operations have been put forward that

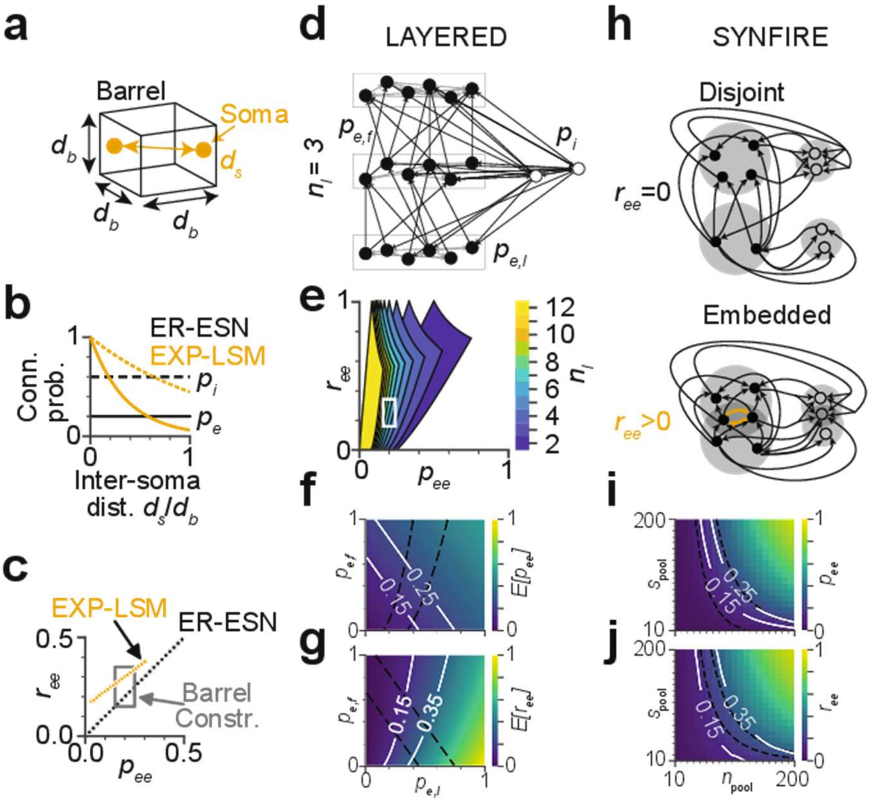

Figure 3-2 Compliance of candidate models with the so-far experimentally determined pairwise barrel circuit constraints in L4 (see Figure 3-1d). **(a)** Illustration of a simplified cortical barrel of width d_b and somata with inter soma distance d_s. **(b)** Pairwise excitatory and inhibitory connection probabilities p_e and p_i are constant over inter soma distance d_s in the Erdős–Rényi echo state network (ER-ESN) and decay in the exponentially decaying connectivity - liquid state machine model (EXP-LSM). **(c)** Possible pairwise excitatory-excitatory connectivity p_{ee} and excitatory-excitatory reciprocity r_{ee} in the ER-ESN and EXP-LSM model satisfy the so-far determined barrel constraints (box). **(d-g)** Layered model: (d) example network with three layers ($n_l = 3$), excitatory forward (between-layer) connectivity $p_{e,f}$, excitatory lateral (within-layer) connectivity $p_{e,l}$ and inhibitory connectivity p_i. (e) Range of p_{ee} and r_{ee} in the LAYERED model for varying number of layers n_l (white box: barrel constraints as in c). (f,g) Expected excitatory pairwise connectivity $E[p_{ee}]$ and reciprocity $E[r_{ee}]$ as function of $p_{e,l}$ and $p_{e,f}$ for $n_l = 3$. Isolines indicate barrel constraints, model parameters in compliance with these constraints: area between intersecting isolines. Note that constraints are fulfilled only for within-layer connectivity $p_{e,l} > 0$, refuting a strictly feedforward network. **(h-j)** Embedded synfire chain model (SYNFIRE). (h) Two subsequent synfire pools in the disjoint (top) and embedded (bottom) synfire chain. Since intra-pool connectivity $p_{e,l}$ is strictly zero, reciprocal connections do not exist in the disjoint case ($r_{ee} = 0$) but in the embedded configuration. (i,j) Pairwise excitatory connectivity p_{ee} and pairwise excitatory reciprocity r_{ee} as function of the number of pools n_{pool} and the pool size s_{pool} for a SYNFIRE network with $N = 2000$ neurons. Respective barrel constraints (white and dashed line). See Figure A3-2 for analogous analysis of FEVER, API and STDP-SORN models.

---

make less explicit structural assumptions (feature vector recombination network (FEVER (Druckmann and Chklovskii 2012)), proposed to achieve stimulus representation constancy on macroscopic timescales within a network; and antiphase inhibition (API (Troyer et al. 1998, Miller et al. 2001)), proposed to achieve contrast invariant stimulus tuning), or that are based on local learning rules (spike timing dependent plasticity/self-organizing recurrent neural network (STDP-SORN (Lazar et al. 2009, Zheng et al. 2013)).

We first had to investigate whether the so far experimentally established circuit constraints of local cortical modules in S1 cortex (Figure 3-1d; number of neurons, pairwise connectivity and reciprocity; see above) were already sufficient to refute any of the proposed models.

Both the pairwise random ER model (Figure 3-2c) and the pairwise random but soma-distance dependent EXP-LSM model are directly compatible with measured constraints on pairwise connectivity and reciprocity (Figure 3-2c). A strictly layered multilayer perceptron model, however, does not contain any reciprocal connections and would in the strict form have to be refuted for cortical circuit modules, in which the reciprocity range is 0.15-0.35. Instead of rejecting such a "deep" layered model altogether, we studied a layered configuration of locally randomly connected ensembles (Figure 3-2d). We found that models with up to ten layers are consistent with the circuit constraints of barrel cortex (Figure 3-2e). In subsequent analyses we considered configurations with 2-4 layers. In this regime, the connectivity within layers is 0.2-0.6 and between layers 0.3-0.6 (Figure 3-2f,g; n_l=3 layers). Similarly, disjoint synfire chains (Abeles 1982) (Figure 3-2h) would have to be rejected for the considered circuits due to lack of reciprocal connections. Embedded synfire chains (e.g., ref. (Trengove et al. 2013)), however, yield reciprocal connectivity for the sets of neurons overlapping between successive pools (Figure 3-2h). This yields a range of pool sizes for which the SYNFIRE model is compatible with the known circuit constraints (Figure 3-2i,j). The other models were investigated analogously (Figure A3-2), finding slight (API, Figure A3-2d-g) or substantial modifications (FEVER, STDP-SORN, Figure A3-2a-c,h-m) that make the models compatible with a local cortical circuit in L4. Notably, the FEVER model as originally proposed (Druckmann and Chklovskii 2012) yields substantially too low connectivity and too high reciprocity to be realistic for local cortical circuits in L4 (Figure A3-2b). A modification in which FEVER rules are applied on a pre-drawn random connectivity rescues this model (Figure A3-2a,b).

Structural model discrimination via connectome statistics

We then asked whether these local cortical models could be distinguished on purely structural grounds, given a binary connectome of a barrel circuit.

We first identified circuit statistics $\boldsymbol{\gamma}$ that could serve as potentially distinctive connectome descriptors (Figure 3-3a). We started with the relative reciprocity of connections within (rr_{ee} and rr_{ii}) and across (rr_{ei} and rr_{ie}) the populations of excitatory and inhibitory neurons. Since we had already found that some of the models would likely differ in reciprocity (see above, Figure 3-2c,g,j, Figure A3-2b,f,g), these statistics were attractive candidates. We further explored the network recurrency $r^{(l)}$ at cycle length l, which is a measure for the number of cycles in a network (Figure 3-3a). This measure can be seen as describing how much of the information flow in the network is fed back to the network itself. So a LAYERED network would be expected to achieve a low score in this measure, while a highly recurrent network, such as SYNFIRE is expected to achieve a high score. We used $r^{(l)}$ with $l = 5$ since for smaller l this measure is more equivalent to the reciprocity r_{ee} and for larger l, the measure is numerically less stable. Moreover, we investigated the in/out-degree correlation of the excitatory population $r_{i/o}$ (Figure 3-3a). This measure was motivated by the notion that $r_{i/o} < 0$ should point towards a separation of input and output subpopulations of L4, as for example expected in the LAYERED model.

For a first assessment of the distinctive power of these six connectome statistics $\boldsymbol{\gamma}$, we sampled 50 L4 connectomes from each of the 7 models (Figure 3-3b). The free parameters of the models were drawn from their respective prior distributions (Figure 3-3b; priors shown in Figure A3-4). For example, for the LAYERED model, the prior parameters were the number of layers $n_l \in [2, 4]$, the forward connectivity $p_{e,f} \in [0.19, 0.57]$ and the lateral connectivity $p_{e,l} \in [0.26, 0.43]$. The proposed network statistics $\boldsymbol{\gamma}$ (Figure 3-3a) were then evaluated for each of the 350 sampled connectomes (Figure 3-3b,c). While the statistics had some descriptive power for certain combinations of models (for example, rr_{ei} seemed to separate API from EXP-LSM, Figure 3-3c), none of the six statistics alone

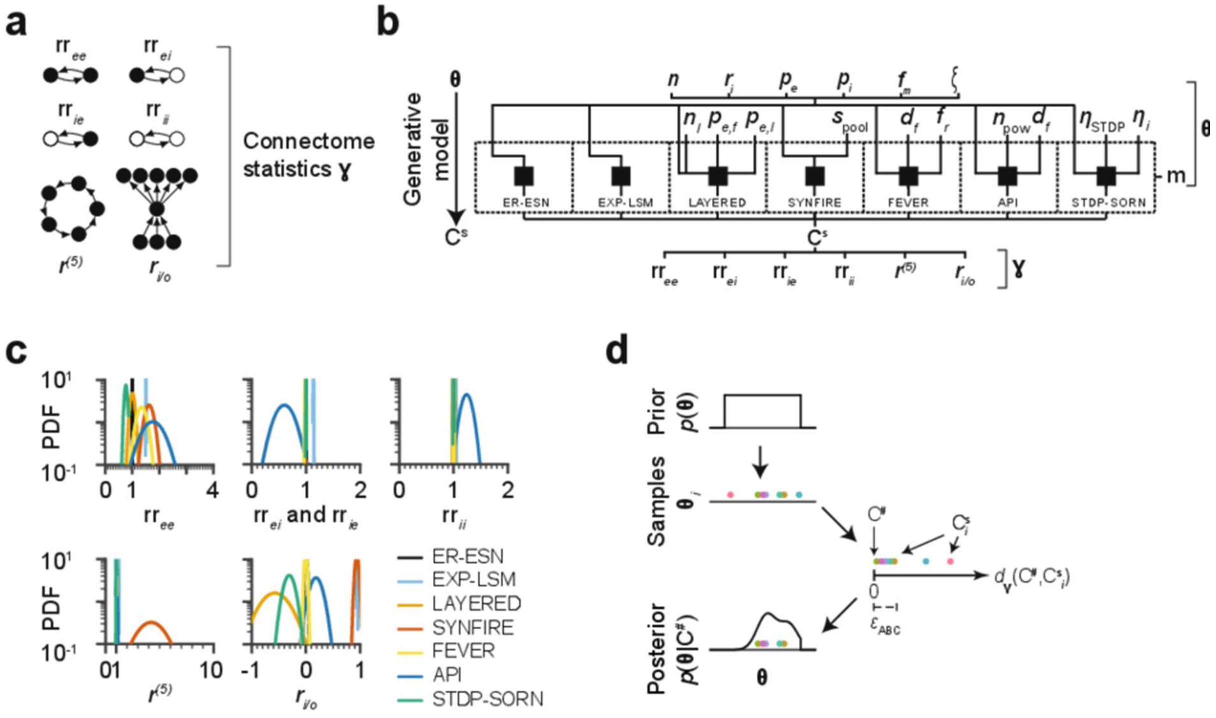

Figure 3-3 Connectome statistics and generative models for approximate Bayesian inference. **(a)** Connectome statistics $\boldsymbol{\gamma}$ used for model distinction: relative excitatory-excitatory reciprocity rr_{ee}, relative excitatory-inhibitory reciprocity rr_{ei}, relative inhibitory-excitatory reciprocity rr_{ie}, relative inhibitory-inhibitory reciprocity rr_{ii}, relative cycles of length 5, $r^{(5)}$, and in-out degree correlation of excitatory neurons $r_{i/o}$. **(b)** Generative model for Bayesian inference: shared set of parameters (top: number of neurons n, fraction of inhibitory neurons r_i, excitatory connectivity p_e, inhibitory connectivity p_i, fractional connectome measurement f_m, noise ξ) and model-specific parameters (middle, model choice m, number of layers n_l, excitatory forward connectivity $p_{e,f}$, excitatory lateral connectivity $p_{e,l}$, pool size s_{pool}, STDP learning rate η_{STDP}, intrinsic learning rate η_i, feature space dimension d_f, feverization ratio f_r, selectivity n_{pow}, see Figure A3-4), generated sampled connectome Cs described by the summary statistics $\boldsymbol{\gamma} = (\mathrm{rr}_{ee}, \mathrm{rr}_{ei}, \mathrm{rr}_{ie}, \mathrm{rr}_{ii}, r^{(5)}, r_{i/o})$. **(c)** Gaussian fits of probability density functions (PDFs) of the connectome statistics $\boldsymbol{\gamma}$ (a) for all models (see Fig. 1b). **(d)** Sketch of ABC-SMC procedure: given a measured connectome $\mathrm{C}^{\#}$, parameters $\boldsymbol{\theta}_i$ (colored dots) are sampled from the prior $p(\boldsymbol{\theta})$. Each $\boldsymbol{\theta}_i$ generates a connectome $\mathrm{C}_i^{\mathrm{s}}$ that has a certain distance $d_{\boldsymbol{\gamma}}(\mathrm{C}^{\#}, \mathrm{C}_i^{\mathrm{s}})$ to $\mathrm{C}^{\#}$ in the space defined by the connectome statistics $\boldsymbol{\gamma}$ (a). If this distance is below a threshold ϵ_{ABC}, the associated parameters $\boldsymbol{\theta}_i$ are added as mass to the posterior distribution $p(\boldsymbol{\theta}|\mathrm{C}^{\#})$, and are rejected otherwise.

could discriminate between all the models (see the substantial overlap of their distributions, Figure 3-3c), necessitating a more rigorous approach for model selection.

Discrimination via Bayesian model selection

We used an Approximate Bayesian Computation-Sequential Monte Carlo (ABC-SMC) model selection scheme (Beaumont et al. 2002, Sisson et al. 2007, Toni et al. 2009) to compute the posterior probability over a range of models given a to-be-measured connectome $\mathrm{C}^{\#}$.

In this approach, example connectomes C^{S} are generated from the models M in question (using the priors over the model parameters $\boldsymbol{\theta}$ (Figure 3-3b,d; see Figure A3-4 for plots of all priors)). For each sampled connectome C^{S}, the dissimilarity $d_{\boldsymbol{\gamma}}(\mathrm{C}^{\mathrm{S}}, \mathrm{C}^{\#})$ to the measured connectome $\mathrm{C}^{\#}$ was computed (formalized as a distance $d_{\boldsymbol{\gamma}}(\mathrm{C}^{\mathrm{S}}, \mathrm{C}^{\#})$ between C^{S} and $\mathrm{C}^{\#}$). The connectome distance was defined as an L1 norm over the six connectome statistics $\boldsymbol{\gamma}$ (Figure 3-3a), normalized by the 20%-to-80% percentile per connectome statistic (see Methods). If the sampled connectome C^{S} was sufficiently similar to the measured connectome $\mathrm{C}^{\#}$ (i.e. their distance $d_{\boldsymbol{\gamma}}(\mathrm{C}^{\mathrm{s}}, \mathrm{C}^{\#})$ was below a preset threshold ϵ_{ABC}, see Methods), the sample was accepted and considered as evidence towards the model that had generated C^{s} (Figure 3-3d). With this, an approximate sample from the posterior $p(\boldsymbol{\theta}|\mathrm{C}^{\#})$ was obtained (Figure 3-3d). The posterior $p(\boldsymbol{\theta}|\mathrm{C}^{\#})$ was iteratively refined by resampling and perturbing the parameters of the accepted connectomes and by sequentially reducing the distance threshold ϵ_{ABC}.

We then tested our approach on simulated connectomes $\mathrm{C}^{\#}$. These were again generated from the different model classes (as in Figure 3-3b); however in the ABC method, only the distances $d_{\boldsymbol{\gamma}}(\mathrm{C}^{\mathrm{s}}, \mathrm{C}^{\#})$ between the sampled connectomes C^{s} and the simulated connectomes $\mathrm{C}^{\#}$ were used (Figure 3-3d). It was therefore not clear a-priori whether the statistics $\boldsymbol{\gamma}$ are sufficiently descriptive to distinguish between the models; and whether this would be the case for all or only some of the models.

We first considered the hypothetical case of a dense, error-free connectomic reconstruction of a barrel circuit under the ER-ESN model yielding a connectome $\mathrm{C}^{\#}$. The ABC-SMC scheme correctly identified this model as the one model class at which the posterior probability mass was fully concentrated compared to all other models (Figure 3-4a). ABC-SMC inference was repeated for *n*=3 ER-ESN models, resulting in three consistent posterior distributions. Similarly, connectomes $\mathrm{C}^{\#}$ obtained from all other investigated models yielded posterior probability distributions concentrated at the correct originating model (Figure 3-4a). Thus, the six connectome statistics γ together with ABC-based model selection were in fact able to distinguish between the tested set of models given binary connectomes.

Discrimination of noisy connectomes

We next explored the stability of our approach in the face of connectome measurements in which $\mathrm{C}^{\#}$ was simulated to contain noise from biological sources, or errors resulting from connectomic reconstruction inaccuracies. The latter would be caused by the remaining errors made when reconstructing neuronal wires in dense nerve tissue (Helmstaedter et al. 2011, Boergens et al. 2017, Motta et al. 2019, Januszewski et al. 2018) and by remaining errors in synapse detection, especially when using automated synapse classifiers (Kreshuk et al. 2011, Becker et al. 2012, Kreshuk et al. 2014, Kreshuk et al. 2015, Dorkenwald et al. 2017, Staffler et al. 2017). To emulate such connectome noise, we first randomly removed 15% of the connections in $\mathrm{C}^{\#}$ and reinserted them again randomly. We then computed the posterior on such noisy connectomes $\mathrm{C}^{\#}$, which in fact became less stable (Figure 3-4b; shown is average of n=3 repetitions with accuracies of 83.0%, 99.8% and 100.0%, respectively).

However, in this setting we were pretending to be ignorant about the fact that the connectome measurement was noisy (see noise prior in Figure 3-4b), and had assumed a noise-free measurement. In realistic settings, however, the rate of certain reconstruction errors can be quantitatively estimated. For example, the usage of automated synapse detection (Staffler et al. 2017) and neurite reconstructions with quantified error rates (Helmstaedter et al. 2013, Takemura et al. 2013, Wanner et al. 2016, Boergens et al. 2017, Januszewski et al. 2018, Motta et al. 2019), provide such error rates explicitly. We therefore next investigated whether prior knowledge about the reconstruction error rates would improve the model posterior (Figure 3-4c). For this, we changed our prior assumption about reconstruction errors ξ from noise-free (Figure 3-4b) to a distribution with substantial probability mass around 0-30% noise (modeled as $p(\xi) \sim \mathrm{Beta}(2{,}10)$, Figure 3-4c). When we applied the posterior computation again to connectomes $\mathrm{C}^{\#}$ with 15% reconstruction noise, these were now as discriminative as in the noise-free case (Figure 3-4c, cf. Figure 3-4a,b).

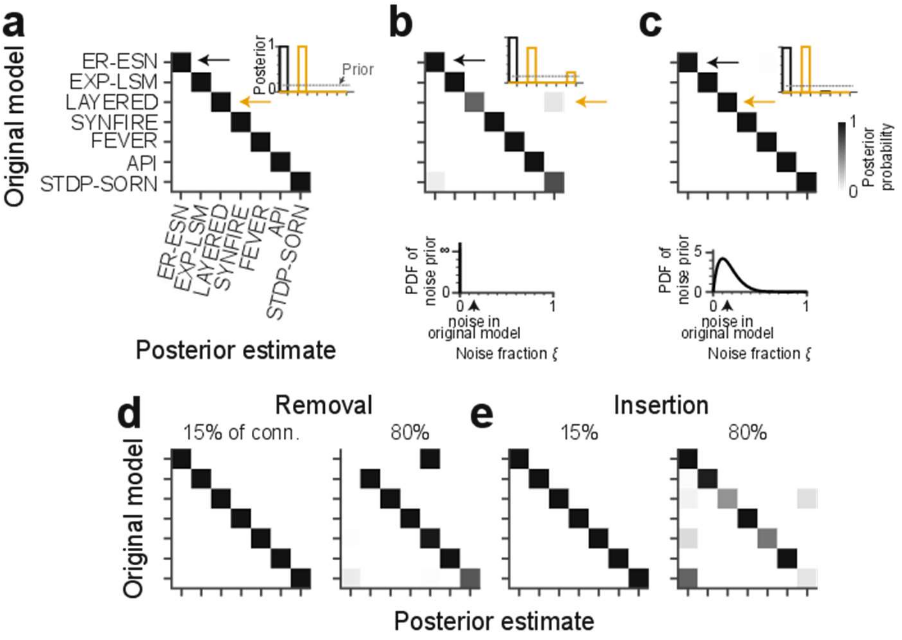

Figure 3-4 Identification of models using Bayesian model selection under ideal and noisy connectome measurements. **(a)** Confusion matrix reporting the posteriors over models given example connectomes. Example connectomes were sampled from each model class (rows; Fig. 3b) and then exposed to the ABC-SMC method (Fig. 3d) using only the connectome statistics (Fig. 3a). Note that all model classes are uniquely identified form the connectomes (inset: average posteriors for ER-ESN and LAYERED connectomes, respectively; n=3 repetitions). **(b)** Posteriors over models given example connectomes to which a random noise of 15% (inset, dashed line) was added before applying the ABC-SMC method. The generative model (Fig. 3b) was ignorant of this noise (n=3 repetitions; bottom: noise prior $p(\xi) = \delta_{\xi,0}$). **(c)** Same analysis as in b, this time including a noise prior into the generative model (n=3 repetitions). Bottom: The noise prior was modeled as $p(\xi) = \mathrm{Beta}(2,10)$. Note that in most connectome measurements, the level of reconstruction errors is quantifiable, such that the noise can be rather faithfully incorporated into the noise prior (see text). Model identification is again accurate under these conditions (compare c and a). **(d)** Confusion matrix when simulating split errors in neuron reconstructions by randomly removing 15% (left) or 80% (right) of connections before ABC-SMC inference. **(e)** Confusion matrix when simulating merge errors in neuron reconstructions by insertion of additional 15% (left) and 80% (right) of the original number of connections into random locations in the connectome before ABC-SMC inference. (d,e) Noise prior during ABC-SMC inference was of the same type as the simulated reconstruction errors (n=1 repetition; noise prior $p(\xi) = \mathrm{Beta}(2,10)$). Color bar in c applies to all panels.

To further investigate the effect of biased noise, we also tested conditions in which synaptic connections were only randomly removed or only randomly added (corresponding to cases in which reconstruction of the connectome may be biased towards neurite splits (Figure 3-4d) or neurite mergers (Figure 3-4e)); and cases in which errors were focused on a part of the connectome (corresponding to cases in which certain neuronal connections may be more difficult to reconstruct than others, Figure A3-5a). These experiments indicate a rather stable range of faithful model selection under various types of measurement errors.

Incomplete connectome measurement

In addition to reconstruction noise, a second serious practical limitation of connectomic measurements is the high resource consumption (quantified in human work hours, which are in the range of 90,000-180,000 h for a full barrel reconstruction today, assuming 1.5 mm/h reconstruction speed, 5-10 km path length per cubic millimeter and a barrel volume of (300 µm)^3 (Helmstaedter 2013, Boergens et al. 2017)). Evidently, the mapping of connectomes for model discrimination would be rendered substantially more feasible if the measurement of only a fraction of the connectome was already sufficient for model discrimination. We therefore next investigated the stability of our discrimination method under two types of fractional measurements (Figure 3-5).

We first tested whether reconstruction of only f_m = 30% of neurons and of their connectivity is sufficient for model selection (Figure 3-5a). We found model discrimination to be 100% accurate in the absence of reconstruction errors (Figure 3-5b). This reconstruction assumes the 3D EM imaging of a tissue volume that comprises an entire barrel, followed by a fractional circuit reconstruction (see sketch in Figure 3-5a). Such an approach is realistic since the speed of 3D EM imaging has increased more quickly than that of connectomic reconstruction (Helmstaedter 2013, Lichtman et al. 2014, Mikula 2016, Schmidt et al. 2017).

We then screened our approach for stability against both measurement noise and incomplete connectome measurement by applying our method on connectomes of varying noise rates ξ and measurement fractions f_m with a fixed noise prior ($p(\xi) \sim \mathtt{Beta}(2{,}10)$). For evaluating classification performance, we used two approaches: first, we averaged the model posterior along the diagonal of the classification matrix (e.g., Figure 3-5b), yielding the average accuracy for a given noise and fractional measurement combination (Figure 3-5c). In addition, we evaluated the quality of the maximum-a-posteriori (MAP) classification, which takes the peak of the posterior as binary classification result (Figure 3-5d). The MAP connectome classification was highly accurate even in a setting in which only 10% of the connectome were sampled, and at a substantial level of reconstruction error of 25%. This implies that we will be able to perform the presented model distinction in a partially mapped barrel connectome consuming 18,000 instead of 180,000 work hours (Helmstaedter 2013, Boergens et al. 2017, Staffler et al. 2017) (Figure 3-5c,d). Evidently, this makes a rather unrealistic reconstruction feasible (note the largest reconstructions to date consumed 14,000-25,000 human work hours (Wanner et al. 2016, Helmstaedter et al. 2013, Takemura et al. 2013, Eichler et al. 2017)).

We then asked whether complete connectomic reconstructions of small EM image volumes (Motta et al. 2019) could serve as an alternative to the fractional reconstruction of large image volumes (Figure 3-5e,f). This would reduce image acquisition effort and thereby make it realistic to rapidly compare how brain regions, species or disease states differ in terms of circuit models. To simulate locally dense reconstructions, we first restricted the complete noise-free connectome to the neurons with their soma located within the imaged barrel subvolume (Figure 3-5e). Importantly, connections between the remaining neurons may be established outside the image volume. To account for the loss of these connections, we further subsampled the remaining connections. We found model selection from dense connectomic reconstruction of a $(150\mu\text{m})^3$ volume (12.5% of the barrel volume) to be unstable (67% average accuracy; Figure 3-5f) due to the confusion between the ER-ESN, EXP-LSM, FEVER and STDP-SORN models (Figure 3-5f). For the dense reconstruction of $(100\mu\text{m})^3$, accuracy of model selection was close to chance level for all models (17% average accuracy; Figure 3-5f). So our tests indicate that an experimental approach in which the image volume comprises an entire local cortical circuit module (barrel), but the reconstruction is carried out only in a subset of about 10-15% of neurons is favored over a dense reconstruction of only 12.5% of the barrel volume. Since the imaging of increasingly larger volumes in 3D EM from the mammalian brain is becoming feasible (Morgan et al. 2016, Schmidt et al. 2017), while its reconstruction is still a major burden, these results propose a realistic experimental setting for connectomic model selection in the cortex.

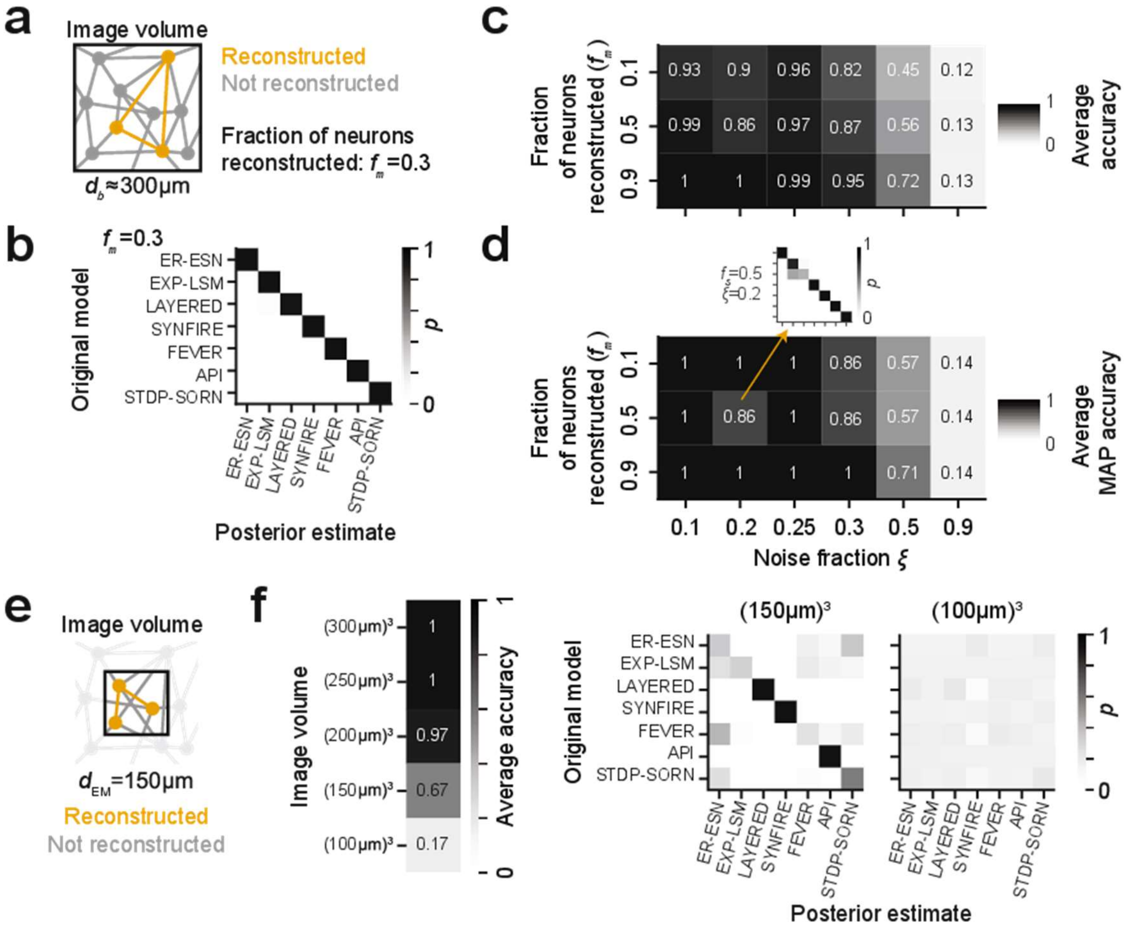

Figure 3-5 Model selection for partially measured and noisy connectomes. **(a)** Fractional (incomplete) connectome measurement when reconstructing only a fraction f_m of the neurons in a given circuit, thus obtaining a fraction f_m^2 of the complete connectome. **(b)** Effect of incomplete connectome measurement on model selection performance for $f_m = 0.3$ (no noise; n=1 repetition). Note that model selection is still faithfully possible. **(c,d)** Combined effects of noisy and incomplete connectome measurements on model selection accuracy reported as average posterior probability (c; n=1 repetition per entry) and maximum-a-posteriori accuracy (d; n=1 repetition per entry). Note that model selection is highly accurate down to 10% fractional connectome measurement at up to 25% noise, providing an experimental design for model distinction that is realistic under current connectome measurement techniques (see text). Model selection used a fixed $p(\xi) = \text{Beta}(2,10)$ noise prior. More informative noise priors result in more accurate model selection (Figure A3-5b). **(e)** Effect of fractional dense circuit reconstruction: Locally dense connectomic reconstruction of the neurons and of their connections in a circuit subvolume. **(f)** Effect of partial imaging and dense reconstruction of the circuit subvolume on average model selection accuracy (left: n=1 repetition per entry). Note that model selection based on dense reconstruction of a (150µm)^3 volume (12.5% of circuit volume) is substantially less accurate than model selection based on complete reconstructions of 10% in the complete circuit volume (see c). Right: Posterior distributions over models for image volumes of (150µm)^3 and (100µm)^3, respectively (n=1 repetition, each).

Incomplete set of hypotheses

Bayesian analyses can only compare evidence for hypotheses known to the researcher. But what if the true model is missing from the set of tested hypotheses? To investigate this question, we excluded the original model during inference of the posterior distribution from a complete noise-free barrel connectome (Figure 3-6a). In these settings, rather than obtaining uniformly distributed posteriors, we found that the probability mass of the posterior distributions was concentrated at one or two of the other models. The FEVER model, for example, which is derived from pairwise random connectivity (ER-ESN) while imposing additional local constraints that result in heightened relative excitatory-excitatory reciprocity, resembles the EXP-LSM model (see Figure 3-3c). Accordingly, these three

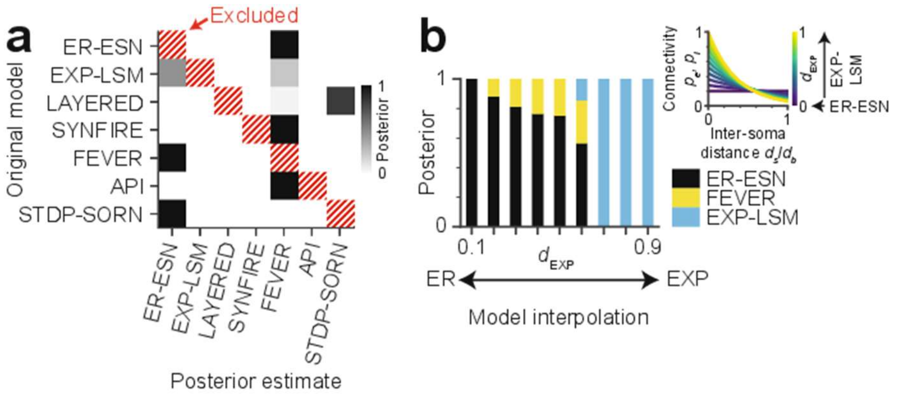

Figure 3-6 Effect of incomplete hypothesis space and of model interpolation on Bayesian model selection. **(a)** Confusion matrix reporting the posterior distribution when excluding the true model (hatched) from the set of tested model hypotheses (*n*=1 repetition). Note that posterior probability is non-uniformly distributed and concentrated at plausibly similar models even when the true model is not part of the hypothesis space. **(b)** Posterior distributions for connectome models interpolated between ER-ESN and EXP-LSM (*n*=1 repetition per bar). Inset: Space constant d_{EXP} acts as interpolation parameter between ER-ESN (d_{EXP}=0) and EXP-LSM (d_{EXP}=1). Note that the transition between the two models is captured by the estimated model posterior, with an intermediate (non-dominant) confusion with the FEVER model.

models (ER-ESN, EXP-LSM, FEVER) showed a high affinity for mutual confusion when the original model was excluded during ABC-SMC (Figure 3-6a). This may indicate that our Bayesian model selection approach assigns the posterior probability mass to the most similar tested models, thus providing a ranking of the hypotheses. Notably, models with zero posterior probability in the confusion experiment (Figure 3-6a) were in fact almost exclusively those at largest distance from the original model. As a consequence, rejecting the models with zero posterior probability mass may provide falsification power even when the “true” model is not among the hypotheses.

In order to investigate whether our approach provided sensible model interpolation in cases of mixed or weak model evidence (Figure 3-6b), we considered the following example. The EXP-LSM model turns into an ER-ESN model in the limit of large decay constants λ of pairwise connectivity (that is modeled to depend on inter-soma distance, see inset Figure 3-6b). This allowed us to test our approach on connectomes that were sampled from models interpolated between these two model classes. When we exposed such “mixed” connectomes to our model discrimination approach, the resulting posterior had most of its mass at the EXP-LSM model for samples with d_{EXP} close to 1 and much of its mass at the ER-ESN model for samples with d_{EXP} close to 0. For intermediate model mixtures, the Bayesian model selection approach in fact yielded interpolated posterior probability distributions. This result gave an indication that the approach had in fact some stability against model mixing.

Connectomic separability of sparse recurrent neural networks trained on different tasks

Finally, we asked whether recurrent neural networks (RNNs) that were randomly initialized and then trained on different tasks could be distinguished by the proposed model selection procedure based on their connectomes after training. To address this question, we trained RNNs on either a texture discrimination task or a sequence memorization task. Initially, all RNNs were fully connected with random connection strengths (Figure 3-7a). During training, connection strengths were modified by error back-propagation to maximize performance on the task. At the same time, we needed to reduce the connectivity p of the RNNs to a realistic level of sparsity (p_{S1}∈[0.15...0.25], see Figure 3-1d) and used the following strategy: Whenever task performance saturated, we interrupted the training to identify the weakest 10% of connections and permanently pruned them from the RNN (Figure 3-7b).

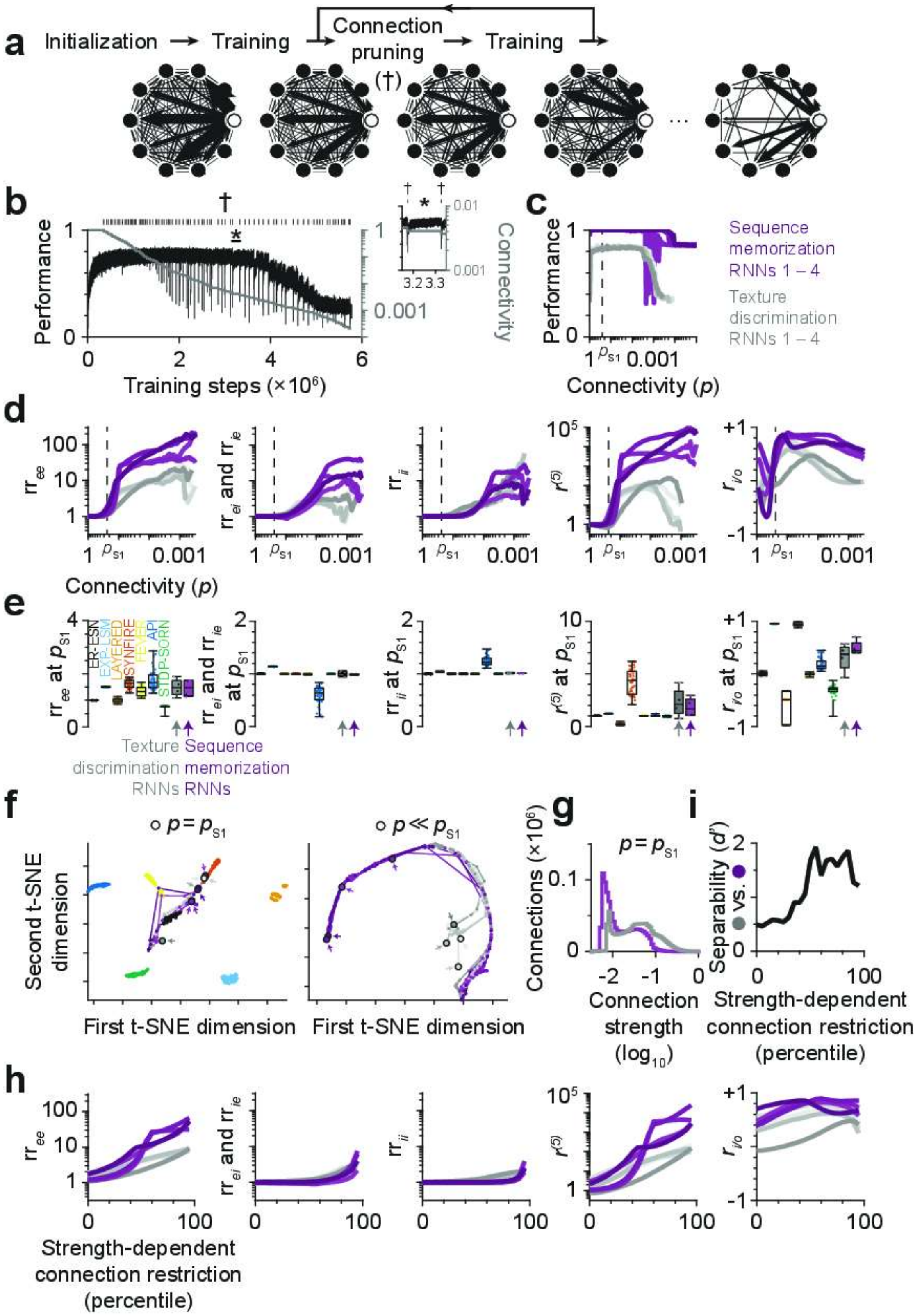

Figure 3-7 Connectomic separability of recurrent neural network (RNNs) with similar initialization, but trained on different tasks. **(a)** Overview of training process: RNNs were initially fully connected. Whenever task performance saturated during training, the weakest 10% of connections were pruned (†) to obtain a realistic level of sparsity. **(b)** Task performance (black) and network connectivity (gray) of a texture discrimination RNN during training. Ticks indicate the pruning of connections. Inset (*): Connection pruning causes a decrease in task performance, which is (partially) compensated by further training of the remaining connections. (Continuation on next page)

(Continuation of previous page) **(c)** Task performance as a function of network connectivity (*p*). Performance defined as: Accuracy (Texture discrimination RNNs, gray); 1 – mean squared error (Sequence memorization RNNs, magenta). Note that maximum observed performance was achieved in a wide connectivity regime including connectivity consistent with experimental data (p_{S1}=24%; dashed line). Task performance started to decay after pruning at least 99.6% of connections. **(d)** Connectome statistics of RNNs over iterative training and pruning of connections (cf. Fig. 3a). **(e)** Distribution of connectome statistics at $p=p_{S1}$ for RNNs and structural network models. Note that structural network models and structurally unconstrained RNNs exhibit comparable variance in connectome statistics (rr_{ee}: 0.088 vs. 0.15 for API; rr_{ei} and rr_{ie}: 0.0019 vs. 0.026 for API; rr_{ii}: 9.35×10-7 vs. 8.17×10-3 for API; $r^{(5)}$: 1.54 vs. 1.51 for SYNFIRE; $r_{i/o}$: 0.057 vs. 0.061 for LAYERED; cf. Fig. 3c). RNNs trained on different tasks did not differ significantly in terms of connectome statistics (rr_{ee}: 1.48±0.30 vs. 1.46±0.29, p=0.997; rr_{ei} and rr_{ie}: 1.00±0.04 vs. 0.99±0.01, p=0.534; rr_{ii}: 1.01±0.01 vs. 1.01±0.00, p=0.107; $r^{(5)}$: 2.28±1.24 vs. 1.84±0.80, p=0.997; $r_{i/o}$: 0.31±0.24 vs. 0.49±0.12, p=0.534; mean±std for n=4 texture discrimination vs. sequence memorization RNNs, each; two-sided Kolmogorov-Smirnov test without correction for multiple comparisons). Boxes: center line is median; box limits are quartiles; whiskers are minimum and maximum; all data points shown. **(f)** Similarity of RNNs based on connectome statistics (lines) as connectivity approaches biologically plausible connectivity p_{S1} (circles and arrows, left) and for connectivity range from 100% to 0.04% (circles and arrows, right). Note that connectome statistics at ≤11% connectivity separate texture discrimination and sequence memorization RNNs into two clusters. **(g)** Distribution of connection strengths at $p=p_{S1}$ for two RNNs trained on different tasks. **(h)** Connectome statistics of RNNs with p_{S1} connectivity when ignoring weak connections. **(i)** Separability of texture discrimination and sequence memorization RNNs with biologically plausible connectivity based on statistics derived from weighted connectome.

This training-pruning cycle then continued on the remaining connections. As a result, connectivity within an RNN was constrained only by the task used for training.

Maximum task performance was reached early in training while connectivity was still high ($p\approx$80%) and started to decay only after pruning more than 99.6% of connections (p<0.4%). Within this connectivity range (80%≥p≥0.4%), task performance substantially exceeded chance level (approx. 82.8-83.8% vs. 14.3% accuracy for n=4 texture discrimination RNNs; 0.000-0.002 vs. 0.125 mean squared error for n=4 sequence memorization RNNs; range of measurements vs. chance level; Figure 3-7c). Importantly, task performance was at the highest achieved level also at realistic connectivity of p_{S1}=24%.

We then investigated the connectome statistics applied to the RNNs during training (Figure 3-7d). We wanted to address the following two questions: First, how strongly are connectome statistics constrained by the training task? In particular, is the variance of connectome statistics in trained RNNs much larger than in network models that are primarily defined by their structure (e.g., LAYERED or SYNFIRE)? Second, does training of RNNs on different tasks result in different connectomic structures? And if so, are the connectome statistics sensitive enough to distinguish RNNs trained on different tasks based only on their structure?

At 24% connectivity, we found the variance of the connectome statistics to be comparable to the variance in structural network models (Figure 3-7e; cf. Figure 3-3c), but connectome statistics of RNNs trained on different tasks were statistically indistinguishable (Figure 3-7e), and RNNs with different tasks were thus only poorly separable (sensitivity index *d'* of 0.495; Figure 3-7f). However, we noticed a separation into two clusters when RNNs were trained and further sparsified to a connectivity of p<<11% (*d'*=1.45±0.23, mean±std.; Figure 3-7f).

To further study the effect of sparsification of a trained RNN, we investigated whether additional information about the strength of connections (Figure 3-7g) could improve the separability of RNNs trained on different tasks. We started with the weighted connectomes of RNNs that were trained and sparsified to 24% connectivity. For the evaluation of connectome statistics, we then restricted the RNNs to strong connections (Figure 3-7h). When ignoring the weakest 50% of connections of each RNN, the texture discrimination and sequence memorization RNNs differed significantly in their relative excitatory→excitatory reciprocity (3.60±0.99 vs. 7.83±1.98, p=0.011) and relative prevalence of cycles (22.19±12.69 vs. 118.16±40.86, p=0.011; Figure 3-7h.) As a result, RNNs trained on different tasks could be separated by the six connectome statistics with 85±3% accuracy (Figure 3-7i, separability d'=1.61±0.24, mean±std.). We concluded that RNNs with biologically plausible connectivity that were trained on different tasks can be distinguished based on the proposed statistics derived from weighted connectomes, in which only the strongest connections were used for connectome analysis.

Discussion

We report a probabilistic method to use a connectome measurement as evidence for the discrimination of local models in the cerebral cortex. We show that the approach is robust to experimental errors, and that a partial reconstruction of the connectome suffices for model distinction. We furthermore demonstrate the applicability to large cortical connectomes consisting of thousands of neurons. Surprisingly, a set of rather simple connectome statistics is sufficient for the discrimination of a large range of models. These results show that and how connectomes can function as arbiters of local cortical models (Denk et al. 2012) in the cerebral cortex.

Previous work on the classification of connectomes addressed smaller networks, consisting of up to 100 neurons, in which the identity of each neuron was explicitly defined. For these settings, the graph matching problem was approximately solved (Vogelstein and Priebe 2015). However, such approaches are currently computationally infeasible for larger unlabeled networks (Vogelstein et al. 2015, Vogelstein and Priebe 2015), which are found in the cerebral cortex.

As an alternative, the occurrence of local circuit motifs has been used for the analysis of local neuronal networks (Milo et al. 2002, Song et al. 2005, Perin et al. 2011). Four of our connectome statistics (Figure 3-3a) could be interpreted as such motifs: the relative reciprocity within and across the excitatory and inhibitory neuron populations, whose prevalence we could calculate exactly. The key challenge of these descriptive approaches is the interpretation of the observed motifs. The Bayesian approach as proposed here provides a way to use such data as relative, discriminating evidence for possible underlying circuit models.

One approach for the analysis of neuronal connectivity data is the extraction of descriptive graph properties (for example those termed clustering coefficient (Watts and Strogatz 1998), small-worldness (Humphries and Gurney 2008), closeness- and betweenness centrality (Freeman 1978)), followed by a functional interpretation of these measures. Such discovery-based approaches have been successfully applied especially for the analysis of macroscopic whole-brain connectivity data (van den Heuvel et al. 2016, Rubinov and Sporns 2010).

The relationship between (static) network architecture and task performance was previously studied in feed-forward models of primate visual object recognition (Yamins et al. 2014, Yamins and DiCarlo 2016), in which networks with higher object recognition performance were shown to yield better prediction of neuronal responses to visual stimuli. Our study considered recurrent neural networks, accounting for the substantial reciprocity in cortical connectivity, and investigated the structure-function relationship for static recurrent network architectures on a texture classification task (Figure A3-1), as well as for sparse recurrent neural networks in which both network architecture and task performance were jointly optimized (Figure 3-7).

Pre-hoc connectome analyses, in which the circuit models are defined before connectome reconstruction, offer several advantages over exploratory analyses, where the underlying circuit model is constructed after-the-fact: First, the statistical power of a test with pre-hoc defined endpoints is substantially higher (Pocock and Stone 2016, Wilson et al. 2015), rendering pre-hoc endpoint definition a standard for example in the design of clinical studies (Pocock and Stone 2016). Especially since so far, microscopic dense connectomes are mostly obtained and interpreted form a single sample, n=1 (White et al. 1986, Varshney et al. 2011, Helmstaedter et al. 2013, Kasthuri et al. 2015), this concern is substantial, and a pre-hoc defined analysis relieves some of this statistical burden. Moreover, the pre-hoc analysis allowed us to determine an experimental design for the to-be-measured connectome, defining bounds on reconstruction and synapse errors and the required connectome measurement density (Figure 3-5c,d). Especially given the substantial challenge of data analysis in connectomics (Helmstaedter 2013), this is a relevant practical advantage.

We considered it rather unexpected that a 10% fractional reconstruction, and reconstruction errors up to 25% would be tolerable for the selection of local circuit models. One possible reason for this is the homogeneity of the investigated network models. For each model, the (explicit or implicit) structural connectivity rules are not defined per neuron individually, but apply to a whole sub-population of neurons. For example, the ER-ESN model implies one connectivity rule for all excitatory neurons and a second one for all inhibitory neurons; the layered model defines one connectivity rule for each layer. Hence, the model properties were based on the wiring statistics of larger populations, permitting low fractional reconstruction and substantial wiring errors. If, on the contrary, the network models were to define for each neuron a very specific connectivity structure, a different experimental design would likely be favorable, in which the precise reconstruction of few individual neurons could suffice to refute hypotheses.

How critical were the particular circuit constraints which we considered for initial model validation (Figure 3-1d)? What if, for example, pairwise excitatory connectivity was lower than concluded from pairwise recordings in slice (Figure 3-1d (Meyer et al. 2011, Feldmeyer 2012, Gibson et al. 1999, Beierlein et al. 2003, Feldmeyer et al. 1999, Lübke et al. 2000, Lefort et al. 2009, Koelbl et al. 2015, Gibson et al. 2005)), and instead for example rather 10%, not 15-25% in L4? The results on discriminability of trained RNNs (Figure 3-7), which was higher for sparser networks, may indicate that model identification would even improve for lower overall connectivity regimes. Also, such a setting would imply that the model priors would be in a different range (Figure A3-4; for example the layered network with four layers would imply a pairwise forward connectivity $p_{e,f}$=27% instead of 53%). Circuit measurements that already clearly refute any of the hypothesized models based on simple pairwise connectivity descriptors would of course reduce the model space a-priori. Once a full connectomic measurement is available, the connectivity constraints (Figure 3-1d) can be updated, the model hypothesis space diminished or not, and then our model selection approach can be applied.

The choice of summary statistics in ABC is generally not unique, and poorly chosen statistics may bias model selection (Fay et al. 2015, Marin et al. 2014, Robert et al. 2011). Our use of emulated reconstruction experiments with known originating models was therefore required to verify ABC performance (Figure 3-4-6). These results also indicate that it was sufficient to use summary statistics that were constrained to operate on unweighted graphs. More detailed summary statistics that also make use of indicators of synaptic weights accessible in 3D EM data (such as size of post-synaptic density, axon-spine interface or spine head volume (Harris and Stevens 1989, Bartol et al. 2015, de Vivo et al. 2017)) may allow further distinction of plasticity models with subtle differences in neuronal activity history. In fact, we found that weighted connectomes were necessary to distinguish between circuit models that were subject to identical structural constraints and that only differed in the tasks that they performed (Figure 3-7).

The proposed Bayesian model selection also has a number of drawbacks.

First, likelihood-free model inference using ABC-SMC depends on efficient simulation of the models. Computationally expensive models, such as recurrent neural networks trained by stochastic gradient descent (Figure 3-7), are prohibitive for sequential Monte Carlo sampling. However, the proposed connectome statistics and the resulting connectomic distance function provide a quantitative measure of similarity even for individual samples (Figure 3-7i). Furthermore, a rough estimate of the posterior distribution over models can be obtained already by a single round of ABC-SMC with a small sample size.

Second, an exhaustive enumeration of all hypotheses is needed for Bayesian model selection. What if none of the investigated models was correct? This problem cannot be escaped in principle, and it has been argued that Bayesian approaches have the advantage of explicitly and transparently accounting for this lack of prior knowledge rather than implicitly ignoring it (Lawrence et al. 2013). Nevertheless, this caveat strongly emphasizes the need for a proper choice of investigated models. Our results (Figure 3-6) indicate that models close to but not identical to any of the investigated ones are still captured in the posterior by reporting their relative similarity to the remaining investigated models. We argue that rejection of models without posterior probability mass provides valuable scientific insights, even when the set of tested hypotheses is incomplete.

Third, we assumed a flat prior over the investigated models, considering each model equally likely a-priori. Pre-conceptions about cortical processing could strongly alter this prior model belief. If one assumed a non-homogenous model prior, this different prior can be multiplied to the posterior computed in our approach. Therefore, the computed posterior can in turn be interpreted as a quantification of how much more likely a given model would have to be considered by prior belief in order to become the classification result, enabling a quantitative assessment of a-priori model belief about local cortical models.

Together, we show that connectomic measurement carries substantial distinctive power for the discrimination of models in local circuit modules of the cerebral cortex. The concrete experimental design for the identification of the most likely local model in cortical layer 4, proposed pre-hoc, will make the mapping of this cortical connectome informative and efficient. Our methods are more generally applicable for connectomic comparison of possible models of the nervous system.

Methods

Circuit constraints

The following circuit constraints were shared across all cortical network models. A single barrel was assumed to consist of 1800 excitatory and 200 inhibitory neurons (Meyer et al. 2011, Feldmeyer 2012). The excitatory connectivity p_e, i.e. the probability of an excitatory neuron to project to any other neuron was assumed to be $p_{\mathrm{ee}} = p_{\mathrm{ei}} = 0.2$ (Gibson et al. 1999, Beierlein et al. 2003, Feldmeyer et al. 1999, Lübke et al. 2000, Lefort et al. 2009), the relative excitatory-excitatory reciprocity rr_{ee}, i.e., the probability of also observing a bidirectional connection given one connection between two excitatory neurons, was assumed to lie in the range $r_{ee} \in [0.15, 0.35]$ (Feldmeyer et al. 1999, Lefort et al. 2009, Feldmeyer 2012, Gibson et al. 1999, Beierlein et al. 2003). The inhibitory connectivity p_i, i.e., the probability of an inhibitory neuron to project onto any other neuron, was assumed as $p_{ii} = p_{ie} = 0.6$ (Koelbl et al. 2015, Gibson et al. 1999, Beierlein et al. 2003, Gibson et al. 2005). Self-connections were not allowed.

Estimates of reconstruction time and synapse number

Neurite path length density was assumed to be $d = 10\text{km}/\text{mm}^3$, barrel volume was assumed to be $V = (300\mu\text{m})^3$, annotation speed was taken as $v = 1.5\text{mm}/\text{h}$ (Boergens et al. 2017) together yielding the total annotation time $T = Vd/v$.

The total number of synapses in a barrel was calculated as $Nf = 3{,}2299{,}091$ with $f = 3.36$ the average number of synapses per connection (Feldmeyer et al. 1999) and $N = 2000 \cdot (1800 \cdot 0.2 + 200 \cdot 0.6)$ the total number of synaptically connected pairs of neurons.

Implementations of cortical network models

Seven cortical models were implemented: the Erdős–Rényi echo state network (ER-ESN (Erdős and Rényi 1959, Jaeger and Haas 2004)), the exponentially decaying connectivity - liquid state machine model (EXP-LSM (Maass et al. 2002, Probst et al. 2012)), the layered model (LAYERED (Rosenblatt 1962, Hubel and Wiesel 1962)), the synfire chain model (SYNFIRE (Troyer et al. 1998, Miller et al. 2001, Abeles 1982)), the feature vector recombination model (FEVER (Druckmann and Chklovskii 2012)), the antiphase inhibition model (API) and the spike timing dependent plasticity self-organizing recurrent neural network model (STDP-SORN (Lazar et al. 2009, Zheng et al. 2013)).

The Erdős–Rényi echo state network (ER-ESN) model was a directed Erdős–Rényi random graph. Each possible excitatory projection was realized with probability $p_e = 0.2$, each possible inhibitory projection with probability $p_i = 0.6$.

For the exponentially decaying connectivity - liquid state machine model (EXP-LSM), excitatory and inhibitory neurons were assumed to be uniformly and independently distributed in a cubic volume of equal side lengths. The excitatory and inhibitory pairwise connection probabilities $p_e(d)$ and $p_i(d)$ were functions of the Euclidean distance d of a neuron pair according to $p_t(d) = p_0 \exp\left(\frac{-d}{\lambda_t}\right)$, $p_0 = p_t + (1 - p_t)d_{\text{EXP}}$, $d_{\text{EXP}} = 1$, $t \in \{\text{e, i}\}$. The length scale parameters λ_t were adjusted to match an overall connectivity of $p_e = 0.2$ in the excitatory case ($t = e$) and a connectivity of $p_i = 0.6$ in the inhibitory case ($t = i$).

The layered model (LAYERED) consisted of n_l excitatory layers. Lateral excitatory-excitatory connections were realized within one layer with connection probability $p_{e,l}$. Forward connections from one layer to the next layer were realized with probability $p_{e,f}$. Inhibitory neurons were not organized in layers but received excitatory projections uniformly and independently from all excitatory neurons with probability $p_e = 0.2$ and projected onto any other neuron uniformly and independently with probability $p_i = 0.6$.

The synfire chain (SYNFIRE) implementation used in this work followed (Trengove et al. 2013). The inhibitory pool size $s_{\text{pool},i} = \frac{n_i}{n_e} s_{\text{pool}}$ was proportional to the excitatory pool size s_{pool}. The network was constructed as follows: (1) An initial excitatory source pool of size s_{pool} was chosen uniformly from the excitatory population. (2) An excitatory target pool of size s_{pool} and an inhibitory target pool of size $s_{\text{pool},i}$ were chosen uniformly. The excitatory source and target pools were allowed to share neurons, i.e., neurons were drawn with replacement. (3) The excitatory source pool was connected all-to-all to the excitatory and inhibitory target pools but no self-connections were allowed. (4) The excitatory target pool was chosen to be the excitatory source pool for the next iteration. Steps (2) to (4) were repeated $\mathrm{round}\left(\frac{\log(1-p_e)}{\log\left(1-\frac{s_{\mathrm{pool}}^2}{n_e^2}\right)}\right)$ times, with $\mathrm{round}(\cdot)$ denoting the nearest integer. Inhibitory neurons projected uniformly to any other neuron with probability $p_{\mathrm{i}} = 0.6$.

The feature vector recombination model (FEVER) network was constructed from an initial ER random graph C^0 with initial pairwise connection probabilities $p_t^0 = p_t - f_r d_f / n$ for $t \in \{e, i\}$ with $f_r \in [0, 1]$ the feverization, $d_f \in \mathbb{N}$ the feature space dimension and n the number of neurons. The outgoing projections $\mathbf{c}_k$ of neuron k were obtained from C^0 according to the sparse optimization problem $\mathbf{c}_k = \mathrm{argmin}_{\mathbf{c}} \left\{ \sum_{l \neq k} \left\| \mathbf{d}_l - \sum_{p \neq k} \mathbf{d}_p \mathrm{c}_p \right\|_2^2 + \lambda_{t(k)} \left\| \mathbf{c}_k^0 - \mathbf{c} \right\|_1 \right\}$, $c_{kk} = 0$, where the $\mathbf{d}_i \in \mathbb{R}^{d_f}$ were the feature vectors drawn uniformly and independently from a unit sphere of feature space dimension d_f and $\mathbf{c}_k^0 \in \mathbb{R}^n$ denoted the initial outgoing projections of neuron k as given by C^0 and $t(k) = e$ if neuron k was excitatory, $t(k) = i$ otherwise. The sparse optimization was performed with scikit-learn (Pedregosa et al. 2011) using the "**sklearn.linear_model.Lasso**" optimizer with the options "**positive=True**" and "**max_iter=100000**" for the excitatory and the inhibitory population individually. The parameter λ_t, $t \in \{e, i\}$ was fitted to match the excitatory and inhibitory connectivity of $p_e = 0.2$ and $p_i = 0.6$ respectively.

In the antiphase inhibition model (API), a feature vector $\mathbf{d}_k$ was associated with each neuron k. The feature vectors were drawn uniformly and independently from a unit sphere with feature space dimension d_f. The cosine similarity $C_{ij} = c_{\mathrm{sim}}(\mathbf{d}_i, \mathbf{d}_j)$ between the feature vectors of neuron i and j were transformed into connection probabilities p_{ij} between neuron i and j according to $p_{ij} = 1 - \left(1 - \left(\frac{C_{ij} s_j + 1}{2}\right)^{n_{\mathrm{pow}}}\right)^{n_{s_j}^{\mathrm{binomial}}}$, where $s_j = 1$ if neuron j was excitatory and $s_j = -1$ if neuron j was inhibitory. The coefficients n_x^{binomial} with $x \in \{-1,1\}$ were fitted to match the excitatory and inhibitory connectivity constraints. The coefficient n_{pow} was in the range $n_{pow} \in [4,6]$ (Figure A3-4f (Troyer et al. 1998)).

The spike timing dependent plasticity self-organizing recurrent neural network model (STDP-SORN) network was constructed as follows: An initial random matrix $\mathrm{C}_0 \in \{0,1,-1\}^{n \times n}$ with pairwise connection probabilities p_t for $t \in \{e, i\}$ was drawn. Let $s_{e,k} = \sum_{\mathrm{l}:\mathrm{C}_{kl} > 0} \mathrm{C}_{kl}$ denote the sum of all excitatory incoming weights of neuron k and similarly $s_{i,k} = -\sum_{l:\mathrm{C}_{kl} < 0} \mathrm{C}_{kl}$ denote the sum of all inhibitory incoming weights of neuron k. Each weight $\mathrm{C}_{kl} > 0$ was normalized according to $\mathrm{C}_{kl} \leftarrow \mathrm{C}_{kl} / s_{e,k}$ and each weight $\mathrm{C}_{kl} < 0$ according to $\mathrm{C}_{kl} \leftarrow \mathrm{C}_{kl} / s_{i,k}$ such that for each neuron the sum of all incoming excitatory weights was 1 and the sum of all incoming inhibitory weights was -1. No self-connections were allowed. The so obtained matrix was the initial adjacency matrix C. The initial vector of firing thresholds $\mathbf{t} \in \mathbb{R}^n$ was initialized to $\mathbf{t} = \mathbf{1}$. The neuron state $\mathbf{x} \in \{0,1\}^n$ and the past neuron state $\mathbf{x}_{\mathrm{old}} \in \{0,1\}^n$ were initialized as zero vectors.

After initialization, for each of the $\tau_{\mathrm{end}} = 10{,}000$ simulation time points, the following steps were repeated (Zheng et al. 2013): (1) Propagation, (2) Intrinsic plasticity, (3) Normalization, (4) STDP, (5) Pruning and (6) Structural plasticity as follows:

Propagation. The neuron state $\mathbf{x} \in \{0,1\}^n$ was updated $\mathbf{x} \leftarrow \Theta(\mathrm{C}\mathbf{x} + \boldsymbol{\xi} - \mathbf{t})$, where $\boldsymbol{\xi}$ was noise with $\boldsymbol{\xi}_k \sim \mathrm{N}(0, \sigma^2)$ iid., $\sigma = 0.05$ and $\Theta(x) = \begin{cases} 1, x \geq 0 \\ 0 \text{ otherwise} \end{cases}$.

Intrinsic plasticity. The firing thresholds were updated $\mathbf{t} \leftarrow \mathbf{t} + \eta_i(\mathbf{x} - f_0)$ where $f_0 = 1/10$ was the target firing rate and η_i the intrinsic plasticity learning rate.

Normalization. The excitatory incoming weights were normalized to 1: If $\mathrm{C}_{kl} > 0$ then $\mathrm{C}_{kl} \leftarrow \mathrm{C}_{kl}/s_{e,k}$.

STDP (Spike timing dependent plasticity). Weights were updated according to $\mathrm{C}_{kl} \leftarrow \mathrm{C}_{kl} + \eta_{\mathrm{STDP}}\left(\mathbf{x}_k \mathbf{x}_{\mathrm{old},l} + \mathbf{x}_k \mathbf{x}_l - \mathbf{x}_{\mathrm{old},k} \mathbf{x}_l\right)$ for $k \neq l$. Finally the past neuron state was also updated $\mathbf{x}_{\mathrm{old}} \leftarrow \mathbf{x}$.

Pruning. Weak synapses were removed: If $0 \leq \mathrm{C}_{kl} < 1/n$ then $\mathrm{C}_{kl} \leftarrow 0$.

Structural plasticity. It was attempted to add $n_{\mathrm{add}} = (n_e^2 p_e - n_s)/(1 - p_e)$ synapses randomly, with $n_s = \sum_{k,l:\mathrm{C}_{kl}>0} 1$ the number of excitatory synapses currently present in the network. For each of these attempts two integers $k, l \sim \mathrm{DiscreteUniform}(0, n_e)$ were chosen randomly and independently. If $k \neq l$ and $\mathrm{C}_{kl} = 0$ then $\mathrm{C}_{kl} \leftarrow 1/n$.

The STDP-SORN model was implemented in Cython and OpenMP.

All code was verified using a set of unit tests with 91% code coverage.

Reconstruction errors and network subsampling

Reconstruction errors were implemented by randomly rewiring connections: A fraction ξ of the edges of the network was randomly removed, ignoring their signs. The same number of edges was then randomly reinserted and the signs were adjusted to match the sign of the new presynaptic neuron. Partial connectomic reconstruction was implemented by network subsampling: A fraction $f_m \in [0,1]$ of the neurons was uniformly drawn. The subgraph induced by these neurons was preserved, its complement discarded.

Connectomic cortical network measures

The following measures (Figure 3-3a) were computed: (1) relative excitatory-excitatory reciprocity, (2) relative excitatory-inhibitory reciprocity, (3) relative inhibitory-excitatory reciprocity, (4) relative inhibitory-inhibitory reciprocity, (5) relative excitatory recurrency, and (6) excitatory in/out-degree correlation. All measures were calculated on binarized networks as follows:

Reciprocity r_{xy} with $x, y \in \{e, i\}$, *e*=excitatory, *i*=inhibitory, was defined as the number of reciprocally connected neuron pairs between neurons of population x and y divided by the total number of directed connections from x to y. If the number of connections from x to y was zero then r_{xy} was set to zero. Hence r_{xy} was an estimate for the conditional probability of observing the reciprocated edge of a connection from y to x, given a connection from x to y. The relative excitatory-inhibitory reciprocity was defined as $\mathrm{rr}_{ei} = r_{ei}/p_{ie}$. I.e., relative reciprocities were obtained by dividing the reciprocity of a network by the expected reciprocity of an ER network with the same connectivity.

Relative excitatory recurrency was defined as $r^{(n)} = \mathrm{tr}(\mathrm{C}_{ee}^n)/(n_e p_e)^n$, where C_{ee} was the excitatory submatrix and tr denoted the trace of the matrix. The cycle length parameter n was set to $n = 5$.

The excitatory in/out-degree correlation $r_{i/o}$ was the Pearson correlation coefficient of the in- and out-degrees of neurons of the excitatory subpopulation. Let $d_{i,k}$ denote the in-degree of neuron k and $d_{o,k}$

the out-degree of neuron k. Let $\overline{d_\imath} = \frac{1}{n_e}\sum_{k=1}^{n_e} d_{i,k}$ and $\overline{d_o} = \frac{1}{n_e}\sum_{k=1}^{n_e} d_{o,k}$, with n_e the total number of excitatory neurons. Then $r_{i/o} = \frac{\sum_{k=1}^{n_e}(d_{i,k}-\overline{d_\imath})(d_{o,k}-\overline{d_o})}{\sqrt{\sum_{k=1}^{n_e}(d_{i,k}-\overline{d_\imath})^2}\sqrt{\sum_{k=1}^{n_e}(d_{o,k}-\overline{d_o})^2}}$.

Bayesian model selection

Bayesian model selection was performed on networks sampled from the seven models as follows: First, a noise-free network C_0 with 2000 neurons was drawn from one of the network models $m \in [1, \dots, 7]$. Second, this noise-free network was perturbed with noise of strength ξ as described above. Then, a fraction f_m of the network was subsampled, yielding $\mathrm{C}^{\#}$.

The Bayesian posterior $p(\boldsymbol{\theta}|\mathrm{C}^{\#})$ was then calculated on the noisy subnetwork $\mathrm{C}^{\#}$ using an approximate Bayesian-sequential Monte Carlo (ABC-SMC) method. The implemented ABC-SMC algorithm followed the ABC-SMC procedure proposed by (Toni and Stumpf 2010) with slight modifications to ensure termination of the algorithm, as described below. The ABC-SMC algorithm was implemented as custom Python library (see https://gitlab.mpcdf.mpg.de/connectomics/discriminatEM).

The network measures $\boldsymbol{\gamma} = (\mathrm{rr}_{ee}, \mathrm{rr}_{ei}, \mathrm{rr}_{ie}, \mathrm{rr}_{ii}, r_{\frac{i}{o}}, r^{(5)})$ described above were used as summary statistics for the ABC-SMC algorithm. The distance between two networks $\mathrm{C}^{\#}$ and $\mathrm{C}_i^{\mathrm{s}}$ was defined as $d_{\boldsymbol{\gamma}}(\mathrm{C}^{\#}, \mathrm{C}_i^{\mathrm{s}}) = \sum_{k=1}^{6} \frac{|\boldsymbol{\gamma}_k(\mathrm{C}^{\#}) - \boldsymbol{\gamma}_k(\mathrm{C}_i^{\mathrm{s}})|}{\boldsymbol{\gamma}_{k,80} - \boldsymbol{\gamma}_{k,20}}$, where the sum over k was taken over the six network measures. The quantities $\boldsymbol{\gamma}_{k,80}$ and $\boldsymbol{\gamma}_{k,20}$ were the 80% and 20% percentiles of the measure $\boldsymbol{\gamma}_k$, evaluated on an initial sample from the prior distribution of size 2000; the particle number, i.e., the number of samples per generation, was set to 2000. If a particle of the initial sample contained an undefined measure (e.g., in-/out-degree correlation), it was discarded. When $\boldsymbol{\gamma}_{k,80}$ and $\boldsymbol{\gamma}_{k,20}$ were equal, the corresponding normalization constant of the distance function was set to the machine epsilon instead. The initial acceptance distance ϵ_{ABC} was the median of the distances $d_{\boldsymbol{\gamma}}(\mathrm{C}^{\#}, \mathrm{C}_i^{\mathrm{s}})$ as obtained from the same initially sampled connectomes $\mathrm{C}_i^{\mathrm{s}}$.

After each generation, ϵ_{ABC} for the following generation was set to the median of the error distances $d_{\boldsymbol{\gamma}}(\mathrm{C}^{\#}, \mathrm{C}_i^{\mathrm{s}})$ of the particles in the current generation. Particles were perturbed hierarchically. First, a model m was drawn from the current approximating posterior model distribution. With probability 0.85 the model m was kept, with probability 0.15 it was redrawn uniformly from all models. Second, given the sampled model, a single particle from the model specific particles was sampled. The sampled particle was perturbed according to a multivariate normal kernel with twice the variance of the variance of the particles in the current population of the given model. The perturbed particle was accepted if the error distance was below ϵ_{ABC}. To obtain again 2000 particles for the next population, 2000 particle perturbation tasks were run in parallel. However, to ensure termination of the algorithm, each of the 2000 tasks was allowed to terminate without returning a new particle if more than 2000 perturbation attempts within the task were not successful. Model selection was stopped if only one single model was left, the maximum number of 8 generations was reached, the minimum $\epsilon_{\mathrm{ABC}} = 0.175$ was reached or less than 1000 accepted particles were obtained for a population. See code for implementation details.

Functional testing

The ER-ESN, EXP-LSM and LAYERED models were trained to discriminate natural texture classes, which were represented by one natural image each. Samples of length 500 pixel of these classes were obtained at random locations of these images. These samples were then fed into LAYERED networks via a single input neuron projecting to the first layer of the network. In the ER and EXP case the input neuron projected to all neurons in the network. Within the recurrent network, the dynamical model was given by $\mathbf{a}(t+1) = (1-\alpha)\mathbf{a}(t) + \alpha \, \mathrm{relu}(\mathrm{C}\mathbf{a}(t) + \mathbf{u}(t))$, where C was the adjacency matrix, $\mathbf{u}$ the input, a the activation, $\alpha = 0.1$ the leak rate and $\mathrm{relu}(\cdot) = \max(0,\cdot)$. Readout was a softmax layer with seven neurons $o_1, \dots, o_7$; one neuron for each class. Adam (Kingma and Ba 2014) was used to train all the forward connections with exception of the input connections. The loss l was the categorical cross entropy accumulated over the last 250 time steps $l = -\sum_{i,c'=1,..,7,t=250\dots500} \delta_{c',\mathrm{c}(i)} \log(o_{c'}(t))$, where i denoted the sample and $\mathrm{c}(i)$ the ground truth class of sample i. At prediction time the predicted class c^* was $c^* = \mathrm{argmax}_{\mathrm{c}\in\{1,\dots,7\}} \sum_{t=250}^{500} o_c(t)$. The model was implemented in Theano (https://deeplearning.net/software/theano) and Keras (https://keras.io) as custom recurrent layer and run on Tesla M2090 GPUs. See code for details of the implementation.

In the SYNFIRE model, a conductance based spiking model was used with membrane potential $\dot{v} = (v_{\mathrm{rest}} - v)/\tau_p$ with $\tau_p = 20\mathrm{ms}$, inhibitory reversal potential $v_{\mathrm{reversal},i} = -80\mathrm{mV}$, excitatory reversal potential $v_{\mathrm{reversal},e} = 0$, resting potential $v_{\mathrm{rest}} = -70mV$, spiking threshold $v_{\mathrm{threshold}} = -55\mathrm{mV}$, inter pool delay $d_{\mathrm{pool}} \sim \mathrm{U}(0.5,2)$, excitatory intra pool jitter $d_{\mathrm{jitter},e} \sim \mathrm{U}(0,0.3)$ inhibitory intra pool jitter $d_{\mathrm{jitter},i} \sim \mathrm{U}(0.3, 0.9)$, excitatory refractory period $\tau_{\mathrm{ref},e} = 2\mathrm{ms}$ and inhibitory refractory period $\tau_{\mathrm{ref},i} = 1\mathrm{ms}$. On spiking of presynaptic neuron j the membrane potential of postsynaptic neuron i was increased by $g_{\mathrm{pre}}(v_{\mathrm{reversal,pre}} - v_{\mathrm{post}})$ where g_{pre} denoted the presynaptic efficacy, $v_{\mathrm{reversal,pre}}$ the presynaptic reversal potential and v_{post} the postsynaptic membrane potential. The excitatory synaptic efficacy g_e and the inhibitory synaptic efficacy g_i were functions of the pool size and were obtained by interpolating $s_{\mathrm{pool}} = [80, 100, 120, 150, 200, 250, 300]$, $\log_{10}(g_e) = [-2.1, -2.25, -2.28, -2.365, -2.6, -2.625, -2.75]$ and $\log_{10}(g_i) = [-0.45, -0.7, -0.763, -0.894, -1.25, -1.25, -1.5]$ linearly.

The fractional chain activation f_{ca} was calculated as follows: Let $n_i(t)$ denote the number of active neurons of pool i between time t and $t + \Delta t$, with $\Delta \mathrm{t} = 0.1\mathrm{ms}$. Let the maximal activation be $\hat{n}(t) = \max_{\mathrm{j}} n_j(t)$ and define the pool activity indicator $\delta_i(t) = I(n_i(t) > \frac{s_{\mathrm{pool}}}{2}, \hat{n}(t) = n_i(t), |\{i|\hat{n}(t) = n_i(t)\}| = 1)$. Let the cumulative activity be $c_i(t) = \sum_{t' \leq t} n_i(t)\delta_i(t)$ and $t_{\mathrm{end}} = \max\{t \big| c_i(t) < 1.2 \, s_{\mathrm{pool}} \, \forall i\}$. The number of activated pools was $N = |\{i | \exists t < t_{\mathrm{end}}: \delta_i(t) = 1\}|$ and the fractional chain activation $f_{\mathrm{ca}} = N/l$ in which l was the chain length. Fractional pool activation f_{pa} at time t was the fraction of neurons in a pool that exceeded a threshold activity $v_{\mathrm{threshold}} = -55\mathrm{mV}$ between time t and $t + \Delta t$, with $\Delta t = 0.1ms$.

Additional model-functional testing was performed. Also SYNFIRE, FEVER, API and STDP-SORN networks were trained to discriminate textures, analogous to the ER-ESN and EXP-LSM models. The test previously applied to the SYNFIRE model was not applied to the remaining models because the SYNFIRE model was the only integrate-and-fire model. The recombination memory test, originally proposed as part of the FEVER model, was also applied to the API model and vice versa the antiphase inhibition test, originally proposed as part of the API model was also applied to the FEVER model. These two tests were not applied to the remaining models because these lacked feature vectors. The test for uncorrelated and equally distributed activity, originally proposed as part of the STDP-SORN model, was also not applied to the remaining models because they did not feature binary threshold neurons. If a model was not able to carry out a given task due to inherent properties of that model such as, e.g., absence of feature vectors, the model was considered to fail that task.

Training, sparsification, and connectomic separability of recurrent neural networks trained on different tasks

Architecture and initialization of recurrent neural networks

Recurrent neural networks (RNNs) consisting of 1800 excitatory, 200 inhibitory and a single input neuron were trained on either a texture discrimination or a sequence memorization task (Figure 3-7). Each of the 2000 neurons in the RNN received synaptic inputs from the input neuron and from all other RNN neurons. The total input to neuron *i* at time *t* was given by $I_{i,t} = W_{i,1} \times A_{1,t-1} + \ldots + W_{i,2000} \times A_{2000,t-1} + \mathbf{v}_i \times u_t + b_i$, where $W_{i,j}$ is the strength of the connection from neuron *j* to neuron *i*. Connections originating from excitatory neurons were non-negative, while connections from inhibitory neurons were non-positive. Self-innervations was prohibited ($W_{i,i} = 0$ for all *i*). $A_{j,t-1} = \max(0, \min(2, I_{i,t-1}))$ is the activation of neuron *j* in at time *t-1*. The input signal u_t was projected to neuron *i* by connection of strength $\mathbf{v}_i$. b_i was a neuron-specific bias.

Prior to training, RNNs were initialized as follows (Figure 3-7a): Neuronal activations $A_{i,0}$ were set to zero. Internal connection strengths $W_{j,i}$ were sampled from a truncated normal distribution (by resampling values with absolute values greater than two). If necessary, the sign of $W_{j,i}$ was inverted. Connections from inhibitory neurons were rescaled such that $\langle W_j \rangle = 0$, where <.> denotes the average. Finally, connection strengths were rescaled to a standard deviation of $(2 / 2001)^{1/2}$ (He et al. 2015). Connections from the input neuron were initialized by the same procedure. Neuronal biases were set to minus $\langle \mathbf{v} \rangle \times \langle \mathbf{u} \rangle$.

Texture discrimination task

RNNs were trained to discriminate between seven different natural textures. The activity of the input neuron, u_t, was given by the intensity values of 100 consecutive pixels in a texture image. For each texture, a different excitatory neuron was randomly chosen as output neuron. The RNNs were trained to activate an output neuron if and only if the input signal was sampled from the corresponding natural texture.

The texture images were split into training (top half), validation (third quarter), and test sets (bottom quarter). Input sequences were sampled by random uniform selection of a texture image, of a row therein, and of a pixel offset. The sequences were reversed with 50% probability. The excitatory character of the input neuron was emulated by normalizing the intensity values within each gray-scale image, clamping the values to two standard deviations and adding a bias of two.

The RNNs were trained by minimizing the cross-entropy loss on mini-batches of 128 sequences using Adam (Kingma and Ba 2014) (learning rate: 0.0001, β_1: 0.9 and β_2: 0.999). The gradient was clipped to a norm of at most 1. Every ten gradient steps, the RNN was evaluated on a mini-batch from the validation set. If the running median of 100 validation losses did not decrease for 20,000 consecutive gradient steps, the connectivity matrix *w* was saved for offline analysis and then sparsified (Figure 3-7a). Following (Han et al. 2015), connections with absolute connection strength below the 10th percentile were pruned (and couldn't be regained thereafter). The validation loss and gradient step counter were reset before training of the sparsified RNN continued (Figure 3-7a).

Four RNNs were trained with different sets of initial parameters and different training sequence orders. Each RNN was trained for around 5 days and 21 hours, corresponding to roughly 5.75 million training steps (Python 3.6.8, NumPy 1.16.4, TensorFlow 1.12, CUDA 9.0, CuDNN 7.4, Nvidia Tesla V100 PCIe; Figure 3-7b,c).

Sequence memorization task

In the sequence memorization task, RNNs were trained to output learned sequences at the command of the input signal. The sequences were 100-samples-long whisker traces from (Clack et al. 2012). The input signal determined the onset time and type of sequence to generate. The activity of the input neuron, u_t, was initially at zero ($u_0 = 0$) and switched to either +1 or -1 at a random point in time. The RNN was trained to output zero while the input is zero, to start producing sequence one at the positive edge, and to generate sequence two starting at the negatives edge in u_t. The whisker traces were drift-corrected, such that they started and ended at zero. The amplitudes were subsequently divided by twice their standard deviation.

Training proceeded as for texture discrimination. The mean squared error was used as loss function. Four RNNs with different random initializations and different training sequence orders were each trained for roughly 15 days and 22 hours, corresponding to 18.5 million training steps.

Analysis of RNN connectomes

Connectivity matrices were quantitatively analyzed in terms of the relative excitatory-excitatory reciprocity (rr_{ee}), the relative excitatory-inhibitory reciprocity (rr_{ei}), the relative inhibitory-excitatory reciprocity (rr_{ie}), the relative inhibitory-inhibitory reciprocity (rr_{ii}), the relative prevalence of cycles of length 5 ($r^{(5)}$), and the in-out degree correlation ($r_{i/o}$) (Figure 3-7d-i). The connectome statistics were then further processed using MATLAB R2017b. Equality of connectome statistics across different tasks was tested using the two-sample Kolmogorov-Smirnov test. To visualize structural similarity of neural networks in two dimensions, t-SNE (Van der Maaten and Hinton 2008) was applied to the six connectome statistics. For a quantitative measure of structural separability of RNNs, the connectomic distance $d_\gamma(\mathrm{C}_i, \mathrm{C}_j)$ (see "Bayesian model selection") was computed for all pairs of RNNs. $d_\gamma(\mathrm{C}_i, \mathrm{C}_j) < \theta$ was used to predict whether RNNs i and j were trained on the same task. The performance of this predictor was evaluated in terms of the area (A) under the receiver operating characteristic (ROC) curve, and accuracy. The sensitivity index d' was computed as $2^{1/2}Z(A)$, where Z is the inverse of the cumulative distribution function of the standard normal distribution.

Whether information about connection strength helps to distinguish texture discrimination and sequence memorization RNNs (Figure 3-7g-i) was tested as follows: For each RNN, the configuration with average connectivity closest to 24% was further sparsified by discarding the weakest 5, 10, 15, .., 95% of connections before computing the connectome statistics. Separability of texture discrimination and sequence memorization network based on the connectome statistics was quantified as above.

Data availability

The data that support the findings of this study are available at https://discriminatEM.brain.mpg.de.

Code availability

All methods were implemented in Python 3 (compatible with version 3.7), unless noted otherwise. All code is available under the MIT license at https://gitlab.mpcdf.mpg.de/connectomics/discriminatEM. To install and run discriminatEM please follow the instruction in the readme.pdf provided within discriminatEM.zip. Detailed API and tutorial style documentation are also provided within discriminatEM.zip in the HTML format (doc/index.html).

Author contributions

Conceived, initiated and supervised the study: MH; supervised the study: CM, FT; carried out simulations, developed methods, analyzed data: EK and AM with contributions from all authors; wrote the paper: EK, MH and AM with input from all authors.

The authors state no conflict of interest. Current affiliations outside academia: T-Systems Inc. (EK).

Acknowledgements

We thank Till Kretschmar for investigation of connectome metrics in an early phase of the project, Jan Hasenauer for discussions, Robert Gütig, and Andreas Schaefer for comments on an earlier version of the manuscript, Fabian Fröhlich for performing an independent reproduction experiment and Christian Guggenberger and Stefan Heinzel at the Max Planck Compute Center Garching for excellent support of the high-performance computing environment.

Chapter 4. Connectomic comparison of mouse and human cortex

Sahil Loomba*, Jakob Straehle*, Vijayan Gangadharan*, Natalie Heike*, Abdelrahman Khalifa*, **Alessandro Motta***, Niansheng Ju, Meike Sievers, Jens Gempt, Hanno S. Meyer, Moritz Helmstaedter.

Science (2022). DOI: 10.1126/science.abo0924

* authors **contributed equally** to this work

Contributions: Development of automated reconstruction methods, originally for an ATUM-mSEM EM volume from mouse primary somatosensory cortex (Sievers unpublished) and then adapted to SBEM datasets (figure 4-1), with Meike Sievers and Martin Schmidt and in collaboration with scalable minds GmbH. Development of methods for the analysis of axonal target distributions from automated reconstructions under consideration of error rates (figures 4-3D and 4-5H). Development of statistical model of cortical neuropil for inference of excitatory and inhibitory synapse proportions and of their respective postsynaptic target distributions (figures 4-4 and 4-5J,K).

Research article summary

Introduction

The analysis of the human brain is a central goal of neuroscience, but for methodological resons, research has focused on model organisms, the mouse in particular. Because substantial homology was found at the level of ion channels, transcriptional programs, and basic neuronal types, a strong similarity of neuronal circuits across species has also been assumed. However, a rigorous test of the configuration of local neuronal circuitry in mouse versus human—in particular, in the gray matter of the cerebral cortex—is missing.

The about 1000-fold increase in number of neurons is the most obvious evolutionary change of neuronal network properties from mouse to human. Whether the structure of the local cortical circuitry has changed as well is, however, unclear. Recent data from transcriptomic analyses has indicated an increase in the proportion of inhibitory interneurons from mouse to human. But what the effect of such a change is on the circuit configurations found in the human cerebral cortex is not known. This is, however, of particular interest also to the study of neuropsychiatric disorders, because in these, the alteration of inhibitory-to-excitatory synaptic balance has been identified as one possible mechanistic underpinning.

Rationale

We used recent methodological improvements in connectomics to acquire data from one macaque and two human individuals, using biopsies of the temporal, parietal, and frontal cortex. Human tissue was obtained from neurosurgical interventions related to tumor removal, in which access path tissue was harvested that was not primarily affected by the underlying disease. A key concern in the analysis of human patient tissue has been the relation to epilepsy surgery, when the underlying disease has required often year-long treatment with pharmaceuticals, plausibly altering synaptic connectivity. Therefore, the analysis of nonepileptic surgery tissue seemed of particular importance. We also included data from one macaque individual, who was not known to have any brain-related pathology.

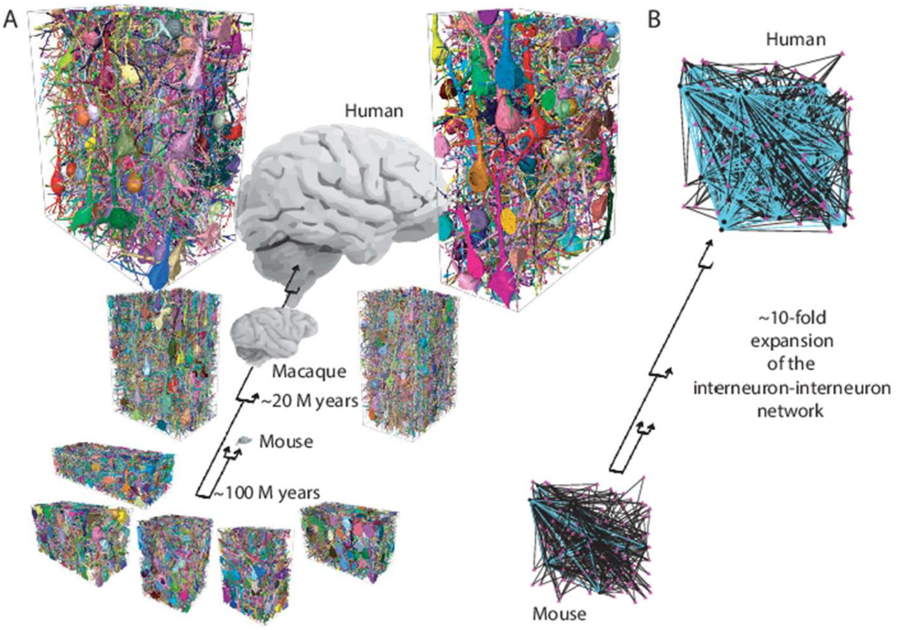

Connectomic screening across mammalian species: Comparison of five mouse, two macaque, and two human connectomic datasets from the cerebral cortex. (A) Automated reconstructions of all neurons with their cell bodies in the volume shown, using random colors. The analyzed connectomes comprised a total of ~1.6 million synapses. Arrows indicate evolutionary divergence: the last common ancestor between human and mouse, approximately 100 million years ago, and the last common ancestor between human and macaque, about 20 million years ago. **(B)** Illustration of the about 10-fold expansion of the interneuron-to-interneuron network from mouse to human.

Results

We acquired three-dimensional electron microscopy data from temporal and frontal cortex of human and temporal and parietal cortex of macaque. From these, we obtained connectomic reconstructions and compared these with five connectomes from mouse cortex. On the basis of these data, we were able to determine the effect of the about 2.5-fold expansion of the interneuron pool in macaque and human cortex compared with that of mouse. Contrary to expectation, the inhibitory-to-excitatory synaptic balance on pyramidal neurons in macaque and human cortex was not substantially altered. Rather, the interneuron pool was selectively expanded for bipolar-type interneurons, which prefer the innervation of other interneurons, and which further increased their preference for interneuron innervation from mouse to human. These changes were each multifold, yielding in effect an about 10-fold expanded interneuron-to-interneuron network in the human cortex that is only sparsely present in mouse. The total amount of synaptic input to pyramidal neurons, however, did not change according to the threefold thickening of the cortex; rather, a modest increase from about 12,000 synaptic inputs in mouse to about 15,000 in human was found.

Conclusion

The principal cells of the cerebral cortex, pyramidal neurons, maintain almost constant inhibitory-to-excitatory input balance and total synaptic input across 100 million years of evolutionary divergence, which is particularly noteworthy with the concomitant 1000-fold expansion of the neuronal network size and the 2.5-fold increase of inhibitory interneurons from mouse to human. Rather, the key network change from mouse to human is an expansion of almost an order of magnitude of an interneuron-to-interneuron network that is virtually absent in mouse but constitutes a substantial part of the human cortical network. Whether this new network is primarily created through the expansion of existing neuronal types, or is related to the creation of new interneuron subtypes, requires further study. The discovery of this network component in human cortex encourages detailed analysis of its function in health and disease.

Research article

The human cerebral cortex houses 1,000 times more neurons than the cerebral cortex of a mouse, but the possible differences in synaptic circuits between these species are still poorly understood. We used 3-dimensional electron microscopy of mouse, macaque and human cortical samples to study their cell type composition and synaptic circuit architecture. The 2.5-fold increase in interneurons in humans compared to mouse was compensated by a change in axonal connection probabilities and therefore did not yield a commensurate increase in inhibitory-vs-excitatory synaptic input balance on human pyramidal cells. Rather, increased inhibition created an expanded interneuron-to-interneuron network, driven by an expansion of interneuron-targeting interneuron types and an increase in their synaptic selectivity for interneuron innervation. These constitute key neuronal network alterations in human cortex.

The human brain, with its 86 billion nerve cells (Herculano-Houzel 2009) forming a network of unparalleled complexity, is of special interest for neuroscience. Yet, over the last 50 years, rodents (in particular the mouse) have emerged as key research subjects, offering methodological opportunities not available for the study of the human brain. Because at the molecular level, evolutionary homology is substantial for ion channels, synaptic receptors, and other key molecular constituents of the brain, similar homology has been assumed for neuronal circuits, especially in the cerebral cortex. However, comparative synaptic-resolution connectomic studies of mouse and human cortex are required to determine the degree to which circuit structure may have evolved between species.

Detailed studies of the human cerebral cortex have provided data on cellular composition of the neuropil (von Bartheld et al. 2016, Hodge et al. 2019, Krienen et al. 2020, Herculano-Houzel 2009, Letinic et al. 2002, Cajal 1899, Kooijmans et al. 2020, Berg et al. 2021, Bakken et al. 2021, Shapson-Coe et al. 2021, Field et al. 2021, Szegedi et al. 2020, Sousa André et al. 2017), synaptic properties (DeFelipe et al. 2002, Rollenhagen et al. 2020, Domínguez-Álvaro et al. 2019, Marco and DeFelipe 1997, Wang et al. 2015, Molnár et al. 2008, Melchitzky et al. 1999, Domínguez-Álvaro et al. 2021, Melchitzky and Lewis 2008, Cano-Astorga et al. 2021, Cragg 1976) and neuronal morphology (Yáñez et al. 2005, Nimchinsky et al. 1999, Boldog et al. 2018, del Río and DeFelipe 1997), yielding a comparative description with reference to rodents that indicates a larger number of glial cells (von Bartheld et al. 2016), larger synapses (Benavides-Piccione et al. 2002, Szegedi et al. 2016, Molnár et al. 2008), and more inhibitory interneurons to form the neuronal network of the human cortex (Bakken et al. 2021). This latter comparison had been confounded by rodent data reporting an interneuron fraction of 8-25%, (Micheva and Beaulieu 1995, Meyer et al. 2011, Džaja et al. 2014, Tasic et al. 2018, Hodge et al. 2019, Krienen et al. 2020, Ren et al. 1992, Beaulieu et al. 1994, Lefort et al. 2009), thus potentially on par with data from primates (range 15-37%, (Beaulieu et al. 1992, Gabbott and Bacon 1996, Hornung and De Tribolet 1994, del Río and DeFelipe 1996, Jones et al. 1994)). Recent transcriptomic data substantiates an at least 2-fold increase (Boldog et al. 2018), suggesting the balance between inhibitory and excitatory synapses to be substantially shifted towards inhibition. Furthermore, based on the about 3-fold larger extent of the dendritic trees of human pyramidal cells, it has been assumed that human cortical neurons receive substantially more synapses than those of rodents (e.g., 10,000 in rodents vs 30,000 in human, (Eyal et al. 2018, Benavides-Piccione et al. 2002, Benavides-Piccione et al. 2013, Mohan et al. 2015, Elston et al. 2001)).

However, a circuit-level analysis of human cortex that addresses the potential effect of multi-fold increased inhibitory circuit elements is still missing. Would, as a result, the inhibitory-to-excitatory synaptic balance be increased in the human cortex? Because inhibitory-to excitatory synaptic balance has emerged as a key set point that might be altered in neuropsychiatric diseases (studied primarily in

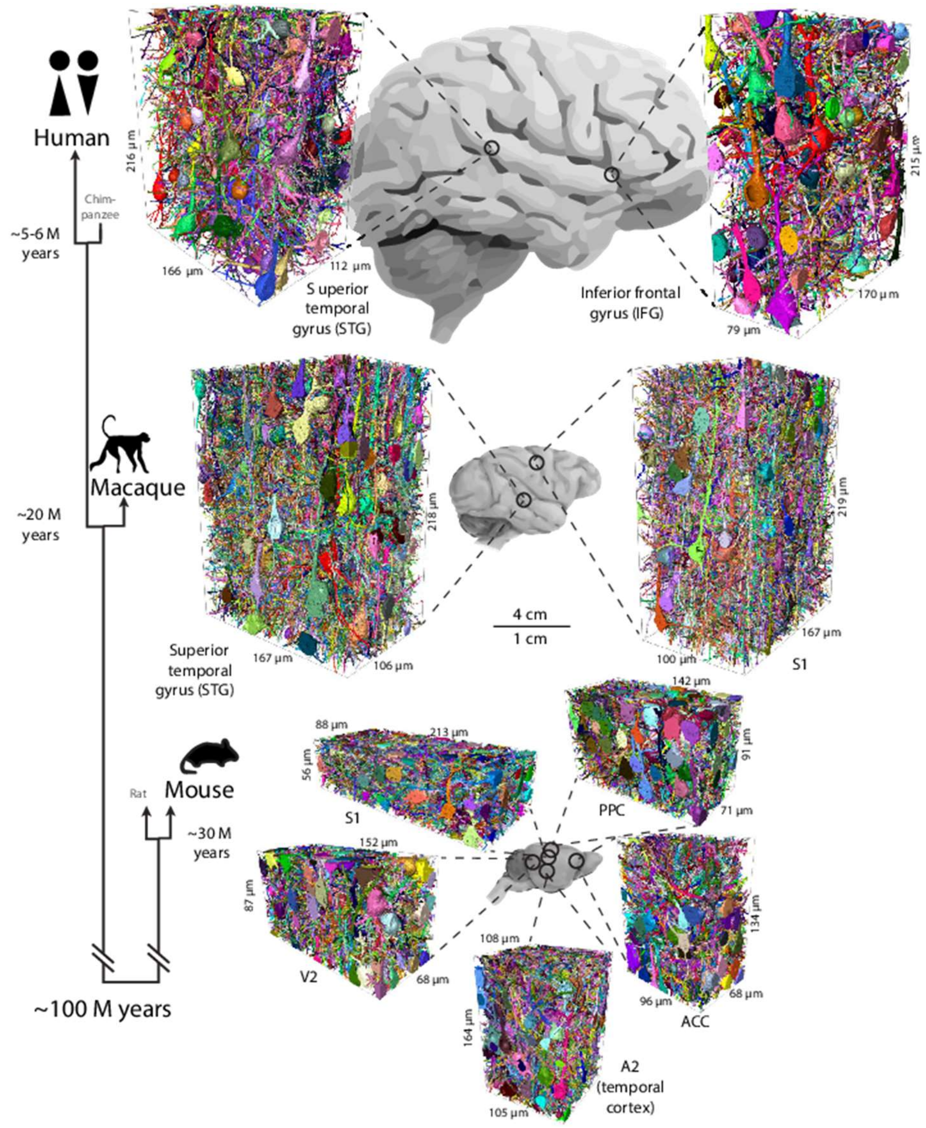

Figure 4-1 Comparative connectomic analysis of mouse, macaque and human cortex. Dense connectomic reconstructions from layer 2/3 of 5 cortical areas of mouse (bottom, n=5 individuals) and from 4 cortical areas of macaque and human (n=3 individuals). Note matched cortical areas (A2, STG) across all 3 species, and paired samples from S1 (mouse, macaque). Total of 202,954 axons and 1,618,129 million synapses analyzed (see Methods). The raw 3D EM data of mouse datasets S1, V2, PPC and ACC were previously published (Karimi et al. 2020), but not their dense reconstruction. Left, simplified phylogenetic tree (based on (Hedges and Kumar 2002)) indicating time to last common ancestor between human (Homo sapiens) and rhesus macaque (Macaca mulatta), mouse (Mus musculus). Scale bars for brain sketches. S1, primary sensory cortex; A2, secondary auditory cortex; V2, secondary visual cortex; PPC, posterior parietal cortex; ACC, anterior cingulate cortex; STG, superior temporal gyrus; IFG, inferior frontal gyrus.

mouse models, (Ramocki and Zoghbi 2008, Rubenstein and Merzenich 2003)), this question is relevant for the healthy and diseased human brain.

We used 3-dimensional electron microscopy followed by sparse and dense circuit reconstruction (Motta et al. 2019) to map the synaptic and cellular composition of layer 2/3 in mouse, macaque and human cortex. Sampling from multiple individuals and cortical regions, we screened for key connectomic alterations between mouse and human cortex, which a single dataset from a given human individual and disease condition would not have allowed (Shapson-Coe et al. 2021). While our human data was from diseased individuals who underwent neurosurgical interventions, the patients had not undergone yearlong treatment for epileptic disorders that could have substantially altered the synaptic network. By including additional data from macaque in our study, we furthermore could ensure that none of the reported effects was exclusively attributable to a diseased state of the human brain.

We determined the circuit effects of an expanded inhibitory neuron population in human cortex and obtained a quantitative picture of the human pyramidal cell synaptic input architecture.

Results

We obtained tissue samples (Figure 4-1) from the cerebral cortex of two human individuals (a 69-year-old female and an 80-year-old male) who underwent neurosurgical operations (access tissue that had to be removed during surgery and would have been discarded otherwise, see Methods) and of one rhesus macaque (Macaca mulatta, 15.6-year old male). Individual age corresponded to 83%, 102% and 52% of statistical life expectancy, respectively.

From these tissue samples, we acquired 3-D electron microscopy (EM) image datasets in cortical layer 2/3 (L2/3) using either serial blockface EM (SBEM) ((Denk and Horstmann 2004), macaque primary somatosensory cortex (S1) dataset sized 176x224x100 μm^3; superior temporal gyrus (STG) sized 175x225x108 μm^3; human (H5) STG sized 166x216x112 μm^3 and human (H6) inferior frontal gyrus sized 170x215x79 μm^3, all at a voxel size of 11.24x11.24x(28-30) nm^3) or ATUM-multiSEM ((Hayworth et al. 2014, Hayworth et al. 2006, Eberle et al. 2015), dataset human (H5) STG spanning all cortical layers, sized 1.7 mm x 2.1 mm x 28.3 µm and dataset from the same sample focused on L2/3 sized 1.1 mm x 1.1 mm x 82 µm (total 0.41 PB of data) both at a voxel size of 4x4x(35-40)nm^3). For comparison with mouse cortex, we densely reconstructed previously published 3D EM datasets from L2/3 of S1, V2, PPC and ACC cortical areas (Karimi et al. 2020) and acquired an additional dataset from mouse A2 cortex sized 115x175x109 μm^3, approximately corresponding to the location of the STG datasets from macaque and human. In the following, we report effects that were multi-fold between mouse (n=5 individuals, n=5 cortical regions) and macaque/human (n=3 individuals, n=4 cortical regions) with a focus on the direct comparison of L2/3 between mouse and human.

Inhibitory vs. excitatory neuronal composition

The fraction of nerve cells that were interneurons (INs), increased 2.5-fold between mouse and macaque/human (Figure 4-2A,B, n=88 of 734 vs. 278 of 914 neurons from n=5 mouse and n=4 macaque/human datasets pooled, $p<0.001$, see Methods, consistent with recent reports from transcriptomic cell type analyses, (Bakken et al. 2021, Krienen et al. 2020)). This change in the neuronal composition of cortical tissue could have profound effects on the synaptic input to pyramidal (excitatory) neurons (ExNs, Figure 4-2C): If all other circuit properties were unchanged between mouse and human, the inhibitory-to-excitatory balance (i/e balance) would also be 2.5-fold shifted towards inhibition compared to mouse.

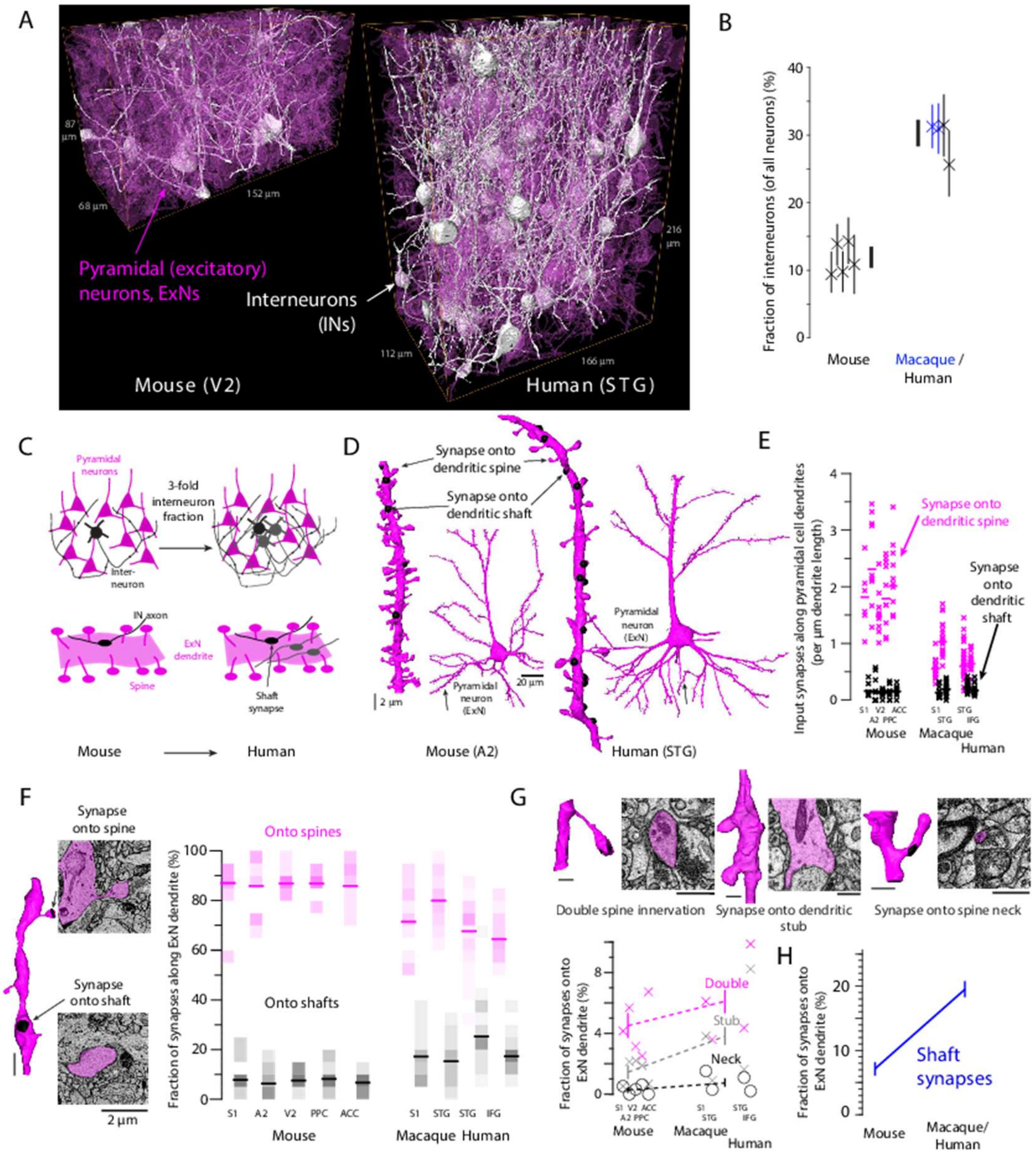

Figure 4-2 Multifold changes in cellular composition and synaptic input of mouse vs. macaque and human cortex. (A,B) Reconstruction of excitatory neurons (ExN, magenta) and inhibitory interneurons (IN, white) shows 2.54-fold expansion of the interneuron pool from mouse to macaque and human, which (C) would predict a similar-fold increase in the inhibitory input onto ExNs, which would substantially alter the set point for the inhibitory vs. excitatory synaptic input balance in human compared to mouse. (D-F) Mapping of the synaptic input to excitatory neuron dendrites (D) showed an unaltered rate of shaft input synapses (E) but a 2.65-fold decrease of spine input synapses (E), resulting in a 2.72-fold increase in the fraction of input synapses made onto dendritic shafts (F). (G) Other dendritic inputs were rare but slightly increased from mouse to macaque and human: doubly innervated spines: 4.49±0.01 vs. 4.68±0.01 and 6.91±0.01 %; stub synapses: 1.44±0.00 vs 2.17±0.01 and 4.71±0.01 %; spine neck innervations: 0.26±0.00 vs 0.84±0.00 and 0.67±0.00 %, n=1111, 598, 1040 total synapses, respectively. Insets in F,G: EM images of example synapses from Human STG multiSEM-imaged (F); Macaque STG, Human IFC and Macaque S1, respectively (left to right in G). (H) Concomitant increase of shaft synapse input could support the altered i/e balance model in C, if axonal properties remain unchanged from mouse to macaque and human, analyzed in Figs. 3 and 4. Scale bars, 1 µm unless indicated otherwise. Data in A from automated reconstructions, in B, D-H from expert reconstructions.

Synaptic inputs to pyramidal cell dendrites

We therefore first analyzed the synaptic input to pyramidal cell dendrites in mouse, macaque and human (Figures 4-2D-H). While the rate of synapses onto the dendritic shaft of pyramidal cells remained largely constant from mouse to macaque and only slightly increased in human (0.16±0.13 per µm of dendritic shaft length vs. 0.17±0.11 and 0.21±0.08; n=46, 36, 49; p=0.6 and p=.003 for mouse to macaque and mouse to human, respectively, Kolmogorov–Smirnov (KS) test; mean±s.d.; Figure 4-2D,E), synapses onto dendritic spines were 2.7-fold sparser in macaque and human (1.99±0.65 per µm of dendritic shaft length (mouse) vs. 0.86±0.36 (macaque) and 0.67±0.25 (human); mean±s.d.; n=46,36,49, respectively; $p<10^{-18}$, KS test mouse vs. macaque and human; Figure 4-2D,E). As a result, the fraction of synapses made onto the dendritic shafts of pyramidal cells (out of all input synapses to these dendrites) was increased 2.7-fold (n=1111 synapses, mouse and n=1638 synapses macaque and human, p<0.001, KS test, Figure 4-2F,H). Synaptic inputs to spine necks, stubs or double innervation of dendritic spines were rare but slightly increased in macaque and human (Figure 4-2G, see figure legend for statistics).

In mouse, synapses onto dendritic spines have been reported to be predominantly excitatory (Braitenberg and Schüz 1998, Motta et al. 2019) and synapses onto dendritic shafts predominantly inhibitory (Karimi et al. 2020, Kwon et al. 2019, Kubota et al. 2016). Therefore, the finding of a 2.7-fold increased fraction of shaft synapses could indicate a substantial shift in the set point for the i/e balance in human (as recently claimed for non-human primate (Wildenberg et al. 2021)). For this to be correct, however, the properties of excitatory and inhibitory axons, in particular their preference for establishing synapses onto dendritic shafts and spines, would have to remain unaltered between mouse and macaque and human. This we investigated next (Figures 4-3 and 4-4).

Synaptic properties of excitatory and inhibitory neurons

We first reconstructed axons of pyramidal cells and interneurons in mouse and human (Figure 4-3A-C) to determine their synaptic preferences. The rate of spine innervation showed the well-documented dichotomy in mouse (Figure 4-3A,B, see (Motta et al. 2019, Karimi et al. 2020, Kuan et al. 2020)): pyramidal cell axons targeted dendritic spines with 61.47±9.26 % (mean±s.d,) of their output synapses (n=11 axons, n=367 output synapses), while interneurons only very rarely made an output synapses as the only synapse onto a dendritic spine (n=1 of 263 IN output synapses in mouse), with no overlap between the populations. In human, however, axons reconstructed from the cell bodies of pyramidal cells made only 30.37±16.16 % (mean±s.d.) of their output synapses onto dendritic spines (n=15 axons, n=1126 output synapses), while interneurons maintained their almost complete exclusion of single spine innervation (Figure 4-3B,C; n=12 axons, n=345 output synapses, of which n=1 were single spine synapses; note that interneuron axons did however innervate dendritic spines as double innervations, in all species, as reported for subtypes of interneurons, (Kubota et al. 2007, del Río and DeFelipe 1995), see Figure A4-3; Note further that only the single spine innervation rate was used for the following analyses,). Thus the distributions of synaptic target properties between pyramidal and interneuron axons reconstructed from their cell body of origin were less separated in human (Figure 4-3B) and indicated a change in axonal synaptic preference from mouse to human.

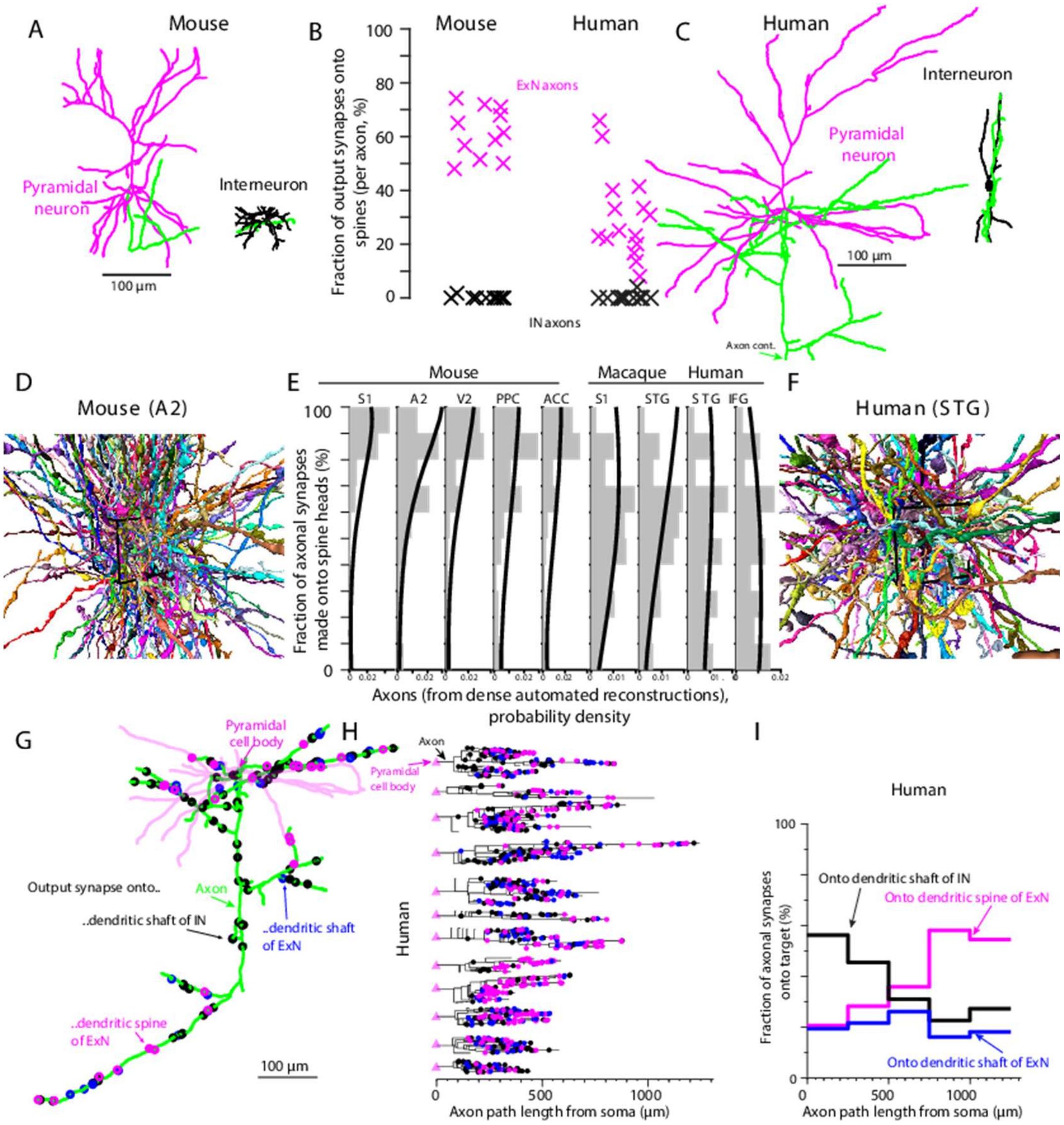

Figure 4-3 Synaptic target properties of excitatory and inhibitory neurons in mouse and human. (A-C) Axonal target properties from identified pyramidal cells and interneurons (n=50 neurons, n=2101 output synapses, cross-validated expert reconstructions, see wklink.org/7881 and wklink.org/3103 (mouse), wklink.org/9448 and wklink.org/2204 (human) for all reconstructions). Absence of single spine innervation for interneurons in mouse and human (B), but shift in spine innervation of excitatory axons from mouse to human, yielding a less separated synaptic preference of excitatory vs. inhibitory axons. (D-F) Axonal target properties from dense axonal reconstructions in mouse, macaque and human. Examples of dense axon populations from mouse A2 (D) and Human STG (F), all axons traversing boxes of 10x10x10 µm3 size shown (n=120 and n=89, respectively). Quantifications in (E) are based on all axons in the respective datasets (n=202,954 axons with 5 to 25 output synapses each; n=1,618,129 synapses). Gray, distribution of spine target fraction for all axons in the datasets, uncorrected. Black lines, average likelihood function of true spine target fraction under consideration of error rates (see methods). Broadening of axon target property distribution towards lower spine targeting in primate/human compared to mouse, that is however less pronounced than in soma-based axon reconstructions (B). (G-I) Path-length dependent axonal synapse sorting (PLASS) as a possible origin of broader axonal target property distributions in human. Example of pyramidal cell axon (G) from Human STG (path length: 3.74 mm, n=132 output synapses; same neuron as shown in C). Colors indicate synaptic target of axonal output synapses. (H,I) Distribution of axonal output synapses along pyramidal cell axons from human STG (n=15 axons, 1126 output synapses, expert reconstructions, n=12 reconstructions from mSEM dataset shown, for 3 axons from SBEM dataset see wklink.org/9448 and wklink.org/2204). Synapse symbols as in (G). Substantial increase in targeting of ExN spines over axonal path length (I). Data in A-C, G-I from expert reconstructions, D-F from dense reconstructions.

In the dense cortical neuropil, only a fraction of axons originates from neurons whose cell body is located in close proximity, while most have more distal origins. To study the target properties of all axons in the neuropil, also those without their cell body of origin in the data set, we next analyzed the dense population of axons in mouse vs. macaque and human that we obtained from the dense automated reconstructions (Figure 4-3D-F, n=202,954 axons total with n=1,618,129 output synapses). Mouse axons predominantly innervated spines (Figure 4-3E), as expected from the soma-based reconstructions (Figure 4-3B) and the small fraction of interneurons (Figure 4-2B). Densely sampled macaque and human axons, however, did not reproduce the soma-based axonal properties, but showed a broader distribution of spine innervation from 0-80% spine preference (here and in the following, spine preference implies fraction of an axon's synapses established as single spine innervations, not considering doubly innervated spines).

What could yield this difference in axonal properties between soma-based and dense reconstructions in macaque and human? In particular we needed to understand the origin of axons with >40% spine targeting in macaque and human (Figure 4-3E) that we had rarely observed in the soma-based reconstructions (Figure 4-3B). Soma-based reconstructions in datasets smaller than the complete axonal arbor bias axonal reconstructions towards local (not distally located) neurons, and to the proximal parts of these neurons' axons. When analyzing the distance-dependence of axonal targeting properties for pyramidal axons from human (Figure 4-3G-I), we indeed found evidence for a substantial change from proximal axonal preference of shaft innervation to distal preference for spine innervation along the axon's path ((Xu et al. 2020, Durand et al. 1996, Lenz et al. 2021) see (Schmidt et al. 2017) for a first report of such a path-length dependent synaptic sorting phenomenon along axons in the mammalian cerebral cortex and (Kornfeld et al. 2017, Carr and Konishi 1990) for earlier reports in the bird brain). We had to take this effect (Figure 4-3B,E,I) into account when comparing the axonal properties in these species (Figure 4-4).

Excitatory vs. inhibitory synaptic input balance

We first identified synapses onto a dendritic shaft of distal pyramidal cell dendrites and reconstructed the presynaptic axon from that synapse ("shaft-seeded" axons). Then we determined these axons' synaptic target properties based on their other output synapses (Figure 4-4A). While in mouse, as expected, axons were clearly identifiable as excitatory vs. inhibitory based on their dichotomy in spine targeting preference (Figure 4-4A), the distributions of axonal properties were much less distinct in human, recapitulating the properties of densely reconstructed axons in macaque and human (Figure 4-4A, compare to Figure 4-3B,E). Because this data did not allow the simple threshold-based classification of axons into inhibitory vs. excitatory that can be used in mouse, we needed a more rigorous approach for axon type determination (Figure 4-4C-E).

We used the notion that the various types of axons and dendrites and their synaptic output and input properties in dense cortical neuropil are ultimately constrained by the synaptic composition of this neuropil volume (Figure 4-4B). The volumetric density of synapses onto dendritic spines in the neuropil, for example, has to be composed by the intermixing of the spine preference of the various axon types present in the neuropil, and similarly for other types of synapses. Because dense 3-D EM data allowed us to concomitantly measure the properties of extended stretches of axons and dendrites together with the dense volumetric synaptic composition of the neuropil, we could determine the occurrence and target properties of excitatory and inhibitory axons without having to make prior assumptions about their relative prevalence (see methods).

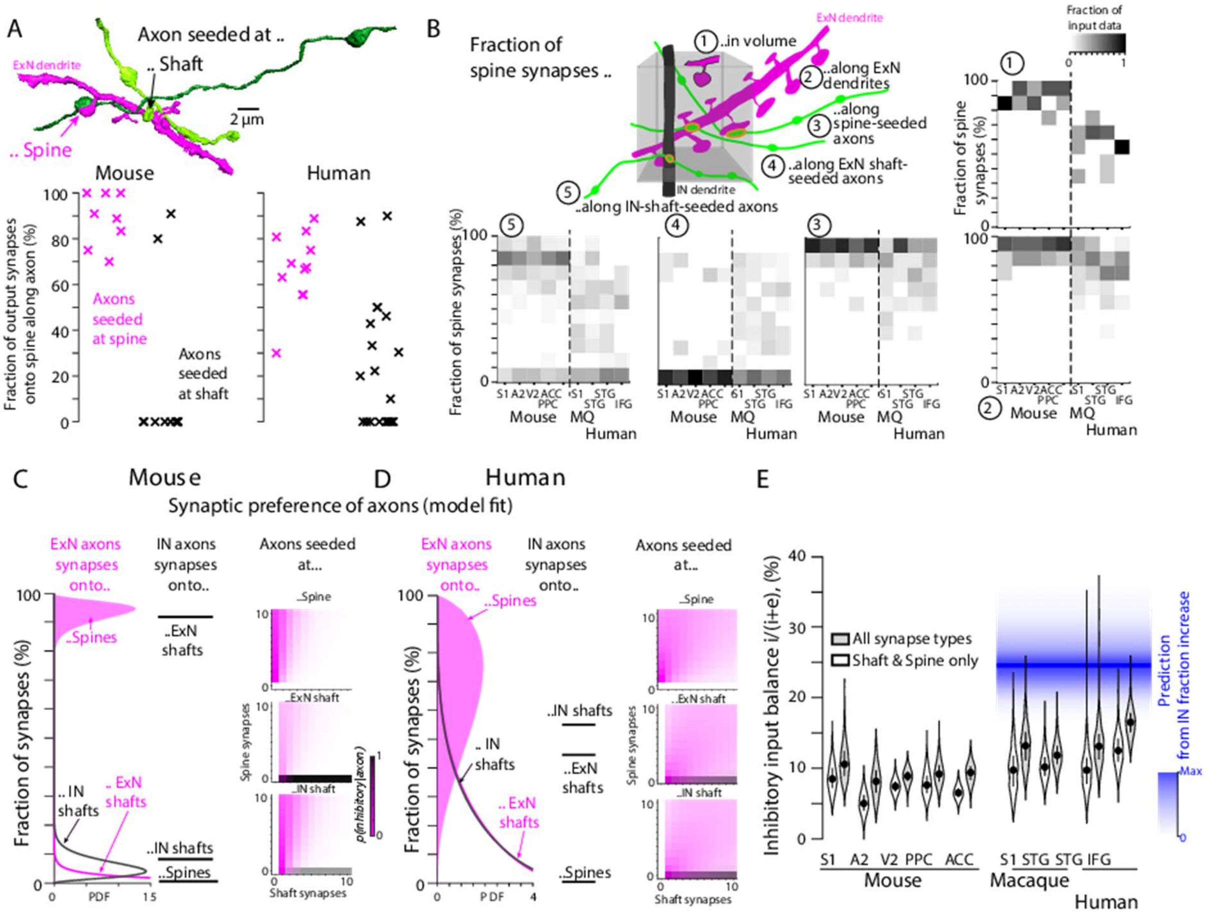

Figure 4-4 Detailed analysis of inhibitory/excitatory input balance onto ExN dendrites. (A) Target properties of axons seeded at dendritic spines and shafts of ExN dendrites in mouse and human. Top, example reconstruction (Macaque STG), bottom, data from expert reconstructions in mouse S1 and Human STG (n=91 axons, n=745 output synapses) showing shift of axonal targeting analogous to densely reconstructed axons in mouse vs. human (compare Fig. 3E). (B-D) Model incorporating dense volumetric synapse densities together with dendritic and axonal targeting properties, but not using any assumption about excitatory vs. inhibitory synapses or axons: input data (B) from expert annotations (n=754 axons, n=11,308 synapses total) that fully constrain the model (C,D) (see Results and Methods; for model validation see Figure A4-2). Shaded magenta curve: distribution of spine targeting by ExN axons; Magenta line: ExN shaft targeting by ExN axons; black line: IN shaft targeting by ExN axons; showing broadening of ExN axons' spine targeting fraction and shift of excitatory and inhibitory shaft targeting from mouse to human. MQ: macaque. (E) Resulting estimates of inhibitory input fraction (i/(i+e) balance) onto ExN dendrites in mouse, macaque and human. Violin plots represent expected inhibitory input synapse fraction along ExN dendrites (distribution across n=1000 bootstrap samples per dataset). Open shading: only shaft and single spine inputs considered; gray shading: including multiply innervated spines and other inputs, see Fig. 2G. Synaptic input balance does not approach the inhibitory bias predicted by the increased fraction of INs in macaque and human (blue shading indicates prediction from mouse to macaque and human, 24.9%±3.2% (mean±s.d.); $p<0.001$, by bootstrap sampling; see Methods). All data from expert reconstructions.

We built a model in which the synaptic properties of excitatory and inhibitory axons, and their relative prevalence were determined (Figure 4-4C,D): Inhibitory axons were modeled by a multinomial distribution based on point estimates for their synaptic target preferences, while for excitatory axons, a distribution of target preference was modeled by a Dirichlet-multinomial to account for the effects of broadened synaptic preference reported in Figure 4-3, see Methods. The model was fully constrained by the following input data, which we obtained from carefully curated expert reconstructions in all datasets (Figure 4-4B, n=11,308 synapses annotated): (1) volumetric fraction of spine synapses; (2) fraction of input synapses onto spines along spiny (ExN) dendrites; (3) fraction of output synapses onto spines along axons seeded from ExN dendritic spines; (4) fraction of output synapses onto spines along axons seeded from ExN dendritic shafts; (5) fraction of output synapses onto spines along axons seeded from IN (smooth) dendritic shafts. Note that these input data did not require a pre-hoc classification of the synapses or axons as inhibitory vs. excitatory, and did not contain the axons reconstructed from identified cell bodies (Figure 4-3A-C). With this input data, we obtained fits of the synaptic target properties of excitatory and inhibitory axons in each dataset (Figure 4-4C,D shown for mouse S1 and Human STG datasets): point estimates for the fraction of synapses made onto ExN spines, ExN shafts and IN shafts for inhibitory axons (Figure 4-4C,D) and distributions of these target fractions for excitatory axons. Together with the modeled relative prevalence of inhibitory vs. excitatory synapses, for any axonal stretch with any combination of x synapses onto shaft and y synapses onto spine, we obtain a probability of this axon to be excitatory vs. inhibitory (Figure 4-4C,D, right panels). For validation of the model, we used the soma-based axon reconstructions (Figure 4-3A-C) for which we had certainty about their excitatory vs. inhibitory property, and sampled local stretches from these ground truth axons, and asked the model to predict their excitatory vs. inhibitory character (E→I and I→E misclassification rates: 0% and 0% for mouse, 6.9% and 8.4% for primates; Figure A4-2).

We then applied the model to determine the expected inhibitory vs. excitatory synaptic properties of ExN dendrites in all datasets (Figure 4-4E, bootstrapped to account for sample size in input data, and controlled for initial conditions, see Methods). We found that the inhibitory input balance increased only moderately from 9.3%±0.8% (mean±s.d.) in mouse to 13.8%±1.4% ($p=0.001$, bootstrap sampling) in macaque and human, revoking a setting in which the inhibitory to excitatory input balance were to change in proportion to the 2.5-fold increase in IN fraction from mouse to macaque and human (Figure 4-4E, compare to Figure 4-3C; $p=0.003$; when also considering all other types of input synapses, $p<0.001$; bootstrap sampling, see Methods). Rather, the increased fraction of shaft input synapses was compensated by a change in axonal targeting properties: excitatory axons made 0.7%±0.3% of their synapses onto ExN shafts in mouse, but 12.0%±1.1% in macaque and human ($p<0.001$, bootstrap), and their IN shaft targeting changed from 4.4%±0.7% to 17.3%±1.7% ($p<0.001$, bootstrap, consistent with the automated axon reconstructions).

This lack of enhanced inhibition onto ExN dendrites was also found for the proximal input domains of pyramidal cells (axon initial segment, soma and proximal dendrites, Figure A4-1), excluding the possibility that inhibitory synapses had been redistributed towards the perisomatic domains.

These data yielded the important question where the expanded inhibitory population in human is establishing its synapses?

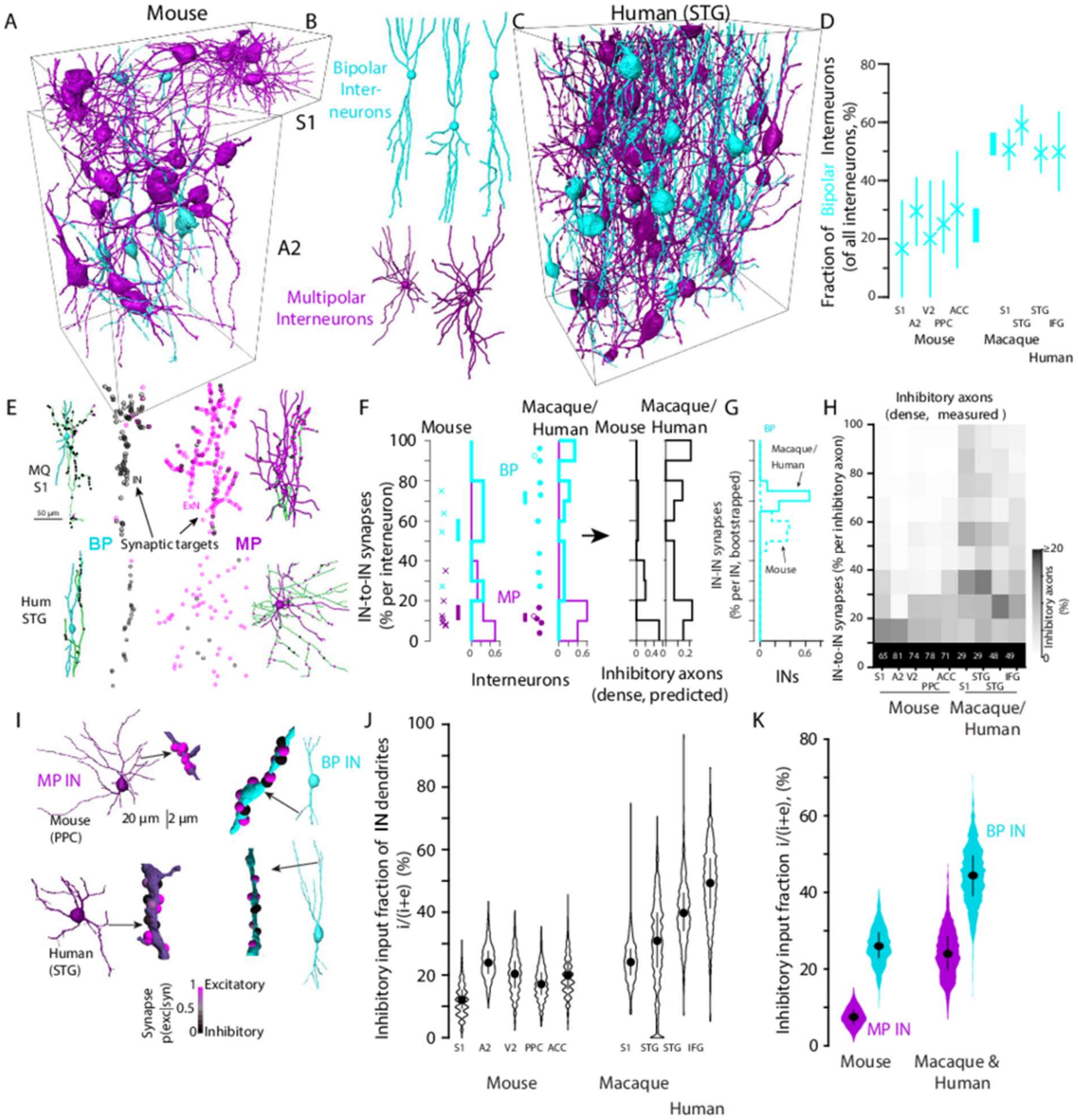

Figure 4-5 Selective expansion of interneuron types and its effect on the inhibitory-to-inhibitory network. (A-C) Dense reconstruction of all interneurons in mouse (A) and human (C) with labeling of multipolar (MP, purple, B) vs. non-multipolar (BP, bipolar, bitufted, cyan, B) interneurons showing sparsity of BP interneurons in mouse (A) compared to human (C). (D) Proportion of BP interneurons 2.3-fold expanded from mouse to macaque and human. (E) Synaptic targets of BP vs. MP interneurons in macaque and human show selectivity for inhibitory (93% of synaptic targets, left) vs excitatory (87% of synaptic targets, right) postsynaptic partners. (F) Broader distribution of interneuron innervation selectivity in macaque and human vs. mouse from soma-based axon reconstructions. This predicts expansion of inhibitory-to-inhibitory connectivity in macaque/human vs. mouse (right panels). (G) Within the BP INs, IN targeting is further enhanced (from 56.63±4.46% to 71.67±2.48%, $p<0.05$, bootstrapped from 126 and 314 synapses respectively for mouse vs macaque and human). (H) Analysis of densely reconstructed inhibitory axons and their targeting of interneuron dendrites (n=94,391 synapses, n=11,384 axons) by inference of the most likely smooth dendrite targeting probability under consideration of the error rates of automated synapse detection. Expansion of IN-to-IN connectivity as predicted from soma-based reconstructions (F). (I-K) Detailed analysis of inhibitory input balance to MP vs. BP IN subtypes across species. (I) example reconstructions of input synapses onto IN dendrites. (J) Inhibitory input determined from the model in Fig. 4 for interneuron dendrites. 2.35-fold increase from mouse to human (18.9%±2.5% to 44.5%±7.3%, mean±s.d.) consistent with the prediction from IN expansion for IN dendrites (p=0.662). (J,K) Separate analysis of inhibitory input to MP vs. BP INs reveals difference in inhibitory input already in mouse (7.6% vs. 26.2%, p=0.001) that is further enhanced in macaque and human (24.2% vs. 44.3%, p=0.026). Data in H from dense reconstructions, otherwise expert reconstructions.

Properties of the expanded inhibitory neuronal network in human

To determine the inhibitory network properties in mouse vs. human we first applied a simple IN classification based on the configuration of IN dendrites as multipolar (MP) vs. non-multipolar (which included bipolar, bitufted, vertically oriented dendritic trees, Figure 4-5A-D, labeled as "bipolar" (BP) for simplicity). The IN pool changed from dominated by multipolar INs in mouse (about 70-82% MP vs. 18-30% BP, Figure 4-5D, n=52 vs. 17) to a majority of bipolar INs in macaque/Human (53% BP; n=122 MP vs. n=135 BP, $p<0.01$, see methods for test Figure 4-5D). When mapping the synaptic target properties of these classes of INs in mouse vs. human (Figure 4-5E,F), we found a fraction of bipolar (BP) INs with almost exclusive innervation of other INs in human that was not found in mouse (Figure 4-5F,G, IN targeting by BP IN axons increased from 56% (70 IN targets out of 126 synapses, N=4 axons) to 72% (225 IN targets out of 314 synapses, N=9 axons), p=0.018, Figure 4-5G, see Methods). The changed IN pool composition together with the changed distribution of IN targeting properties would predict a substantial increase of IN-preferring inhibitory axons in the dense neuropil of human vs. mouse (Figure 4-5F). In fact, when analyzing the target preferences of inhibitory axons for smooth (IN) dendrites in mouse vs. macaque and human from the dense automated reconstructions (Figure 4-5H), we find a substantial shift towards interneuron-to-interneuron connectivity that can account for the inhibitory synapses contributed by the expanded IN pool in macaque and human (average smooth dendrite targeting probability of inhibitory axons: 8.0%±15.0% in mouse vs. 21.4%±29.0% in human; n=6565 vs. n=2048 axons; $p=2.2\times10^{-104}$, one-sided Kolmogorov-Smirnov test). Together with the increased interneuron fraction (Figure 4-2B), this would estimate the IN-to-IN network to expand 6.7-fold from mouse to human. Based on the model (Figure 4-4) we estimated the expansion to be 8.6-fold (from 1.0±0.2% IN-IN connectivity in mouse to 8.6±1.4% in macaque and human, Figure A4-2F, and Materials and Methods in appendix A4).

To better understand the contributions of types of INs to this enhanced network, we then analyzed the synaptic input balance onto IN dendrites in MP and BP-INs in mouse, macaque and human (Figures 4-5I-K). To our surprise, already in mouse, MP-INs and BP-INs have different inhibitory input balance (Figure 4-5I,K): While MP-INs receive 7.6±2.5% inhibitory input (bootstrapped mean±s.d.; n=105 axons from n=5 mouse datasets, n=977 synapses total), BP-INs receive 26.2±5.0% (n=88 axons, n=694 synapses, p=0.001). In macaque and human, MP-INs receive inhibitory input that is commensurate to the fraction of INs in the cortex (24.2±6.4%, n=69 axons from n=4 datasets, n=514 synapses; p=0.6 for scaling by IN fraction increase), while BP receive further enhanced inhibition (44.3±7.8%, n=71 axons, n=506 synapses, p=0.026). These data indicate differential inhibitory targeting across species, and may imply separate IN-to-IN circuits to be substantially enhanced in macaque and human.

Excitatory synaptic network

Finally, we wanted to determine the magnitude of the synaptic input to pyramidal cells in human cortex. With the expanded size of pyramidal cell dendritic trees, it has been assumed that human pyramidal cells receive a larger number of input synapses than mouse pyramidal cells (from about 10,000 to about 30,000, (Benavides-Piccione et al. 2002, Benavides-Piccione et al. 2013, DeFelipe et al. 2002, Elston et al. 2001, Eyal et al. 2018). Because we found a strongly reduced spine-targeting synapse density in human cortex (Figure 4-2E), we wondered what the quantitative input structure of human pyramidal cells would in fact be (Figure 4-6A,B, and Figures A4-1 and A4-4).

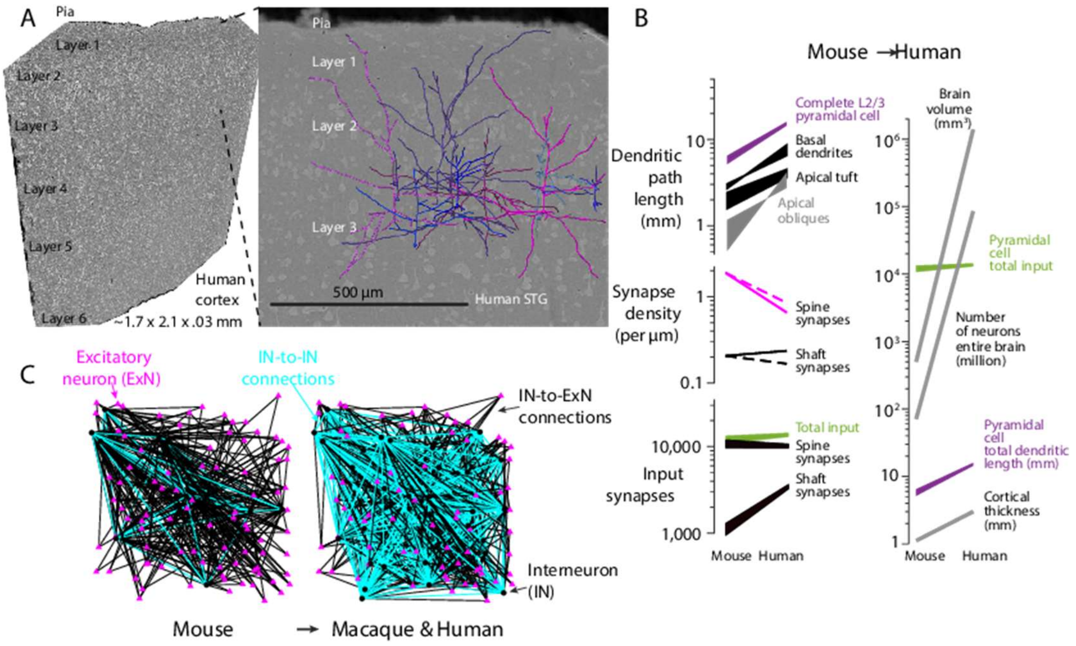

Figure 4-6 Scaling of pyramidal cell synaptic input and network properties from mouse to human. (A) Large-scale 3D EM dataset spanning all cortical layers from human cortex (STG) for reconstruction of dendritic arbors of L2/3 pyramidal neurons. (B) With about 3-fold reduced spine density from mouse to human, the about 3-fold increase in pyramidal cell dendritic path length yields only moderately increased number of input synapses for human pyramidal cells compared to mouse. Dashed lines, macaque. (C) Expanded IN-to-IN network, illustrated based on model fit (Fig. 4, Figure A4-2F, and Materials and Methods in appendix A4). Note 8.6-fold expansion of IN-to-IN connectivity from mouse to macaque and human. Data in A,B from expert reconstructions. In B right, lower limits of pyramidal cell total dendritic length and total input based on (Mohan et al. 2015), upper limits based on data in current study. Brain volume based on (Hofman 2014), number of neurons in entire brain based on (Herculano-Houzel 2009).

We used our large-scale 3D EM datasets obtained in one human individual that spanned the entire depth of cortical gray matter to reconstruct a substantial portion of L2/3 pyramidal cells. Based on these reconstructions, we extrapolated to the full extent of the dendritic tree. The large dataset extent in-plane allowed us to map some pyramidal cell dendrites in their full extent from soma to dendritic tip, and use the properties of these completely mapped dendrites for estimating the total path length of pyramidal cell dendrites in human (see Methods). The resulting estimates of total dendritic path length (about 9-20 mm path length, Figure 4-6B, Figure A4-4) were consistent with light-microscopic reconstructions (Eyal et al. 2018, Mohan et al. 2015). Because we measured synaptic input density in parallel, we could exclude a compensation of lower dendritic path length by higher spine-targeting synapse density for individual pyramidal cells. Together, total synaptic input to pyramidal cells was 12,000-17,000 in human L2/3, far below an increase corresponding to the about 3-fold thicker cerebral cortex yielding about 3-fold larger pyramidal cell dendritic trees compared to mouse (Figure 4-6B).

Discussion

The comparative analysis of mouse, macaque and human cortical neuronal networks revealed that the most substantial changes in neuronal architecture, the increase of pyramidal cell size and the numeric expansion of the interneuron pool, have not resulted in the most immediate possible circuit changes: neither an increase of total synaptic input on pyramidal cells, nor an overall shift of their synaptic input balance towards inhibition. Rather, we found an about 6-8-fold expanded interneuron-to-interneuron network in human cortex (Figure 4-6C, Figure A4-2F). These circuit alterations point towards interneuron-to-interneuron connectivity as a key evolutionary change from mouse to primates including human.

Dependence of spine rates on age

Our finding of an almost constant total synaptic input to human pyramidal cells when compared to mouse may be affected by a reported age-dependent decline of dendritic spines in cortex (Micheva and Beaulieu 1996, Calì et al. 2018, Bourgeois and Rakic 1993) which could amount to a reduction in spine density of 45-48% during puberty (Bourgeois and Rakic 1993). In fact, the human samples were from individuals in the upper quarter of expected life length. However, we found low spine rates in macaque, as well, at about 50% life expectancy. Similarly, rodents of 50-80% life expectancy show spine rates comparable to those reported here for younger mice (Karimi et al. 2020, Schmidt et al. 2017). It is therefore unlikely that age-related effects have dominated the finding of reduced spine rates in human compared to mouse. Also, while temperature-dependent changes in spine rates have been reported (Kirov et al. 2004), these are unlikely the cause of our measured spine rates (Figure 4-2E, see Materials and Methods in appendix A4 (Elston et al. 2001, Benavides-Piccione et al. 2013, Benavides-Piccione et al. 2002, Glantz and Lewis 2000, Medalla et al. 2017, Hsu et al. 2017, Gilman et al. 2017, Karimi et al. 2020, Lenz et al. 2021)).

Synaptic strength vs. synaptic number

Our data indicates the maintenance of the relative number of inhibitory vs. excitatory input synapses on the dendrites of pyramidal cells in human vs. mouse. The effective balance between inhibition and excitation could be altered by different strength of synapses. Evidence for larger unitary EPSPs and for larger synapses and presynaptic vesicle pools has been found in experiments on human cortical slices (Gidon et al. 2020, Eyal et al. 2016, Szegedi et al. 2016, Rollenhagen et al. 2020). At the same time, the impact of single inhibitory synapses is enhanced (Wang et al. 2015, Molnár et al. 2008). Whether synaptic number is a proper indicator of overall synaptic impact is a matter of investigation, with evidence in ferret (Scholl et al. 2021) pointing towards a dominant effect of synapse number, as we quantified here.

Increased complexity of inhibitory networks

The interneuron-to-interneuron network expansion found in macaque and human could have a multitude of dynamic effects. While the most immediate consequence could be a more evolved disinhibitory network capability, for example for the gating of otherwise inhibited excitatory activity (Letzkus et al. 2011, Letzkus et al. 2015), theoretical studies have also indicated possible effects on the maintenance of working memory via enhanced interneuron-to-interneuron connectivity and the ensuing network dynamics (Kim and Sejnowski 2021). Our data indicate that a detailed investigation of such phenomena is required for an understanding of human cortex. In particular, alterations in interneuron-to-interneuron connectivity should become a focus of study in the context of possible pathological alterations of human cortex.

Methods

Animal experiments and human tissue samples

All animal-related experimental procedures were performed according to the law of animal experimentation issued by the German Federal Government under the supervision of local ethics committees and according to the guidelines of the Max Planck Society. Experimental procedures were approved by Regierungspräsidium Darmstadt, AZ: F 126/1002 (mouse) and Regierungspräsidium Marburg AZ: V54 -19c 20 15 h 01 MR 13/1 Nr. 78/2012 (macaque).

The human brain tissue samples were collected during neurosurgical procedures that were indicated for medical reasons and independently from this research project at the Department of Neurosurgery at the Klinikum rechts der Isar of the Technical University of Munich. They were obtained from access tissue (i.e., presumably healthy brain parenchyma that had to be removed as part of the procedure and would have been discarded otherwise) before removal of the respective target lesions, as approved by the Ethics Committee of the Technical University of Munich School of Medicine (Ethikvotum 184/16S and 273/21 S-EB). All patients had given their written informed consent.

The macaque brain tissue sample was collected at German Primate Center (DPZ) GmbH, Göttingen.

Tissue extraction and preparation

Mouse tissue was processed and imaged as described previously ((Karimi et al. 2020, Gour et al. 2021, Motta et al. 2019). These consisted of four 3D-EM datasets from layers 2/3 of mouse somatosensory (S1), secondary visual (V2), posterior parietal (PPC) and anterior cingulate cortex (ACC) sized between 72 × 93 × 141 μm^3 and 88 x 56 x 213 μm^3 (Figure 4-1) acquired at a voxel size of 11.24–12 × 11.24–12 x 28–30 nm^3 the present study densely reconstructed and reanalyzed these published datasets from mouse, together with a newly acquired dataset from mouse secondary auditory (A2) cortex. The published mouse dataset "PPC-2" (Karimi et al. 2020) covering layers 1-5 was also used for expert reconstructions.

The human and macaque samples were processed as follows. All tissue specimen were fixed by either immersion (human) or transcardial perfusion (macaque) using an EM fixative composed of 2.5 % paraformaldehyde (Sigma), 1.25 % glutaraldehyde (Serva) and 2 mM calcium chloride (Sigma) in 80mM cacodylate buffer adjusted to pH 7.4 with an osmolarity ranging from 700 to 800 mOsmol/kg (Hua et al. 2015).

The human "H5" tissue was obtained from the right superior temporal gyrus of an 80 year old male patient during resection of a temporal mass lesion (final diagnosis: glioblastoma multiforme). After removal the sample was immersed in cold (13°C) EM fixative and transported to a nearby laboratory (transport time about 6 min). Partially submerged in cold fixative the sample was manually trimmed along the pia-WM axis and mounted on a vibratome stage. Then, submerged in cold EM fixative, the sample was cut into 500 µm thick slices with a vibratome (Leica VT 1200S). The slices were then transported in 8-12°C cooled fixative and stored over night at 4°C. The next day, samples spanning the entire cortical depth and about 1.5-1.7 mm in width were cut out and prepared for electron microscopy as described in (Karimi et al. 2020) with the modification that the sample was embedded in Epon Hard for sectioning in the ATUM. For this, samples were infiltrated through a graded series (3:1 for 4h, 1:1 12h/overnight, 1:3 for 4h) of aceton and Epon resin (Epon hard mixture: 5.9g Epoxy, 2.25g DDSA, 3.7g NMA, 205ul DMP; Sigma-Aldrich). Samples were then incubated in pure resin for 4h at room temperature, 12h/overnight at 4°, and another 4-5h at room temperature. Samples were directly embedded in pure resin on aluminium pins and kept in a pre-warmed oven (60°) for 2-3 days. Fresh resin was prepared for each incubation step.

The cured sample was trimmed into a hexagonal shape (size 3.1 mm x 1.8 mm) with a diamond milling head using an EM trimmer (Leica EM TRIM2, Leica Microsystems, Wetzlar, Germany). Next, the sample was cut into 35 nm to 40 nm thick slices at 0.3 mm s^{-1} cutting speed using a 4 mm ultra35° knife (DiATOME, Nidau, Switzerland). The ultrathin sections were collected on plasma-treated, carbon coated Kapton tape (custom-processed) with a customized ATUM-tome (RMC Boeckeler, Tucson, USA)(Hayworth et al. 2006, Hayworth et al. 2014). The tape was then mounted on silicon wafers using double-sided adhesive carbon tape (P77819-25, Science Services GmbH, Munich, Germany). In total, 7009 slices (corresponding to an extent of 270.25 µm) were cut.

The human "H6" sample was obtained from inferior frontal gyrus from a 69 year old female patient during surgical removal of frontal mass lesion (final diagnosis: glioblastoma multiforme). Following surgical removal, tissue was directly collected in fix solution kept at 4°C. The tissue was immediately sliced into 500 µm thin slices in cold fixative using vibratome. Slices were kept at 4°C overnight.

Samples were then collected using 1mm circular medical biopsy punch (covering L2/3) and prepared for SBEM as described in (Karimi et al. 2020).

The macaque sample was acquired from a 15.6 year old right handed male animal. Transcardial perfusion was performed under anesthesia (Ketamin, Xylazin) after an additional lethal dose of Barbituate (90-120 mg/kg i.v.). After flushing with ~2 l of 0.15 M cacodylate buffer (pH 7.4, duration 15 min) the perfusion solution was changed to ~2 l of EM fixative. The brain was removed and the anterior half of the brain was sectioned into 5 mm thick coronal sections. The sections were subsequently immersed in cold EM fixative, transported to the research laboratory and kept at 4°C over night. Within 48 h the tissue was further dissected (with storage in 4°C EM fixative between processing steps). A ~5 mm wide tissue block centered on the anatomically defined arm/finger region of the left postcentral gyrus (Area 3a/b) medially adjacent to the rostral end of the intraparietal sulcus was dissected. The block was placed in 0.15 M cacodylate buffer and cut along the medio-lateral axis into 600 µm thick slices using a vibratome (Microm HM650V, Thermo Scientific). Using a medical biopsy punch (KAI medicals, USA), a 1.5 mm-wide sample spanning almost the entire thickness of the cortex was cut and subsequently prepared according to the methods described in (Karimi et al. 2020)using an automated tissue processor (Leica EM AMW).

3D EM imaging and image alignment

SBEM datasets of the human (H5, H6), macaque and mouse (A2) samples were acquired using a custom-built SBEM microtome ((Denk and Horstmann 2004) courtesy of W. Denk) mounted inside the chamber of a scanning electron microscope (FEI Verios, Thermo Fisher Scientific, USA). The image acquisition and SBEM microtome were controlled using custom written software (Karimi et al. 2020). Focus and stigmation were adjusted using custom written auto-correction routines. Imaging parameters were as follows: 4x6 (macaque, H5, H6) or 3x4 (mouse A2) mosaic tiles of images sized 4096 x 3536 voxels with an in-plane voxel size of $(11.24\ \text{nm})^2$ and 30 nm nominal cutting thickness at 400 ns (macaque) or 700 ns (H5, H6, A2) dwell time with a nominal beam current of 800 pA (macaque) or 400 pA (H5, H6, A2).

Two Multi-SEM datasets of sample H5 were acquired as follows. In one experiment, 767 slices (476 at 35 nm, 291 at 40 nm) were imaged with a 61-beam MultiSEM (MultiSEM 505, Carl Zeiss Microscopy GmbH, Oberkochen, Germany) at a landing energy of 1.5 kV, a pixel size of 4 nm and a pixel dwell time of 50 ns with an FOV per slice of 1.7 mm x 2.1 mm. In a second experiment (H5_ext), 1342 additional slices (thickness 35-40 nm, corresponding to about 54 µm extent) were imaged with a smaller FOV per slice (1.1mm x 1.1mm) and aligned together with the previous experiment resulting in a total of 82 µm depth.

Image alignment for SBEM datasets was performed using global 3D relaxation of shift vectors calculated by SURF feature detection as in (Drawitsch et al. 2018) followed by subimage alignment as in (Motta et al. 2019). The aligned image volume was then saved in the webKnossos (Boergens et al. 2017) three-dimensional image format. Human STG (H5), human IFG (H6), macaque (STG) and mouse (A2) SBEM datasets were aligned by scalable minds, Postdam, see Materials and Methods in appendix A4.

Image alignment for the two multiSEM datasets from sample H5 (H5 and H5_ext) were performed similar to (Karimi et al. 2020), following the alignment routines in (Scheffer et al. 2013) and https://github.com/billkarsh/Alignment_Projects with modifications.

Cell type classification

For analyses in Figures 4-2A-B, cell bodies were manually annotated by an expert annotator in webKnossos (Boergens et al. 2017). All cell bodies were identified and classified into pyramidal cell, interneuron and glia. Pyramidal cells were identified based on presence of an apical dendrite directed towards the pia, an axon initial segment directed towards the white matter, and spiny dendrites. Interneurons were identified based on their large somata, which contained large numbers of mitochondria, an axon often exiting from a dendrite, lack of a clear apical dendrite or, if presence of an apical-like dendrite, lack of basal dendrites and WM-directed AIS, and smooth dendrites. Non-neuronal cells were distinguished primarily by their smaller cell bodies and different nuclear shapes.

For distinction of multipolar vs. bipolar INs (Figures 4-5A-D), the dendrites of all identified interneurons were reconstructed and inspected in the coronal and tangential plane (Peters 1984, Somogyi and Cowey 1981, De Lima and Morrison 1989, DeFelipe et al. 1989, DeFelipe et al. 1990, Somogyi et al. 1982, Cauli et al. 1997, Kawaguchi and Kubota 1996, Pfeffer et al. 2013). Interneurons with short dendritic lengths were excluded from this classification.

Dendrite reconstructions

Pyramidal and interneuron dendrites (Figures 4-2D-G) were reconstructed by an expert annotator by following their trajectory throughout the dataset volume and placing nodes as described previously in (Karimi et al. 2020, Gour et al. 2021). From these dendrites for which the identity of the originating cell body had been determined, a distal stretch of 3-49 µm length (mouse) and 7-44 µm length (macaque and human) was used for annotation of all input synapses.

Annotation of input synapses on dendrite, soma, axon initial segments

Analyses reported in Figures 4-2D-G and Figure A4-1 were conducted as follows. For a given postsynaptic target class (dendrites, somata, or AIS), all input synapses were identified based on the presence of a presynaptic vesicle cloud and postsynaptic density [as described in (Gour et al. 2021, Karimi et al. 2020, Schmidt et al. 2017); see following section]. These synapses were labelled as single spine when only one presynaptic bouton was found for a dendritic spine; double spine when two input synapses were found for which a clear distinction into primary (excitatory) and secondary (inhibitory) was not possible; primary spine and secondary spine when two input synapses were found for which this distinction was possible; neck for spine neck innervations, stubby spine synapses when a short dendritic protrusion of larger diameter than a spine neck and without clear diameter change at the end (i.e. no clear spine head) was synaptically innervated, and shaft synapses when the synapse was clearly placed on the main dendritic process without noticeable protrusion. Distances of synapses from the soma were measured using minimum spanning tree on the annotated nodes of the dendrites (see “skeleton” class in code repository).

Soma based axon reconstructions

Analyses reported in Figures 4-3A-C, G-I, 5E,F were conducted as follows. The axons of identified pyramidal cell and interneurons were reconstructed by first identifying the exit at the axon initial segment (AIS). Then the trajectory of the axon was followed throughout the dataset and comments were added at the outgoing synapses. The post-target of each synapse was further classified into excitatory or inhibitory class based on their spine-targeting synapse density (when target was dendritic) or cell body type (when target was a soma or an axon initial segment). Axons with fewer than 10 synapses were excluded to allow higher signal-to-noise ratio per axon.

Synapse-seeded axon reconstructions

Analyses reported in Figures 4-4A,B were conducted as follows. For a given postsynaptic target with identified input synapses, a skeleton node was placed in the presynaptic axon’s vesicle cloud and commented as “seed” synapse. The presynaptic axon was then reconstructed throughout the entire dataset volume, and all of the axons’ other output synapses and their corresponding post-synaptic targets were identified as described in the following section. The “seed“ synapse was excluded when quantifying axonal spine target properties in Figure 4-4A.

Synapse identification for reconstructed axons

For analyses reported in Figures 4-3A-C,G-I, 4-4A,B, 4-5E,F, the following synapse identification was applied. For each reconstructed axon, synapses were identified manually when following the trajectory of axon. First, vesicle clouds in the axon were identified as accumulations of vesicles. Subsequently, the most likely postsynaptic target was identified by the following criteria: direct apposition with vesicle cloud; presence of a darkening and slight broadening of the synaptic membrane; vesicles at close proximity to the plasma membrane at the site of potential synaptic contact. Synapses were marked as uncertain whenever the signs of darkened postsynaptic density could not be clearly identified. All analysis in this study were conducted only on synapses that had been classified as certain. For each axon, at every subsequent synapse location, a node was placed in the vesicle cloud and commented with the corresponding postsynaptic target’s identity (i.e., if the postsynaptic target was soma, AIS, dendritic shaft, dendritic single spine, dendritic double-innervated spine, spine neck, stub, somatic spines or filopodium). All synapses were annotated by an expert annotator; for unclear cases, these were re-annotated for expert consensus between 2-3 experts.

Volumetric model of synapse and axon types, inference of synapse and axon types, automated reconstruction and error analysis

These methods are reported in the Materials and Methods in appendix A4.

Estimates of total dendritic path length of human pyramidal cells

For the estimation of the complete synaptic input onto a L2/3 pyramidal cell (Figure 4-6A,B, and Figure A4-4), all dendrites of 10 L2/3 pyramidal cells were reconstructed until their end in dataset H5, which was either the actual ending of the dendrite in the neuropil, or the end of the dendrite at the dataset boundary (4-6A). In addition, 9 pyramidal cells in the extended dataset H5_ext were analyzed with a larger fraction of in-dataset dendrite endings. Results from both datasets yielded similar ranges for total dendritic path length estimates, as detailed in the following.

For the following calculations, only dendrites with actual in-dataset endings were used (one exception were apical tuft dendrites in which some dendrites without in-dataset endings had more branch points and were therefore included in the estimate). This approach could correspond to an underestimation of dendrite length; therefore, in addition to the length measurements described here, we also used length reports from light-microscopically imaged human L3 pyramidal neurons, which provided similar path length measurements (ranges in Figure 4-6B, (Mohan et al. 2015)).

For each pyramidal cell, the following dendritic compartments were distinguished: (i) apical dendrite trunk (measured from the exit at the cell body towards pia along the cortical axis, until the main bifurcation), (ii) apical tuft (measured from the main bifurcation point of the apical dendrite), (iii) oblique dendrites (measured from the exit at the apical dendritic trunk), and (iv) basal dendrites (all dendrites existing at the cell body except the apical dendrite) (Karimi et al. 2020).

For the basal, oblique and apical tuft compartment N=226, 211, 167 dendrites were reconstructed of which N=25, 28 and 32 dendrites with in-dataset endings were found (N=21 cells).

For the estimation of the average number of branchpoints for the apical tuft compartment dendrites without in-dataset endings were included to avoid an underestimation of dendrite length as some of them had more branch points than the dendrites with in-dataset endings. For this, all apical tuft dendrites beyond a 300µm threshold were included (N=64 dendrites, with N=32 in-dataset endings, N=21 cells).

The estimations for the lengths of the above compartments were done as follows. The length for apical dendrite trunk compartment was estimated by averaging the lengths over all the samples from their soma exit until the main bifurcation. For each of the remaining compartments (i.e. apical tufts, oblique and basal dendrites), the path lengths ("PLs") between consecutive branch points ("BPs") were measured until a true end was reached. The order of a branch point ("order") was defined as the number of edges along the unique path between it and the cell body node (e.g. order is 0 at the cell body node, 1 at first branch point, 2 at second branch point and so on). Then for the entire compartment (i.e. apical tuft, oblique or a basal dendrite), the total length was calculated by summing the path lengths of each segment times 2 to the power order of the corresponding branch point: $\sum_{order}^{BP} \quad PL_{seg\_order} * 2^{order}$ where order = order of a branch point, BP = mean number of branch points for each compartment and PL_{seg_order} = path length of the succeeding segment at the corresponding branch point order. Then, the resulting total length of each compartment was multiplied with the average number of basal, oblique or apical tuft exits to estimate lengths for all basal, oblique and apical tufts respectively. The model of the branching as binary to the final branch point order would likely overestimate total dendritic path length, thus not affecting the conclusion about low total input synapse numbers in human.

To estimate the number of input synapses for each of the dendritic compartments, we proceeded as follows. For each compartment (i.e. apical trunk, apical tuft, oblique or basal dendrite), dendritic segments of path length 10-50 µm were sampled and all input synapses were annotated. For computing the spine-targeting synapse density per dendritic shaft path length, both single spine head and primary spine head synapses were included. For shaft synapse density, only the shaft synapses were included. For total synapse density, additionally secondary spine head, spine neck and dendrite "stub" synapses were included (total fraction of these additional synapses: less than 10%). The average spine, shaft and total synapse densities were then multiplied with the total path lengths of the corresponding compartments. The apical dendrite trunk was additionally distinguished into a proximal segment (up to 50 µm from cell body) and a distal segment (50 µm from soma until the main bifurcation). Similarly, the basal dendrites were additionally distinguished into a proximal segment which showed high shaft synapse rate (up to 30 µm from cell body for mouse, 80 µm for human).

For the basal compartment we measured spine-targeting and shaft synapse densities of 0.66 ± 0.23 per µm and 0.23 ± 0.09 per µm (N=13), for the oblique compartment 0.67 ± 0.23 per µm and 0.19 ± 0.06 per µm (N=14), for the apical tuft compartment 0.73 ± 0.34 per µm (N=12) and 0.25 ± 0.07 per µm (N=12) respectively.

For the proximal segment of the apical trunk we measured spine-targeting and shaft synapse densities of 0.06 ± 0.14 per µm and 0.44 ± 0.16 per µm (N=9), for the distal segment until the main bifurcation 0.45 ± 0.39 per µm and 0.20 ± 0.08 per µm (N=7) respectively.

Statistical tests

All statistical tests were Kolmogorov-Smirnov for fractions and ratios, and Wilcoxon ranksum tests, otherwise. Data is shown as box or violin plots with median, 25th and 75th percentile and outliers (using MATLAB, Mathworks). All tests are documented in the code repository (see next section).

The test of significance for increase in interneuron fraction from mouse to macaque/human was done by pooling all identified excitatory neurons and interneurons counts per species group and generating 1000 bootstrap samples with replacement. Interneuron fraction (IN_{frac}) was computed for each bootstrap sample. The p-value was calculated as the fraction of bootstrap samples in mouse for which IN_{frac} was greater than or equal to the lowest IN_{frac} in macaque/human bootstrap group (Figure 4-2B, error bars 10th-90th percentiles). The same bootstrap approach was used as a test of significance for increase in non-multipolar IN fraction from mouse to macaque/human by pooling all multipolar and non-multipolar INs in volume per species group (Figure 4-5D, error bars 10th-90th percentiles) and similarly for testing increase of interneuron-targeting fraction of non-multipolar IN axons from mouse to macaque/human by pooling all output synapses of non-multipolar IN axons per species group (Figure 4-5F,G).

Data availability

All electron microscopy datasets are publicly available for browsing at webknossos.org:

Macaque L2/3 (S1):	https://wklink.org/1186
Macaque L2/3 (STG):	https://wklink.org/1319
Human (H5) L23 (STG):	https://wklink.org/7861
Human (H5) L23 (STG) MultiSEM:	https://wklink.org/5364
Human (H5) L1-6 (STG) MultiSEM:	https://wklink.org/1742
Human (H6) L2/3 (IFG):	https://wklink.org/7299
Mouse L2/3 (S1):	https://wklink.org/9045
Mouse L2/3 (PPC):	https://wklink.org/2581
Mouse L2 (ACC):	https://wklink.org/7415
Mouse L2/3 (V2):	https://wklink.org/3592
Mouse L2/3 (A2):	https://wklink.org/7193
Mouse L1-5 (PPC-2):	https://wklink.org/4814

Acknowledgements

We thank K Mätz-Rensing at German Primate Center and F Bremmer and A Kaminiarz at University of Marburg for providing tissue of macaque brain, anonymous individuals H5 and H6 for consent to provide tissue from neurosurgery interventions, H Wissler for support with visualizations and for management of the neuron reconstruction team, I Wolf and J Kim for staining support, A Karimi, F Drawitsch and KM Boergens for providing custom written image acquisition and alignment routines, S Babl, L Bezzenberger, R Jakoby, R Kneisl and M Kronawitter for annotator training and task management, and scalable minds, Potsdam, Germany for collaboration on automated data analysis.

Funding: Funding was provided by the Max-Planck Society. **Author contributions:** MH conceived, initiated and supervised the study. JS, NH, AMK, VG and NJ carried out experiments. HSM and JG provided human tissue. MS provided ATUM-mSEM methodology. AM developed and applied analysis methodology. SL, JS, NH, AK, VG and MH provided reconstructions and analyzed data. SL and MH wrote the manuscript with contributions from all authors. Current affiliations: Department of Neurosurgery, University Freiburg, Germany and Berta-Ottenstein Clinician Scientist Program, Faculty of Medicine, University Freiburg (JS). Institute for Beta Cell Biology, German Diabetes Center, Leibniz Center for Diabetes Research at Heinrich Heine University Düsseldorf, Düsseldorf, Germany (VG). **Competing interests:** The authors declare no competing financial interests. **Data and Materials availability:** All image data and reconstructions are publicly available through https://ww.webknossos.org/ under the links at the end of the materials and methods section. All software used for analysis is available at the following address and have been made publicly available under the MIT license. https://gitlab.mpcdf.mpg.de/connectomics/human_primate

Discussion

This thesis explored the challenges (chapter 1) and opportunities (chapters 2–4) of scaling up electron microscopy (EM)-based synapse-resolution circuit mapping (called connectomics hereafter) in the mammalian cerebral cortex. Over the last years, EM volumes from mammalian cerebral cortex increased from 80,000µm^3, corresponding to a volumetrically equivalent cube of roughly (43µm)^3, (Kasthuri et al. 2015) to around a cubic millimeter (Shapson-Coe et al. 2021, MICrONS consortium et al. 2021, Sievers unpublished). This required improvements to sample preparation and EM techniques. However, the limiting factor of EM-based connectomics was and still is the circuit reconstruction from EM image volumes (chapter 1). This is exemplified by the fact that only ~1500µm^3—less than two percent—of the aforementioned 80,000µm^3 volume from mouse somatosensory cortex were densely reconstructed (Kasthuri et al. 2015); automated reconstructions were too erroneous, and manual annotations and proofreading too laborious for substantially larger reconstructions.

In chapter 2, we have used semi-automated reconstruction methods in which manual interventions are focused onto the relatively rare locations where the automated reconstruction was likely wrong. This allowed us to efficiently and densely reconstruct ~500,000µm^3 from layer 4 of mouse primary somatosensory cortex, containing 1.8 meters of axons, more than half a meter of spine necks, and around 400,000 synapses. However, despite the extent of around 62×95×93µm^3, this EM volume was still smaller than even the small dendritic trees of spiny stellate neurons. As a result, almost none of the neurites in this EM volume could be traced to the soma of the corresponding neuron. The connectome extracted from this EM volume was thus not a neuron-to-neuron connectome, but rather a subcellular connectome. As a further consequence, the reconstructed neurites could not directly be related to known morphological cell types. However, we have demonstrated in chapter 2 how the richness of purely structural information in subcellular connectomes can be used, for example, for the definition of connectomic cell types (figure 2-4) and for a quantitative analysis of the circuit fraction that is consistent with saturated Hebbian plasticity (figure 2-7).

Subcellular and cellular target specificities

The analysis in chapter 2 illustrates that synaptic connectivity data are sufficient for identification and unbiased quantification of axons with subcellular target specificities. Subcellular target specificities of inhibitory cortical axons have previously been reported, e.g., for morphologically or molecularly defined cell types [P(subcellular target | cell type)]. But the conditioning on select cell types by these methods makes unbiased quantification of the prevalence of such target specificities difficult. In contrast, a dense connectomic reconstruction provides unbiased estimates of the distribution of synapses in the volume [P(subcellular target | synapse)] and along individual axons [P(subcellular target | axon) and P(axon)]. Together, these data allow the identification of non-random and thus of specific subcellular targeting, and the quantification of the prevalence of such axons [P(axon | subcellular targeting rate)].

Axonal target specificities in mammals have also been the subject of other connectomic studies. For example, Gour et al. (2021) used manual reconstructions in SBEM volumes from mice of six different ages to investigate the postnatal development of inhibitory subcellular target specificities. This revealed target-specific developmental timelines. Furthermore, a clever analysis of the absolute innervation rates of the various postsynaptic targets across ages indicated differential contributions of anti-specific synapse pruning and pro-specific synapse genesis. Schneider-Mizell et al. (2021) investigated the synaptic inputs onto the axon initial segment (AISs) of pyramidal neurons in layer 2/3 of mouse visual cortex and separated the presynaptic axons into likely Chandelier and likely non-

Chandelier types based on their AIS specificity. They found the number of Chandelier synapses to be highly variable across pyramidal neuron AISs, with an average contribution of around 60% of AIS synapses that is consistent with previous reports from somatosensory cortex (Gour et al. 2021). These studies still focused on subcellular target specificities; cell type-specific targeting was studied in the following two works: Karimi et al. (2020) found that inhibitory axons that innervate the main bifurcation of pyramidal neurons at the border between cortical layers 1 and 2 preferentially innervate either the bifurcations of layer 2 pyramidal neurons or these of pyramidal from deeper layers (most likely layer 3 or 5). Furthermore, in a comparably large SBEM volume from rat medial entorhinal cortex, Schmidt et al. (2017) were able to identify the postsynaptic target neurons innervated by excitatory neurons and found an axonal path length-dependent cell type specificity: preferential innervation of interneurons by the axon close to the soma, and preferential innervation of excitatory neurons more distally.

In chapter 4, we found axonal path length-dependent target specificity to be a prominent feature of layer 2/3 pyramidal neurons in the human cerebral cortex: On the most proximal ~500µm of these axons, the most likely innervated subcellular target was the dendritic shaft of interneurons (around 50% of output synapses; figure 4-3I); only >750µm from the soma were spine heads of excitatory neurons clearly the most likely subcellular target (more than 65% of output synapses) as in mouse cerebral cortex. On average, 55% of synapses in layer 2/3 of macaque and human cerebral cortex are onto spine heads of excitatory neurons. Thus, axons of pyramidal neurons in layer 2/3 of primate cerebral cortex change from anti- to pro-specificity for dendritic spines of excitatory neurons in a path length-dependent manner.

In the presence of such path length-dependent connectivity patterns, soma-based axon reconstructions in small EM volumes (relative to the entire axonal tree) result in biased connectivity estimates. Again, many such biases can be overcome by analysis of the unbiased set of all axons contained in a dense reconstruction. However, in chapter 4, an alternative approach was used:

Axons and their output synapses were reconstructed starting from synapses onto various subcellular targets (figure 4-4B). This provided estimates of the conditional target distributions P(synapse onto target Y | synapse onto target X) as in (Karimi et al. 2020, Gour et al. 2021). To estimate the prevalence of the various subcellular targets [P(target | synapse)], we have further annotated dendrites of known cell types and, importantly, of random subvolumes of cortical neuropil (figure 4-4B). Together, these data provide an unbiased estimate of the distribution of subcellular target co-innervation rates [P(synapses onto targets X and Y)]. We then modelled cortical neuropil by a mixture of two axon populations with distinct distributions of subcellular target innervation rates (figures 4-4C,D): Inhibitory axons were modelled by a multinomial distribution, whereas excitatory axons were modelled by a Dirichlet-multinomial distribution to account for the path length-dependent changes in subcellular targeting. The model parameters were derived from the above annotations by likelihood maximization. Afterwards, the probability of corresponding to an excitatory or inhibitory axon could be inferred for each of the reconstructed axon fragments (insets figures 4-4C,D), thereby providing estimates of the relative contributions of excitatory and inhibitory axons to the synapses onto pyramidal neuron dendrites (figure 4-4E). In summary, this model-based method allows the unbiased estimation of the synaptic composition of cortical neuropil, of the synaptic outputs of separate axon types, and of the synaptic inputs onto dendrites of separate dendrite types without dense, but sparse subcellular connectomic reconstructions.

Analysis of fully automated dense reconstructions

Other analyses in chapter 4 were performed on fully automated dense reconstructions (figures 4-3E and 4-5H). This was made possible by improvements in two areas compared to chapter 2:

First, more accurate, robust and efficient automated reconstructions methods were developed in collaboration with Meike Sievers, Martin Schmidt, and scalable minds GmbH for the reconstruction of a petabyte-scale ATUM-multiSEM volume from mouse primary somatosensory cortex (Sievers unpublished) and later adapted for SBEM volumes. On a random set of axons in the SBEM volume from layer 4 of mouse primary somatosensory cortex, these methods achieved an expected run length (ERL) of ~130µm. Compared to the roughly 8µm ERL achieved by the automated reconstruction methods used in chapter 2, this is a more then 16-fold improvement.

Despite this improvement, the fully automated dense reconstructions in chapter 4 still contained errors, such as false positive and false negative synapse detections, and spine synapses that were misclassified as shaft synapses and vice versa. The second improvement used in chapter 4 thus consisted of error-aware analysis methods: The error rates of synapse detection were calibrated on relatively small test volumes. On the assumption of independent errors, we then inferred for each automatically reconstructed and thus potentially flawed axon reconstruction an estimate of the true output synapse distribution. Not only did this provide an estimate of error-free axonal properties, but it also provided a quantification of the estimate's uncertainty.

Error-aware analysis methods might thus provide accurate results from flawed, but fully automated connectomic reconstructions. And because of the information richness especially of dense reconstructions, many biological analyses remain possible despite the drawback of larger uncertainty.

This has important implications. First, manual proofreading and correction of automatically generated reconstructions might be unnecessary for many biological analyses. The sensitivity to the different types and rates of reconstruction errors, and therefore the need for error-aware analysis methods, depends on the biological question. In fact, analyses of synapse size similarity in bisynaptic connections (figure 2-7) were found to produce similar results when comparing manually proofread to fully automated reconstructions, even without error-aware analysis methods (Kornfeld et al. 2020, Schmidt et al. 2022). Second, in chapter 1 we have identified accuracy and computational cost of automated reconstruction methods as limiting factors of scaling up connectomic analyses. Error-aware analysis methods could contribute to easing these burdens by reducing the demand for accuracy and by allowing for the use of less accurate, but computationally more efficient reconstruction methods.

In chapter 4, we have shown how error-aware analysis methods can contribute to scaling up connectomics to many subcellular connectomic reconstructions. This was shown at the example of "connectomic screening" of inter-species circuit differences. The same error-aware analysis approach is also applicable to connectomic screening of subcellular circuit differences across cortical layers, brain areas, age, pathologies, etc. But with recent improvements in sample preparation techniques and in EM technology, and the resulting availability of cubic millimeter-sized connectomic datasets from mouse cerebral cortex (MICrONS consortium et al. 2021, Sievers unpublished), automated analysis methods are increasingly put to the test of reconstructing neuron-to-neuron connectomes. In chapter 3, we have shown how error-aware methods could also be used in the context of circuit model selection from neuron-to-neuron connectomes.

Connectomic correlates of synaptic plasticity

In chapter 2, we have used the unprecedented size of the volumetrically dense connectomic in mammalian cerebral cortex to identify thousands of bisynaptic excitatory connections (i.e., pairs of synapses from the same presynaptic excitatory axon onto the same postsynaptic dendrite) and to derive from them upper bounds on the circuit fraction that could have been shaped by saturated Hebbian plasticity (Figure 2-7).

This analysis was based on a number of assumptions:

First, we have assumed that the structural features accessible in three-dimensional electron micrographs provide a sufficiently accurate estimate of synaptic strength (i.e., expected synaptic conductance in response to a somatic action potential). Here, the area of the axon-spine interface (ASI) was used as structural correlate of synaptic strength. This was based on experimental observations that the ASI area is proportional to the area of the postsynaptic density (PSD), which in turn is proportional to the number of AMPA receptors and to the spine head volume, which was itself correlated to the amplitude of the evoked postsynaptic potential (EPSP) through this synapse. These experiments have been review in the introduction (see “Inferences about synaptic strength and plasticity”).

Second, we have assumed that synaptic strengths are determined by an idealized version of Hebbian plasticity. Specifically, it was assumed that the synaptic strengths in a bisynaptic connection would always change in the same direction (i.e., have the same sign of change) in response to a pair of pre- and postsynaptic action potentials. This idealization ignores, for example, that action potential propagation might fail between the two synapses; that vesicular release at the two synapses is stochastic and largely independent; and that additional inhibitory synaptic inputs onto the postsynaptic spines might differentially modulate the local ion concentrations and plasticity mechanisms. These limitations are discussed below; see “Limiting and opposing factors of Hebbian plasticity”.

Third, we have assumed that synaptic strengths are constrained to a strictly positively bounded interval. In other words, synaptic strength never decreases to zero and never exceeds a finite maximum. Both the lower and upper bounds are biologically plausible: An upper bound on synaptic strength is likely imposed by the cost of maintaining the molecular machinery and resting ion concentrations for synaptic transmission. These metabolic costs must be covered by finite locally available energy sources, such as mitochondrial ATP. An argument for strictly positive minimal synaptic strength can be made based on the observation of a roughly constant number of NMDA receptors across glutamatergic synapses in the rat somatosensory cortex (Kharazia and Weinberg 1999). Thus, it could be argued that synapse-specific and plastic AMPA-mediated strengths are offset by a roughly constant and minimal NMDA-mediated synaptic strength. (However, this argument is tied to the somewhat unintuitive implication of non-zero synaptic strength at the moment of synapse elimination or generation.)

Under these assumptions, repeated LTP induction would result in both synapses in a bisynaptic connection approaching the maximal strength. And with that, the average of the two synapse strengths would converge towards the maximal strength as well. At the same time, the absolute strength difference between them would decrease. The relative difference (i.e. the ratio between the absolute strength difference and the average strength) would decrease as well. In fact, the relative difference in bisynaptic connections is proportional to the coefficient of variation (CV). Thus, repeated LTP under these assumptions would result in multi-synaptic connections converging towards synapses with high average strength and low CV (Figure 2-7A). (Even if synaptic strength were unbounded, additive LTP would lead to the same predictions. Multiplicative LTP in the absence of synaptic strength bounds would result in an increase in average synapse strength at constant CV.) Similarly, repeated LTD events would result in multi-synaptic connections converging towards configurations with low average synaptic strength and low coefficient of variation. (In general, LTD-induced strength changes must be non-linear as synapses converge towards the minimal strength. If the minimal strength is zero and is approached exponentially as a result of LTD, the average synapse strength decreases at constant CV (yellow arrows in figure 2-7A).)

Electron microscopy-based analyses of multi-synaptic connections had been previously performed in hippocampus of rats (Sorra and Harris 1993, Bartol et al. 2015, Bromer et al. 2018) and mice (Bloss et al. 2018), and in the mouse somatosensory cortex (Kasthuri et al. 2015). These analyses indicated that synapses in multi-synaptic connections had unexpectedly similar PSD areas (Sorra and Harris 1993, Kasthuri et al. 2015, Bloss et al. 2018) and spine head volumes (Sorra and Harris 1993, Bartol et al. 2015, Kasthuri et al. 2015, Bloss et al. 2018) and number of presynaptic vesicles (Kasthuri et al. 2015). Since the publication of chapter 2, over-similarity of synapse or spine head sizes have also been reported in songbird basal ganglia (Kornfeld et al. 2020) and mouse visual cortex (Dorkenwald et al. 2021).

Coefficient of variation of synapse sizes in bisynaptic connections

Bartol et al. (2015) analyzed the relationship between the average spine head volume and the CV of spine head volumes in stratum radiatum of rat hippocampus CA1 across ten bisynaptic connections. Because no correlation was detected between these two quantities, it was concluded that the CV was constant across all connections. The CV was then interpreted as measure of noise in synaptic strengths relative to the contribution of Hebbian plasticity. Based on this value and the observed range of synapse sizes, the authors concluded that the synaptic strength range consists of 26 reliably distinguishable states (at signal-to-noise ratio of 1). With this, Bartol et al. (2015) inferred a synaptic information storage capacity of $\log_2(26) \approx 4.7$ bits.

In our dense connectomic reconstruction in layer 4 of mouse primary somatosensory cortex, we have identified 5290 excitatory bisynaptic connections onto dendritic spines. Synaptic size was measured in terms of axon-spine interface (ASI) area (Desmond and Levy 1988, Cheetham et al. 2014, de Vivo et al. 2017). Consistent with previous reports, we found that synapses in bisynaptic connections were more similar in size than random pairs (Figure 2-7H). However, we found the average CV to be substantially higher (0.43) than previously reported for rat CA1 synapses (0.09; (Bartol et al. 2015)).

In part, the higher CV could be due to the use of automatically computed ASI area as measure of synapse size instead of manual and redundant annotations of spine head volumes. The automated ASI area calculation likely is less precise than manual spine head volume annotations, which were estimated to have a median error of only 1% (Bartol et al. 2015). Furthermore, spine head volume is arguably more strongly correlated to synaptic strength than ASI area: The immediate increase in synaptic currents after LTP induction was found to be associated with a near-simultaneous increase in spine head volume (Matsuzaki et al. 2004, Harvey and Svoboda 2007), but PSD-associated molecules reportedly increase with a delay of roughly one hour (Bosch et al. 2014, Meyer et al. 2014). Accordingly, spine head volume within the first hour of LTP induction was found to be larger than in control synapses with comparable PSD areas (Bosch et al. 2014, Meyer et al. 2014). Because the ASI comprises both PSD and non-PSD surface, it is unclear to what degree it follows the time courses of PSD area or spine head volume within the first hour of LTP.

More likely, however, the higher CV in layer 4 of mouse primary somatosensory cortex compared to CA1 of rat hippocampus reflects an actual difference in the contributions of Hebbian plasticity to synaptic strengths in these regions. Evidence for this comes from two lines: First, when Bartol et al. repeated the same analysis in rat dentate gyrus, a CV of 0.40 was measured (Bromer et al. 2018). Second, the high CV in mouse cerebral cortex was later corroborated by an independent study: An analysis of bisynaptic connections between pyramidal neurons in layer 2/3 of mouse visual cortex in terms of spine head volumes reported data that indicate an average CV of 0.46 (Dorkenwald et al. 2021).

Upper bounds on circuit fraction consistent with saturated Hebbian plasticity

To better understand the relationship between the coefficient of variation (CV) and the average ASI area in bisynaptic connections, we used the 5290 bisynaptic connections in our reconstructions from layer 4 of mouse primary somatosensory cortex to map this two-dimensional configuration space (Figure 2-7E). Specifically, we used kernel density estimation to calculate approximate frequencies of all configurations. For control, random permutations of the synapses in actual bisynaptic connections were used to estimate the configuration frequencies for random pairs of synapses. Consistent with previous results, the difference between actual and control configuration frequencies indicated an overrepresentation of bisynaptic connections with low CV (Figure 2-7F).

Furthermore, we noticed that the statistically overrepresented low-CV configurations could be separated into configurations with low CV and large average ASI areas and configurations with low CV and small average ASI areas (Figure 2-7F). We found that 16%–20% of bisynaptic connections have configurations with low CV and large average ASI area. Under the above assumptions, connections subjected to repeated Hebbian LTP are expected to converge onto such configurations. Thus, we concluded that at most 16%–20% of bisynaptic connections are consistent with saturated Hebbian LTP. Similarly, the 15%–19% of bisynaptic connections with low CV and small average ASI areas are, under the above assumptions, consistent with and were thus interpreted as an upper bound on connections subjected to repeated Hebbian LTD.

Synaptic plasticity *in vivo*

To date, cortical synaptic plasticity has been studied mainly *ex vivo* and in response to artificial pharmacological, electrical or sensory stimulation. Under these conditions, almost all connections between excitatory neurons have been found susceptible to the artificial induction of LTP or LTD. However, the synchronized activation of many synaptic inputs that is often used for artificial induction of synaptic plasticity stands in contrast to the sparse cortical activity observed *in vivo* (O'Connor et al. 2010). Thus, it is still largely unknown how the mechanisms of LTP and LTD operate under physiological conditions *in vivo* and to what extent they—as opposed to other mechanisms, such as molecular surface recognition, heterosynaptic or homeostatic plasticity, or random fluctuations—shape synaptic connectivity under representative sensory inputs.

The role of Hebbian plasticity *in vivo* has been studied extensively in the context of fear conditioning. In one study (Nabavi et al. 2014), a foot shock was associated with optogenetic activation of auditory afferents to the amygdala. After training, optogenetic stimulation was sufficient to evoke the conditioned response. Training also increased the ratio of AMPA- to NMDA-mediated currents, consistent with LTP induction. Subsequent low-frequency photostimulation (“optical LTD”) of the auditory afferents was found to eliminate the association. And if high-frequency photostimulation (“optical LTP”) followed optical LTD, then the association could be reinstantiated. Together, these observations were interpreted as evidence for a causal role of bidirectional Hebbian plasticity in associative memory formation in the amygdala. However, a later study reported that Hebbian plasticity was necessary but insufficient for learning a fear memory in few trials (Johansen et al. 2014). Instead, fear memory formation was found to depend on the co-activation of Hebbian plasticity and neuromodulatory processes.

In the adult cerebral cortex, learning-related synaptic plasticity has been studied predominantly in the primary motor cortex. Motor learning was found to correlate with increased rates of elimination and generation of structurally and functionally clustered dendritic spines (Yang et al. 2009, Xu et al. 2009, Fu et al. 2012, Hedrick et al. 2022). Molecular labeling of potentiated spines indicated that motor task learning was associated in layer 2/3 of mouse primary motor (M1) cortex with potentiation in roughly 2% of spines (Hayashi-Takagi et al. 2015). Spontaneous, motor learning-independent synaptic potentiation was roughly half as frequent and less stable. These studies provide first quantifications of learning related synaptic plasticity *in vivo*. "Upper bounds" on structural synaptic plasticity *in vivo* were derived in anesthetized mice by 2P glutamate uncaging at spines on the apical tuft of layer 5/6 pyramidal neurons (Noguchi et al. 2019). Spine enlargement could be induced in 22% of spines. In hippocampal slices, for comparison, spine enlargement could be induced in 95% of spines (Matsuzaki et al. 2004). Spine shrinkage could be induced at 35% of spines in the cerebral cortex, which is similar to experimental data from hippocampal slices.

Our connectomic upper bounds were derived in tissue from a briefly anesthetized and then transcardially fixative-perfused mouse and without artificial sensory stimulation. Thus, the circuit structure studied here should closely reflect the connectivity under physiological conditions. The connectomic upper bound on saturated Hebbian LTP (16%–20%) is similar to the rate of spine enlargement inducible *in vivo* (Noguchi et al. 2019), while the connectomic upper bound on saturated Hebbian LTD (15%–19%) is lower than derived *in vivo*. This might indicate that the available LTP and LTD mechanisms get activated at different rates *in vivo*. However, the difference might also reflect a difference between synaptic connections onto dendritic spines in cortical layer 4 as opposed to superficial connections onto the apical tuft of layer 5 pyramidal neurons.

Connection-specificity of synapse size and plasticity

Compared to control connections, configurations with low CV and large average ASI areas, and low CV and small average ASI areas were overrepresented by 3.6–3.9 and 3.0–3.4 percentage points, respectively. It is tempting to interpret these numbers as lower bounds on the fraction of connections shaped predominantly by saturated Hebbian LTP and LTD, respectively. However, these too might be the result of mechanisms other than Hebbian plasticity. For example, synaptic strengths might be regulated by mechanisms similar to these involved in synaptic specificity (see "Quantification of subcellular target specificities of interneurons"); synaptic strength could be regulated by recognition molecules in an activity-independent, but connection-specific manner.

In our analysis, the observed bisynaptic configurations were compared to control connections generated by random permutation of the synapses in actual bisynaptic connections. Control connections are thus based on the assumption that, in the absence of homosynaptic plasticity mechanisms, each synapse could adopt any of the observed synapse sizes. However, this assumption is violated when the set of bisynaptic connections consists of two or more types of connections with different synapse size distributions. For example, it has been argued that individual synapses between layer 4 neurons and between layer 5 neurons differ in efficacy and reliability (Feldmeyer and Sakmann 2000), which could be associated with different synapse sizes. In this case, the variance and the absolute difference of synapse sizes are smaller in actual bisynaptic connections than in random pairs of synapses from all connections.

To reduce this confounding effect in the interpretation of overrepresented low CV connections as evidence for Hebbian synaptic plasticity, we repeated the above analysis for separate connection subtypes, such as bisynaptic connections from thalamocortical axons (Figure 2-7I) or onto apical dendrites. This consistently revealed statistically significant overrepresentations of bisynaptic connections that are consistent with saturated Hebbian LTP and LTD, respectively.

The contributions of Hebbian plasticity to shaping synaptic strength might differ across connections. Indeed, pre- before postsynaptic action potentials were found to induce LTP in connections between layer 2/3 pyramidal neurons (Egger et al. 1999) and between layer 5 pyramidal neurons (Markram et al. 1997), but induced LTD in connections between layer 4 spiny stellate neurons (Egger et al. 1999). Even the output synapses of individual excitatory neurons were found to differ in short- (Markram et al. 1998) and long-term plasticity (Lu et al. 2007) depending on the postsynaptic cell types. Postsynaptically, LTP and LTD induction by spike timing dependent plasticity was found to depend on dendritic location (Froemke et al. 2005, Sjöström and Häusser 2006, Letzkus et al. 2006) and depolarization (Sjöström and Häusser 2006, Letzkus et al. 2006). Specifically, a distance-dependent shift from LTP (proximal) to LTD (distal) with depolarization-dependent conversion of LTD into LTP was observed.

Our connectomic upper bounds on saturated Hebbian LTP were found to differ across connection types: Of the bisynaptic connections onto apical dendrites, at most 10% were found to be consistent with saturated LTP. And at most 16% of thalamocortical bisynaptic connections were consistent with saturated LTP. Of corticocortical bisynaptic connections onto spiny layer 4 neurons, the fraction consistent with saturated LTP is at most 17%.

In connections between layer 4 spiny stellate neurons, dual whole-cell recordings / stimulations in slices from juvenile rat somatosensory cortex were unable to induce LTP (Egger et al. 1999). What could explain this apparent discrepancy with our data?

One hypothesis is that these connections were already saturated to the maximum connection strength. Indeed, these connections have been characterized as highly reliable and effective (Feldmeyer et al. 1999). Evidence for saturating LTP was obtained in rat motor cortex (Rioult-Pedotti et al. 2000) and in mouse visual cortex (Cooke and Bear 2010). In rat motor cortex, motor task learning was found to increase the magnitudes of evoked local field potentials and of inducible LTD and to reduce the magnitude of inducible LTP, consistent with learning-related strengthening of connections within a constant range (Rioult-Pedotti et al. 2000). Similarly, visual experience was found to increase in layer 4 of mouse visual cortex the magnitude of visually evoked potential and to reduce the magnitude of inducible LTP at thalamocortical synapses (Cooke and Bear 2010). Consistent with this hypothesis, synaptic connections between excitatory neurons in layer 4 of guinea pig visual cortex expressed both LTP and LTD after plasticity induction, with LTP associated with initially weak and unreliable connections, and LTD associated with initially strong and reliable connections (Sáez and Friedlander 2009). Interestingly, synapses that expressed neither LTP nor LTD were associated with even higher initial connection strength.

Another hypothesis regarding the apparent discrepancy is the following: Due to the limited EM volume, we were unable to distinguish in our estimation of the upper bound on saturated LTP in corticocortical connections onto spiny neurons in layer 4 between the different subtypes of presynaptic corticocortical axons or different subtypes of postsynaptic excitatory neurons. Spiny stellates make up an estimated 70%–80% of the excitatory neurons in layer 4 of mouse somatosensory cortex, with star pyramids making up the remaining 20%–30% (Lefort et al. 2009, Hua et al. 2022). The vast majority of excitatory corticocortical connections onto these neurons are thought to originate from other excitatory neurons in layer 4 (Feldmeyer et al. 1999, Schubert et al. 2003, Lefort et al. 2009). Thus, the bisynaptic corticocortical connections onto spiny neurons in layer 4 comprise at least four different types of connections. These connections might differ in terms of LTP and LTD mechanisms and of activations thereof. Furthermore, connectomic analysis of thalamocortical and local inhibitory connections in layer 4 suggests functional differences between spiny stellate and star pyramid neurons (Hua et al. 2022). This highlights the importance of large-scale EM volumes and cellular connectomes for the definition of morphological cell types and the analysis of homotypic synaptic connections.

Binary versus analog synaptic strengths

Since the publication of chapter 2, a detailed analysis of multi-synaptic connections has been performed in mouse primary visual cortex layer 2/3 (Dorkenwald et al. 2021). Because of the comparably large EM volume of 250×140×90µm^3, it was possible to identify 334 pyramidal neurons and 1735 homotypic connections between them. The distribution of synapse sizes in these homotypic connections was found to be broader than expected from a log-normal distribution, but to be fit well by a mixture of two log-normal distributions termed “S” (for small) and “L” (for large). In logarithmic space, the two distributions had similar variance. Based on this observation it was noted that synapse sizes between pyramidal neurons in mouse primary visual cortex layer 2/3 were “well-modeled by the sum of a binary variable and an analog variable drawn from a log-normal distribution (Dorkenwald et al. 2021).” Overall, 23% of synapses were estimated to be in binary state “L”.

When analyzing 160 bisynaptic connections between layer 2/3 pyramidal neurons, the average synapse size was found to be larger than the average across all synapses between these neurons. Accordingly, the proportion of synapses in binary state “L” in bisynaptic connections was 36%–42% (compared to 23% overall). In agreement with previous reports from cerebral cortex (Kasthuri et al. 2015, Motta et al. 2019), synapse sizes in these bisynaptic connections were found to be correlated. Intriguingly, however, the authors (Dorkenwald et al. 2021) found that bisynaptic connections were explained well by a model in which not the log-normal, but only the binary synapse size components were correlated. Correlation of the binary states, as quantified by the phi coefficient, was 0.64. Correspondingly, bisynaptic connections in which both synapses are in the binary “L” and “S” states were overrepresented and made up 33% and 49% of connections, respectively.

How are these percentages to be interpreted, and how do they relate to the connectomic upper bounds on LTP and LTD derived in chapter 2? Indeed, at most 33% and 49% of bisynaptic connections analyzed by Dorkenwald et al. (2021) are consistent with saturated Hebbian LTP and LTD, respectively. However, the correlation of binary states is not perfect, and the phi coefficient of 0.64 could be interpreted as fraction of bisynaptic connections shaped by homosynaptic mechanisms. Furthermore, even if binary synapse states were independent, 18% and 34% of bisynaptic connections would be expected to consist of synapses both in the “L” and “S” state, respectively. Because many potential confounders can be excluded in this analysis of homotypic synapses, it could be argued that evidence for homosynaptic up- and downregulation of binary synapse sizes can be found in 15% of bisynaptic connections, each. The expected coefficients of variation (CVs) of pairs of synapses in the same “L” and “S” states, respectively, are roughly 0.36 and 0.39. When accounting for the inferred frequencies of binary state combinations, the expected CV is 0.46. This is consistent with the average CV of 0.43 measured in our data. Analysis of this correlated mixture of log-normal distributions by the method in chapter 2 yields upper bounds on saturated LTP and LTD of roughly 29% and 39%, respectively.

A bimodal synapse size distribution has recently also been observed in SBEM volumes from stratum radiatum in CA1 of mouse hippocampus (Spano et al. 2019). Electrophysiological characterizations of CA3-to-CA1 synapses reported LTP induction to occur in a step-like all-or-none manner (Petersen et al. 1998) and found that LTP and LTD amplitudes were consistent with transitions between two discrete synaptic strengths that differ by roughly a factor of two (O'Connor et al. 2005). Furthermore, roughly 20%–30% of synapses were estimated to be of high strength under physiological conditions (O'Connor et al. 2005). However, these observations are seemingly in contradiction to electrophysiological experiments on pyramidal neurons in layer 2/3 of juvenile rat visual cortex, where LTP was found to gradually increase to saturation with increasing number of paired stimulations (Froemke et al. 2006), though the apparent gradual increase could be composed of multiple upregulations of binary synapses.

Bimodal synapse size distributions could also be the result of bi-stable activity-dependent mechanisms acting on synapses with continuous states. For example, Hebbian plasticity alone could produce bimodal synapse strength distributions if the circuit consisted of two functionally anti-correlated neuron populations (e.g., through mutual inhibition). Furthermore, a model of spike timing dependent plasticity together with a homeostatic mechanism for stable mean firing rates was able to produce both stable unimodal and bimodal synaptic strength distributions (Toyoizumi et al. 2007). Simulation of visual receptive field development in this model indicated that bimodality increased with stimulation duration and strength. Thus, competition between neurons or synapses could result in bimodal synaptic strength distributions in an activity-dependent manner.

Indeed, the circuit analyzed by Dorkenwald et al. (2021) was reconstructed from a sample of the visual cortex that prior to the EM experiment has been functionally characterized. For this, neuronal response properties were recorded by two-photon imaging of a genetically encoded calcium indicator over 4.5 hours of artificial visual stimulation (Turner et al. 2020). Plausibly, these artificial conditions induced artificial neuronal and synaptic dynamics. To exclude that the bimodal synapse size distribution underlying the claim of binary synapse states corresponds to saturated continuous-state synapses, it might be necessary to repeat the analysis in tissue from unstimulated animals.

If saturated continuous-state synapses were in fact to underlie the bimodal synapse distribution, then Dorkenwald et al. (2021) would in effect have mapped for a homotypic set of neuronal connections the range of synapse sizes. The ratio of the 99th to 1st percentiles of synapse sizes differ roughly 37.4-fold. Following the argument of Bartol et al. (2015), this range together with an average CV of 0.46 results in an estimated storage capacity of roughly 2.5 bits per synapse. While less than the estimated 4.7 bits per synapse in rat hippocampal CA1 (Bartol et al. 2015), this roughly matches the 2.7 bits of synaptic storage capacity inferred in rat dentate gyrus (Bromer et al. 2018) and, importantly, is substantially more than the upper bound of 1 bit per binary synapse. In fact, when accounting for the redundancy in correlated and thus non-uniform distribution of binary synapse states inferred by Dorkenwald et al. (2021), the information storage capacity is closer to 0.74 bits per binary synapse. (Note that these estimates ignore the roughly 0.6 bits of information encoded in the presence or absence of synapses between each pair of layer 2/3 pyramidal neurons.)

Whether cortical synapses are “digital” or “analog” thus has important implications for memory storage capacity. Beyond capacity, two important characteristics of memory storage are learning speed and memory retention durations.

Limiting and opposing factors of Hebbian plasticity

Hebbian plasticity is an activity-dependent plasticity mechanism. Thus, pre- and postsynaptic action potential firing is a necessary condition for Hebbian learning. The prediction of bisynaptic connections adopting similar (i.e., low-CV) synaptic strengths also depends on pre- and postsynaptic action potentials. As a result, the speed with which bisynaptic connections converge towards low-CV configurations might differ across brain regions or connections, depending on the mean action potential firing rates.

While necessary, pre- and postsynaptic action potential firing is insufficient for the induction of low-CV bisynaptic connections: The Hebbian drive towards low-CV connections is limited or even actively countered by opposing factors. These opposing factors include, for example, the stochasticity of presynaptic vesicle release, of diffusion of glutamate molecules across the synaptic cleft, and of these molecules binding to and opening postsynaptic AMPA and NMDA receptors. Because these stochastic processes are largely independent across synapses even in multi-synaptic connections, the lowest possible synapse size CV is strictly positive. Inhibitory co-innervation of dendritic spines in bisynaptic connections would have a similar effect.

In addition to these "passive" factors that limit the lowest possible CV, there are "active" opposing factors that increase the synapse size CV. Heterosynaptic plasticity is one such example.

Heterosynaptic synaptic plasticity was first described in CA1 of rat hippocampus (Lynch et al. 1977), only shortly after the discovery of LTP (Bliss and Lømo 1973). After LTP induction in connections from Schaffer collaterals onto apical dendrites of CA1 pyramidal neurons, the commissural connections onto the basal dendrite of these neurons were found to express LTD, and vice versa (Lynch et al. 1977). Since then, many forms of heterosynaptic plasticity have been described, with the common feature being that homosynaptic plasticity induction at one synapse also affects other, non-activated synapses. These heterosynaptic effects were recently reviewed by Jenks et al. (2021) and separated into three categories: In "compensatory" heterosynaptic plasticity, homosynaptic plasticity is often (but not exclusively) associated with opposite strength changes in other synapses. This can be mediated by modification of existing synapses or by structural plasticity (e.g., elimination or generation of synapses). In "facilitative" heterosynaptic plasticity, a homosynaptic plasticity event does not directly affect the strength of other synapses, but rather facilitates the induction of homosynaptic plasticity in them (e.g., (Harvey and Svoboda 2007)). And in "cooperative" heterosynaptic plasticity, dendritically clustered synaptic inputs express long-term plasticity in response to synchronous activation, even in the absence of a postsynaptic action potential (e.g., (Weber et al. 2016)). These heterosynaptic plasticity mechanisms were reported to operate on spatial scales of a few tens of micrometers. In the absence of synaptic clustering, the ensuing cross-talk between neighboring synapses on the same dendritic tree acts in opposition to the Hebbian alignment of strengths in multi-synaptic connections.

While heterosynaptic plasticity mechanisms operate on tens of micrometers of the dendritic tree, homeostatic synaptic plasticity is a neuron-wide mechanism that regulates the strength of input synapses to maintain a stable average action potential firing rate (Turrigiano et al. 1998, Turrigiano and Nelson 2004). Blocking of neuronal activity in cortical cultures was found to induce a compensatory increase in EPSC amplitudes, whereas blocking of GABAergic inhibition resulted in a compensatory decrease of EPSC amplitudes over two days (Turrigiano et al. 1998). Importantly, the changes in EPSC amplitudes appeared to be proportional to the initial EPSC amplitudes (Turrigiano et al. 1998). This is important because such a multiplicative synaptic rescaling—contrary to a potential additive form of homeostatic plasticity—preserves relative synaptic strengths and thus also the relative strength difference in multi-synaptic connections.

Sleep has been proposed as another mechanism of synaptic homeostasis (Tononi and Cirelli 2014). This proposal was based on experimental observations that wake and sleep are associated in the rodent cerebral cortex with net increases and decreases, respectively, in synaptic strengths as measured by EPSC amplitudes in slice preparations (Liu et al. 2010) and, in juvenile animals, in spine densities *in vivo* (Maret et al. 2011). Recently, the effects of wake and sleep on synaptic ultrastructure were investigated (de Vivo et al. 2017, Spano et al. 2019). In mouse cerebral cortex, sleep was found to be associated with a decrease in ASI areas by ~18% (de Vivo et al. 2017). However, instead of purely multiplicative rescaling of ASI areas that would preserve relative synapse sizes, the model that best explained the difference in ASI area distributions between wake and sleep was one in which the smallest 65%–90% of synapses were rescaled to around 80% of their size. ASI areas of synapses onto large spine heads and onto spine heads of dendrites with high synapse densities were found to be mostly preserved during sleep.

In summary, the induction and preservation of strengths with small relative difference (low CV) in multi-synaptic connections by Hebbian plasticity depends on sufficiently reliable mechanisms of synaptic transmission and plasticity and on sufficiently strong or frequent activation of these mechanisms to exceed the effects of opposing mechanisms, such as heterosynaptic plasticity. The observation of unexpectedly low average synapse size CVs in bisynaptic connections is indicative of connections in which Hebbian contributions to synaptic strength still exceeds these of opposing factors. However, there are different potential explanations for these observations, with two extremes described in the following.

One extreme is a fully plastic circuit in which Hebbian and opposing mechanisms are in competition at every synaptic connection. Each connection is subjected to events of Hebbian plasticity that induce a corresponding increase in relative synapse size similarity, but which is constantly being eradicated by the effects of opposing mechanisms. Because all connections are assumed equal, the upper bound on the fraction of bisynaptic connections that are consistent with saturated Hebbian plasticity is thus to be interpreted as an upper bound on the probability that Hebbian contributions outweigh these of opposing mechanisms in any given connection at any given *time*. Thus, the effect of Hebbian long-term potentiation of a synaptic connection would, generally, be short-lived. And Hebbian long-term memories would have to be constantly reinforced, potentially transferred to other synaptic connections. The other extreme is a circuit consisting of two distinct sub-circuits: one dominated by Hebbian plasticity, and one in which the contributions of Hebbian plasticity are negligible. The connectomic upper bound on the fraction of bisynaptic connections consistent with Hebbian plasticity would thus reflect the relative sizes of these sub-circuits.

Where on this spectrum a given circuit lies is difficult to assess from a single connectomic snapshot. In hippocampal CA1, the low synapse size CV on average across bisynaptic connections (Bartol et al. 2015) despite the high spine turnover (Attardo et al. 2015) and many forms of heterosynaptic plasticity (Jenks et al. 2021) is indicative of an effective Hebbian plasticity mechanisms that is activated at high rates at most connections. This is consistent with the hypothesized role of the hippocampus in the acquisition and temporary storage of episodic memories before consolidation in the cerebral cortex (Squire and Zola-Morgan 1991). In the cerebral cortex, the dichotomy of large persistent and small transient spines (Holtmaat et al. 2005) and of large stable and small down-scaling synapses during sleep (de Vivo et al. 2017) rather indicates connection-specific specialization. In the future, dense connectomic reconstructions might help to address whether the stability/plasticity of cortical connections is associated with specific neuronal connections, with proximity to inhibitory synapses or with neuromodulatory axons.

Higher-order circuit predictions of Hebbian plasticity

In chapter 2, we have interpreted the unexpected synapse size similarity in bisynaptic connections as evidence for an activity-dependent homosynaptic bidirectional plasticity mechanism, such as Hebbian plasticity. We have also noted that the synapse size similarity could be the result of confounding factors, such as connection type-specific synapse size distributions. With EM volumes sufficiently large for the reconstruction of neuron-to-neuron connectomes, it becomes possible to exclude many of these confounding factors by restricting the analysis to homotypic synapses. However, it remains unclear whether the unexpected synapse size similarity is, in fact, the result of a Hebbian plasticity mechanism or of another homosynaptic mechanism that is governed by activity-independent variables that are uniform across the presynaptic axon and the postsynaptic dendrite.

Further evidence for Hebbian plasticity could be obtained by testing higher-order circuit predictions.

Hebbian plasticity is often described as a mechanism for correlation-based learning. For example, the covariance learning rule (Sejnowski and Tesauro 1989) predicts that synaptic strength change is proportional to the correlation of pre- and postsynaptic action potential firing rates. For example, the connection strength between neurons X and Y would increase if and only if the firing rates were positively correlated ($\rho_{XY}>0$). Let us further assume that neurons *Y* and *Z* have action potential firing rates that are correlated with ρ_{YZ}. Knowing the correlations of neurons *X* and *Y*, and *Y* and *Z*, what can we say about the correlation ρ_{XZ} of action potential firing between neurons *X* and *Z*? In fact, ρ_{XZ} is bounded by $\rho_{XY}\ \rho_{YZ} \pm [(1- \rho_{XY}^2)\ (1- \rho_{YZ}^2)]^{1/2}$ (Langford et al. 2001). If synapse sizes are governed by such a correlation-based mechanism, then a synapse size-weighted neuron-to-neuron connectome should reflect this prediction of Hebbian plasticity for feedforward connections.

If such a correlation-based plasticity mechanism is the dominant determinant of synapse sizes, then, conversely, structurally inferred connection strength would be predictive of functional correlation. This, in turn, would allow connectomic tests of further plasticity-related circuit structures. For example, spatial clustering of correlated or functionally similar synaptic inputs along the dendritic tree of individual neurons has been reported in the somatosensory and visual cortex (Takahashi et al. 2012, Wilson et al. 2016) and was found to emerge as consequence of learning-related structural plasticity in motor cortex (Hedrick et al. 2022). If the purely structural data of a neuron-to-neuron connectome allows inference of functional correlations, then so would it allow testing for dendritic clustering of functionally correlated synapses and for potential causal heterosynaptic plasticity mechanisms.

In summary, the large number of synaptic and structural plasticity mechanisms and their interactions makes it challenging to study any one of these mechanisms in isolation, especially under the relevant physiological conditions *in vivo*. However, in combination, these mechanisms and their higher-order consequences put strong constraints on the synaptic connectivity. As a result, even a single connectomic snapshot in its comprehensive description of synaptic connectivity might help to test hypotheses and thereby further our understanding of dynamic processes, such as synaptic plasticity, learning and memory.

Conclusion

In this thesis, we have presented methods for the efficient semi-automated reconstruction and for the analysis of electron microscopy-based volumetrically dense connectomes from the mammalian cerebral cortex. In particular, we have proposed a method for purely connectivity-based detection of axons with evidence for above-random, specific targeting of subcellular targets. This method was used to compare the relative contributions of excitatory and inhibitory synapses to the synaptic inputs onto spiny dendrites in mouse, macaque and human. We have also proposed a method to derive upper bounds on the fraction of connections that are consistent with saturated Hebbian plasticity.

Recent advances in sample preparation techniques and electron microscopy technology have enabled the acquisition of first image volumes from the mammalian cerebral cortex that are sufficiently large for the reconstruction of neuron-to-neuron connectomes. We have reviewed this progress and discussed the limiting factors in scaling up connectomic analyses. Furthermore, a method for the inference of cortical circuit models from connectomes was described. Specifically, we have provided simulation-based evidence that statistics derived from a weighted neuron-to-neuron connectome might be sufficient to distinguish between circuits that were defined only by their functions.

Appendices

A1. Appendix to chapter 1

Methods

Data rates and dataset size (Figure 1-1a)

Macroscale connectomics (Human Connectome Project)

Data volumes were measured for scans of a randomly chosen subject of the Human Connectome Project's (Van Essen et al. 2013) "1200 subjects data release" (accessed on 21 and 22 August 2018; see https://www.humanconnectome.org/study/hcp-young-adult/document/1200-subjects-data-release for reference manual, 10 April 2018 update). Only 3T scans in uncompressed form were considered. "Ancillary files copied into multiple structural subdirectories, in order to facilitate using standardized scripts and pipelines" were ignored.

- Structural MRI: 52.4 MB over 7min 40s to 8min 24s (0.11 MB / s)
- Functional MRI:
  - Resting: 6.1 GB over 14min 33s (1.75 MB / s)
  - Task-evoked: 5 GB over 48min 46s (1.71 MB / s)
- DTI: 5.8 GB over 6 sessions of 9min 50s, each (1.64 MB / s)
- MEG: 8.1 GB over 86min (26.2 kB / s)
- Total amount of data provided by the Human Connectome Project (including 7T scans): 15.2 TB of unprocessed data, and 81.4 TB when considering raw, preprocessed and analyzed data

Mesoscale connectomics (Allen Mouse Brain Connectivity Atlas)

- Oh et al. (2014): 6 microscopes running in parallel. 750 GB of image data over 18.5h per mouse brain. 1,772 brains total (Kuan et al. 2015)
- Range of data rate: 750 GB / 18.5h corresponds to 11.3 MB / s per microscope. Effective data rate of running 6 microscopes in parallel is 67.6 MB / s.
- Total amount of data: 750 GB per brain. 1,772 brain tomographs published in Oh, Harris, Ng et al. 2014 Nature. The number of image volumes available in the Allen Mouse Brain Connectivity Atlas has since grown (e.g., (Harris et al. 2019)) and reached 2,995 as of 12 September 2018.

Nanoscale connectomics

All data sizes calculated under assumption of 8 bit / voxel.

Single-beam scanning EM (SEM)

- Conventional tiling mode (in which scanning of sample surface and stage movement are temporally non-overlapping): 0.03-0.5 MHz effective imaging speed
  - Denk and Horstmann (2004): Pixel dwell times of 25 µs and 30 µs. Corresponds to maximal effective imaging rates of 0.033 - 0.04 MHz.
  - Briggman et al. (2011): Pixel dwell times of 1.9 µs (e2198) and 5 µs (k0563). Corresponds to maximal effective imaging rates of 0.2 - 0.53 MHz.
  - Kasthuri et al. (2015): Effective imaging rate 0.5 MHz ("…scan rate was 1M pixels per s. Time is also spent …, roughly halving the overall throughput.")
  - Schmidt et al. (2017): Effective imaging rate of 0.4 MHz reported for conventional mosaic imaging

- Conventional tiling mode: 1 – 2 MHz effective imaging speed
    - Wanner et al. (2016): 2 MHz nominal imaging rate. 173×288×98 µm^3 at 9×9×25 nm^3 resolution in 32 days corresponds to 0.82 MHz effective imaging speed.
    - Kornfeld et al. (2017): 5 MHz and 2.1 MHz of nominal and effective imaging rates, respectively
    - Svara et al. (2018): Nominal imaging rate of 5 MHz reported. Estimate of effective data rate: Assuming same microscope (Zeiss UltraPlus) and per-slice overhead (62.9 s; based on in-plane area and voxel size, and raw and effective data rates) as in Kornfeld et al. (2017). Adding overhead estimate to 13.5 s of image acquisition results in 0.9 MHz effective image rate. If the overhead is linearly scaled to accommodate for the smaller field of view (74 µm vs. 166 µm), the effective data rate is 1.6 MHz.
- Continuous stage movement with simultaneous image acquisition: 6 MHz
    - Schmidt et al. (2017): 5.9 MHz effective image rate reported.
- Conventional tiling mode: 6 - 12 MHz
    - Morgan et al. (2016): Nominal imaging rate of 20 MHz reported. Effective imaging rate of 12 MHz, when ignoring microscope downtimes. Around 1 TB/days (incl. microscope maintenance, retakes, software development 100 TB / 6months) corresponds to effective imaging speed of 6 MHz over whole experiment.

Transmission EM (TEM)

- TEMCA: 1 – 5 MHz
    - Bock et al. (2011): 5-8 MHz net imaging rate (per section throughput). 450×350×52 µm^3 at 4×4×45 nm^3. 20 min for imaging a section. Estimate of effective data rate: Assume 3 sections / grid and 10 min. overhead per grid (see Zheng et al. (2018); presumably improved, thus in favor of Bock et al. 2011 Nature). This results in 4.3 - 6.9 MHz effectively.
    - Lee et al. (2016): Similar to Bock et al. (2011). 450×450×150 µm^3 at 4×4×40 nm^3. Net rate of 5-6 MHz. Estimate of effective data rate: Same assumptions as above. 4.3 - 5.1 MHz effective data rate.
- TEMCA2: 27 MHz
    - Zheng et al. (2018): TEMCA2 (used for 85 % of series): 50 MHz per-section (includes stage-movement overheads). 27 MHz per-grid (grid contains around 3 sections; includes overheads from grid-exchange and ROI definition).

Focused ion-beam – single-beam scanning electron microscopy (FIB-SEM)

- 0.035 MHz
    - Korogod et al. (2015): Reported 90s for milling and imaging a 2048×1536 px^2 slice. That's around 35 kHz effective imaging rate. Pixel dwell time is 10 µs (i.e., 0.1 MHz nominal imaging rate).
- 0.6 MHz
    - Xu et al. (2017): See below
    - Takemura et al. (2017): Around 40×50×120 µm^3 imaged at (8 nm)^3 voxel size and 1.25 MHz nominal imaging rate within 5 weeks. The Z-step size was originally 2 nm (60,000 ablation and imaging cycles), four images were then averaged in Z to get the final dataset, resulting in an effective acquisition data rate (i.e., prior to down-sampling) of about 0.6 MHz.

Multi-beam scanning EM (mSEM)

- 120 – 230 MHz effective imaging speed: 50 ns pixel dwell time per beam correspond to absolute imaging rates of up to 1.2 GHz and 1.8 GHz on 61-beam and 91-beam setups, respectively (Eberle et al. 2015). Effective imaging rates are reduced by stage movement, autofocus and autostigmation measurement, stage calibration and wafer exchange overheads. Effective imaging rates of 190 MHz (100 ns pixel dwell time per beam) and 230 MHz (50 ns pixel dwell time per beam) have been routinely achieved on a 61-beam setup at 1 s stage movement and settling time per hexagon, 12 µm inter-beam distance, and 4 nm pixel size.

Data compressibility (Figure 1-1b)

Compression factors and compression latency for nanoscale connectomics

We assume a binary connectome consisting of N neurons and 1,000 postsynaptic partners per neuron. The encoding of each connection is assumed to occupy 1 byte. All image data is assumed to be recorded at 8 bit per 4x4x35 nm^3 voxel.

Time for analysis is calculated as follows:

- Sample preparation and image acquisition: Recursive, parallel binary hot-knife partitioning (at 0.1 mm / s; (Hayworth et al. 2015)) of whole brain into a sufficiently large number of slabs for image acquisition on multiple 91-beam Zeiss multiSEM microscopes operating at (4 nm)^2 pixel size and 20 MHz sampling rate (ignoring any overheads due to, e.g., stage settling). 8 days were assumed for sample extraction, staining and embedding. Automated cutting of slabs at 35 nm thickness and collection onto tape at 10 µm / h. Farms of 8 to 128 microscopes were assumed.
- Automated data analysis: Segmentation, agglomeration, neurite type classification and synapse detection for a 0.5 x (100 µm)^3 volume of SBEM data from mouse somatosensory cortex acquired at 11.24×11.24×28 nm^3 voxel size took 4.5 days on a compute cluster of 384 cores (Motta et al. 2019). Time for these analysis steps was corrected to brain volume in question and 4×4×35 nm^3 voxel size. Compute resources of 2,304 to 191,664 CPU cores (CPU cores of IBM Summit as of August 2018; see https://www.olcf.ornl.gov/summit) at 8 GB / core and around 0.067 EUR / core hour (https://aws.amazon.com/ec2/pricing/on-demand) were assumed.
- Focused neurite reconstruction: Dense reconstruction of SBEM data from mouse somatosensory cortex required 4,000 annotator work hours (Motta et al. 2019) at 10 EUR / h. This number was adjusted for the brain volume in question. The following two annotator workforces were considered:
    - 225,000 annotators, each working every few days (2.5 times per week) for 2 hours per session (EyeWire; https://scistarter.org/eyewire), and
    - around 935,000 concurrently working annotators (corresponding to average number of concurrent players of the video game "PlayerUnknown's Battlegrounds" on Steam as of 23.08.2018; https://store.steampowered.com/stats/Steam-Game-and-Player-Statistics).

Reconstruction of whole-brain binary connectomes:

- Human brain: 86.1 billion neurons (Azevedo et al. 2009) in average brain volume of 1,191 cm^3 (Allen et al. 2002). The binary connectome is 86.1 TB in size and thus around 25 million times smaller than the 2.1 ZB of image data (at 4×4×35 nm^3 voxel size, see above). Time to analysis: 0.3 – 29 million years (96 - 229 days of sample preparation, 290 – 4,600 years of imaging, 0.3 – 29 million years of automated data analysis, 1.2 – 160 thousand years of manual proofreading).

- Mouse brain: 70.9 million neurons (Herculano-Houzel et al. 2006) in 450 mm^3 brain volume (Mikula 2016) results in a 70.9 GB connectome that is around 11 million times smaller than the 0.8 EB of image data. Time to analysis: 130 – 11,000 years (14 – 24 days of sample preparation, 40 – 640 days of imaging, 130 – 11,000 years of automated data analysis, 0.4 – 61 years of manual proofreading).
- Etruscan shrew: 11.5 million neurons (based on scaling law in Sarko et al. (2009) and brain mass of 64.4 mg from Naumann et al. (2012)) in 80 mm3 brain volume (Mikula 2016) results in 11.5 GB connectome that is 12.4 million times smaller than the 0.1 EB of image data. Time to analysis: 23 – 2,000 years (12 – 17 days of sample preparation, 7 – 114 days of imaging, 23 – 2,000 years of automated data analysis, 29 days – 11 years of manual proofreading).
- Adult fly brain: 100,000 neurons in 0.08 mm^3 brain volume (Zheng et al. 2018) results in 0.1 GB connectome that is 1.4 million times smaller than the 143 TB of image data. Time to analysis: 17 days – 2 years (8 – 9 days of sample preparation, less than 1 day of imaging, 9 days to 2 years of automated data analysis, up to 4 days of manual proofreading).
- Larval fly brain: 11,000 neurons in a brain volume 45 times smaller than that of the adult (Schlegel et al. 2017, Zheng et al. 2018) results in 11 MB connectome that is around 290 thousand times smaller than the 3.2 TB of image data. Time to analysis: 8 – 24 days (8 days of sample preparation, less than one day of imaging, up to 16 days of automated data analysis, less than one day of manual proofreading).

Light-sheet microscopy (LSM)

- Data rates: 2.8 GB / s (10 TB per hour) of raw (Liu and Keller 2016) image data.
- Compression rates: 4.5- to 60-fold live-compression reduces the data stream to 0.05 - 0.6 GB /s (Amat et al. 2015)

Multi-electrode array (MEA)

- Hildebrand et al. (2017) (“Neuropixel” probes): Two probes, each with 960 recording sites, 384 of which may be recorded simultaneously. Action potential and local field potential signals are recorded separately at 10 bits per sample, and 30 kHz and 2.5 kHz sampling rate, respectively. This corresponds to 31.2 MB / s.
- Shein-Idelson et al. (2017): Array of 26,400 electrodes. Simultaneous recording from 1,024 electrodes at 20 kHz sampling rate and 10 bits per sample yields 25.6 MB / s.
- Compression ratio: Recording spikes of 1,200 sorted units with 1-bit coding at 0.5 ms temporal resolution uses 300 kB / s. This is corresponds to 85-fold compression.
- Compression delay: Spike sorting is typically performed offline and roughly at the same speed as data acquisition (Wouters et al. 2018). The compression delay thus roughly corresponds to typical experiment durations of one hour.

Genome sequencing

- Illumina NovaSeq 6000 (https://www.illumina.com/systems/sequencing-platforms/novaseq/specifications.html): 6 trillion bases read in 36 – 45 hours, two bits per base results in a data rate of 10.3 MB / s.
- Total data volume predicted for year 2025: 40 EB (Stephens et al. 2015)

CERN

- Data rate and compression factor: 12.3 PB of data stored in October 2017 (https://home.cern/news/news/computing/breaking-data-records-bit-bit) corresponding to an average rate of 4.6 GB / s. Only 100 – 200 out of 600 million events per second are stored. The raw data rate is thus around 18.4 PB / s.

- Compression delay: Events are discarded live using software- and hardware-based filters (https://home.cern/science/computing/processing-what-record).
- Total data volume: 200 PB as of 29 June 2017 (https://home.cern/news/news/computing/cern-data-centre-passes-200-petabyte-milestone)

Retina

- Data rate: Two retinae with 1.19 million retinal ganglion cells, each (average of 1.07 million in (Curcio and Allen 1990) and 1.31 million in (Harman et al. 2000)), and 8.75 bits / s per retinal ganglion cell (Koch et al. 2006) results in around 2.6 MB / s.
- Total data volume: 70 year lifetime with 16 waking hours per day results in 3.8 PB of visual input.

Estimates for human brain nanoscale connectome (Figure 1-2a)

EM imaging: Human brain volume of 1,191 cm^3 at 20 MVx/s effective imaging speed per beam, 4x4x35 nm^3 voxel size yields 3.4 million electron beam years. Allowing 1 billion EUR cost over 5 years yields required cost per 20MVx/s electron beam of 1,470 EUR, about 30-fold less than current mSEM setups (and bout 60-100-fold less than current TEM setups).

Computational cost: Extrapolating from (Motta et al. 2019) (which is at least as efficient than Januszewski et al. (2018)) yields 5.8*10^{14} CPU core hours at 0.067 EUR per core hour (current amazon web service (AWS) rates for the required memory allocation of 12GB RAM/core), i.e. 3.9*10^{13} EUR, thus about 4*10^4 –fold reduction needed to process at a budget of 1 billion EUR for one human brain.

Human annotation cost: Extrapolating from Motta et al. (2019), 10^{13} human work hours would be required, i.e. about 10^{14} EUR cost, thus a factor of 10^5 above a putative investment of 1 billion EUR. Note that this investment currently yields remaining error rates that are about 10^3 -10^4 off the size of single human neurons. So far, human annotation accuracy has been boosted by redundant annotation (Helmstaedter et al. 2011), with a factor of 10-50 for a 10^3 accuracy improvement, which may however saturate. This would yield a required factor of 10^6-10^7 for plausible human annotation cost improvement (Figure 1-2a). However, when accuracy reaches a level at which a substantial fraction of neurons is error-free, human annotation may become entirely dispensible since statistics over neurons can be applied. For human neurons (1-10 cm cable length), this accuracy is about a factor of 10^3-10^4 from today's results.

Label usage (Figure 1-2b)

The "label fraction" for convolutional neural networks (CNNs) is calculated under the assumption of 1 vx^3 output volumes. Such CNN configurations are provided with one label per input volume during training. The label fraction thus corresponds to the inverse of the number of voxels in the CNN's (theoretical) field of view.

- SegEM (Berning et al. 2015): 279 million labeled voxels in training set. Field of view of SegEM architecture is 51×51×21 vx^3, resulting in a "label fraction" of 1.8 × 10^{-5}.
- Flood-filling networks (FFN; Januszewski et al. (2018)): 131 million labeled voxels in training set. Field of view of FFN network (ignoring information flow due to recursive application) is 37×37×25 vx^3, resulting in a label fraction of 2.0 x 10^{-5}.
- Membrane detection of SyConn (Dorkenwald et al. 2017): 6 × 13.5 µm^3 of label volume in training data. At 9x9x20 nm^3 voxel size this corresponds to 50 million labeled voxels.

- SynEM (Staffler et al. 2017): Training set consists of 150,766 labeled interfaces. The largest of these was 861,001 vx in size, resulting in a label fraction of 1.2×10^{-6}.
- Synapse detection in Parag et al. (2018) (ignoring pruning network): Training volume of “rat cortex” dataset consists of around 5 million labeled voxels (97 images, each assumed to be $(228\ \text{px})^2$ in size). Field of view of $89 \times 89 \times 29\ \text{vx}^3$ corresponds to label fraction of 4.4×10^{-6}.
- Infant learning the concept of a tree: Around 77 TB of visual input at 1.5 years of age (assuming 15 waking hours per day and visual input rate of 2.6 MB / s; see “data rates” section). 4 % of (unlabeled) visual input is assumed to be trees. The label “tree” is given ten times, resulting in a label fraction of 3.2×10^{-12} labels per unlabeled byte.

A2. Appendix to chapter 2

Materials and Methods

Subimage alignment

To further improve the precision of image alignment, which we found to critically impact the quality of the automated volume segmentation, we performed the following steps. Each image of the raw dataset was cut into smaller images sized 256x256 pixels each. The offset calculation was run as described above (with the shift between neighboring subimages from the same original image set to zero). Additionally, we used a mask for blood vessels and nuclei (see below) to determine images which mostly contained blood vessels or somata. These images were assigned a decreased weight in the relaxation step. After the least-square relaxation, the shifts obtained for the subimages were used to create a smooth non-affine morphing of the original images, which were then exported to the 3D KNOSSOS format as above. All raw image data is available for inspection at demo.webknossos.org (see section on data availability). All code used for image alignment is available at https://gitlab.mpcdf.mpg.de/connectomics/L4dense

Blood vessel detection and correction for brightness gradient

Blood vessels were detected (Figure A2-1) by automated identification of regions of at least 0.125 µm^2 with extreme brightness values (below 50 or above 162 at 8 bit depth) in each image plane, followed by manual inspection to exclude false positives. Image voxels within blood vessels were assigned the mean brightness of the entire dataset (mean=121).

To correct brightness gradients across the image volume, the mean brightness was calculated for non-overlapping image blocks of 64 x 64 x 29 vx^3, respectively, and the resulting marginal brightness distributions along the X, Y, and Z axes were smoothed and used to assign a multiplicative correction factor to each image block. The correction factor was linearly interpolated and multiplied to the brightness value of all non-blood vessel voxels within each of the image blocks.

Nuclei and myelin detection

For the automated detection of nuclei and myelin, the following heuristics were applied. First, the voxel-wise brightness gradient was computed in the image data after smoothing by a 3-D kernel of size 21 x 21 x 9 vx and a standard deviation of ~33.5 nm. Nuclei were identified as regions of at least about 1.8 µm^3 in size with small brightness gradient and image brightness close to the mean image brightness. Myelin was detected as regions of low brightness sized at least about 0.35 µm^3. Both nuclei and myelin detection were applied on overlapping image volumes of 912 x 912 x 416 vx^3 size which were then truncated to non-overlapping volumes of 512 x 512 x 256 vx^3 size, yielding a 3D "soma map" and "myelin map". The relevant code files at https://gitlab.mpcdf.mpg.de/connectomics/L4dense are additionalHeuristics.m, localDetectionMyelin.m and localDetectionNuclei.m in the preprocessing/ folder.

Volume segmentation using SegEM

To generate an initial automated volume segmentation, SegEM (Berning et al. 2015) was applied to image data cubes of size 1024 x 1024 x 512 vx^3 with 256, 256, and 128 vx overlap along X, Y, and Z, respectively, using CNN 20130516T2040408,3 with parameters θ_{ms} = 10 vx and θ_{hm} = 0.25 (see Table 1 in (Berning et al. 2015)). At the edge of myelinated regions (see previous section), the CNN output was replaced with the minimum output value of -1.7 to enforce splits during the subsequent watershed-based volume segmentation. The employed computational routines can be found at https://gitlab.mpcdf.mpg.de/connectomics/L4dense in +Myelin/enforceMyelinSegments.m and segmentation/segmentForPipeline.m.

Segmentation neighborhood graph

For the determination of neurite continuity and synaptic interfaces (Figure 2-2B,E), a segment neighborhood graph (region adjacency graph) was constructed in each of the non-overlapping segmentation cubes created by the SegEM step (see previous section). The neighborhood graph was constructed as in SynEM (Staffler et al. 2017). Briefly, two volume segments were called adjacent if there was a boundary voxel that contained both segments in its 26-neighborhood. The borders between adjacent segments were calculated as the connected components of all boundary voxels that had both segments in their 26-neighborhood. For each border, an edge between the corresponding segments was added to the neighborhood graph. The segment neighborhood graph is thus an undirected multigraph.

To extend the neighborhood graph beyond the non-overlapping segmentation cubes, pairs of segmentation cubes that shared a face in the x, y or z-direction were considered, and segments in the juxtaposed segmentation planes from the two segmentation cubes were matched if the number of matched voxels for a given pair of segments in the two planes was at least 10, and if the matched voxels constituted more than 90% of the area of the smaller segment. In these cases, an edge between the corresponding segments from the neighboring segmentation cubes was added to the neighborhood graph.

The employed computational routines can be found at https://gitlab.mpcdf.mpg.de/connectomics/L4dense in +SynEM/+Svg/findEdgesAndBorders.m and correspondence/calculateGlobalCorrespondences.m.

Synapse detection with SynEM

For synapse detection, SynEM was applied to the segment neighborhood graph (see previous section) as in (Staffler et al. 2017). In brief, for each pair of adjacent volume segments, the subvolumes for SynEM feature aggregation (see (Staffler et al. 2017)) were determined by dilating the border between the two volume segments with spherical structuring elements of radius 40 nm, 80 nm and 160 nm, respectively, and then intersecting the dilated border the two adjacent volume segments, each. Interfaces with a border size of less than 151 voxels were discarded. Then, all interfaces in the segment neighborhood graph were classified using the SynEM classifier, yielding two SynEM scores for each interface, one for each of the two possible synapse directions.

In contrast to (Staffler et al. 2017), separate classifiers for interfaces onto spine segments (retrieved by TypeEM) and for all other interfaces were used. For interfaces onto spine segments, the classifier from (Staffler et al. 2017) was used. All interfaces onto spine segments with at least one score larger than -1.2292 according to the SynEM classifier (corresponding to 89% recall and 94% precision for spine synapses; see the test set of (Staffler et al. 2017)) were considered as synaptic interface candidates. For all other interfaces, a second classifier was trained using training data of synapses onto shafts and somata (examples in Figures A2-2 to A2-5) and a different feature representation of interfaces as follows: The training set of the second classifier consisted of all shaft and soma synapses of the SynEM training set and the shaft and soma synapses from two additional training volumes of size 5.75 x 5.75 x 7.17 µm^3. The feature representation of interfaces for the second classifier consisted of all features of SynEM described in (Staffler et al. 2017), extended by four additional texture filter responses. The additional filter responses were voxel-wise probability maps for synaptic junctions, mitochondria, vesicle clouds and a background class obtained using a multi-class CNN. The CNN was trained on seven volumes of dense annotations for synaptic junctions, vesicle clouds and mitochondria (six volumes of size 3.37 x 3.37 x 3.36 µm^3 that were also used for the methods comparison in (Staffler et al. 2017), and one additional volume of size 5.75 x 5.75 x 7.17 µm^3) using the elektroNN framework (elektronn.org; see also (Dorkenwald et al. 2017)). Interfaces onto segments that were not classified as spines by TypeEM with at least one directional SynEM score larger than -1.28317 according to the second classifier (corresponding to 69% recall and 91% precision evaluated on all shaft synapses of the test set for inhibitory synapse detection of SynEM) were considered as synaptic interface candidates in addition to the synaptic interface candidates onto spines.

Synapses onto somata and dendritic shafts: criteria for identification

The detection of shaft and soma synapses in 3D EM is notoriously challenging when compared to primary excitatory spine synapses.

We used the following criteria for synapse identification: Typically large vesicle-filled bouton; Apposition of vesicles towards one interface; At that interface indications of a darkening of the synaptic interface; Comparison with other possible synaptic interfaces of the same bouton in cases of doubt. Examples from the training set of SynEM for inhibitory axons are shown in Figures A2-2-5.

ConnectEM classifier

To determine the continuity between adjacent volume segments (Figure 2-2B), for each interface (see previous section) sized at least 10 vx, the SynEM filter bank and aggregation volumes (Staffler et al. 2017) were applied to the image and CNN output data, resulting in 6,426 texture- and 22 shape-features per interface. The features were used as input to an ensemble of 1,500 decision tree stumps trained with LogitBoost (Friedman et al. 2000) on 76,379 labeled edges obtained from proofread dense skeleton annotations of three (5 µm)^3 cubes of neuropil. To adapt the SynEM interface classification method to a task on undirected edges, the ensemble was trained on both the forward and reverse direction of the labeled edges. Each edge in the segment neighborhood graph was then assigned a continuity probability by applying the classifier to the corresponding interface in random direction. Interfaces with less than 10 vx were treated as having a continuity probability of zero, edges across segmentation cubes were assigned a continuity probability of one. The employed computational routines can be found at https://gitlab.mpcdf.mpg.de/connectomics/L4dense in calculateFeatures.m, connectEM/classifierTraining.m and predictDataset.m in the +connectEM folder.

TypeEM classifier

To determine whether a volume segment belonged to a dendrite, an axon, or an astrocyte, and whether it was likely a dendritic spine head, we developed a set of four classifiers ("TypeEM") as follows. Each volume segment was expanded into an agglomerate of up to 5 segments by iteratively adding the neighboring segment with the highest edge continuity probability to the agglomerate. Agglomeration was restricted to the subgraph induced by the edges with at least 92% continuity probability to prevent merge errors.

Then, the following set of features was computed for the agglomerates: 918 texture features from the SynEM filter bank (Staffler et al. 2017) applied to the image and CNN output data and pooled over the segment agglomerate volume; 6 shape features as in SynEM; the 0th- to 2nd-order statistical moments of the agglomerate volume; the eigendecomposition of the 2nd order statistical moment; the 0th-to-2nd order statistical moments of the surface of the agglomerate after rotation of the agglomerate to the principal component of all its voxels; same as before but for the convex hull of the agglomerate; volume-to-surface area ratio, compactness (i.e., (surface area)^3 / volume^2), clusters of normal unit vectors, hull crumpliness and packing (Corney et al. 2002); estimates of the distance (Osada et al. 2001) and thickness (Yi et al. 2004) histograms from sampling random point pairs on the agglomerate's surface.

This yielded a total of 1,207 shape features and 924 SynEM features; these were then taken as input to an ensemble of 1,500 decision tree stubs trained using LogitBoost (Friedman et al. 2000). 14,657 training samples were obtained by one expert (AM) marking all spine head segments and assigning the neurite / glia type to each process in three densely reconstructed (5 µm)^3 cubes of neuropil (same cubes as in previous section "ConnectEM classifier").

Together, these data were used to train one-versus-all TypeEM classifiers for axons, dendrites, and astrocytes. The classifiers reached the following classification performance on a separate test cube sized (5 µm)^3: Axon classifier: 91.8% precision (P) and 92.9% recall (R); dendrite classifier: 95.3% P, 90.7% R; astrocyte classifier: 97.2% P, 85.9% R (at maximum area under precision-recall curve). The spine head classifier was trained on a feature set calculated as above, with the exception that the agglomeration step was omitted, and achieved 92.6% P and 94.4% R.

For subsequent processing, the TypeEM classifier scores were transformed to probabilities using Platt scaling (Platt 2000). Finally, the one-versus-all axon, dendrite, and astrocyte probabilities of each segment were combined to multi-class probabilities by rescaling them by the inverse of their sum.

The employed computational routines can be found at https://gitlab.mpcdf.mpg.de/connectomics/L4dense in +TypeEM/buildFeatures.m and +TypeEM/buildPredictions.m.

Automated reconstruction of dendrites

For the reconstruction of dendrites, we first selected all SegEM segments with a TypeEM dendrite probability of at least 0.3 and a volume of at least 500 vx. In the subgraph induced by these segments we deleted all edges that corresponded to an interface of less than 300 vx size or a neurite continuity probability below 98%. The graph was then used to cluster the dendritic segments into connected components, yielding dendrite agglomerates.

To reduce the effect of TypeEM misclassifications, we used the fraction of myelinated surface area to identify and remove likely axonal agglomerates from the dendrite class (calibrated based on 50 random agglomerates with a myelinated surface fraction between 0.05 and 0.5): Agglomerates were moved from the dendrite to the axon class if they had a total volume of at least 200,000 voxels, had a myelinated surface fraction above 0.25 (or above 0.08 if the agglomerate comprised more than 25 segments); and did not contain somatic segments.

For the computation of the myelinated surface fraction, for each agglomerate with a total volume of above 5 µm^3, all neighboring segments of the agglomerate were identified according to the neighborhood graph, and the area of interfaces onto neighboring myelin segments was computed. Myelin segments were defined as having at least 50% of their volume intersecting with the myelin map as derived above (section "nuclei and myelin detection"). This area was then divided by the total area of all interfaces between the agglomerate and other segments.

Reconstruction of cell bodies (somata)

Cell bodies were reconstructed from the volume segmentation of each cell's nucleus (see above). First, we identified all SegEM segments which were contained in a nucleus with at least 50% of their volume. Then we added all direct neighbors of these segments according to the neighborhood graph. Then we iteratively extended the soma volumes along the neighborhood graph with the following constraints: only consider segments with a size of at least 2,000 voxels and a center of mass at a maximal distance of 8 µm from the center of mass of the corresponding nucleus; only consider edges in the neighborhood graph with a continuity score above 0.98; do not consider edges if the segments' vessel score or its myelin score were above 0.5. Then, all connected components of segments that were completely enclosed by soma segments according to the neighborhood graph were added to the respective soma. Finally, all segments with more than 80% of their surface adjacent to soma segments were added iteratively (10 iterations).

The employed computational routines can be found at https://gitlab.mpcdf.mpg.de/connectomics/L4dense in +Soma/agglomerateSoma_BS.

Soma-seeded reconstruction of neurons

For the reconstruction of those neurons that had their cell body in the dataset (n=89 with dendrites reconstructed in the dataset, Movie A2-1), all dendrite agglomerates from the automated dendrite reconstruction that overlapped with a given soma volume (see previous section) were combined into one agglomerate for each of the neurons.

Iterative semi-automated correction of whole cell agglomerates

The remaining errors in the soma-seeded neuron reconstructions (see previous section) were corrected in a semi-automated procedure that consumed 9.7 hours for all neurons, i.e. 5.18 minutes per neuron. Soma-based neuron reconstructions were inspected for merger errors in the 3D view of webKnossos, and mergers were corrected by deletion of nodes in the neighborhood graph of the neuron reconstruction. Then, endings of the neuron were detected (see below), and reconstructions at the endings were performed in webKnossos until a dendrite agglomerate was reached that was obtained from the automated dendrite reconstruction (see previous section). The inspection for mergers and the detection of endings in the dataset was iterated until only real endings or endings at the dataset boundary were left.

Automated axon reconstruction

For the reconstruction of axons, we first selected all SegEM segments with a volume of at least 300 vx and a TypeEM axon probability of at least 50%. The subgraph induced by these segments was partitioned into connected components (axon agglomerates) after removal of edges corresponding to interfaces with less than 60 vx size or with a neurite continuity probability below 97%. Next, for each segment that was part of an axon agglomerate, we computed the first principal component of its voxel locations and used its degree of variance explanation as an indicator for the directedness of the segment. We then determined for each interface between the agglomerate’s segments and all neighboring segments the alignment of the interface’s normal vector with the segment direction. Based on this, we obtained an ending score for each interface of the segment, and at locations with high scores, the axon agglomerate was grown into neighboring segments under the following additional constraints: the neighboring segment had an axon probability of at least 30%; the interface had a size of at least 40 vx; the neighborhood graph edge had a neurite continuity probability of at least 80%. This growth process was repeated ten times.

Finally, we compensated for the heightened rate of merge errors in proximity to the dataset boundary that results from decreased alignment quality. Edges that were closer than 2 µm to dataset boundary and had a neurite continuity probability below 98% were removed from the axon agglomerates.

Then, all axon agglomerates of length 5 µm and above were used for the following focused annotation steps. Length of agglomerates was computed as the summed Euclidean length of all edges in the minimal spanning tree of the center of masses of the agglomerate’s segments.

FocusEM ending detection and query generation

To determine the endings of axons at which focused annotation could be seeded, we used the following procedure. For each segment in an axon agglomerate we took the segments that are direct graph neighbors or that come within 1 µm distance, and computed the first principal component of their volume. We then identified all segments where the principal component of the local surround explains at least 50% of the variance, and determined the borders on the axon agglomerate surface that were aligned to that axis (i.e., all interfaces for which the vectors from the center of mass of the local surround to the center of mass of the interface were at an angle of at most $\cos^{-1}(0.8) \approx 37$ °). Finally, the identified interfaces were grouped using a cutoff distance of 600 nm and reduced to the interface best aligned to the surround's principal component. We determined the point within 500 nm of each interface that is closest to the core of the axon agglomerate and used it together with the principal component of the local surround as the start position and orientation of a focused annotation query in webKnossos (Boergens et al. 2017). Interfaces within 3 µm of the dataset boundary were excluded from query generation.

FocusEM axon queries were performed in webKnossos flight mode (Boergens et al. 2017). The volume map of all axon agglomerates larger than 5 µm was used to dynamically terminate flight paths when a user entered already reconstructed agglomerates (this was implemented in a custom script using the webKnossos frontend API, see https://gitlab.mpcdf.mpg.de/connectomics/L4dense/+connectEM/+Flight/dynamicStoppingScript.js). To reduce the delay between subsequent queries, we implemented a "hot switching mode" in webKnossos (Boergens et al. 2017) such that the next query was already loaded in the background while answering the current query. With this, an immediate switching (amounting to a jumping to query locations in the dataset) was possible that yielded negligible lag between tasks.

Query analysis

FocusEM queries yielded linear skeletons from webKnossos flight mode. For each node of a given skeleton we determined the overlap with axon agglomerates in the $(3\ \mathrm{vx})^3$ cube around each skeleton node (a skeleton was considered to overlap with an axon agglomerate if the agglomerate was contained in at least 54 vx around the skeleton nodes). For the overlapping agglomerates, we determined the corresponding agglomerate endings within 300 nm distance from the skeleton nodes. Based on the configuration of agglomerate overlaps, agglomerate endings reached by the queries and proximity of the query to the dataset boundary, the query results were either accepted as is, re-queried or discarded (see code files below for detailed decision tree). When locations were queried multiple times, the information on agglomerate and ending overlap was used to keep only minimal subsets of skeleton tracings for the final axon agglomerates (see "Iteration between ending and chiasma detection"). For connectome analysis and display, volume segments that had not yet been assigned to any axon agglomerate and that overlapped with the user skeleton from the flight mode queries were collected and added to the agglomerate volume.

The employed computational routines can be found at https://gitlab.mpcdf.mpg.de/connectomics/L4dense in getAggloQueryOverlapA.m, getAggloQueryOverlapB.m, flightEndingOverlap.m, makeEndingCaseDistinctions.m and createNewSuperagglos.m of the +connectEM folder

Chiasma detection and queries

To identify mergers, we detected geometric configurations (Figure 2-2H) with more than two-fold neurite crossings after agglomeration. Chiasmata were detected by counting the number of intersections of the graph representation of an agglomerate with a sphere centered on the nodes of the graph. For this, the agglomerate was reduced to the connected component contained within a sphere of 10 µm radius around the current node followed by pruning of all edges within a sphere of 1 µm radius. The remaining graph components that reach a distance of at least 2 µm from the center were considered sphere exits. If four or more sphere exits were found, the node at the sphere center was labeled as a chiasmatic node. Within axon agglomerates, the chiasmatic nodes were clustered using a cutoff distance of 2 µm and subsequently reduced to the node closest to the center of mass of the cluster. At these locations, queries from the sphere exits pointing towards the sphere center were generated and annotated as described for the ending queries (Figure 2-2F,G). The webKnossos flight mode annotations of chiasma queries were stopped when the annotator left the bounding box around all exit locations. In the final iterations of the analysis, 3-fold chiasmata were also detected and annotated.

The employed computational routine can be found at https://gitlab.mpcdf.mpg.de/connectomics/L4dense in +connectEM/detectChiasmata.m.

Chiasma query interpretation

To decide which of the exits contributing to a given chiasma should remain connected and which should be disconnected, we used the query results from all chiasma exits. The full set of results enabled the detection of chiasmata with contradictory query answers, partial automated error correction, and the re-querying of a minimal set of exits. Chiasmata with a full and contradiction-free set of answers were solved by removing the edges within the center 1µm sphere from the agglomerate and by subsequent reconnection of the exits based on a minimal set of flight queries.

The employed computational routines can be found at https://gitlab.mpcdf.mpg.de/connectomics/L4dense in +connectEM/splitChiasmata.m and +connectEM/splitChiasmataMultiLogic.m.

Iteration between ending and chiasma detection

Following automated axon reconstruction, the FocusEM queries were iterated as detailed in +connectEM/README.md.

Spine head detection

Spine heads were detected as segments with TypeEM spine head probability above 50%. In 14.9% of cases, spine heads were split in the initial segmentation and then agglomerated by connecting neighboring segments with a TypeEM spine head probability above 50% that were connected by an edge with neurite continuity probability of at least 98% (note that in 11.3% of cases, spine heads were split at the interface of segmentation cubes; i.e. only in 3.6% of cases, spine heads were split in the original SegEM segmentation). Together, this yielded 415,797 spine head agglomerates. (See +Spine/+Head/buildAgglos.m).

Spine attachment

Of the 415,797 spine head agglomerates, 5.6% got attached to a dendritic shaft during automated dendrite agglomeration (see above). We then implemented a greedy walk strategy from spine heads to the corresponding dendritic shafts (Figure 2-2D). The walk was terminated upon reaching a dendrite agglomerate of at least ~1.1 µm^3 ($10^{5.5}$ vx) and was restricted to at most ten steps along continuity edges, each having a neurite continuity probability of 25% or more and only involving segments with axon probability below 80%. With this, an additional 206,546 (49.7%) spine heads could be attached to the corresponding dendrite. For the remaining spines, SegEM mergers in the very thin spin necks typically prevented the spine attachment heuristics to be successful. We instead seeded manual annotation in the 164’969 remaining spine heads with a distance of at least 3 µm from the dataset boundary, asking annotators to connect these to the dendritic shafts (+L4/+Spine/+Scripts/prepareSpineTasksWKOrtho.m). This consumed 900 work hours total and resulted in a final spine head recall of 88.6% for spine heads further than 10 µm from the dataset boundary. The relevant code can be found in (+L4/+Spine/+Scripts/prepareSpineTasksWKOrtho.m).

Synapse agglomeration

Synaptic interface candidates (n = 864,405 out of which 605,569 were onto spine segments and 258,836 onto other segments) detected by interface classification were discarded if the score both synapse scores were larger than -2 or the continuity probability of the corresponding edge was larger than 0.7, or the myelin score of the pre- or postsynaptic segment was larger than 0.375 or the presynaptic segment was contained in the soma volumes. The remaining synaptic interface candidates (n= 862,350) were restricted to those with a center of mass more than 3 µm from the segmentation volume boundary (yielding n=696,149 synaptic interfaces with a pre- and postsynaptic segmentation object, each, that are used in the following analyses).

To consolidate synaptic interfaces, the following steps were applied: First, all presynaptic segmentation objects contributing to any of the synaptic interfaces were combined, if they were connected to each other by at most two steps on the segmentation neighborhood graph with each step restricted to edges with a ConnectEM score of greater than 0.98. The same was applied to all postsynaptic segmentation objects. Then, all synaptic interfaces between the combined pre – and postsynaptic segmentation objects were combined into one synapse, each. Synapse agglomerates for which at least one postsynaptic segment was part of the spine head agglomerates were considered as spine synapse agglomerates. A spine synapse agglomerate was called "primary spine innervation" if it contained the interface with the highest SynEM score onto a given spine head agglomerate, and "secondary spine innervation" otherwise. Multiple synapse agglomerates between an axon agglomerate and a spine head agglomerate were merged into a single synapse agglomerate. The center of mass for a synapse agglomerate was calculated as the component-wise mean of the centers of mass of the individual interfaces. The area of a synapse agglomerate was calculated as sum of the border areas of the individual interfaces.

The employed computational routine can be found at https://gitlab.mpcdf.mpg.de/connectomics/L4dense in +Synapses/+Scripts/synapseDetection_v3.m.

Connectome aggregation

The connectome was constructed using the axon agglomerates, postsynaptic agglomerates (dendrites, somata and axon initial segments), and synapse agglomerates. For each pair of an axon and postsynaptic agglomerate, all synapse agglomerates that had a presynaptic segment in the axon agglomerate and a postsynaptic segment in the postsynaptic agglomerate were extracted and associated with the corresponding axon-target connection. The total number of synapses of a connection was defined as the number of synapse agglomerates associated with that connection. The total border area of a connection was defined as the sum of the border area of all synapse agglomerates. All of the following analyses were restricted to axons with at least ten output synapses.

Target class detection heuristics

To determine the post-synaptic target classes apical dendrites (AD), smooth dendrites (interneuron dendrites, SD), axon initial segments (AIS), proximal dendrites (PD) and cell bodies (SOM), the following heuristics were used:

Cell bodies were identified based on the detection of nuclei as described in "Reconstruction of cell bodies". The non-somatic postsynaptic components of the soma-based neuron reconstructions were marked as proximal dendrites. Smooth dendrites were identified by having a spine rate (i.e., number of spines per dendritic trunk path length) below 0.4 per µm (Kawaguchi et al. 2006), Figure 2-3D, unless identified as apical dendrites. For the analysis of target class specificities and geometric predictability, the dendrites of soma-based interneuron reconstructions were considered as smooth, but not proximal dendrites.

For the identification of apical dendrites, all dendrite agglomerates that intersected with the pia- and white matter-oriented faces of the dataset were manually inspected in webKnossos (total of 422 candidates, total inspection time 5 hours for an expert annotator) with the inspection criteria: directed trajectory along the cortical axis; maximally two oblique dendrites leaving the main dendrite; spine rate of non-stubby spines of at least about one every two micrometers.

Contradictory class assignments between SD and AD occurred for 46 dendrites and were resolved by manual inspection in webKnossos.

The axonal part of soma-based neuron reconstructions which was more proximal than the first branch point was considered as axon initial segment. Vertically oriented agglomerates that entered the dataset from the pia-end of the dataset and had no spines or output synapses, and transitioned into a clearly axonal process closer to the white matter boundary of the dataset were also identified as axon initial segments.

Definition of inhibitory and excitatory axons

Inhibitory and excitatory axons were separated based on the fraction of their synapses marked as primary spine innervations (see “synapse agglomeration”) (Figure 2-4A,B). To automatically resolve remaining merge errors between these two axon classes, we split axons between the two modes of the spine rate distribution (20 to 50% of synapses being primary spine innervations) at all their branch points (see “Chiasma detection and queries”). Then, we defined excitatory axons as those with more than 50% of synapses being primary spine innervations and termed axons with less than 20% primary spine innervations inhibitory.

Definition of thalamocortical axons

To identify those excitatory axons that were likely originating from the thalamus we used the fact that thalamic axons from VPM have been described to establish large multi-synaptic boutons at high frequency in mouse S1 cortex ((Bopp et al. 2017), Figure A2-6). We quantitatively applied these criteria by measuring the density of primary spine innervations (PSI) per axonal path length, the average number of PSI per axonal bouton, the fraction of axonal boutons with multiple PSIs, and the median bouton volume. Boutons were defined as clusters of PSI with an axonal path length of less than 2.4 µm between the cluster centers. In a calibration set of ten manually identified corticocortical and ten thalamocortical axons these features were discriminatory. We combined them into a single thalamocortical axon probability using logistic regression. Excitatory axons with a TC probability of at least 60% were identified as thalamocortical.

Spatial synapse distributions

To quantify the effect of soma location on synaptic innervation, we calculated the center of mass of all somatic segments and the fraction of excitatory input synapses that originate from thalamocortical axons for each soma-based neuron reconstruction. Bivariate linear regression was used to estimate the effect of soma position within the plane tangential to the cortical surface on the synaptic input composition.

The primary dendrites of the soma-based neuron reconstructions were then identified to assess the effect of dendritic orientation on synaptic inputs. The orientation of a dendrite was calculated as the volume-weighted mean of the unit vectors from the soma (as above) to the center of mass of the corresponding SegEM segments. The fraction of excitatory synapses onto a primary dendrite contributed by thalamocortical axons was corrected for the value expected based on somatic position (as above). Finally, the dot product dp of the resulting vector (after renormalization) with the unit vector along the cortical axis was put in relation to the ratio of the dendritic synapse fraction to the synapse fraction of the corresponding neuron. The linear regression of these two quantities was evaluated based on the coefficient of determination, whereas the pia- ($dp < -0.5$) and white matter-oriented dendrites ($dp > 0.5$) were compared based on a two-sample *t*-test.

For further analysis of the synapse input composition of L4 neurons, all soma-based neuron reconstructions and their individual dendrites were considered if they received at least 100 and 50 input synapses, respectively. The correlation to the fraction of excitatory synapses contributed by TC axons (TC / (TC + CC)) was computed for the fraction of inhibitory synapses and the 7 target-preferring axon classes defined in Figure 2-4. Statistical tests and Bonferroni correction see Statistical Methods.

Comparison between dense reconstructions

For the comparison of published dense reconstructions and the invested resources (Figure 2-2I,J), we used the following numbers: Dense reconstruction in the mouse retina (Helmstaedter et al. 2013): about 640 mm reconstructed neuronal path length, about 20,000 invested work hours; Dense reconstruction in the mouse cerebral cortex (Kasthuri et al. 2015): 6.75 mm of path length reconstructed within 253 hours (37.5 h/mm, 4.5 µm/µm^3, 1500 µm^3 reconstructed; see (Berning et al. 2015) for derivation of numbers); Dense reconstruction in the zebrafish olfactory bulb (Wanner et al. 2016): 492 mm path length with 25,478 invested work hours; Dense reconstruction in the fly larval nervous system (Eichler et al. 2017): 2.07 meters (based on skeleton reconstructions in Supplement of (Eichler et al. 2017)) with 28,400 hours investment (73 µm / h; see (Schneider-Mizell et al. 2016)); L4 dense reconstruction: 2.724 meters (of these in mm: dendritic shafts 342, dendritic spines 551, dendrites connected to a cell body in the volume 62.5, axons connected to a cell body in the volume 6.5; axons 1760; note about 80% of the volume is dense neuropil) within 3,982 hours.

Computational cost estimate

For the estimation of the total computational cost, a runtime of 5 hours for SynEM, 72 hours for TypeEM and 24 hours for all other routines on a cluster with 24 nodes each with 16 CPU cores and 16 GB RAM per core was used. The runtime was converted to resources using 0.105 USD/h per CPU core with 16 GB RAM (Amazon EC2: 6.7 USD/h for 64 CPU cores with 1000 GB RAM). The computational cost for Flood-Filling Networks was calculated using 1000 GPUs that ran for a total wall time of 16.02 hours (Suppl. Table 3 in ref. (Januszewski et al. 2018)) and a cost of 0.9 USD/h for a single GPU which was multiplied by the ratio of the sizes of our dataset (61 x 94 x 92 µm^3) and the dataset used in (Januszewski et al. 2018) (96 x 98 x 114 µm^3).

Error Measurements

To quantify the errors remaining after axon reconstruction, we chose the same 10 randomly selected axons (total path length, 1.72 mm) that had also been used for error rate quantification in (Boergens et al. 2017). These axons were not part of any training or validation set in the development of FocusEM. Repeating the analysis described in (Boergens et al. 2017) for the largest axon agglomerate overlapping with the ground truth axon, respectively, yielded a total number of 22 errors, of which 15 were continuity errors (compare to panels 1l,m in (Boergens et al. 2017)).

The error rates and recall of soma-based dendrite reconstructions were calculated from proofread ground truth annotations comprising a total of 89 cells and 64.08 mm path length. Each node of the ground truth skeleton was marked as recalled if it overlapped with the corresponding dendrite agglomerate (see “Query analysis”), or flagged invalid if placed outside the segmented volume. A ground truth edge was considered recalled if both end nodes were recalled, or invalid if any of the end nodes was invalid. 54.51 mm, or 87.3%, of the 62.46 mm valid ground truth path length were recalled. Split errors, by definition, result in partial dendrite reconstructions and were thus detected as non-recalled ground truth fragments with at least 5 µm path length. The detected were proofread, yielding a total of 37 split errors.

The identification of axonal target specificity (Figure 2-4) was insensitive to split- and merger errors, because as long as axonal reconstructions were long enough to provide meaningful statistical power for the analyses, split axons were expected to correctly sample target specificities and mergers of axons were expected to only dilute specificities. Therefore the results about the existence of target specific inhibitory and excitatory axon classes represent a lower bound of specific wiring. The results on the lack of geometric predictability (Figure 2-5) were similarly unaffected by remaining split and merge errors.

For the finding that no inhibitory axons show target specificity for AIS in L4 (Figure 2-4E), however, we needed to control that this lack of specificity was not induced by remaining axonal merge errors. We manually inspected a subset of 10 axons innervating AIS. Only one synapse (out of more than 100 synapses) was erroneously added to an AIS innervating axon due to a merger, thus providing no evidence that the lack of AIS target specificity could be an artifact of merged axons.

For the results on synaptic input composition (Figure 2-6) we varied the sensitivity of our detection of TC axons and found that also for detections with a higher TC axon recall and a lower recall at higher precision the conclusions were unchanged.

The results on synaptic size consistency could be strongly affected by the remaining merge errors in axons, diluting data on consistent synapses when merging unrelated axons together. To control for this, we obtained the results in Figure 2-7 using axons for which all 3-fold intersections in all axons had been artificially split before the analysis. For the results in Figure 2-4, we repeated analyses after splitting of axons and found the key conclusions unaltered.

Supplementary text

Controls for definition of excitatory and inhibitory axons

Previous reports have described that a subset of excitatory axons in cortical L4 preferentially target the shafts of dendrites in some species (McGuire et al. 1984, Lübke et al. 2000): a study of L4 spiny neurons' axons in juvenile rat found preferential innervation of small-caliber dendritic shafts (and only 27% of synapses onto spines, (Lübke et al. 2000)), and in cat visual cortex, a subset of corticortical excitatory axons from layer 6 has been described to establish preferentially shaft synapses onto spiny dendrites in L4 at the end of short axonal branches, yielding boutons terminaux (McGuire et al. 1984, Ahmed et al. 1994). To check whether these axons would confound our assignment of shaft-preferring axons as inhibitory, we randomly selected 20 shaft synapses onto spiny dendrites and manually reconstructed the presynaptic axons with their output synapses. We first asked whether any of these axons would preferentially establish *boutons terminaux* onto shafts, as described in cat, but found no such axon, indicating that this innervation phenotype comprises less than 5% or is absent in our data from mouse L4 (compare to the estimate of more than 40% of such inputs in cat L4 (McGuire et al. 1984)). We then checked whether any of the 20 axons showed both a preference for shaft innervation and in a minority of cases any clear primary spine head innervation, as described for the L4 axons in juvenile rat. We found no such example, indicating that none of the shaft-preferring axons was excitatory. This is consistent with data from cat which suggested that L4 axons preferentially target spines (Ahmed et al. 1994). Together, we conclude that in our data from mouse L4, excitatory axons preferentially establish primary spine head innervations (Figure 2-4B) and inhibitory axons preferentially innervate the shafts of dendrites.

Synaptic size consistency: additional controls for cell-type effects

In order to further study the effect of cell types and potential cell-type dependent synaptic weight differences, we measured the size of synapses between cell types in L4 that are known to show different mean synaptic efficacy: L4-to-L4 connections (in juvenile rat barrel cortex) were reported to have an average EPSP amplitude of 1.59 mV (Feldmeyer et al. 1999), while L4-to-L5A connections were shown to have a unitary EPSP amplitude of 0.6 mV (Feldmeyer et al. 2005). We used the reconstructed output axons in our dataset (n=59, Figure A2-7A,B) and identified those synapses made onto other L4 neurons (n=32 manually verified connections) and those onto ADs (n=12). While the distribution of synapse size appeared to be biased towards lower synapse size in the L4-to-AD (L5) connections (Figure A2-7B), this effect did not reach statistical significance for the small number of synapses (synapses between L4 neurons were 28 % larger than those from L4 neurons onto ADs (0.25 μm^2 vs. 0.19 μm^2, p=.058, t-test for log ASI, Figure A2-7B). Interestingly, the distribution of synapse size for L4-to-L4 neurons was indistinguishable from that onto unidentified targets, indicating the vast majority of synapses to be of the L4-to-L4 type.

We then asked whether, assuming a subtype of smaller synapses as in L4-to-L5 connections, these two different synaptic connection types could give rise to the observed synaptic size similarity effects studied in Figure 2-7. Even when assuming that 50% of synapses were of the L4-to-AD type (substantially more than expected), the effect on above-random synaptic size consistency was small: the CV-size map showed a slight peak for smaller but not for larger synapse sizes. With this, the observed effects of synaptic size similarity (Figure 2-7) could not be solely caused by synaptic size differences for known intracortical cell types.

Control for mutual interaction between upper bounds on LTP and LTD

To control for the mutual interaction between the upper bounds on LTP and LTD, we performed the following analyses: The two-dimensional size and size-similarity distributions of same-axon same-dendrite (SASD) synapse pairs and random pairs of SASD synapses were compared to define candidate LTP and LTD regions (see methods). We then identified the SASD connections contained in the candidate LTD region and asked whether repeated analysis of only the SASD connections outside this region still yields statistically significant evidence for a subpopulation of connections with similarly sized and large synapses. We found that the upper bounds on LTD in all excitatory, corticocortical, and thalamocortical connections are compatible with up to 2.9 %, 3.3 % and 6.7 % of LTP, respectively. Analysis of the SASD connections outside the LTP region did not produce any evidence for LTD. In between these extremes, other combinations of LTP and LTD frequencies are possible.

Position of the sample with reference to barrels

The position of the coronal slice from which the sample was extracted was aimed at targeting barrel cortex; the position in barrel cortex was further confirmed by cytochrome oxidase staining of the contralateral hemisphere which showed the large barrel structures in layer 4. To determine whether the sample was located within a barrel or within the septa between barrels, we used the fact that TC axons from VPM have been reported to preferentially target the barrels (not the septa) in L4 of S1 cortex. Since furthermore the identification of TC boutons based on the criteria in (Bopp et al. 2017) were shown to be valid for thalamocortical afferents from the thalamic nucleus VPM but not from the nucleus PoM (projecting to the septa, (Bopp et al. 2017)), the presence of high density of likely VPM boutons in our sample indicated a location within a barrel. In fact, the tangential plane projection of VPM-TC bouton density showed a radially oriented gradient suggesting a position of the sample within a S1 barrel (data not shown). Finally, we needed to consider whether the sample was in upper L4 or lower L3 (Figure 2-1A). Based on the soma distribution, we estimated it to be in L4. Post-hoc, the absence of any chandelier-type innervation of AIS in the dataset strongly supports the location in L4, not L3.

Additional acknowledgements

We thank A. M. M. Al-Shaboti, M. S. E. A. Aly, C. Arras, N. Aydin, D. Baltissen, A. Bamberg, F. Y. Basoeki, N. Berghaus, A. Berghoff, L. Bezzenberger, N. M. Böffinger, S. M. Bohne, O. J. Brandt, A. B. Brandt, J. Buss, L. Buxmann, D. E. Celik, H. Charif, N. O. Cipta, L. Decker, K. Desch, T. Engelmann, T. Ernst, J. Espino Martinez, T. A. R. Füller, D. J. Goffitzer, V. Gosch, J. C. Hartel, H. Hees, B. Heftrich, J. L. L. Heller, R. C. Hülse, O.-E. Ilea, R. Jakob, L. H. Janik, A. Jost Lopez, M. J. D. G. Jüngling, V. C. Kalbert, M. Karabel, A. Kessler, L. Kirchner, R. Kneissl, T. Köcke, P. König, K. Kramer, F. K. Krämer, L. C. R. Kreppner, M. S. Kronawitter, J. Kubat, B. Kuhl, D. Kurt, C. Kurz, E. P. Laube, C. T. Lossnitzer, R. N. Lotz, L. A. Lutz, L. E. U. Matzner, S. Mehlmann, I. M. Meindl, I. Metz, M. Mittag, M.-L. Nonnenbroich, M. Nowak, N. Plath, A.-L. Possmayer, L. Präve, M. Präve, S. Reibeling, S. Reichel, K. J. P. Remmele, A. C. Rix, C. F. Sabatelli, D. J. Scheliu, N. Schmidt, L. M. Schütz, C. M. Schumm, A. K. Spohner, S. T. Stahl, B. L. Stiehl, K. T. Strahler, K. M. Trares, S. N. Umbach, S. S. Wehrheim, M. Werr, J. Winkelmeier, T. Winkelmeier, and S. Zimbelmann for webKnossos annotation work.

Supplementary figures

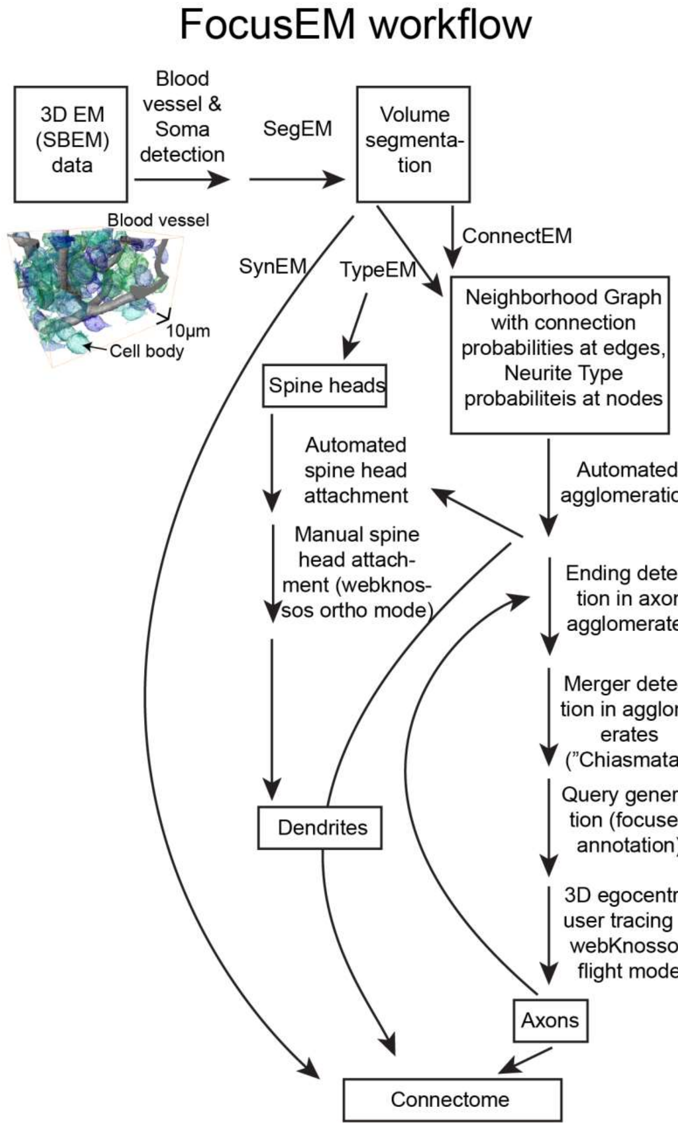

Figure A2-1 FocusEM workflow. Detailed workflow of FocusEM reconstruction, including the iterations between split and merger detection (compare simplified workflow in Figure 2-2A). Methodological details in Materials and Methods

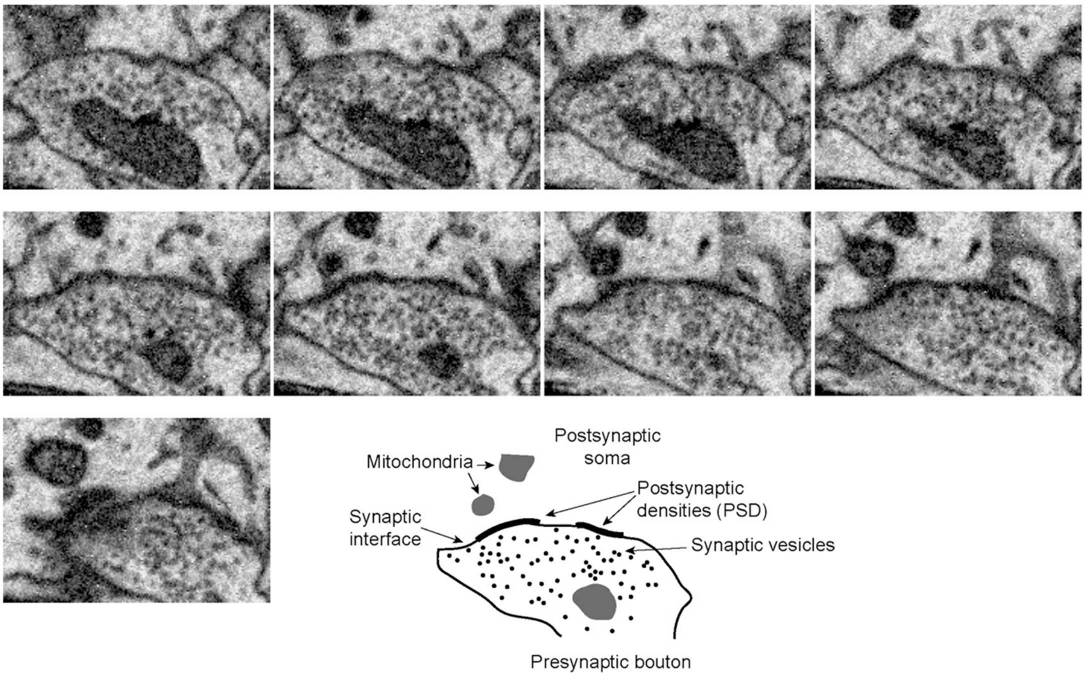

Figure A2-2 Examples of soma and shaft synapses from the training set of SynEM for inhibitory axons (example 1, synapse onto soma). Large bouton almost completely filled with synaptic vesicles; mitochondrion in bouton; large contact interface with a soma; at this interface close packing of synaptic vesicles; darkening of bouton-soma interface. All of the features are visible in several EM sections, not just one. Image size: 1.9x1.4 µm. Direct link to webKnossos: https://wklink.org/2495

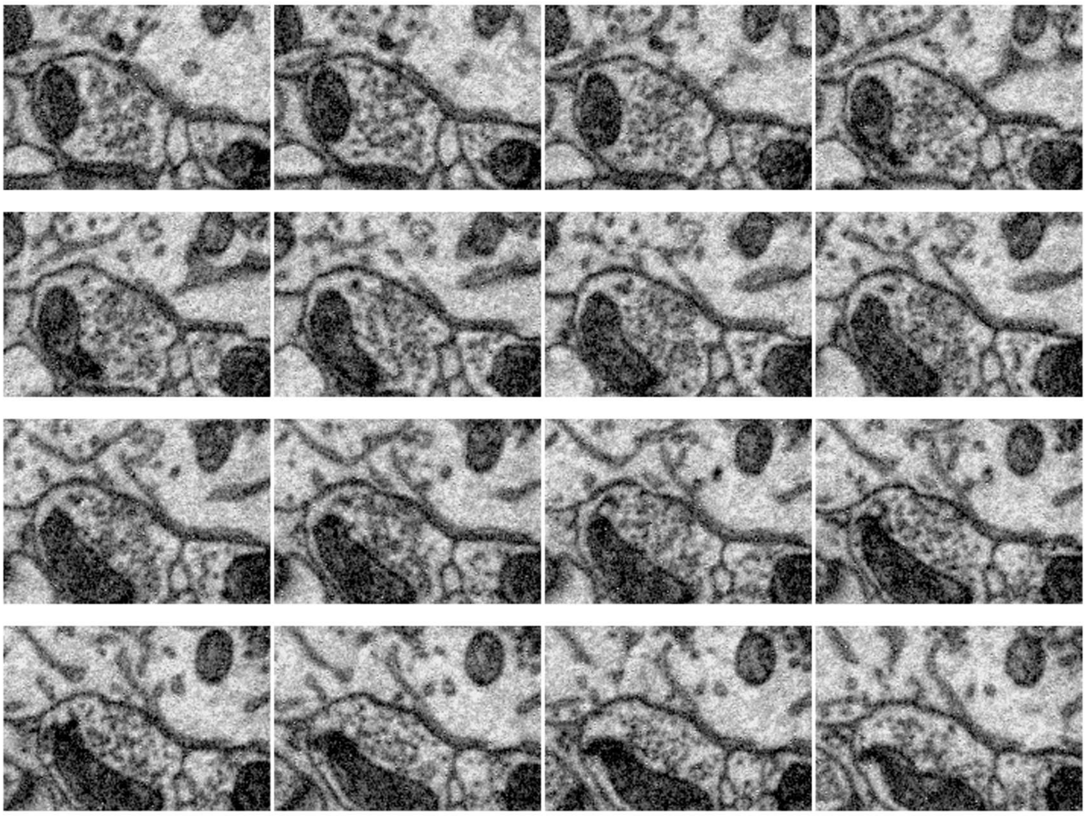

Figure A2-3 Examples of soma and shaft synapses from the training set of SynEM for inhibitory axons (example 2, synapse onto soma). Relatively large axonal bouton, completely filled with synaptic vesicles except for one large mitochondrion. Large interface with some, close proximity of vesicles with that interface; darkening of the bouton-soma interface; other interfaces of the same bouton lack these criteria. Image size: 1.9x1.4 µm. Direct link to webKnossos: https://wklink.org/7852

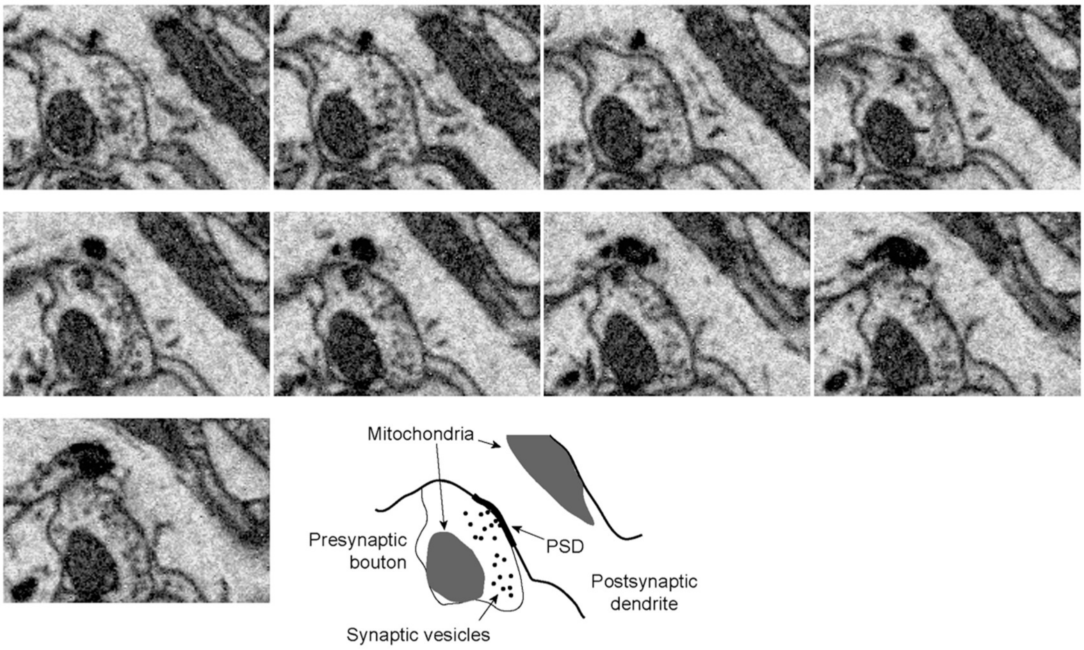

Figure A2-4 Examples of soma and shaft synapses from the training set of SynEM for inhibitory axons (example 3, synapse onto dendritic shaft). Axonal bouton filled half with synaptic vesicles (rest filled with a large mitochondrion). Vesicles approach bouton-shaft interface, interface has slight darkening. No other plausble partner of that bouton with the same characteristics. Image size: 1.9x1.4 µm. Direct link to webKnossos: https://wklink.org/6141

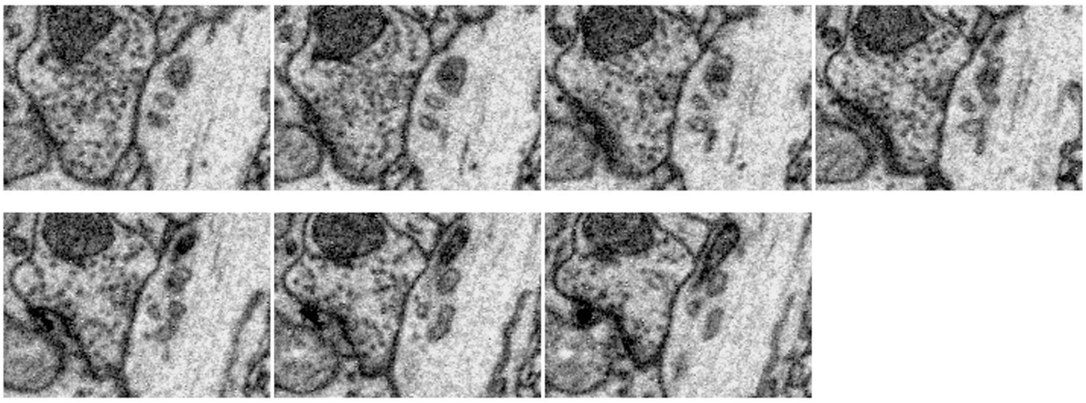

Figure A2-5 Examples of soma and shaft synapses from the training set of SynEM for inhibitory axons (example 4, synapse onto dendritic shaft). Large axonal bouton filled with vesicles and one large mitochondrion. Vesicles approach two processes: dendritic shaft to the right and a glial cell to the left. Apposition of vesicles towards dendritic partner, darkening of that interface. Features visible in several image planes. Image size: 1.9x1.4 µm. Direct link to webKnossos: https://wklink.org/9156

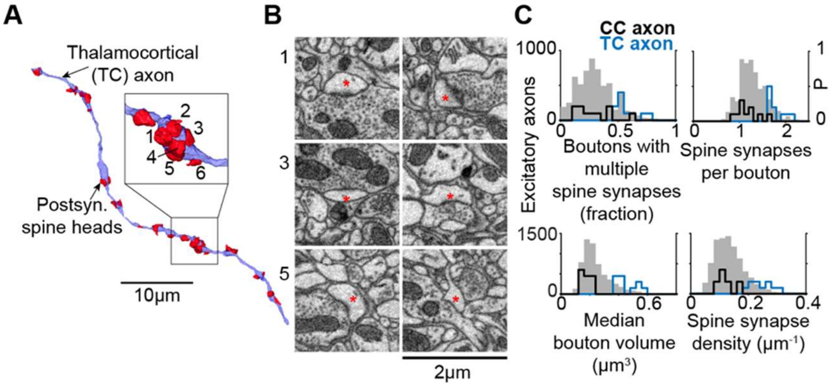

Figure A2-6 Identification of thalamocortical axons from thalamic nucleus VPM by previously established morphological criteria in S1 mouse cortex. **(A)** Example TC axon with indication of postsynaptic spine heads. Note innervation of multiple spine heads by single axonal boutons, example of 6 spine heads targeted by one bouton shown. **(B)** EM images of the six targets of one axonal bouton (see inset in A). **(C)** Criteria for definition of TC axons (from (Bopp et al. 2017)): High frequency of large boutons with multiple synaptic targets (example in A,B; red asterisks, postsynaptic spine heads of same TC bouton). Quantification of these properties for all excitatory axons (gray shaded) and test sets of expert-annotated thalamocortical (TC, blue) and cortico-cortical (CC, black) axons (relative distributions, right axes). See Table A2-1.

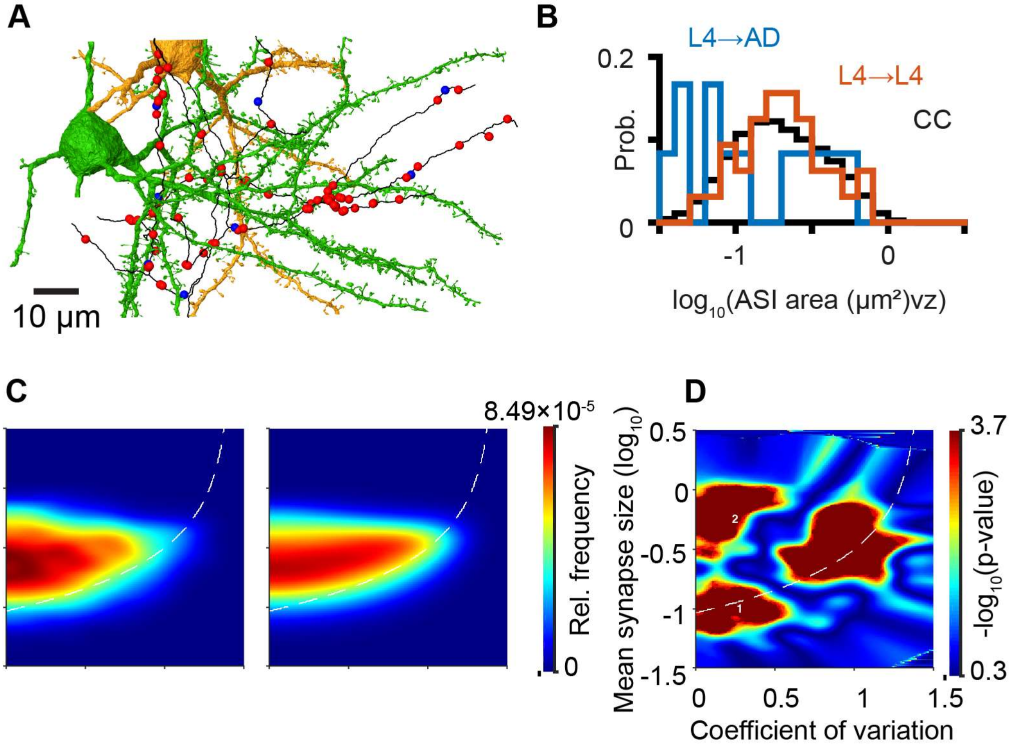

Figure A2-7 Controls for synaptic size consistency analysis. **(A,B)** Comparison of synapse size for output synapses of L4 neurons (L4-to-L4, red, and L4-to-apical dendrites, blue) to overall cortico-cortical synapses in the dataset. Note that L4-to-L4 synapses are indistinguishable from the overall CC synapses, revoking the possibility that the L4-to-L4 connections are the sole source of the subset of larger and more similar synapses found in Figure 2-7. Note also that synapses onto apical dendrites have a trend to be smaller. **(C,D)** Details of the synaptic size consistency analysis (Figure 2-7): data on synaptic size and synaptic strength in pairs of joint synapses (C, left) and randomly drawn pairs of synapses (C, right). Subtraction of the two maps (Figure 2-7F) exposes overrepresented synapse pair configurations. (D) Analysis of statistical significance (one-sided permutation test, 5,000 Monte Carlo samples) yields a map of p-values. Thresholding of this map at p=0.05 and p=0.005 (isolines) yields regions within which the fraction of synapse pairs was counted and reported in Figure 2-7F.

Supplementary tables

Table A2-1 Error assessment for reported quantifications and findings

Result	Relevant figure panels of chapter 2	Methods involved, control performed	Resulting error assessment
Path length measurements	1G, 2I-J, 5A-D, A2-6C	Determination of correction factor for path length measurement based on minimum spanning tree of segment centers (automated reconstruction) compared to skeleton length (manual reconstruction)	Axons: correction factor 0.881 Dendrites: correction factor 0.454 These corrections were applied to all reported path lengths
		Comparison to reported statistical values by Braitenberg and Schüz (1998)	Length density reported by Braitenberg and Schüz (1998): 1-4.1 km of axonal path length / mm^3 0.456 km of dendritic trunk length / mm^3 Axon-dendrite ratio: 2.2:1 – 9:1 Our measurement: 3.37 km of axonal path length / mm^3 0.645 km of dendritic trunk length / mm^3 Axon-to-dendrite ratio: 5.2:1
Volume fraction measurements		Comparison to reported values by Braitenberg and Schüz (1998)	Neuropil volume consists to 34 % of axons and to 49 % of dendrites (35 % of trunk,+ 14 % of spines) Our measurement: Neuropil volume consists to 38 % of axons and to 47 % of dendrites.
		Comparison to reported values by (Mishchenko et al. 2010, Kasthuri et al. 2015)	(Mishchenko et al. 2010): Hippocampal neuropil volume consists to 50 % of axons, to 40 % of dendrites (31 % trunk + 9 % spines), and to 8 % of glial cells. (Kasthuri et al. 2015): 92 % of neuropil volume is occupied by neurites.
Final path length error rate		Comparison of axon reconstructions after all reconstruction steps as reported in the manuscript with a fully manual reconstruction of 10 randomly selected axons from the dataset center. These axons were the same as those used for calibration of human tracing errors in (Boergens et al. 2017). These axons had not been part of any training or validation set here. Error quantification procedure was exactly as in (Boergens et al. 2017).	22 errors (15 of which are continuity errors, see (Boergens et al. 2017)) over total axonal path length of 1.72 mm, i.e. 12.8 errors per mm.
Measurement of spine rates	3B,D	Quantification of spines attached to a dendrite (see section "spine attachment" in Table A2-2): Dendritic shaft path length measurement as described above ("Path length measurements") with correction applied.	88.6 % of automatically detected spine heads got attached to a dendrite. The resulting spine recall is thus 83.6 %. Note this does not include filopodia which have no spine head. Thus systematic underestimation of spine rates by 16.4% (indicated in Figure 2-3).

Definition of apical dendrites (ADs)	3A	First, those automatically reconstructed dendrite agglomerates were identified that intersected with the tangential planes at the top (towards pia) and bottom (towards white matter) of the dataset. All these dendrites (n=423) were inspected by an expert annotator, and the following criteria were used to identify apical dendrites: orientation along the radial cortex axis; unbranched or branches exiting at a shallow angle towards the pia; diameter at least about 0.7 µm; large spines could be immediately found without extensive search. Based on these criteria, n=183 apical dendrites were identified.	AD recall: The procedure used systematically misses oblique branches from ADs not contained in the dataset. The criterion of AD diameter may yield an exclusion of thin ADs from L4 star pyramidal cells or L6 cells. Finally, if the automated dendrite reconstructions failed to continue the dendrite from bottom to top of the dataset, it would be missed. The latter is unlikely due to the large diameter of ADs. Together, these factors reduce the recall of ADs. Consequently, the analysis of AD specificity will yield an underestimate of AD innervation. It is stated throughout the manuscript that the found target specificities with respect to ADs constitute a lower bound. This strengthens the conclusions about inhibitory and excitatory AD specificity (Figure 2-4). AD precision: The following neurites could confound AD identification: basal dendrites of L3 pyramidal cells, axon initial segments, IN dendrites. The criterion of AD alignment with the cortex axis makes confusion with L3 basal dendrites unlikely, since these are predominantly obliquely oriented to the cortex axis. AIS were excluded by the spine criterion. The remaining confounder are IN dendrites oriented along the cortex axis (such as bitufted or bipolar IN dendrites) which may partly be spiny. Since these INs are reported to bear more stubby than mushroom spines, and are a small fraction of neurons (not more than half of the IN population, i.e. less than 7%), this possible misidentification will dilute results about specific innervation by less than 10% (and systematically underestimate specificity, as above). Together, the strategy of AD identification systematically yields an underestimate of AD specific axons, strengthening the conclusions in Figure 2-4.
Definition of smooth dendrites (SDs) as likely interneuron (IN) dendrites	3B	Smooth dendrites were identified as dendrites with spine rate of less than 0.4 per µm (Kawaguchi et al. 2006).	Spine rates were systematically underestimated (see above point “Measurement of spine rates”). This applies to all dendrites and is therefore unlikely to affect the spine rate criterion. However, spine identification primarily relies on the identification of spine heads. If INs have systematically smaller spines with systematically smaller spine heads, recall could be lower. This would further reduce the apparent measured spine rate, thus assuring inclusion of such dendrites in the SD category. Conversely, if excitatory dendrites with peculiar spine morphology exist, their spine rate may be underestimated, and they may be misclassified as SD. Figure 2-3D illustrates that this would correspond to a small (less than 5%) fraction of identified SDs. Possible IN dendrites that are indistinguishable from excitatory dendrites in spine morphology and rate would be missed by the chosen procedure.

Definition of axon initial segments (AIS)	3C	Two procedures were used for AIS identification: First, axons exiting somata contained in the dataset were identified, and the stretch until first branching, first output synapse or onset of myelination was defined as end of AIS. This yielded a set of n = 58 AIS. Secondly, to identify AIS of pyramidal cell somata from L3 that would enter the dataset from the top, we identified neurites oriented along the cortex axis that intersected with the upper tangential dataset border and had a part classified as axon linked to a part classified as dendrite (since the AIS did not contain axonal features such as vesicles). All of these n=533 agglomerates were inspected by an expert annotator and assigned to the AIS class if no spines were found; the lower end of the neurite either intersected with the lower dataset border or branched into axonal branches or became myelinated. This yielded an additional set of n=58 AIS.	The AIS exiting from cell bodies can be considered rather faithfully identified based on their unique properties. For the AIS without a soma in the dataset, possible confounders are non-spiny IN dendrites and obliquely oriented AIS. The latter are expected to be missed, and would likely be misclassified into the SD class. Of the 58 AIS connected to somata, 55 were rather well aligned with the cortex axis. The estimate rate of missed AIS is thus 5.2%. As to non-spiny IN dendrites: These could be confounding those AIS that did not make output synapses, did not branch into axonal branches, and did not get myelinated. These (n=27 of 116 AIS, i.e. 23.3%) constitute an upper bound for the false-AIS identifications in the data. Together, the definition of AIS is estimated to be of >95% recall and >76% precision. Therefore, the finding of absence of AIS-specific innervation in L4 is unlikely to be affected by the quality of the AIS definition (see below for further controls for this finding).
Classification of axons as inhibitory vs. excitatory	3E, 4A-B, E,G-I, 5A-D,H, 6C-D	Using a high fraction of primary spine innervations as criterion for the definition of excitatory axons implied the following caveats: systematic underestimation of spine-targeting synapses; existence of excitatory axons with preference for establishing shaft synapses. Both were addressed as follows.	
		Underestimation of spine synapses: This could be caused by merger errors between inhibitory and excitatory axons. 25 randomly sampled axons with 25% to 50% primary spine synapses were inspected to estimate the prevalence of merge errors.	To reduce merge errors, all axons with primary spine synapse fractions between 20% and 50% were split at all (true or merger error-induced) branch points, reducing the number of axons between 20 and 50% spine synapse fraction from 528 to 192 of axons with at least 10 synapses.
		Misidentification of shaft-preferring excitatory axons: In reports from cat L4 (McGuire et al. 1984), axons of L6 pyramidal neurons were described to form most boutons at the end of short side twigs (33 / 35). 72 % of their synapses were onto dendritic shafts of smooth / sparsely spiny cells. To test for these, we randomly sampled 10 shaft synapses onto spiny dendrites, reconstructed the axons and inspected them for these properties.	No axon (0/10) showed the feature of frequent end boutons onto shafts.
		Furthermore, we randomly sampled 25 axons with 25% to 50% primary spine synapses, less than 25% secondary spine synapses and less than 10% soma synapses.	None of these axons (0/25) had clear asymmetric primary spine synapses.
		Reports from juvenile rat L4 indicated a high rate of L4 spiny neuron -to-L4 spiny neuron synapses onto shafts (Feldmeyer et al. 2005).	We investigated n=3 output axons of spiny neurons (n=112 synapses total) in our data and found spines as synaptic targets in 66, 76 and 84 % of cases, making it unlikely that

			excitatory L4 axons preferentially target dendritic shafts in our dataset.
Identification of TC axons	A2-6A-C, 5A-D, 6A-B,D,F,G,H-K, 7I-J	TC axons were identified using the detailed published analysis by (Bopp et al. 2017). This work reports that VPM boutons in L4 of mouse S1 cortex are unique in their size and the number of synapses based on electron microscopy with immunoreactive staining for VGLUT2.	Based on (Bopp et al. 2017), the estimated precision and recall for individual VPM boutons is 79.8% and 60.9%, respectively. The detection of TC processes is improved by considering axons with at least ten synapses instead of individual axonal boutons. Then, TC axon identification is estimated to carry a precision of up to 95.9% at 96.9% recall.
		Potential confounders: overlapping feature distributions between VGLUT2$^+$ and VGLUT2$^-$ boutons; errors in feature calculation for axon reconstructions.	Split and merge errors in axon reconstructions, and false negative synapses lead to a false negative classification of true TC axons, which we estimate to yield a recall of about 70% for TC axons. Note that this could only contribute to an overestimation of the TC gradient if recall was inhomogeneous over cortex depth. Since however TC axons mostly enter from the WM-oriented side of the sample, and detection operates on the entire TC axon in the dataset, such a local TC recall effect is rather unlikely. The false discovery rate of spine synapses (6%; see Table A2-2) is unlikely to introduce false positive TC axons, such that TC axon detection precision can be estimated to be as high as determined above (above 95%).
Determination of axonal target specificities	4D-I, 6H-K	For the results on connectomically defined axonal target preferences (Figure 2-4), we identified the following possible confounders: merging of axons; splits of axons; incorrect automated synapse detection; confusion of excitatory and inhibitory axons (see above) with misinterpretation of excitatory target specificities. These were controlled for as follows:	
		Remaining merge errors in axon reconstruction	The merging of axons of different types results in a dilution of axonal target specificities. The detected target specificities (Figure 2-4) thus correspond to a subset, with the fraction of axons per specificity class being lower bounds. For lack of AIS specificity, see below.
		Control by artificially splitting all reconstructed axons at (true and merge error-induced) branch points	When repeating the analysis of target specificities with a set of axons in which all axons were artificially split at branch points, the detected target specificities of inhibitory and excitatory axons remain unchanged. For lack of AIS specificity, see below.
		Remaining split errors in axon reconstruction	The incorrect splitting of axons would yield an erroneous count of axons, but would not affect the (average) distribution of synaptic targets of that axon class (unless extreme inhomogeneities in axon target distribution were expected). If the incorrect splitting of axons reduced the number of synapses per axon it would decrease the sensitivity of our methods; the fact that we were able to detect the described axonal specificities nevertheless (Figure 2-4) indicates that this effect did not dominate the analysis. For lack of AIS specificity, see below.

		Effect of false positive synapse detection	The rate of false positive spine and shaft synapse detections were measured separately by proofreading 20 random synapses per postsynaptic target class. The specificity analysis for inhibitory axons was then repeated 20 times, with synapses being randomly removed proportionally to the false positive rate. The inhibitory specificities remained statistically significant across all rounds, with AD specificity most sensitive to these control measurements.
		Confusion of excitatory and inhibitory axons. The report of the target specificity of excitatory axons (Figure 2-4) could have been a result of misclassifying inhibitory axons (for which such specificity had been reported before) as excitatory. To control for this, we randomly selected 5 excitatory axons, each, with specificity for smooth, apical or proximal dendrites.	All 15 inspected axons identified as specific show clear primary spine innervations with asymmetric synapses. Since some axons contained merge errors, we repeated the analysis with split axons, yielding the same results. We conclude that the specificities of excitatory axons are stable against these controls.
		All confounders reported would, if anything, yield an underestimation of the level of synaptic target specificity, and an underestimation of the fraction of axons exhibiting such specificity. Therefore, all quantitative values in Figure 2-4 are interpreted as lower-bound measurements. One exception is the lack of specificity for AIS targets, which could have been caused by the above confounders.	
		Lack of specificity of axons for AIS in L4. This could have been caused by the confounders listed above. To control for this, we manually inspected 10 AIS innervating axons for merge errors.	2 out of 10 axons were found to contain merge errors which could not explain the lack of specificity. While a large fraction of AIS synapses were FP detections, an independent manual control reconstruction (A. Gour, pers. Communication) confirmed the lack of AIS specificity in L4 axons.
			The specificity analysis was repeated using a multinomial null model with little effect on the first-hit probabilities and no effect on the detected target specificities.
Peters' rule: comparison between Peters' models	5A-D	Instead of path length fractions, fractions of surface area could be used (which would also include somatic surface that has no path length equivalent). Dendritic spine length can be considered as path length, as well.	When computing the model predictions (Figure 2-5A-D) with surface area instead of path length, and when including or excluding dendritic spine neck length, all conclusions were stable.
		Differential precision and recall for the automated detection of spine vs. shaft synapses could confound the observed underestimates of smooth dendrite innervation. Correction of synapse counts as count * precision / recall	When accounting for precision and recall of synapses, all conclusions were stable.
		The finding of substantial AD innervation by TC axons (since not found by Peters) was inspected for 10 random detected TC-to-AD innervations.	In 2 of 10 cases, the synapse was a FP detection of SynEM (Staffler et al. 2017). 1 AD definition was disputable (oblique AD dendrite vs. non-AD). Recall could be 70-80%. Therefore, only deviations of the Peters' predictions from actual innervation of more

			than 25% were considered significant and are indicated in Figures 2-5A-D (range 0.75-1.25 was shown in white)
Geometric prediction of synaptic innervation for individual axons	5E-H	We corrected the observed innervation variance for the variance contribution by binomial sampling, which is a relevant source of variability for low n measurements. This correction overcompensated the measured variance in the case of innervation of smooth dendrites by inhibitory axons. We therefore compared the prediction in the uncorrected form and found that it was similar to the prediction for inhibitory innervation of AIS	Curve for AIS in Figure 2-5H, bottom right panel, is representative of SD targets as well.
TC synapse gradient	6A-G	Other synapse distributions	Our data: TC synapse density increases by 93% (relative to pia-facing end of EM volume) over ~50 µm. Gradient is not present in IN synapses or CC synapses.
		Literature controls	In hindsight, the Panel 3f of (Oberlaender et al. 2012) shows indications of an increase in the estimated TC bouton density within D2 barrel of rat by 83% over first 50 µm of L4 (relative to L3/L4 border).
Correlation of other synaptic input to the TC input fraction	6H-K	Search for correlation among 4 input fractions, correction for multiple testing, see Statistical Methods.	Significance after correction for multiple testing, both for single-dendrite and per-neuron correlation.
		Control for possible distance-dependent effect: test if TC input fraction was related to the length of the primary dendrite.	No correlation between TC input fraction and length of primary dendrites.
		Control for influence of dendrites with no AD-preferring inhibitory innervation (zero values in Figure 2-6I-K).	Correlations are similar or stronger when only considering measurements with at least one inhibitory innervation of the AD and Soma preferring type (Figure 2-6I-K).
Analysis of synapse pairs	7	For the result on synaptic size homogenization the following potential confounders were identified: false multi-synaptic connections due to merge errors in axons or false positive synapse detections; missed multi-synaptic connections due to false negative synapses; size-dependent bias in synapse detection.	To prevent the effect of false multi-synaptic connections, all analyses in Figure 2-7 were performed after splitting excitatory axons at all branch points. This eliminates false connections and reduces true connections in an unbiased manner. Based on the 6% false discovery rate of spine synapses, the fraction of false bi-synaptic connections is estimated to be less than 12%. False negative spine synapses could result in bi-synaptic connections being missed, thus reducing the sensitivity of the analysis. FN synapses could also cause false detection of, e.g., tri-synaptic connections as bi-synaptic. Due to the low prevalence of connections with more than two synapses, the latter error is assumed to be small. The detection of synapses is size-dependent (Staffler et al. 2017). To reduce this potential error source, the bi-synaptic connections are compared to random pairs sampled from the

		pool of all synapses in bi-synaptic connections. The null model thus accounts for synapse size-dependence.
	Usage of axon-spine interface area (ASI) instead of postsynaptic density area (PSD). This could add variability to the measurement.	We followed the same strategy as (de Vivo et al. 2017), whose experiments were performed under rather similar conditions (SBEM, mouse S1 and M1 cortex). For the relation between ASI and PSD area: This was subject to earlier work: Volumetric ssTEM images from L2/3 of adult rat barrel cortex were used in (Cheetham et al. 2014) to quantify ASI and PSD areas for spine synapses and found these to be highly correlated (R^2 = 0.89). No evidence of a size-dependent relative variance that could have induced a broadened CV distribution for large synapses was found in (Cheetham et al. 2014).

Table A2-2 Methodological error considerations

Method	Error quantification performed	Resulting error assessment
Automated volume segmentation (SegEM)	Published inter-error distance measurement of SegEM ((Berning et al. 2015); by comparison to manually traced neurites) CNN parameters (see Table 1 in (Berning et al. 2015)): 20130516T204040$_{8,3}$ Watershed parameters "whole cell segmentation" (see Table 2 in (Berning et al. 2015)): θ_{ms} = 10 vx, θ_{hm} = 0.25	Results for automated segmentation (excluding agglomeration and FocusEM, see below): Inter-error distance: 4.48 μm Inter-split distance: 4.56 μm Inter-merge distance: 241.52 μm As reported in Table 2 of (Berning et al. 2015). (2-vx overlap)
Automated synapse detection (SynEM): synapses onto spines	Classification accuracy as reported in (Staffler et al. 2017). Error measurement by comparison to consensus expert annotations in ((Staffler et al. 2017); Supplemental Synapse Gallery).	Precision of synapse detection (including partner detection): 94% precision; recall 89%
	Measurement of false-positive synapses by inhibitory axons onto spines ("secondary spine innervations") after full axon reconstruction. Comparison to expert annotation.	FP rate for *spine synapses* by inhibitory axons (these comprise less than one fourth of inhibitory synapses): proximal dendrites: 33.3 % (6 / 18) apical dendrites: 33.3 % (6 / 18) smooth dendrites: 25 % (4 / 16) other dendrites: 35.3 % (6 / 17) These false positive rates were taken into account for analysis of inhibitory specificities (Figures 2-4D-I) see Table A2-1. For the effect of synapse size on detection accuracy see below. Precision and recall were taken into account for the analysis of Peters' rule (Figures 2-5A-D), see Table A2-1.
Synapses onto shafts (Figures A2-4-5)	Improved version of shaft synapse detection from ((Staffler et al. 2017); added CNN predictions as additional texture filters in SynEM; training was restricted to shaft and soma synapses (extended training set), see Methods for details). Error measurement by comparison to consensus expert annotations.	Performance on test set of inhibitory shaft synapses: 92% precision (68 / 74) 69% recall (68 / 98) The lower recall for shaft synapses could yield errors in fractional target innervation measurements (Figure 2-4) if recall was dependent on the target class. This was controlled by manual annotations (see Table A2-1, section "Determination of axonal target specificities").
	Identification of false-positive synapses by inhibitory axons onto shafts/non-spines after full axon reconstruction. Comparison to expert annotation.	FP rate for shaft/non-spine synapses by inhibitory axons onto somata: 5 % (1 / 20) proximal dendrites: 5.3 % (1 / 19) apical dendrites: 29.4 % (5 / 17) smooth dendrites: 5.9 % (1 / 17) axon initial segments: 22.2 % (4 / 18)

		other dendrites: 17.7 % (3 / 17) These false positive rates were taken into account for analysis of inhibitory specificities (Figure 2-4D-I), see section ”Determination of axonal target specificities” of Table A2-1. Precision and recall were taken into account for the analysis of Peters’ rule (Figures 2-5A-D), see Table A2-1.
Synapses onto somata (Figures A2-2-3)	Detection of synapses onto somata similar to the detection of synapses onto shafts (see above). Error measurement by comparison to consensus expert annotations of inhibitory axons.	Performance on test set of soma synapses: 85% precision (33 / 39) 97% recall (33 / 34) This was taken into account when reporting somatic innervation specificity (see Table A2-1, section ” Determination of axonal target specificities”, Figure 2-4D-I) Note that synapse detection was best for larger synapses (Suppl. Synapse Gallery in (Staffler et al. 2017)), with 100% recall for synaptic interfaces larger than 0.25 µm^2.
Automated classification of neurite types (axon, dendrite, spine head, glia) (TypeEM)	Classification performance measured using an expert-annotated dense test set (available at +TypeEM/+Data/tracings/ex145-07x2-roi2017/dense-v2/region-4.nml)	Precision (P) and recall (R) for detection of axons: 91.8 % (P), 92.9 % (R) dendrites: 95.3 % (P), 90.7 % (R), astrocytes: 97.2 % (P), 85.9 % (R), spine heads: 92.6 % (P), 94.4 % (R) 415,797 spine heads detected
Automated neurite agglomeration (connectEM): dendrites	Parameters were optimized by grid search. The automated reconstructions were compared against 8 ground truth tracing of dendritic trunks (3.18 mm total) in terms of path length recall, split rate, merge rate. Percolation of merge errors was evaluated by the volume contained in the ten largest agglomerates. The parameter set was chosen as to optimize split rate and recall at a merge rate close to zero. The tracings used to optimize the parameters are available in +connectEM/evaluationData	Identified parameters: Minimum border size: 300 vx Minimum segment size: 500 vx Minimum dendrite probability: 30 % Minimum edge continuity probability: 98 % Corresponding errors: 2.516 mm of ground truth tracings are covered by dendrite reconstructions yielding 79.2 % path length recall 43 split errors (ignoring spines) yielding 58.5 µm inter-split distance 1 merge error yielding 2.516 mm inter-merger distance Note that the dendrite split rate was strongly dependent on dendrite size; therefore large ADs were recovered. Their density was in the range of the expected density of pyramidal cells from infragranular layers (based on data from rat S1 (Meyer et al. 2010) in the volume 214 ADs from L5 would be expected, which would indicate a recall of about 85%.).
Axons (initial agglomeration)	Parameters were optimized using the method described for dendrites. The agglomerates were compared against 10 ground truth tracings of axons (1.72 mm total).	Identified parameters: Minimum border size: 60 vx Minimum segment size: 300 vx Minimum axon probability: 50 %

	The tracings used to optimize the parameters are available in +connectEM/evaluationData/new_axon_gt_ROI2017	Minimum edge continuity probability: 97 % Corresponding errors: 0.981 mm of ground truth tracings are covered by axon reconstructions yielding 57.0 % path length recall 320 split errors yielding 3.1 µm inter-split distance 2 merge errors yielding 491 µm inter-merger distance
Axons (directionality-based growth)	Parameters were optimized using the method described for dendrites. The agglomerates were compared against 10 ground truth tracings of axons (1.72 mm total). The tracings used to optimize the parameters are available in +connectEM/evaluationData/new_axon_gt_ROI2017	Identified parameters: Minimum latent score: 0.8 Minimum border size: 40 vx Minimum directionality score: 0.9 Minimum axon probability: 30 % Minimum edge continuity probability: 80 % Number of steps: 10 Corresponding errors: 1.299 mm of ground truth tracings are covered by axon reconstructions yielding 75.5 % path length recall 363 split errors yielding 3.6 µm inter-split distance 19 merge errors yielding yielding 68.4 µm inter-merger distance
FocusEM: Detection of annotator query locations (split errors)	Identification of qualitatively sound parameters. Note that the results of all methods contributing to neurite reconstruction were summarily evaluated by comparison of the final reconstruction to fully manually traced neurites (see Section “Final path length error rate” in Table A2-1 for details).	Identified parameters: Latent score: 0.5 Segment directionality: 0.8 Distance cut-off: 600 nm (see +connectEM/calculateDirectionalityOfAgglomerates.m)
Detection of annotator query locations (merge errors, “chiasmata”)	Iterative refinement by inspection of random subsets of detections by experts. Note that the results of all methods contributing to neurite reconstruction were summarily evaluated by comparison of the final reconstruction to fully manually traced neurites (see Section “Final path length error rate” in Table A2-1 for details).	Identified parameters: Radius of outer sphere: 10 µm Radius of inner sphere: 1 µm Minimum distance from center: 2 µm Distance cut-off: 2 µm Corresponding errors: Precision of 90-100% (10/10) for 4-fold chiasmata Precision of 75% (15/20) for 3-fold chiasmata
User queries in webKnossos “flight mode”; final reconstruction	All methods contributing to neurite reconstruction were summarily evaluated by comparison of the final reconstruction to fully manually traced neurites (see Section “”Final path length error rate in Table A2-1 for details).	
Spine head attachment: Automated	Parameters for automated spine attachment were optimized on a set of ground truth annotations by “grid search” in parameter space. Ground truth tracings available in +ConnectEM/+Spine/+Data/attachment-	The following parameters were used: Maximum astrocyte probability: 100 % Maximum axon probability: 80 % Minimum dendrite probability: 0 % Minimum edge probability: 25 % Maximum number of steps: 10

	ground-truth	58.9 % of spine heads were automatically attached (evaluated for spine heads at least 10 µm from dataset boundary) Automated spine density: 0.672 spines per µm of dendritic shaft length
Manual	Spine heads that did not get attached to a dendrite by automation (n=164,969) were manually annotated (see Methods). 49,000 of the detected spine heads (11.8 % of total) were less than 3 µm from dataset border and were excluded from manual annotation. The precision of the spine head attachment was evaluated on a randomly selected subset of attached spine heads (n=24).	Resulting spine head attachment recall: 88.6 % of detected spine heads further than 10 µm from dataset boundary. This corresponds to an attachment rate of 96.3 % when correcting for false positive spine head detections (see section "Automated classification of neurite types"). Resulting dendritic spine density: 0.959 per µm of dendritic path length. Resulting spine head attachment precision: Around 92 % (22 / 24) of the attached spine heads were connected to the correct dendrite.

Supplementary movies

The following supplementary movies are available for download at:
https://www.science.org/doi/10.1126/science.aay3134

Movie A2-1

Gallery of soma-based single-cell reconstructions.

Movie A2-2

Example of FocusEM queries for ending and merger resolution.

The user is presented with a new task start point automatically after each finished task to reduce annotation delays. The queries are limited to a certain sphere around the start location, since the possible trajectories in the chiasma configurations (Figure 2-2H) are known. Light-gray shading in the user viewport indicates end of task.

A3. Appendix to chapter 3

Detailed treatment of models: structural properties

ER-ESN. We first considered a directed Erdős-Rényi (ER) model (Figure 3-2b-c) (Erdős and Rényi 1959). ER graphs were, for example, proposed as the computational substrate of Echo State Networks (ESNs) (Jaeger and Haas 2004, Buehner and Young 2006, Xue et al. 2007, Lukoševičius and Jaeger 2009, Jaeger 2010, Pascanu and Jaeger 2011, Lukoševičius et al. 2012, Yildiz et al. 2012, Manjunath and Jaeger 2013). In these studies, single neurons were allowed to make both excitatory and inhibitory synapses. However, to obey the biological constraint of neurons establishing either excitatory or inhibitory synapses - "Dale's law", (Dale 1935) - we implemented ER-ESNs to comprise separate excitatory and inhibitory neuron populations. Connection probabilities were independent of inter-soma distance (Figure 3-2b, cf. the next model). The reciprocity of ER networks equals the excitatory connectivity, $r_{ee} = p_{ee}$, satisfying the experimentally observed constraints (Figure 3-2c).

EXP-LSM. We next considered pairwise random but distance-dependent connectivity (Figure 3-2b-c). Such architectures have been proposed as models for real-time computations without stable states (Liquid State Machines, (LSMs), (Maass et al. 2002, Maass and Markram 2004, Maass et al. 2004, Maass et al. 2004, Maass et al. 2006, Auer et al. 2008, Buonomano and Maass 2009, Sussillo and Abbott 2009, Manevitz and Hazan 2010, Hazan and Manevitz 2012, Probst et al. 2012, Sussillo and Barak 2012). To model neuronal connectivity dependent on the distance between neuronal cell bodies, soma positions were independent and identically uniformly distributed within a L4 model cube of size 300 μm (Figure 3-2a). We assumed the pairwise connection probabilities $p_e(d_s) = \exp(-d_s/\lambda_e)$, $p_i(d_s) = \exp(-d_s/\lambda_i)$, to decay exponentially with inter-soma distance d_s (Figure 3-2b). The decay lengths λ_e, λ_i were adjusted to satisfy the L4 connectivity constraints (Figure 3-1d). The reciprocity constraint was then found to be also satisfied (Figure 3-2c). Notably, the distance dependence of the EXP-LSM model implied a reciprocity higher than in ER networks, but was still within the experimentally observed regime (Figure 3-2c).

LAYERED. We next investigated the hypothesis of hierarchical, layered processing in local cortical networks (Figure 3-2d). Layered models were first proposed as the multi-layer perceptron (Rosenblatt 1962). Many studies of early sensory processing, particularly visual processing made use of such models (Fukushima 1979, Fukushima 1980, Griffith 1963, Hubel and Wiesel 1962, Ivakhnenko 1971, Ivakhnenko and Lapa 1965, LeCun et al. 1989, LeCun et al. 1998, Malsburg 1986, Rosenblatt 1962, Schmidhuber 2015). Pure multi-layer perceptrons lack reciprocated connections and thus violate basic circuit properties found in local cortical networks. When instead considering a stacked recurrent neural network, however, a layered model could be made comply with the observed circuit constraints. For this, excitatory neurons were uniquely grouped into sequentially ordered layers. Connections within a layer were implemented using a pairwise connection probability $p_{e,l} > 0$. However, only unidirectional connections from one layer to the subsequent layer were allowed with pairwise connection probability $p_{e,f}$ (Figure 3-2d). Inhibitory neurons were not organized in layers but provided global inhibition (Figure 3-2d). Obviously, as the number of layers increases, high average reciprocity and high average pairwise connectivity become mutually exclusive (Figure 3-2e), such that the number of layers in a LAYERED model is limited by the connectivity and reciprocity constraints. For $n_l = 2$ to $n_l = 4$ layers, the connectivity constraints (Figure 3-2f-g) could be robustly satisfied.

SYNFIRE. We then investigated embedded synfire chains (Figure 3-2h). A variety of synfire chain-like models has been proposed (Griffith 1963, Abeles 1982, Abeles 1991, Bienenstock 1995, Herrmann et al. 1995, Hertz and Prügel-Bennett 1996, Diesmann et al. 1999, Gewaltig et al. 2001, Levy et al. 2001, Aviel et al. 2003, Mehring et al. 2003, Abeles et al. 2004, Aviel et al. 2005, Goedeke and Diesmann 2008, Kumar et al. 2008, Schrader et al. 2008, Trengove et al. 2013, Zheng and Triesch

2014). Some of these models were defined as structurally separated neuronal pools with sequential activation chains (Griffith 1963, Abeles 1982), similar to the LAYERED model introduced above, but for $p_{e,l} = 0$ (Figure 3-2d). Most studies however considered embedded synfire chain models, in which synfire pools were allowed to overlap (Abeles 1982, Abeles 1991, Bienenstock 1995, Herrmann et al. 1995, Aviel et al. 2003, Aviel et al. 2005, Schrader et al. 2008, Trengove et al. 2013). We considered embedded synfire chains (Trengove et al. 2013). Excitatory synfire pools were uniformly drawn with replacement. Pools were then sequentially connected all-to-all (Figure 3-2h). The neuronal populations belonging to a synfire pool could overlap (Figure 3-2h) such that reciprocated connections emerged during this process (Figure 3-2h). Connectivity and reciprocity were found to lie within the experimentally observed constraints for pool size s_{pool} between 80 and 300 and the number of pools n_{pool} between 60 and 190 (Figure 3-2i,j).

FEVER. Then, the feature-vector recombination (FEVER) model (Druckmann and Chklovskii 2010, Druckmann and Chklovskii 2012) was considered, which was proposed to allow sustained neuronal representations on macroscopic time scales (seconds; “short-term memory”) (Figure A3-2a). Here, connectivity is based on the neurons’ receptive fields represented by feature vectors: The postsynaptic neurons' feature vectors are additively and sparsely recombined to approximate the presynaptic neuron's own feature vector (Figure A3-2a). The FEVER model in its original formulation yielded lower pairwise connectivity (range 0-0.1) and higher reciprocity (range 0.45-0.6) than given by the barrel circuit constraints (Figure A3-2b). We therefore constructed an adapted FEVER model by initializing the connectivity using an ER model with connectivity $p_{\text{init},c} > 0$, $c \in \{e, i\}$. Subsequently, connections were added according to the FEVER rule, which now had to incorporate the initial random connections, as well. As a consequence, the average FEVER rule error $\|\mathrm{D} - \mathrm{DW}\|$ of a modified FEVER network with $f_d = 200$ and initial excitatory connectivity 0.14 was 10% larger than the average FEVER rule error of an unmodified FEVER network with $f_d = 400$ (see Figure A3-2c). In fact, a fraction of the resulting modified FEVER model instantiations complied with the barrel circuit constraints (Figure A3-2b). However, the question whether these modified models still provided the functional properties originally proposed for the FEVER networks had to be investigated (see below).

API. Lastly, we investigated the anti-phase inhibition (API) model (Figure A3-2d), which was originally proposed to explain contrast invariant stimulus tuning in the primary visual cortex (Troyer et al. 1998, Miller et al. 2001, Hansel and van Vreeswijk 2002, Kayser and Miller 2002, Hansen and Neumann 2004), and has been extended to the primary somatosensory cortex (Miller et al. 2001). In the original API model, a hidden feature vector is associated with each neuron, and connections between neurons are determined based on a connectivity rule that depended only on the correlation between the feature vectors of the pre- and postsynaptic neurons (Figure A3-2d). The shape of this connectivity rule determined the pairwise connectivity and reciprocity. For excitatory presynaptic neurons k with feature vector $\mathbf{d}_k$, connections were not established with a candidate postsynaptic neuron l if the cosine similarity of their feature vectors was negative ($c_{\text{sim}}(\mathbf{d}_k, \mathbf{d}_l) < 0$), and the connection probability was set to rise steeply for positively correlated feature vectors (Figure A3-2d). Similarly for inhibitory neurons, connections were not established if the feature vector of the candidate postsynaptic neuron was positively correlated, but connection probability was set to rise steeply for increasingly negative feature vector correlations. The particular shapes of this connectivity rule as proposed in the original model, however, yielded too many reciprocated excitatory connections (Figure A3-2e-g), reciprocity range 0.8-1) since bidirectional connections between neurons with similar feature vectors were strongly favored. We therefore adapted the shape of the API connectivity rule to reduce this bias (Figure A3-2d), decreasing the frequency of reciprocal connections and satisfying the local cortical circuit constraints for excitatory connections (Figure A3-2f,g). For inhibitory connections, the constraint to reach connectivity beyond 50% (Figure 3-1d) was not fulfillable with the original API connectivity rule (Figure A3-2d,e), which yielded an effective limit at 50% connectivity. We therefore modified the API connectivity rule for inhibitory connections to allow these also between neurons with negative cosine similarity of their feature vectors (Figure A3-2d-g).

Thus, in summary, 3 of the 7 models (ER-ESN, EXP-LSM, SYNFIRE) satisfied the biological circuit constraints in a barrel module as they had been originally proposed; 4 models (LAYERED, STDP-SORN, FEVER, API) did not satisfy these constraints in their original formulation. These however were made comply with these circuit constraints by minor (LAYERED, API) or more substantial (STDP-SORN, FEVER) alterations. We had to investigate next whether these altered models could still perform the computations they had been proposed for, tested in the context of potentially relevant stimulus transformations in a barrel module.

STDP-SORN. We next considered a model in which local cortical circuity is shaped mainly by generative local learning rules such as spike timing dependent plasticity (STDP) (Gerstner et al. 1996, Markram et al. 1997); such rules have been used in networks labeled self-organizing recurrent neural networks (SORN) (Lazar et al. 2007, Lazar et al. 2009, Zheng et al. 2013, Zheng and Triesch 2014, Aswolinskiy and Pipa 2015). Here, cortical circuity is formed by STDP, synaptic normalization, intrinsic plasticity and structural plasticity (Figure A3-2h-l). The original SORN formulation yielded however substantially lower excitatory reciprocity than found experimentally (range 0-0.0038 compared to 0.15-0.45, (Figure A3-2m) and we therefore introduced the following modifications to the SORN model: originally, the STDP rule increased the synaptic weight by an amount η_{STDP} whenever the presynaptic neuron fired one time step before the postsynaptic one and decreased it by η_{STDP} if the firing order was reversed (Figure A3-2i). We modified this rule such that the synaptic weight was also increased by η_{STDP} if both neurons fired at the same time (Figure A3-2i). Originally, the structural plasticity rule prescribed a fixed number of synapse creation attempts per time step (Figure A3-2k). We introduced a homeostatic structural plasticity rule which attempted to keep the number of connections constant (Figure A3-2j,k). Synapses were added with initial weight c_{add}. The synaptic weight developed over time following the STDP rule (Figure A3-2l). Together, these alterations of the STDP-SORN model yielded pairwise connectivity properties that complied with the experimentally observed ones in the barrel circuit (Figure A3-2m).

Detailed functional investigation of models

To investigate the models' functional properties, we considered the sensory input to a barrel module, which is dominated by the response to the aligned principal whisker (Brecht and Sakmann 2002). An awake behaving mouse is frequently swiping its whiskers across objects with different surface texture (von Heimendahl et al. 2007, Prigg et al. 2002, Carvell and Simons 1990, Guić-Robles et al. 1989). When doing so, neurons in thalamus and cortex have been shown to exhibit specific responses to troughs and elevations in the surfaces the whisker is exposed to ("slip – stick events", (Jadhav et al. 2009, Wolfe et al. 2008)). We therefore considered the discrimination of surface textures, represented as height – correlated activity, as a simple realistic model test, and exposed the ER-ESN, EXP-LSM and LAYERED models to such a texture discrimination task. The API model had been already specifically proposed for rodent S1 (Miller et al. 2001), and we therefore tested the anti-phase stimulus representation property directly. The FEVER model had been proposed to allow extended representation of sensory stimuli on time scales relevant for short-term working memory, so we used the correlation between the representations in the network at the beginning and end (after 20 neuronal time constants) as a test of model functionality. Finally, the STDP-SORN and SYNFIRE models have so far been mainly tested for basic stability properties, namely the lack of correlated firing modes in SORN (Lazar et al. 2009) and the faithful transmission of activity across pools in SYNFIRE

(Trengove et al. 2013), which we therefore considered as the required readouts for model functionality for SORN and SYNFIRE.

ER-ESN, EXP-LSM, LAYERED. The ER-ESN, EXP-LSM and LAYERED models were tested using a texture classification task (Figure A3-1a). We assumed that texture elevation Δz (Figure A3-1a,b) is converted into a temporal activity when the whisker is sweeping over that surface (Figure A3-1b, see above). Such elevation profiles were sampled from 7 textures (Figure A3-1a,c) and presented as network input activity (Figure A3-1d,e, this would correspond to thalamic input to layer 4). The neurons in the presumed L4 network were then connected to dedicated readout neurons, $o_1, \ldots, o_7$, whose activity was interpreted as (continuous) texture classification readout (Figure A3-1e, top). In order to extract a texture class prediction from the activity of the output neurons, their activity was integrated over the second half of the texture presentation, and the highest activity was interpreted as texture choice (Figure A3-1f). For the ER-ESN and EXP-LSM models, only the readout projections from the L4 pool to $o_1, \ldots, o_7$ were trained. In the LAYERED model, all inter-layer projections $p_{e,f}$ (Figure 3-2d) were trained in addition. Training was performed using the "Adam" adaptive moment estimation method (Kingma and Ba 2014).

While the performance of the LAYERED model was substantially higher than that of ER-ESN and EXP-LSM models (accuracies 90.8% vs 66.1%, 66.5%, Figure A3-1g), all models performed substantially above chance level (chance level 14% accuracy, Figure A3-1g).

SYNFIRE. Synfire chains were proposed as a model to explain synchronous propagation of cortical activity (Abeles 1982). We therefore tested whether the initial activation of a single neuron pool in our modified SYNFIRE model still yielded a propagation of activity along the embedded SYNFIRE chain in a sequential manner (Figure A3-1h). For this we first activated all neurons in one neuron pool, and then tracked whether the subsequent pools were also activated, and in the right sequence. We considered a pool to be activated if at least half of its neurons were active (Figure A3-1i). We found that the SYNFIRE model did indeed support stable propagation within the imposed circuit constraints (Figure A3-1h,i). The average activated fraction of the chain f_{ca} was substantially above 95% for pool sizes $s_{\mathrm{pool}} \geq 100$ (Figure A3-1j) and reached about 80% for $s_{\mathrm{pool}} = 80$ (Figure A3-1j). Since the structural constraints had defined a range of pool sizes 80-300 (Figure 3-2h-j), the modified SYNFIRE model was considered to still be sufficiently viable.

FEVER. For the adapted FEVER model, we evaluated whether it could faithfully maintain a given input stimulus representation over time, as proposed in the original work in the context of short-term memory (Druckmann and Chklovskii 2012). We compared the imprinted state at the beginning of a trial (imposed as activity in (Druckmann and Chklovskii 2012) to each neuron) to the represented state at the end of a trial (using the cosine similarity as measure (Figure A3-3a,b)). In fact, the representation was robustly stable over time for a range of feverization ratios f_r (range 0.5-1, Figure A3-3b). Thus, although the FEVER error had increased by 11% compared to the original model (Suppl. Fig. 2c), the modified FEVER network still provided its key proposed functional feature: to keep stimuli represented over macroscopic time scales within a network.

API. The originally proposed API network (Troyer et al. 1998) was intended to convert the purely excitatory thalamocortical input impinging on L4 neurons (Figure A3-3c) into an intracortical activity that was inhibition-dominated for those neurons whose feature vectors were anticorrelated to that of the thalamic input (Figure A3-3d). Similarly, the intracortical synaptic input to neurons with feature vectors orthogonal to that of the thalamic input was intended to be close to zero, and the intracortical synaptic input was intended to be excitation-dominated for neurons with feature vector aligned to that of the thalamic input (Figure A3-3d). We took the inhibition-dominated regime as the key property of this network (“antiphase inhibition”) and tested whether for neurons with a feature vector anticorrelated with the thalamic input feature vector in fact increasingly inhibition-dominated input could be found after $t_{\text{end}} = 100$ time constants of the network simulation (Figure A3-3d). We found that also in the modified API model, neurons with a feature vector tuned antiphasic to the thalamic input were inhibited (Figure A3-3d). Since furthermore the correlation between cortical feature vectors of antiphasic tuned neurons and thalamic feature vectors decreases with increasing feature space dimension (Figure A3-3e), the API tuning property vanished for feature space dimension above about 50 (Figure A3-3e; see inset in Figure A3-3e for an example of the API tuning property for a higher feature space dimension of 93). Since this was in the range of possible thalamic feature space dimensions (note that only about 250 thalamic neurons project to a L4 barrel), we considered the API tuning property to be sufficiently realized for our adapted API model, as well.

STDP-SORN. The STDP-SORN model was proposed as an example of network self-organization, demanding that neuronal activity in this network would neither overly synchronize nor be limited to a small subset of the neuronal population (Figure A3-3f). We used a simple measure of median correlation between the activities in all pairs of neurons in the network to detect overly synchronized network activity. We found that for learning rates η_{STDP} of 0.0006-0.0014 and intrinsic learning rates η_i of 0.05-0.1 (Figure A3-3f), this network activity correlation remained below 0.0422, indicating that the modified STDP-SORN model fulfilled this basic functional requirement. Similarly, the spike source entropy (SSE) was greater than 0.99, similar to the original work (Lazar et al. 2009), for the modified STDP-SORN model indicating equally distributed activity.

In summary, the process of adapting the previously proposed models to basic experimentally determined circuit constraints in L4 of barrel cortex (Figure 3-2, Figure A3-1, Figure A3-2) did not compromise the basic functional properties that these models were expected to exhibit in the context of sensory input to cortex (Figure A3-1, Figure A3-3).

Supplementary methods: functional properties of STDP-SORN, API, FEVER

The STDP-SORN model was tested for pairwise neuronal correlation. The Pearson product-moment correlation coefficients $\mathrm{C}_{n,n}$ were calculated for the activity traces of each neuron pair. The median $\mathrm{med}(\mathrm{C}_{n,n})$ of these correlations was calculated to represent the whole network. It was also tested for equal activity distribution through the spike source entropy (SSE), defined by $\mathrm{SSE} = \frac{\sum_{k=1}^{n_e} \rho_k \log_2 \rho_k}{\log_2 1/n_e}$ in which ρ_k denoted the mean firing probability of neuron k across the complete trial.

The API model was tested for its antiphase inhibition property. The dynamical model was $a(t+1) = (1-\alpha)a(t) + \alpha C \mathrm{relu}(a(t) + u_0)$ with $\alpha = 1/10$. Neuron k received input $u_{0,k}$ given by $u_{0,k} = \mathrm{relu}\,(c_{\text{sim}}(\mathbf{stim}, \mathbf{d}_k), 0)$. The stimulus was $\mathbf{stim} = \mathbf{d}_{k^*}$ where $k^* \sim \mathrm{DiscreteUniform}(0, n)$ was a randomly chosen neuron. At the end of a trial the feature vector-stimulus cosine similarity $c_{\text{sim}}(\mathbf{d}, \mathbf{stim})$ was calculated. The simulation was implemented in Theano.

The FEVER dynamics were given by $a(t+1) = a(t) + \alpha((\mathrm{C}-1)\, f\big(a(t)\big) + u(t))$ according to (Druckmann and Chklovskii 2012), with $f(x) = \min(\max(x, 0), 2/10)$, $\alpha = 1/100$, $u(t) = u_0 \mathrm{I}(t < 0.05\, t_{max})$ and $\mathbf{u_0} = f(\mathbf{r})$ where $\mathbf{r}$ was a random vector with components $\mathbf{r}_k = \mathbf{u}_k / \|\mathbf{u}\|$, $\mathbf{u}_k = \mathbf{e}_k \boldsymbol{\delta}_k$ with $\mathbf{e}_k \sim \mathrm{U}(-1,1)$ iid. and $\delta_k \sim \mathrm{Ber}(1/10)$ iid.. At the end t_{end} of the trial the represented state $\mathbf{d}_{\text{end}} = \mathrm{D}a(\mathrm{t}_{\text{end}})$, with D the feature vector matrix, was compared to the target state $\mathbf{d}_0 = \mathrm{D}\mathbf{u}_0$ via the cosine similarity $c_{\text{sim}}(\mathbf{d}_0, \mathbf{d}_{\text{end}})$.

Supplementary methods: extended analysis of incomplete and erroneous circuit measurements

Edge removal only. A fraction of the edges (connections) was uniformly at random removed from the network irrespective of whether their pre- and postsynaptic neurons were excitatory or inhibitory.

Edge addition only. A fraction of the number of edges present in the unperturbed network was added between previously non connected neurons. Neuron pairs were chosen uniformly at random irrespective of whether their pre- and postsynaptic neurons were excitatory or inhibitory. Connections were then added and the sign of the added connection determined according to the type of the presynaptic neuron.

Biased perturbation. Removal and addition of edges was biased towards a subnetwork. A subnetwork consisting of a fraction f_m of the excitatory and of the same fraction f_m of the inhibitory neurons, i.e. $f\ n_e$ excitatory and $f\ n_i$ inhibitory neurons was chosen uniformly at random from all subnetworks with such excitatory and inhibitory neuron numbers. A total number of $\xi(n_e + n_i)$ connections were then first removed from the subnetwork and reinserted again.

Locally dense reconstruction of a barrel subvolume. Neurons and connections were assumed to be uniformly and independently distributed in the barrel cube of side length d_b (Figure 3-2a). The locally dense reconstruction of a barrel subcube of side length d_{EM} was simulated as follows: First, the connectome was restricted to neurons located within the subcube. Each neuron had a probability $p = (d_{\mathrm{EM}}/d_b)^3$ of being located within the subcube. Of the remaining connections, the ones not located within the subcube were discarded. Each connection had a probability p of being located within the subcube. Note that the minimum acceptance distance ϵ_{ABC} was set to zero for the simulation of locally dense reconstructions.

Supplementary figures

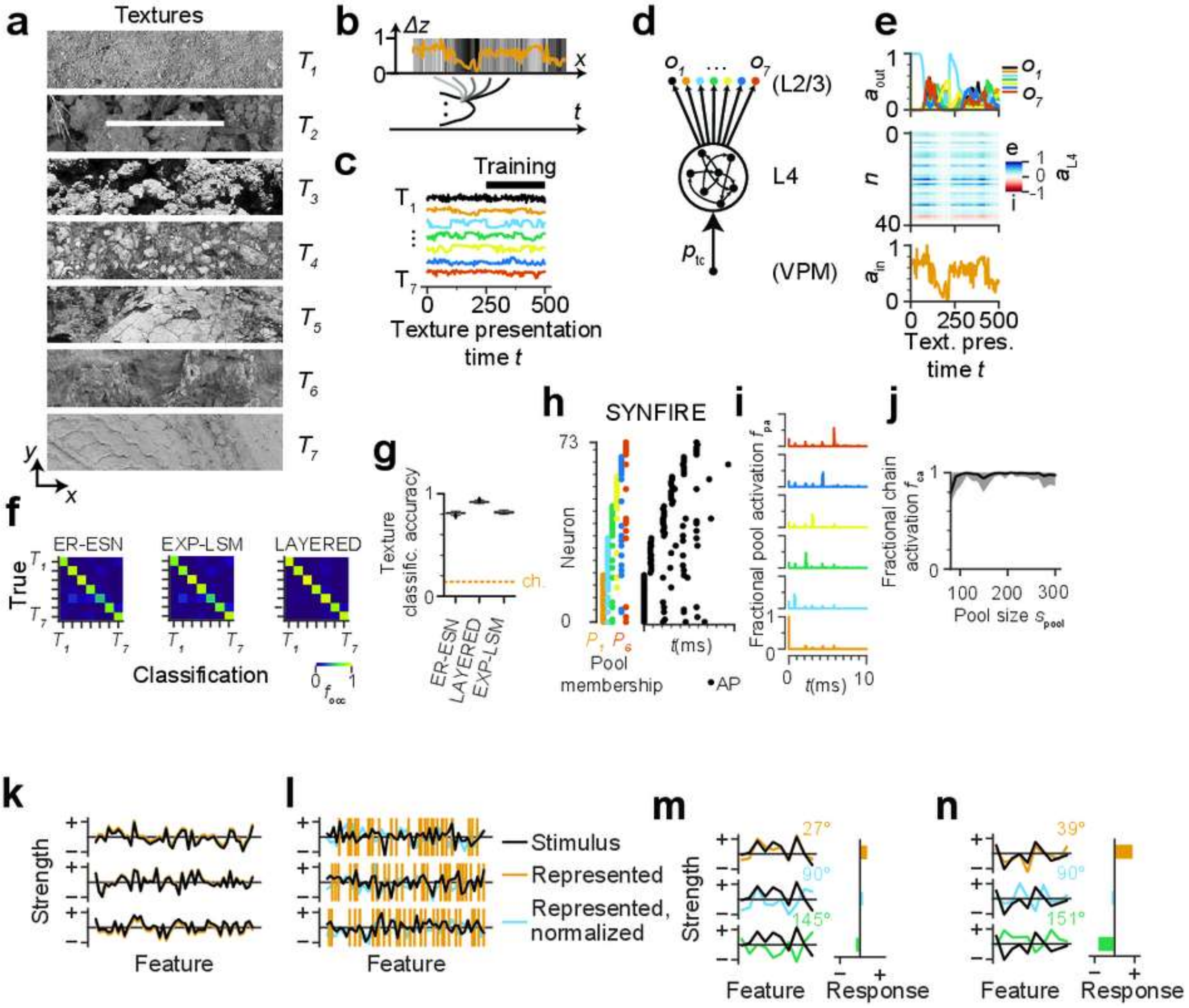

Figure A3-1 Functional performance of candidate models in the local circuit context of a barrel in primary somatosensory cortex. **(a)** Example input to the whisker-pathway: surface texture profiles $T_1 \dots T_7$ (sampled from two dimensional (x and y) images, white line). **(b)** Sketch of transformation of the texture elevation Δz into a temporal activity trace through whisker movement. **(c)** Example texture traces from textures $T_1, \dots, T_7$ that were fed into the modeled L4 network for the ER-ESN, EXP-LSM and LAYERED models. Note that the networks were trained during the second half of the texture presentation (black line). **(d)** Discrimination of thalamocortical input by a L4 network with output to L2/3. The thalamic input was modeled as the texture traces (a-c). Models were trained to classify by output to seven classification units (for example in L2/3). **(e)** Example activities in the network: thalamocortical input signal a_{in} (bottom), intra-L4 activity a_{L4} of 40 example neurons n (excitatory neurons (e), blue; inhibitory neurons (i), red, middle), activity a_{out} of readout neurons $o_1, \dots, o_7$ potentially located in L2/3 (top). Average readout activity in the second half of presentation time was used for determining the classification result. **(f)** Classification results for the ER-ESN, EXP-LSM and LAYERED models determined from 4497 randomly selected test-set texture exposures. **(g)** Classification accuracy for the results in (f) (box plot of bootstrapped texture classification tests, n=100 bootstrap samples; center line, median; box limits, upper and lower quartiles; whiskers, 1.5x interquartile range; points, outliers). Note that all models provide high classification accuracy (above 80%) in this texture discrimination task, well above chance level (dashed line). **(h-j)** Functional properties of the SYNFIRE model as implemented for the model discrimination in Fig. 4-6. **(h)** Example activity (right) in an embedded SYNFIRE model with 6 pools of size s_{pool}=290 neurons each (i.e. r_{ee} of 0.15, r_{ee} of 0.33, see Fig. 2h-j). Random subset of 74 neurons (of the 1780 neurons in the circuit) and their pool membership (left) shown. Note that in the embedded SYNFIRE model, neurons belong to multiple pools. **(i)** Fractional pool activation (fraction of neurons per pool active over time) for the example in h. **(j)** Fractional chain activation over pool size. Each pool size was evaluated 200 times on networks with 2000 neurons (center line: mean; shading: s.d.). **(k)** Short-term memory in the FEVER model; three examples shown. The stimulus to be represented (black) and the state actually represented by the FEVER network (orange) are closely aligned. **(l)** Short-term memory in the API model; three examples shown. The state actually represented by the API model is dissimilar to the stimulus. Also the normalized represented state (blue) is not aligned with the stimulus. **(m)** Stimulus tuning in the FEVER model; three examples shown. All responses are weak. **(n)** Stimulus tuning in the API model; three examples shown. The aligned neuron (39° relative tuning) responds strongly positive, the anti-aligned neuron (151° relative tuning) responds strongly negative.

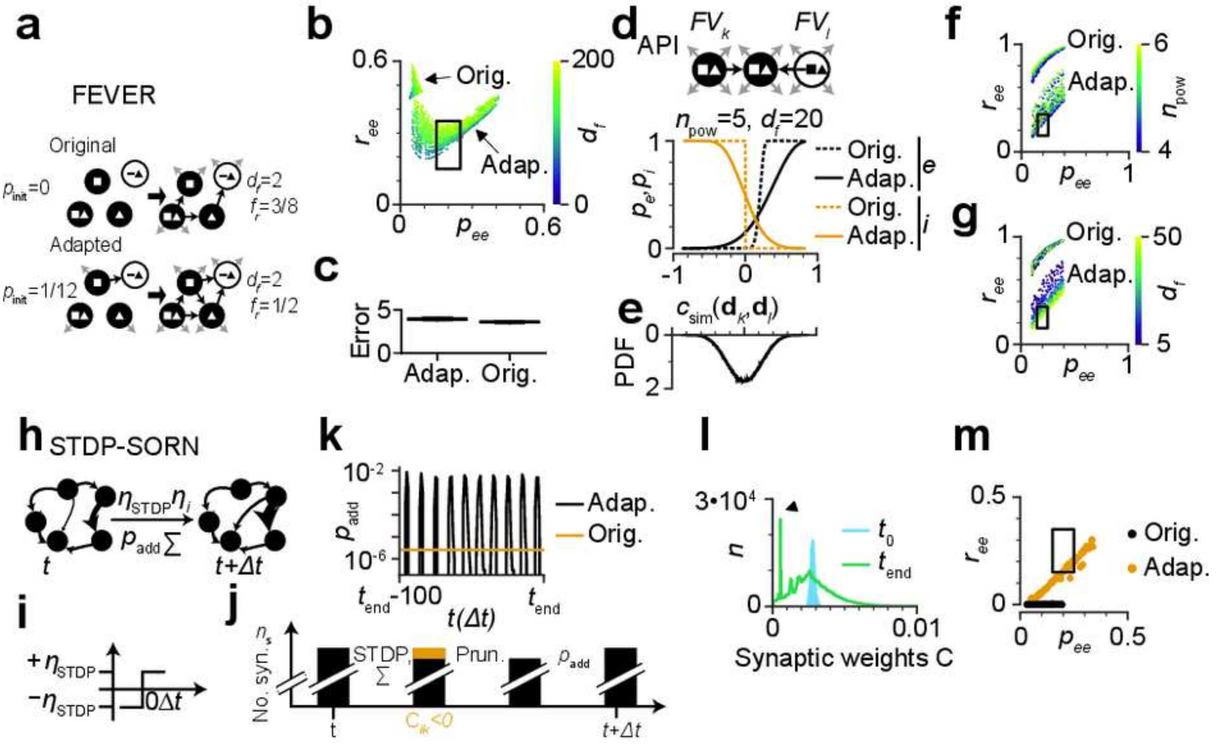

Figure A3-2 Compliance of candidate models with the so-far experimentally determined pairwise circuit constraints in L4 (see Fig. 1d): FEVER, API and STDP-SORN. **(a)** Adaptation of the feature vector recombination model (FEVER). The adapted model starts with a randomly initialized network, whereas the original model starts with an empty network. **(b)** Excitatory reciprocity r_{ee} over excitatory pairwise connectivity p_{ee} for the original and adapted FEVER model. The feature space dimension d_f is color coded. **(c)** Average FEVER error for the original and the adapted FEVER model. Errors bars indicate 95% confidence intervals from 1000 bootstrapped iterations. **(d)** Adaptation of the antiphase inhibition model (API). Excitatory and inhibitory connection probability p_e and p_i over cosine similarity of the feature vectors $c_{\mathrm{sim}}(\mathbf{d}_k, \mathbf{d}_l)$ of feature vector $\mathbf{d}_k$ and feature vector $\mathbf{d}_l$. **(e)** Distribution of cosine similarities in an API network for $n_{\mathrm{pow}} = 5$ and $d_f = 20$. **(f)** Excitatory reciprocity r_{ee} over excitatory pairwise connectivity p_{ee} for the original and adapted API model. The conversion factor n_{pow} is color coded. **(g)** Excitatory reciprocity r_{ee} over excitatory pairwise connectivity p_{ee} for the original and adapted API model. The feature space dimension d_f is color coded. **(h)** Spike timing dependent plasticity / self-organizing recurrent neural network (STDP-SORN) model. Transition from time t to time $t + \Delta t$. The network is modified through spike timing dependent plasticity with learning rate η_{STDP}, intrinsic plasticity with learning rate η_i, random synapse addition with probability p_{add}, and synaptic normalization Σ. **(i)** A synaptic weight is increased by η_{STDP} if a postsynaptic spike is emitted after an interval Δt after the presynaptic spike has occurred or if the postsynaptic spike is emitted at the same time. A synaptic weight is decreased by η_{STDP} if a presynaptic spike is emitted after an interval Δt after the postsynaptic spike. **(j)** Evolution of the number of synapses N_s from time t through time $t + \Delta t$. The number of synapses n_s is not modified by the spike timing dependent plasticity STDP or the synaptic normalization Σ. The negative synapses $C_{ik} < 0$ are removed in a subsequent pruning step. New synapses are then added with probability p_{add}. **(k)** Probability of adding a synapse p_{add} over time t is adjusted such that pruned synapses are replaced. **(l)** Histogram of excitatory synaptic weights C at the start t_0 and the end t_{end} of a SORN simulation. Randomly added synapses are initialized with weight c_{add} (black triangle). **(m)** Excitatory reciprocity r_{ee} over excitatory pairwise connectivity p_{ee}. Orange dots represent the adapted model, black dots the original model (black box: known barrel circuit constraints, see Fig. 1d).

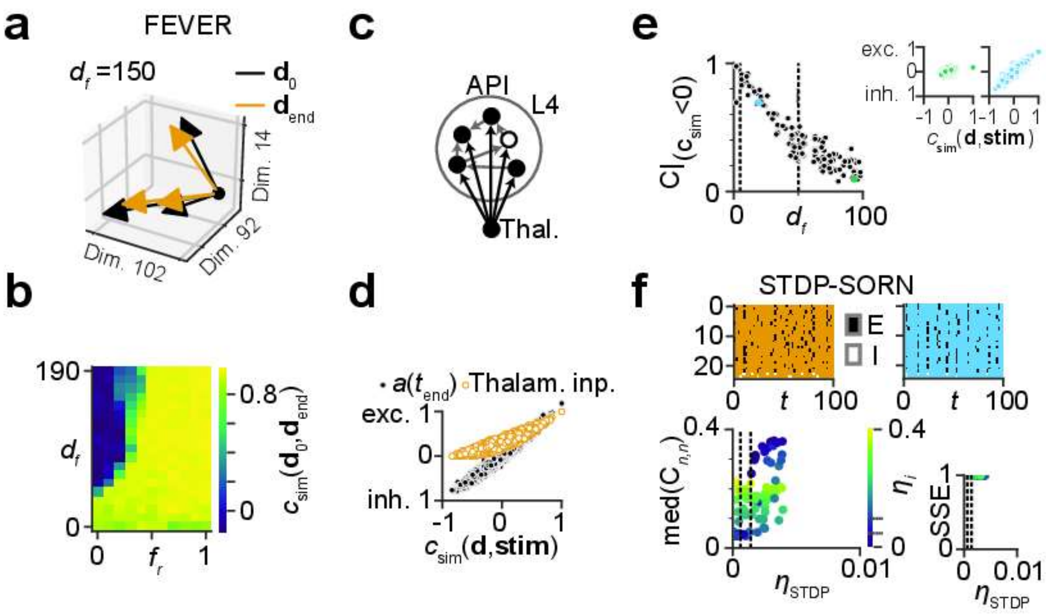

Figure A3-3 Functional performance of candidate models in the local circuit context of a barrel in primary somatosensory cortex: FEVER, API, SDTP-SORN models. **(a)** FEVER model. Dimensions 14, 92, and 102 of the imprinted state $\mathbf{d}_0$ and the represented state at the end of the trial $\mathbf{d}_{\text{end}}$ for a feature space with dimension $d_f = 150$. **(b)** Cosine similarity $c_{\text{sim}}(\mathbf{d}_0, \mathbf{d}_{\text{end}})$ of $\mathbf{d}_0$ and $\mathbf{d}_{\text{end}}$ over feature space dimension d_f and feverization ratio f_r. **(c)** API model. **(d)** Activity at the end of the trial $a(t_{\text{end}})$ and thalamic input for the API model. Excitation (exc.) and inhibition (inh.) are plotted on the ordinate, the cosine similarity between feature vector and stimulus $c_{\text{sim}}(\mathbf{d}, \mathbf{stim})$ on the abscissa. **(e)** Correlation of $a(t_{\text{end}})$ with $c_{\text{sim}}(\mathbf{d}, \mathbf{stim})$ for those neurons with $c_{\text{sim}}(\mathbf{d}, \mathbf{stim}) < 0$ as function of the feature space dimension d_f. The full data corresponding to the blue and green dots is shown in the insets **(f)** Example STDP (SORN) activity for excitatory neurons (E) and inhibitory neurons (I). Top left: Example with low median activity correlation $\text{med}(C_{n,n})$. Top right: Example with high median activity correlation $\text{med}(C_{n,n})$. Bottom left: Median activity correlation $\text{med}(C_{n,n})$ over STDP learning rate η_{STDP} and intrinsic learning rate η_i. The dashed bars in the scatter plot and the black lines at the color bar indicate the support of the prior distribution. Bottom right: spike source entropy.

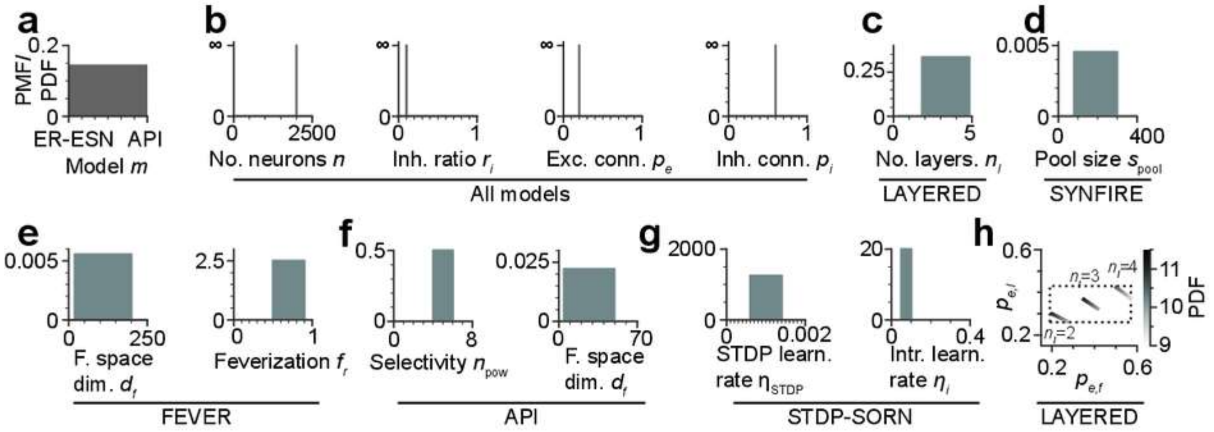

Figure A3-4 Probability mass or density functions of the priors used for Bayesian model selection (Fig. 3). **(a)** Uniform prior over the model classes m. **(b)** Parameters shared across models: number of neurons n, inhibitory ratio r_i, excitatory connectivity p_e, and inhibitory connectivity p_i. **(c)** Number of layers n_l for the LAYERED model. **(d)** Pool size s_{pool} for the SYNFIRE model. **(e)** Feature space dimension d_f and feverization f_r for the FEVER model. **(f)** Selectivity n_{pow} and feature space dimension d_f for the API model. **(g)** STDP learning rate η_{STDP} and intrinsic learning rate η_i for the STDP-SORN model. **(h)** Excitatory forward connectivity $p_{e,f}$ and excitatory lateral connectivity $p_{e,l}$ for the LAYERED model (dotted: $p_{e,f} \times p_{e,l} \in [0.19, 0.57] \times [0.26, 0.43]$).

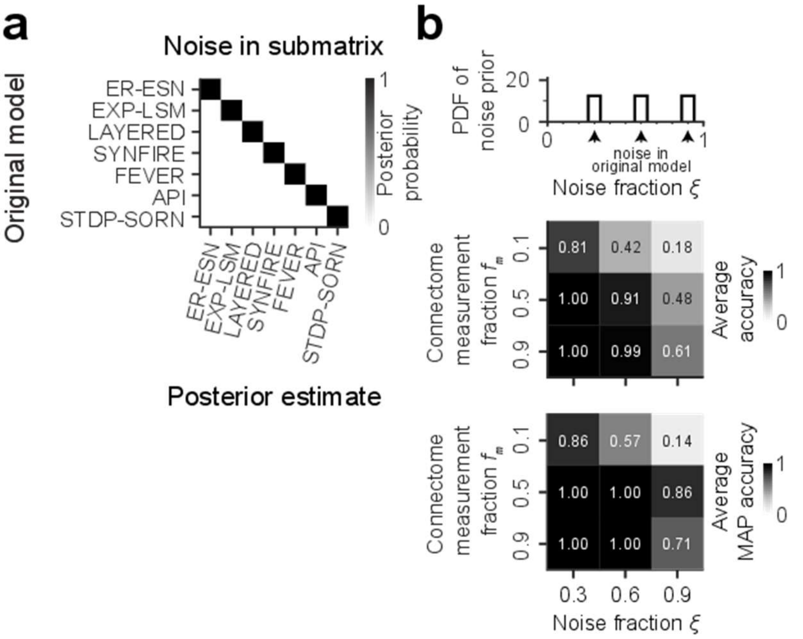

Figure A3-5 Extended analysis of noisy and incomplete circuit measurements. Noise prior during ABC-SMC inference was of the same type as the perturbations to the measured connectome. **(a)** Biased perturbation: 15% of the connections of the unperturbed network were randomly removed from a randomly chosen sub-network of size $f_m = 30\%$ of the original network. The same amount of connections was then randomly reinserted in the same sub-network before ABC-SMC inference (*n*=1 repetition; noise prior of Beta(2,10)). **(b)** Effect of highly informative noise prior on accuracy of model selection from noisy and incomplete circuit measurements. Top: Uniform distributions centered on true noise levels with scales of 8 percentage points were used as noise priors. Middle and bottom: model selection accuracy reported as average posterior probability and maximum-a-posteriori accuracy (*n*=1 repetition per entry), respectively. Note that highly informative noise priors result in more accurate model selection compared to Beta(2, 10) noise priors (Fig. 5c,d).

A4. Appendix to chapter 4

Materials and Methods

Alignment of datasets

Human STG (H5), human IFG (H6), macaque (STG) and mouse (A2) SBEM datasets were aligned with Voxelytics (scalable minds, Postdam, Germany), which implements a least-squares optimization of SIFT feature matches. It minimizes the match distances for neighboring tiles in the 3D tile grid in multiple steps, first using translation only, then one affine transformation per tile, and finally fine-grained mesh transforms. It also includes several heuristics to exclude false matches, including RANSAC optimization (Fischler and Bolles 1981).

Volumetric model of synapse and axon types

The model used to obtain classification criteria for inhibitory vs. excitatory axons (Figure 4-4B-E) was defined as follows. To analyze synaptic inputs onto spiny and smooth dendrites (Figures 4-4C-E, 4-5I-K), it was assumed that the cortical volume contains two distinct axon populations: excitatory axons and inhibitory axons. The two axon populations were assumed to differ in prevalence and potentially also in synapse densities. As a result, it was assumed that the fraction of excitatory synapses in the cortical neuropil was p_{exc}.

Furthermore, it was assumed that excitatory and inhibitory axons differed in the fraction of synapses established onto spine heads (of spiny dendrites), onto shafts of spiny dendrites, and onto shafts of smooth dendrites.

The probabilities of an inhibitory axon to innervate spine heads (p_{in}^{spine}), shafts of spiny dendrites ($p_{inh}^{spiny\ shaft}$), or shafts of smooth dendrites ($p_{in}^{smoot\quad shaft}$) were assumed to be constant across interneurons and constant along individual interneuron axons. Additionally, the targets of synapses along inhibitory axons were assumed to be independent. Together, these assumptions allowed inhibitory axons to be modeled by a multinomial distribution.

For excitatory axons, it was observed that the prevalence of postsynaptic target changes with distance to soma (Figure 4-3H,I). To account for this, excitatory axons were modeled by a Dirichlet-multinomial distribution with parameters $\alpha_{exc} = \left(\alpha_{exc}^{spine}, \alpha_{exc}^{spiny\ shaft}, \alpha_{exc}^{smoo\quad shaft}\right)$.

Data and parameter inference

To analyze the neuropil composition, five types of measurements were taken:

1. In boxes of cortical neuropil (average total volume per dataset: 375 µm^3 for mouse, 1200 µm^3 for primate), the number of synapses onto spine heads and the number of synapses onto dendritic shafts were measured (average total number of synapses per dataset: 338 for mouse, 322.8 for primate). For macaque S1 and human STG, the shaft synapses were further subdivided into shaft synapses onto spiny dendrites and into shaft synapses onto smooth dendrites.
2. Along distal segments of spiny dendrites (minimum distance from soma: 30 µm for mouse, 45 µm for macaque, 80 µm for human), the number of synapses onto spine heads and the number of synapses onto dendritic shafts were measured (average number of dendrites and of synapses per dendrite: 9.2 and 23.3 per mouse dataset, 21.2 and 17.1 per primate datasets).
3. Random spine synapses onto distal pyramidal neuron dendrites were used as “seeds” for the local reconstruction of the presynaptic axon and its postsynaptic targets

(average number of axons and of synapses per axon: 13.8 and 8.4 per mouse dataset, 21.8 and 6.9 per primate dataset).

4. As in 3, but with shaft synapses onto distal spiny dendrites as (average number of axons and of synapses per axon: 16.8 and 7.7 per mouse dataset, 34.8 and 8.9 per primate dataset).
5. As in 3, but with shaft synapses onto distal dendrites of inhibitory interneurons (minimum distance from soma: 30 µm) as seeds (average number of axons and of synapses per axon: 47 and 8.1 per mouse dataset, 35 and 6.3 per primate dataset).

Synapses onto other postsynaptic targets (e.g., spine necks) were ignored. From these data, the maximum likelihood estimates of the parameters p_{exc}, α_{exc}^{spine}, $\alpha_{exc}^{spiny\ sha}$, $\alpha_{exc}^{smoot\ \ shaft}$, p_{in}^{spine}, $p_{inh}^{spiny\ shaft}$, and $p_{inh}^{smo\ \ \ \ sha}$ were derived. The likelihood was given by:

$$\mathcal{L} = \mathcal{L}_{vol.} \times \mathcal{L}_{sp.\ dend.} \times \mathcal{L}_{spine-seede\ \ ax.} \times \mathcal{L}_{spiny\ shaft-seeded\ ax.} \times \mathcal{L}_{smooth\ shaft-seeded\ ax.}$$

$$\mathcal{L}_{vol} = \prod_{b=1}^{N_{boxes}} \text{Binomial}\left(V_b^{spine}\,\middle|\,V_b^{all}, p_{vol}^{spine}\right),$$

where $p_{vol}^{spine} = p_{exc}p_{exc}^{spine} + (1-p_{exc})p_{in}^{spine}$
and $p_{exc}^{t} = \alpha_{exc}^{t}/\|\boldsymbol{\alpha}_{\boldsymbol{exc}}\|_1$ for all targets.

$$\mathcal{L}_{spiny\ dend.} = \prod_{d=1}^{N_{spiny\ dend.}} \text{Binomial}\left(D_d^{spine}\,\middle|\,D_d^{all}, p_{spiny\ dend}^{spine}\right),$$

where $p_{spiny\ dend}^{spine} = \dfrac{p_{exc}p_{exc}^{spine} + (1-p_{exc})p_{inh}^{spine}}{p_{exc}\left(p_{exc}^{spine} + p_{exc}^{spiny\ shaft}\right) + (1-p_{exc})\left(p_{inh}^{spine} + p_{inh}^{spiny\ shaft}\right)}$

$$\mathcal{L}_{spine-seeded\ ax.} = \prod_{a=1}^{N_{axons}} \left[f_{exc} \frac{A_a^{spine}\ \text{BetaBinomial}\left(A_a^{spine}\,\middle|\,A_a^{all}, \alpha_{exc}^{spine}, \alpha_{exc}^{spiny\ shaft} + \alpha_{exc}^{smooth\ shaft}\right)}{A_a^{all}p_{exc}^{spine}} + \left(1-f_{exc}\right)\frac{A_a^{spine}\ \text{Binomial}\left(A_a^{spine}\,\middle|\,A_a^{all}, p_{in}^{spine}\right)}{A_a^{all}p_{inh}^{spine}} \right],$$

where $f_{exc} = \dfrac{p_{exc}p_{exc}^{spine}}{p_{exc}p_{exc}^{spine} + (1-p_{exc})p_{in}^{spine}}$

$$\mathcal{L}_{spiny\ shaft-seeded\ ax.} = \prod_{a=1}^{N_{axons}} \left[\begin{array}{l} f_{exc} \displaystyle\sum_{n=0}^{B_a^{shaft}} \frac{n\,\text{DirichletMultinomial}(B_a^{spine}, n, B_a^{shaft} - n | \boldsymbol{\alpha_{exc}}}{B_a^{all} p_{exc}^{spiny\ shaft}} \\ + \left(1 - f_{exc}\right) \displaystyle\sum_{n=0}^{B_a^{shaft}} \frac{n\,\text{Multinomial}(B_a^{spine}, n, B_a^{shaft} - n | \boldsymbol{p_{inh}}}{B_a^{all} p_{inh}^{spiny\ shaft}} \end{array} \right],$$

where $f_{exc} = \dfrac{p_{exc} p_{exc}^{spiny\ shaft}}{p_{exc} p_{exc}^{spiny\ shaft} + \left(1 - p_{exc}\right) p_{inh}^{spiny\ shaft}}$

$$\mathcal{L}_{smooth\ shaft-seed\quad ax.} = \prod_{a=1}^{N_{axons}} \left[\begin{array}{l} f_{exc} \displaystyle\sum_{n=0}^{C_a^{shaft}} \frac{n\,\text{DirichletMultinomial}(C_a^{spine}, C_a^{shaft} - n, n | \boldsymbol{\alpha_{exc}}}{C_a^{all} p_{exc}^{smooth\ shaft}} \\ + \left(1 - f_{exc}\right) \displaystyle\sum_{n=0}^{C_a^{shaft}} \frac{n\,\text{Multinomial}(C_a^{spine}, C_a^{shaft} - n, n | \boldsymbol{p_{inh}}}{C_a^{all} p_{inh}^{smooth\ shaft}} \end{array} \right],$$

where $f_{exc} = \dfrac{p_{exc} p_{exc}^{smooth\ shaft}}{p_{exc} p_{exc}^{smoot\quad shaft} + \left(1 - p_{exc}\right) p_{inh}^{smooth\ shaft}}$

To compute the maximum likelihood parameter estimates, the fmincon function of MATLAB (R2017b) was used to minimize the negative log-likelihood. $p_{inh}^{smooth\ shaft}$ was defined as $1 - p_{inh}^{spine} - p_{inh}^{spiny\ shaft}$. The parameters were constrained as follows: $0.5 < p_{exc} < 1$, $0 < p_{inh}^{spine} < 0.5$, $0 < p_{inh}^{spiny\ shaft} < 1$, $p_{inh}^{spine} + p_{inh}^{spiny\ shaft} < 1$, $0 < \alpha_{exc}^{t}$ for all targets, and $\alpha_{exc}^{spiny\ shaft} + \alpha_{exc}^{smooth\ shaft} < \alpha_{exc}^{spine}$. The parameters were initialized to $p_{exc} = 90\%$, $p_{inh}^{spine} = 20\%$, $p_{inh}^{spiny\ shaft} = 40\%$, $\alpha_{exc}^{spine} = 9$, $\alpha_{exc}^{spiny\ shaft} = 1.5$, $\alpha_{exc}^{smoot\quad shaft} = 1.5$.

The expected fraction of synapses onto spiny dendrites that originate from inhibitory axons is

$$I = \frac{(1 - p_{exc})(p_{inh}^{spine} + p_{inh}^{spiny\ shaft})}{(1 - p_{exc})\left(p_{inh}^{spine} + p_{inh}^{spiny\ shaft}\right) + p_{exc}\left(p_{exc}^{spine} + p_{exc}^{spiny\ shaft}\right)}.$$

For the quantification of uncertainty and for statistical testing, bootstrap sampling was used (Efron 1979): The measurements for each of the five types of input data were resampled with replacement while keeping the number of measurements unchanged. These data were then used for inference of maximum likelihood parameter estimates and of the expected inhibitory synaptic input fractions for spiny and smooth dendrites. This process was repeated n=1000 times per dataset.

To predict how a change in the proportion of excitatory and inhibitory neurons affects I, the following model was used: Let f_i denote the fraction of (inhibitory) interneurons. It follows that the expected synapse contribution of interneurons relative to excitatory neurons is $c = [(1 - f_i)I]/[f_i(1 - I)]$. Assuming that the neuronal synapse contributions remain constant, a change in the fraction of inhibitory neurons to $\hat{f}_i$ results in a predicted inhibitory synaptic input fraction of $\hat{I} = c\hat{f}_i/\left[c\hat{f}_i + 1(1 - \hat{f}_i)\right]$.

For statistical testing, I was computed as the average inhibitory input synapse fraction of spiny dendrites across all mouse datasets. f_i and $\hat{f}_i$ were obtained by bootstrap sampling the pooled excitatory neuron and interneuron counts across all mouse and human datasets, respectively. $\hat{I}$ was then compared against the average inhibitory input synapse fraction of spiny dendrites across all human datasets (I_{human}). To compute a p-value, this comparison was repeated across 1000 bootstrap samples. Specifically, the p-value was calculated as the fraction of bootstrap samples in which $I_{human} \geq \hat{I}$.

To validate the initial parameters of the likelihood maximization procedure, the following approach was used. Model parameters were randomly sampled: p_{exc} uniformly between 0 and 1; p_{inh}^{spine}, $p_{inh}^{spiny\,shaft}$, and $p_{in}^{smoot\quad shaft}$ uniformly from the 2-simplex; p_{exc}^{spine}, $p_{exc}^{spiny\,shaf}$, and $p_{exc}^{smoo\quad shaft}$ uniformly from the 2-simplex, and $\alpha_{exc}^{total} = 10^z$ with z uniformly between -1 and +2. α_{exc}^{target} was set to $\alpha_{exc}^{total} p_{exc}^{target}$ for all targets. For each dataset, 10,000 sets of random model parameters were generated this way and evaluated in terms of the likelihood of the model input data. The random model parameters with maximum likelihood were then used as initial parameter values for the likelihood maximization procedure (as above). For all nine datasets, the inhibitory synaptic input fractions for spiny and smooth dendrites inferred this way were identical (≥3 significant digits) to the values inferred using fixed initial model parameters.

To account for the confusion of excitatory and inhibitory synapses in macaque and human, we considered the extreme case of true inhibitory synapses getting misclassified as excitatory. This would result in the strongest under-estimation of I/(I+E) in primates. Let X = I/(I+E) denote the true inhibitory synapse fraction. Assuming that a fraction C=8.4% of true inhibitory synapses gets misclassified as excitatory (see Figure A4-2), the measured inhibitory synapse fraction is (1-C)×I / [(1-C)×I + (C×I + E)] = (1-C)×I/[I+E] = (1-C)×X. Thus, the upper bound on the true value of I/(I+E) is Y / (1-C). For statistical testing, the bootstrap samples of the inhibitory synapse fractions for macaque and human were corrected as above before comparison against the predictions from mouse. We found that even the upper bound on I/(I+E) for macaque and human was significantly lower than the prediction from mouse (15.0%±1.5% vs. 24.9%±3.2%; p<0.001).

Connectivity estimates

The connectivity within and across excitatory neuron (ExN) and inhibitory interneuron (IN) populations (Figure A4-2F) was computed as follows: $p_{ExN\rightarrow ExN} = p_{exc}\left(p_{exc}^{spine} + p_{exc}^{spiny\,shaft}\right)$, $p_{ExN\rightarrow IN} = p_{exc} p_{exc}^{smooth\,shaft}$, $p_{IN\rightarrow ExN} = (1 - p_{exc})\left(p_{in}^{spine} + p_{inh}^{spiny\,shaft}\right)$, and $p_{IN\rightarrow IN} = (1 - p_{exc}) p_{in}^{smooth\,shaft}$. For the illustration of inhibitory connectivity in Figure 4-6C, IN→ExN connections were established with probability $kp_{IN\rightarrow ExN}/[f_i(1 - f_i)]$ and IN→IN connections with probability $kp_{IN\rightarrow IN}/f_i^2$, where f_i is the interneuron fraction and k is a constant, such that each IN innervates on average 30% of all other neurons. Notably, it was assumed that the average number of synapses in IN→ExN and IN→IN connections is equal.

Dense reconstruction

For the analyses reported in Figures 4-3D-F and 4-5H, the following methods were employed. 3D EM datasets were processed using voxelytics (scalable minds, Potsdam, Germany, developed in collaboration with MPI Brain Research, Dept. of Connectomics). Briefly, a convolutional neural network (CNN; modified from (Lee et al. 2017)) was used to infer voxel-wise affinities from which an initial volume segmentation was generated by seeded watershed transform. For the reconstruction of neurites, volume segments were grouped into agglomerates by median-affinity-based hierarchical agglomeration with additional constraints to reduce the rate of merge errors. These constraints include: i) neurite type-based restrictions to avoid merge errors between, for example, axons and dendrites; ii) a restriction to avoid merge errors between cells whose cell body is located within the image volume;

and iii) agglomerate volume-based restrictions. Neurite types were inferred using a CNN for voxel-wise semantic segmentation of axons, dendrites, spine heads, astrocytes, myelin, and other objects. For connectome inference, a CNN for semantic segmentation of synapses, vesicle clouds, and mitochondria was used in combination with a decision tree forest that was trained to classify agglomerate-to-agglomerate contacts as synaptic or non-synaptic based on summary statistics of the CNN outputs. The CNNs and decision tree forests were trained on previously published training data from layer 4 of mouse S1 (Motta et al. 2019) and, optionally, on additional dataset-specific training data.

To separate axonal, dendritic, and other (e.g., glial) agglomerates, the volume-weighted average of voxel-wise neurite type probabilities were computed. Agglomerates were classified as axonal or dendritic if they exceeded dataset-specific axon and dendrite probability thresholds (see below), respectively. Automatically detected synapses were classified into spine synapses, shaft synapses, and other synapses based on the average type probabilities at the postsynaptic site. Spine synapses were further sub-classified into spine synapses into singly vs. multiply innervated spine heads. For subsequent analyses, only spine synapses onto singly innervated spine heads and shaft synapses with presynaptic axon and postsynaptic dendrite agglomerates were considered.

Estimation of error rates

To estimate error rates of the automated reconstructions and to optimize analysis parameters, ground truth annotations were generated for each dataset. The ground truth consisted of synapse annotations in neuropil volumes of (5 µm)^3 for mouse, (7 µm)^3 for macaque, and (7 µm)^3 for human. Synapses were classified into spine synapses, shaft synapses, and other synapses. The postsynaptic dendrites were classified as either spiny or smooth. For spine synapses, the corresponding dendrite was identified.

The following parameters and error rates were estimated from these annotations:

- Minimum axon probability for axon agglomerates (manually optimized for high recall based on the axon probability distribution across agglomerates presynaptic to ground truth synapse annotations)
- Minimum dendrite probability for dendrite agglomerates (as for axons)
- Average automated spine synapse fractions for dendrite agglomerates corresponding to spiny (p_{spiny}^{spine}) and smooth dendrites (p_{smoot}^{spine}), respectively
- Precision and recall of automated spine synapse detection and confusion rate of true spine synapses as shaft synapses
- Precision and recall of automated shaft synapse detection and confusion rate of true shaft synapses as spine synapses

Inference of axonal spine targeting probability

To classify axon agglomerates as excitatory or inhibitory, the model of excitatory and inhibitory axons derived from manual annotations was reused (see above). Specifically, each axon agglomerate was classified based on its spine targeting probability. First, the number of automatically detected spine (N_{spine}) and shaft synapses (N_{shaft}) was computed. To account for the error rates of automated synapse detection, the normalized likelihood $\mathcal{L}_{axon}^{spine}(p_{spine}) = \mathrm{P}(N_{spine}, N_{shaft} | p_{spine})$ was estimated was follows:

For a given p_{spine}, the effect of imperfect synapse detection was simulated by a forward model for all axon configurations $n_{spine} \sim \mathrm{Binomial}(n_{total}, p_{spine})$ with $n_{total} \in [0,100]$. The un-normalized likelihood of p_{spine} was then approximated by the probability mass corresponding to the combination of N_{spine} and N_{sha} after the forward model. The forward model was evaluated for $p_{spine} = 0\%, 1\%, \dots, 100\%$. For details, see MATLAB function +HNHP/+Auto/+inferSpineSynapseFraction.m.

Given the likelihood $\mathrm{P}(N_{spine}, N_{shaft} | p_{spine})$ and the model of excitatory and inhibitory neurons, the posterior probability of being excitatory or inhibitory was computed for each axon agglomerate. For subsequent analyses, inhibitory axon agglomerates were defined as axon agglomerates with a posterior probability of being inhibitory above 50%.

Inference of smooth dendrite targeting probability for inhibitory axons

To compute the smooth dendrite targeting probability of inhibitory axons, spiny and smooth dendrites had to be separated. For a dendrite with N_{spine} input synapses onto spine heads and N_{shaft} input synapses onto the dendritic shaft, the probability of being a smooth dendrite was computed by:

$$p_{dend}^{spi} = \frac{\mathrm{Binomial}(N_{spine} | N_{spine} + N_{shaft}, p_{spiny}^{spine})}{\mathrm{Binomial}(N_{spine} | N_{spine} + N_{shaft}, p_{spiny}^{spine}) + \mathrm{Binomial}(N_{spine} | N_{spine} + N_{shaft}, p_{smoo}^{spine})}$$

The smooth dendrite targeting probability of inhibitory axons was then computed by:

$$p_{axon}^{smoo} = 1 - \underset{p_{axon}^{spiny}}{\arg\max} \int_{p_{axon}^{spine|spiny}} \mathcal{L}_{axon}^{spine} \left(p_{axon}^{spiny} p_{axon}^{spine|spiny} \right) \prod_{\substack{postsynaptic \\ dendrites}} [\hat{p}_{axon}^{spiny} p_{dend}^{spiny} + (1 - \hat{p}_{axon}^{spiny})(1 - p_{dend}^{spiny})]$$

where p_{axon}^{spiny} is the true probability of targeting spiny dendrites, $p_{axon}^{spine|spiny}$ is the true spine synapse fraction among synapses onto spiny dendrites, and $\hat{p}_{axon}^{spiny}$ is the expected probability of targeting spiny dendrites when accounting for the error rates of automated spine and shaft synapse detection. Notably, the transformation of the former two parameters into the latter is based on the assumption that smooth dendrites are devoid of spines. For details, see MATLAB script +HNHP/+Auto/runAnalysis.m.

Supplementary text

Possible effect of temperature on stability of dendritic spines

Reports about a temperature-dependent change in spine rates, shown for slices of mammalian hippocampus (Kirov et al. 2004), could be of concern as a potential contributor to the observed low spine rates in human cortex (Figure 4-2E). While our tissue was immersed in cooled liquid, this liquid was fixative in our case, which would quickly halt any additional modifications of the neuropil; in fact, we saw no evidence of ultrastructural change in macaque and H5 that has been described as a corollary of temperature-induced tissue alterations (Kirov et al. 2004). Sample H6 showed occasional dendrites with swellings (beady morphology), which were excluded from analyses. Control experiments using cold fixative on mouse samples did not yield substantially altered spine rates (1.2±0.4 per µm dendrite in mouse data fixed at 4°C, n=4). Together, we have to conclude that our finding about the synaptic input to human cortical pyramidal cells should be taken to treat reports of extremely high spine rates in human (Benavides-Piccione et al. 2013, Elston et al. 2001) with caution (see also (Benavides-Piccione et al. 2002, Glantz and Lewis 2000, Medalla et al. 2017, Hsu et al. 2017)), even if some of the differences are attributable to variations between cortical areas in human and primates (Elston et al. 2001, Medalla et al. 2017, Gilman et al. 2017), but similar variability was not reported in mouse (Karimi et al. 2020).

Additional methodological acknowledgments

We thank T. Garbowski and D. Lechner at Zeiss team for help with setting up multiSEM; M. Fahland and N. Prager at Fraunhofer FEP, Dresden for collaboration on Kapton tape; R. Schalek and J. Lichtman at Harvard University for initial advice on setting up ATUM; G. Tushev for ATUM software; and A. Kotowicz and T. Zeller for initial setup of data transfer line from multiSEM.

Supplementary figures

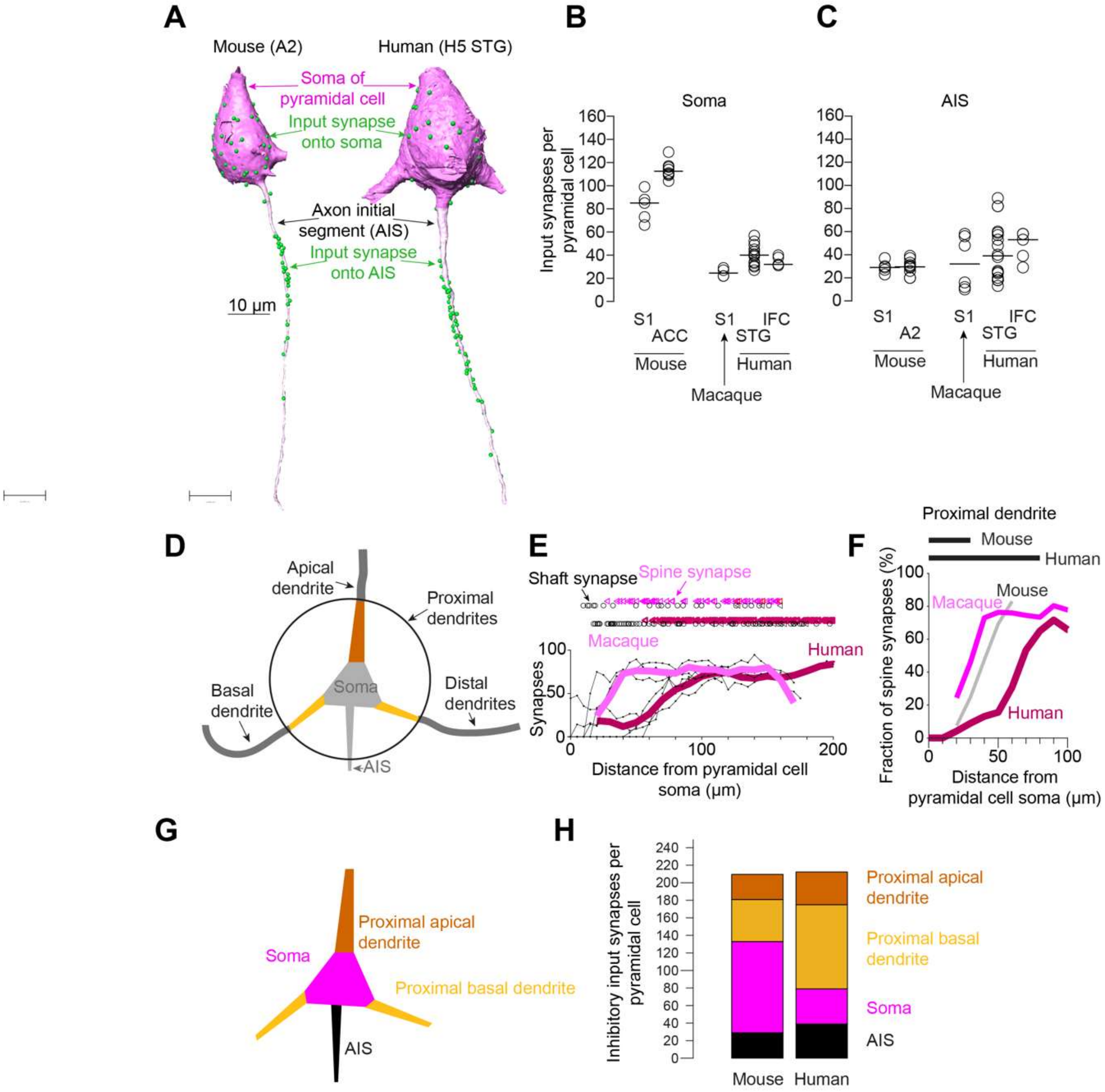

Figure A4-1 Synaptic input to pyramidal cells at their soma, axon initial segment and proximal dendrites. **(A)** Example reconstructions of pyramidal cell bodies and axon initial segments (AIS) from mouse A2 and Human STG datasets. All input synapses to soma and AIS were manually annotated (green). Note sparsity of somatic input synapses in human. **(B,C)** Quantification of total input synapses onto soma and AIS per neuron in mouse, macaque and human. Note 2.9-fold drop of somatic input from mouse to macaque and human (104 ± 17 input synapses, N=17 somata in mouse to 36 ± 9 input synapses, N=22 somata in macaque and human, mean ± s.d., p-value<0.001, Kolmogorov-Smirnov test, B), while input to AIS is only slightly enhanced (40% increase, 29 ± 6 input synapses, N=15 AIS in mouse vs. 42 ± 23 input synapses, N=29 AIS in macaque and human, mean ± s.d., p-value<0.01, Kolmogorov-Smirnov test, C). **(D-F)** Analysis of proximal dendritic input: definition of proximal dendrites as those with reduced input spine density. Input spine density increases to distal levels within about 30µm in mouse and about 80µm in human (F), which were used as thresholds for definition of proximal dendrites in G,H. **(G,H)** Quantification of total inhibitory synaptic input to proximal dendrites using total dendritic path length per neuron of these compartments (123 ± 30 µm for proximal basal, N=10 cells and 40 ± 14 µm, N=7 cells for proximal apical in mouse and 395 ± 60 µm, N=17 cells, and 121 ± 66 µm, N=21 cells in human, respectively, mean ± s.d) and shaft input synapse densities. In the proximal dendrite, 95% and 75% of shaft inputs were inhibitory in mouse and human, respectively. **(I)** Summary of inhibitory synaptic input to the non-distal input domains AIS, Soma, proximal dendrites. Note that total inhibitory input in these domains is largely constant from mouse to human, with a potential shift of synapses from soma to AIS and proximal dendrites. Notably, there was no sign of an increased inhibition in Human in these input compartments (excluding compensation of the finding of largely similar distal i/(i+e) in mouse, macaque and human, Fig. 4E). All data based on expert reconstructions.

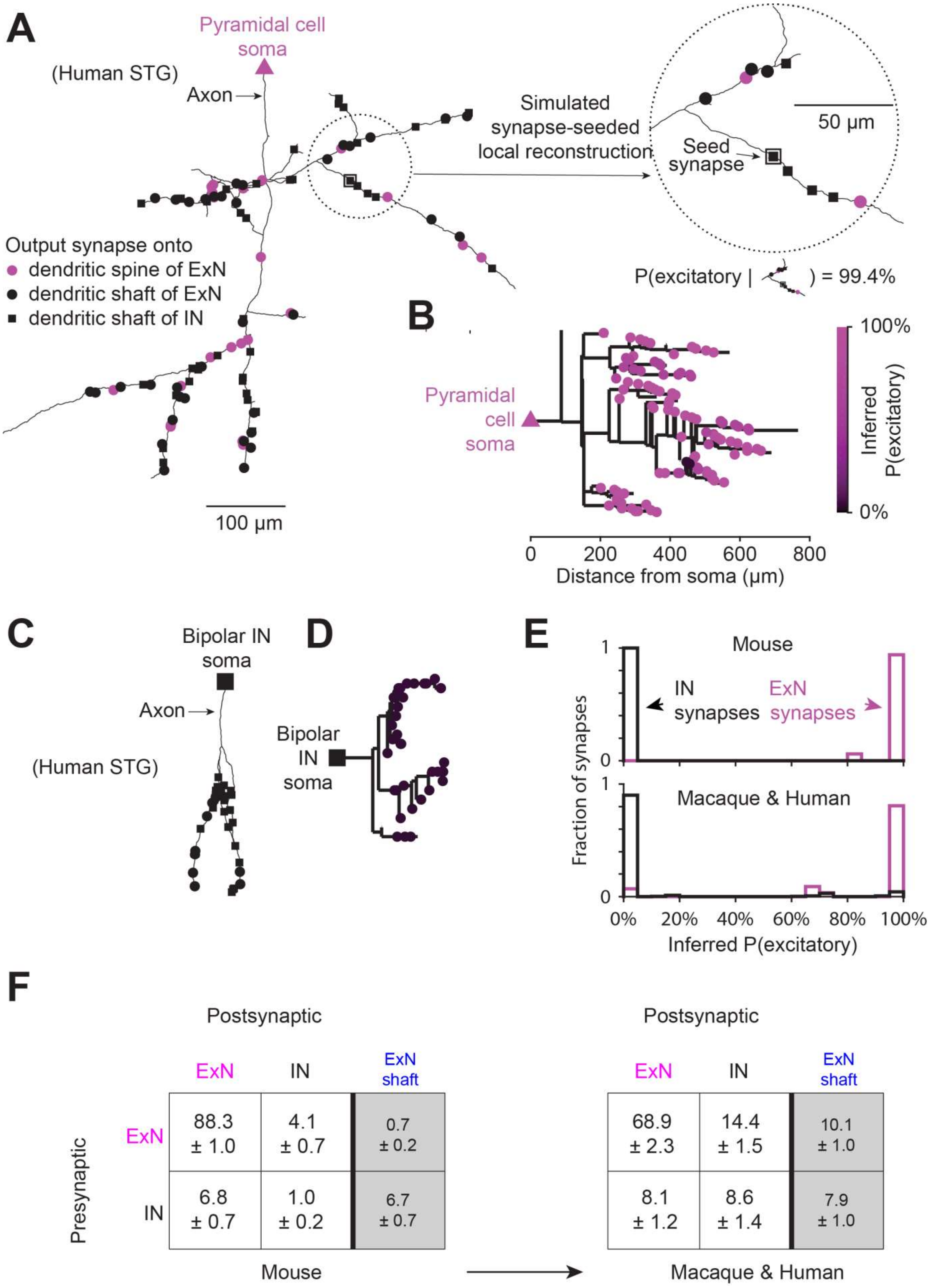

Figure A4-2 Validation of excitatory and inhibitory axon definition, and network expansion. **(A)** Example pyramidal neuron axon from human STG with excitatory output synapses onto dendritic spines of excitatory neurons (ExN) (magenta circles), onto dendritic shafts of excitatory neurons (black circles), and onto dendritic shafts of interneurons (IN) (black squares). Right: Simulation of local axon reconstruction seeded from a shaft synapse onto an IN dendrite (black square with outline). The local axon reconstruction spans the seed synapse and the nine synapses closest to it (2 onto dendritic spines, 7 onto dendritic shafts). (Continuation on next page)

(Continuation of previous page) The inferred probability of the local axon reconstruction being part of an excitatory axon is 99.4%. **(B)** Axonogram of axon in (A) with each output synapse colored by inferred excitatory probability of the corresponding simulated local reconstruction. Note that 99 out of the 101 excitatory synapses have an inferred excitatory probability >50%. **(C)** Example bipolar interneuron axon from human STG with inhibitory output synapses (symbols and scale bar as in (A)). **(D)** Axonogram of axon in (C). All 34 inhibitory synapses have an inferred excitatory probability <50%. **(E)** Histogram of inferred excitatory probability for synapses from ExN and IN axons from mouse, and macaque and human. In mouse, all 33 excitatory and 167 inhibitory synapses were correctly classified. In macaque and human, 93.1% of the 1,239 excitatory and 91.6% of the 356 inhibitory synapses were correctly classified. All data based on expert reconstructions. **(F)** Connectivity estimates from the model for mouse and macaque and human (see Suppl. Methods "Connectivity estimates"). ExN postsynaptically comprises shaft and spine targets. ExN shaft connectivity (gray shading) reported separately in rightmost column, this is part of the ExN column. Note 8.6-fold expansion of IN-to-IN connectivity, and 14.4-fold expansion of ExN connectivity at shaft synapses.

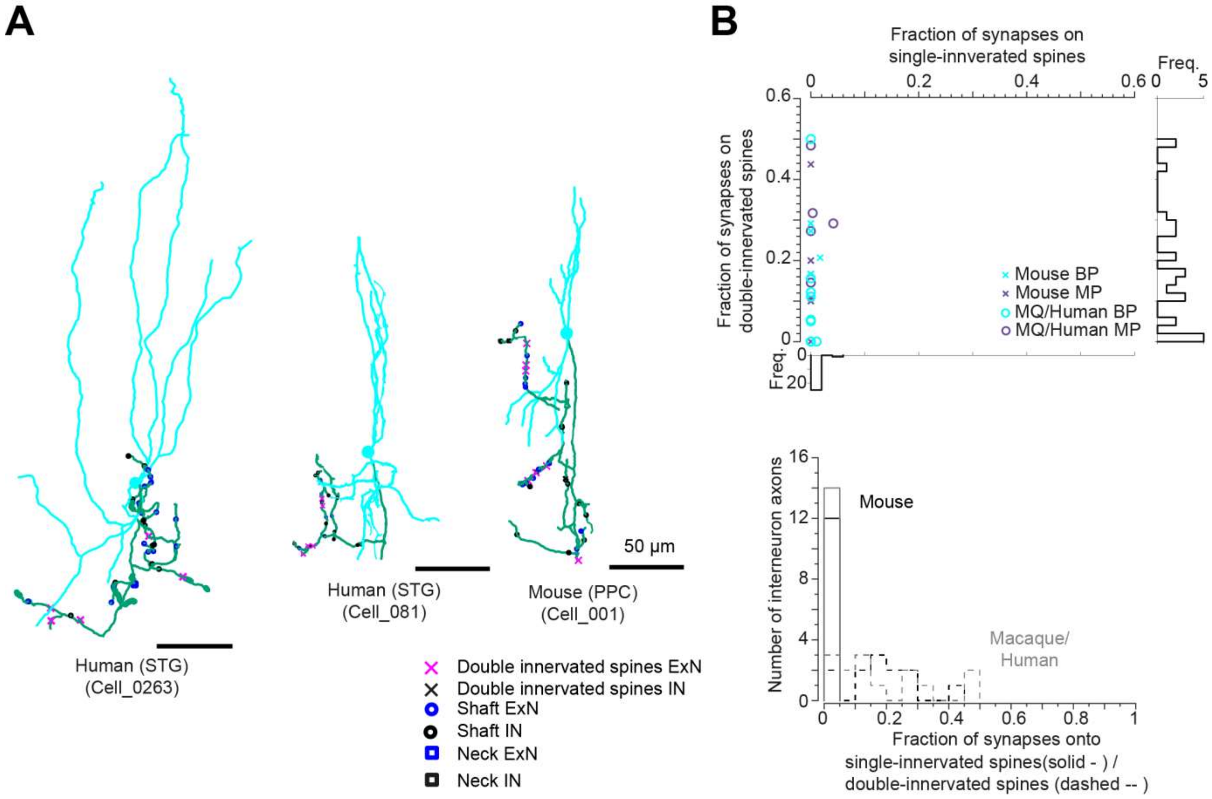

Figure A4-3 Spine-targeting interneurons. **(A)** Example reconstructions of bipolar interneurons with output synapses onto spines, which could resemble double bouquet INs (61-63). **(B)** Quantification of spine targeting by IN axons. Note spine targeting is almost exclusively onto spines that are doubly innervated, therefore not confounding the classification of axons based on single-spine innervation (cf. Fig. 4). All data based on expert reconstructions.

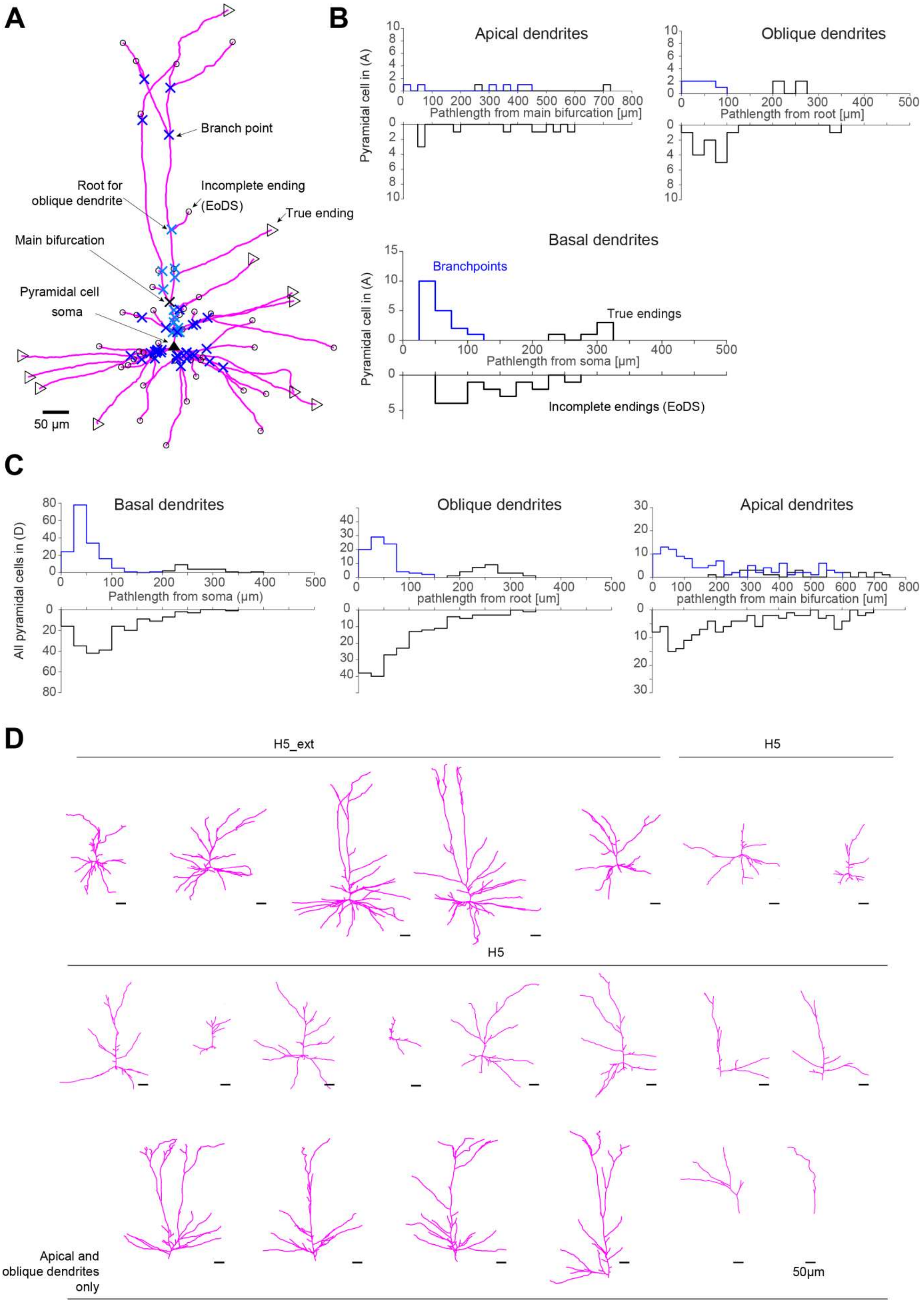

Figure A4-4 Dendritic path length estimates for human pyramidal cells. **(A)** Example reconstruction of a dendritic tree of a L3 pyramidal cell (PC) in Human STG dataset. Dendrites were traced either until the end of the dataset (EoDs) or until an actual ending (true). (Continuation on next page)

(Continuation of previous page) **(B)** Example quantification of measured dendrite path lengths from the L3 PC shown in (A) to their endings eods, true) and their branchpoints. Plotted separately for each compartment (apical, oblique, basal). Path lengths were either measured from the main bifurcation (apical), from the root of the apical trunk (oblique) or from the soma (basal). **(C)** Quantification of measured dendrite path lengths as shown as in (B) based on all PC reconstructions in Human STG datasets (H5, H5_ext). For the basal, oblique and apical tuft compartment N=226, 211, 167 dendrites were analyzed, of which N=25, 28 and 32 dendrites with true endings were found (N=21 cells). No EoDS ending exceeded true ending path lengths, which minimized the chance of missing longer dendrites leaving the dataset. Note the early branching especially for the basal compartment. **(D)** Reconstructions of dendritic trees of L2/3 PCs in Human STG datasets (H5 and H5_ext) with either all compartments (first and second row, n=15) or only apical compartment (below, n=6). Note that due to the smaller depth in z for the H5 dataset the PC reconstructions appear sparser than in H5_ext. Scale bars 50 µm. All data based on expert reconstructions.

Bibliography

Abbott, L.F. and Nelson, S.B. (2000). "Synaptic plasticity: taming the beast." Nature Neuroscience **3**(11): 1178-1183.

Abeles, M. (1982). Local Cortical Circuits, Springer Berlin, Heidelberg.

Abeles, M. (1991). Corticonics: Neural Circuits of the Cerebral Cortex, Cambridge University Press.

Abeles, M., Bergman, H., Margalit, E. and Vaadia, E. (1993). "Spatiotemporal firing patterns in the frontal cortex of behaving monkeys." Journal of Neurophysiology **70**(4): 1629-1638.

Abeles, M., Hayon, G. and Lehmann, D. (2004). "Modeling Compositionality by Dynamic Binding of Synfire Chains." Journal of Computational Neuroscience **17**: 179-201.

Abraham, W.C. (2003). "How long will long-term potentiation last?" Philosophical Transactions of the Royal Society of London. Series B: Biological Sciences **358**(1432): 735-744.

Aellen, M., Burkart, J.M. and Bshary, R. (2022). "No evidence for general intelligence in a fish." Ethology **128**(5): 424-436.

Ahissar, E. and Kleinfeld, D. (2003). "Closed-loop Neuronal Computations: Focus on Vibrissa Somatosensation in Rat." Cerebral Cortex **13**(1): 53-62.

Ahmed, B., Anderson, J.C., Douglas, R.J., Martin, K.A.C. and Nelson, J.C. (1994). "Polyneuronal innervation of spiny stellate neurons in cat visual cortex." Journal of Comparative Neurology **341**(1): 39-49.

Ahrens, M.B., Li, J.M., Orger, M.B., Robson, D.N., Schier, A.F., Engert, F. and Portugues, R. (2012). "Brain-wide neuronal dynamics during motor adaptation in zebrafish." Nature **485**(7399): 471-477.

Ahrens, M.B., Orger, M.B., Robson, D.N., Li, J.M. and Keller, P.J. (2013). "Whole-brain functional imaging at cellular resolution using light-sheet microscopy." Nature Methods **10**(5): 413-420.

Alksne, J.F., Blackstad, T.W., Walberg, F. and White, L.E. (1966). Electron Microscopy of Axon Degeneration: A Valuable Tool in Experimental Neuroanatomy. New York, Springer, Berlin, Heidelberg.

Allen, J.S., Damasio, H. and Grabowski, T.J. (2002). "Normal neuroanatomical variation in the human brain: An MRI-volumetric study." American Journal of Physical Anthropology **118**(4): 341-358.

Amari, S.I. (1972). "Learning Patterns and Pattern Sequences by Self-Organizing Nets of Threshold Elements." IEEE Transactions on Computers **C-21**(11): 1197-1206.

Amat, F., Höckendorf, B., Wan, Y., Lemon, W.C., McDole, K. and Keller, P.J. (2015). "Efficient processing and analysis of large-scale light-sheet microscopy data." Nature Protocols **10**(11): 1679-1696.

Andres, B., Köthe, U., Helmstaedter, M., Denk, W. and Hamprecht, F.A. (2008). Segmentation of SBFSEM Volume Data of Neural Tissue by Hierarchical Classification, Berlin, Heidelberg, Springer Berlin Heidelberg.

Arellano, J., Benavides-Piccione, R., DeFelipe, J. and Yuste, R. (2007). "Ultrastructure of dendritic spines: correlation between synaptic and spine morphologies." Frontiers in Neuroscience **1**.

Ascher, P. and Nowak, L. (1988). "The role of divalent cations in the N-methyl-D-aspartate responses of mouse central neurones in culture." The Journal of Physiology **399**(1): 247-266.

Ascoli, G.A., Alonso-Nanclares, L., Anderson, S.A., Barrionuevo, G., Benavides-Piccione, R., Burkhalter, A., Buzsáki, G., Cauli, B., DeFelipe, J., Fairén, A., Feldmeyer, D., Fishell, G., Fregnac, Y., Freund, T.F., Gardner, D., Gardner, E.P., Goldberg, J.H., Helmstaedter, M., Hestrin, S., Karube, F., Kisvárday, Z.F., Lambolez, B., Lewis, D.A., Marin, O., Markram, H., Muñoz, A., Packer, A., Petersen, C.C.H., Rockland, K.S., Rossier, J., Rudy, B., Somogyi, P., Staiger, J.F., Tamas, G., Thomson, A.M., Toledo-Rodriguez, M., Wang, Y., West, D.C., Yuste, R. and The Petilla Interneuron Nomenclature, G. (2008). "Petilla terminology: nomenclature of features of GABAergic interneurons of the cerebral cortex." Nature Reviews Neuroscience **9**(7): 557-568.

Aswolinskiy, W. and Pipa, G. (2015). "RM-SORN: a reward-modulated self-organizing recurrent neural network." Frontiers in Computational Neuroscience **9**: 36.

Attardo, A., Fitzgerald, J.E. and Schnitzer, M.J. (2015). "Impermanence of dendritic spines in live adult CA1 hippocampus." Nature **523**(7562): 592-596.

Auer, P., Burgsteiner, H. and Maass, W. (2008). "A learning rule for very simple universal approximators consisting of a single layer of perceptrons." Neural Networks **21**: 786-795.

Aviel, Y., Mehring, C., Abeles, M. and Horn, D. (2003). "On Embedding Synfire Chains in a Balanced Network." Neural Computation **15**: 1321-1340.

Aviel, Y., Horn, D. and Abeles, M. (2005). "Memory Capacity of Balanced Networks." Neural Computation **17**: 691-713.

Azevedo, F.A.C., Carvalho, L.R.B., Grinberg, L.T., Farfel, J.M., Ferretti, R.E.L., Leite, R.E.P., Filho, W.J., Lent, R. and Herculano-Houzel, S. (2009). "Equal numbers of neuronal and nonneuronal cells make the human brain an isometrically scaled-up primate brain." Journal of Comparative Neurology **513**(5): 532-541.

Backus, J. (1978). "Can programming be liberated from the von Neumann style? a functional style and its algebra of programs." Commun. ACM **21**(8): 613–641.

Bae, J.A., Mu, S., Kim, J.S., Turner, N.L., Tartavull, I., Kemnitz, N., Jordan, C.S., Norton, A.D., Silversmith, W.M., Prentki, R., Sorek, M., David, C., Jones, D.L., Bland, D., Sterling, A.L.R., Park, J., Briggman, K.L. and Seung, H.S. (2018). "Digital Museum of Retinal Ganglion Cells with Dense Anatomy and Physiology." Cell **173**(5): 1293-1306.e1219.

Bakken, T.E., Jorstad, N.L., Hu, Q., Lake, B.B., Tian, W., Kalmbach, B.E., Crow, M., Hodge, R.D., Krienen, F.M., Sorensen, S.A., Eggermont, J., Yao, Z., Aevermann, B.D., Aldridge, A.I., Bartlett, A., Bertagnolli, D., Casper, T., Castanon, R.G., Crichton, K., Daigle, T.L., Dalley, R., Dee, N., Dembrow, N., Diep, D., Ding, S.-L., Dong, W., Fang, R., Fischer, S., Goldman, M., Goldy, J., Graybuck, L.T., Herb, B.R., Hou, X., Kancherla, J., Kroll, M., Lathia, K., van Lew, B., Li, Y.E., Liu, C.S., Liu, H., Lucero, J.D., Mahurkar, A., McMillen, D., Miller, J.A., Moussa, M., Nery, J.R., Nicovich, P.R., Niu, S.-Y., Orvis, J., Osteen, J.K., Owen, S., Palmer, C.R., Pham, T., Plongthongkum, N., Poirion, O., Reed, N.M., Rimorin, C., Rivkin, A., Romanow, W.J., Sedeño-Cortés, A.E., Siletti, K., Somasundaram, S., Sulc, J., Tieu, M., Torkelson, A., Tung, H., Wang, X., Xie, F., Yanny, A.M., Zhang, R., Ament, S.A., Behrens, M.M., Bravo, H.C., Chun, J., Dobin, A., Gillis, J., Hertzano, R., Hof, P.R., Höllt, T., Horwitz, G.D., Keene, C.D., Kharchenko, P.V., Ko, A.L., Lelieveldt, B.P., Luo, C., Mukamel, E.A., Pinto-Duarte, A., Preissl, S., Regev, A., Ren, B., Scheuermann, R.H., Smith, K., Spain, W.J., White, O.R., Koch, C., Hawrylycz, M., Tasic, B., Macosko, E.Z., McCarroll, S.A., Ting, J.T., Zeng, H., Zhang, K., Feng, G., Ecker, J.R., Linnarsson, S. and Lein, E.S. (2021). "Comparative cellular analysis of motor cortex in human, marmoset and mouse." Nature **598**(7879): 111-119.

Bargmann, C.I. and Marder, E. (2013). "From the connectome to brain function." Nature Methods **10**(6): 483-490.

Bartol, T.M., Jr., Bromer, C., Kinney, J., Chirillo, M.A., Bourne, J.N., Harris, K.M. and Sejnowski, T.J. (2015). "Nanoconnectomic upper bound on the variability of synaptic plasticity." eLife **4**: e10778.

Bates, A.S., Schlegel, P., Roberts, R.J.V., Drummond, N., Tamimi, I.F.M., Turnbull, R., Zhao, X., Marin, E.C., Popovici, P.D., Dhawan, S., Jamasb, A., Javier, A., Serratosa Capdevila, L., Li, F., Rubin, G.M., Waddell, S., Bock, D.D., Costa, M. and Jefferis, G.S.X.E. (2020). "Complete Connectomic Reconstruction of Olfactory Projection Neurons in the Fly Brain." Current Biology **30**(16): 3183-3199.e3186.

Beaulieu, C., Dyck, R. and Cynader, M. (1992). "Enrichment of glutamate in zinc-containing terminals of the cat visual cortex." NeuroReport **3**(10).

Beaulieu, C., Kisvarday, Z., Somogyi, P., Cynader, M. and Cowey, A. (1992). "Quantitative Distribution of GABA-immunopositive and-immunonegative Neurons and Synapses in the Monkey Striate Cortex (Area 17)." Cerebral Cortex **2**(4): 295-309.

Beaulieu, C., Campistron, G. and Crevier, C. (1994). "Quantitative aspects of the GABA circuitry in the primary visual cortex of the adult rat." Journal of Comparative Neurology **339**(4): 559-572.

Beaumont, M.A., Zhang, W. and Balding, D.J. (2002). "Approximate Bayesian Computation in Population Genetics." Genetics **162**(4): 2025-2035.

Becker, C., Ali, K., Knott, G. and Fua, P. (2012). Learning Context Cues for Synapse Segmentation in EM Volumes. Medical Image Computing and Computer-Assisted Intervention – MICCAI 2012, Berlin, Heidelberg, Springer Berlin Heidelberg.

Beier, T., Pape, C., Rahaman, N., Prange, T., Berg, S., Bock, D.D., Cardona, A., Knott, G.W., Plaza, S.M., Scheffer, L.K., Koethe, U., Kreshuk, A. and Hamprecht, F.A. (2017). "Multicut brings automated neurite segmentation closer to human performance." Nature Methods **14**(2): 101-102.

Beierlein, M., Gibson, J.R. and Connors, B.W. (2003). "Two Dynamically Distinct Inhibitory Networks in Layer 4 of the Neocortex." Journal of Neurophysiology **90**(5): 2987-3000.

Benavides-Piccione, R., Ballesteros-Yáñez, I., DeFelipe, J. and Yuste, R. (2002). "Cortical area and species differences in dendritic spine morphology." Journal of Neurocytology **31**(3): 337-346.

Benavides-Piccione, R., Fernaud-Espinosa, I., Robles, V., Yuste, R. and DeFelipe, J. (2013). "Age-Based Comparison of Human Dendritic Spine Structure Using Complete Three-Dimensional Reconstructions." Cerebral Cortex **23**(8): 1798-1810.

Bengio, Y. (2009). "Learning Deep Architectures for AI." Foundations and Trends® in Machine Learning **2**(1): 1-127.

Berg, J., Sorensen, S.A., Ting, J.T., Miller, J.A., Chartrand, T., Buchin, A., Bakken, T.E., Budzillo, A., Dee, N., Ding, S.-L., Gouwens, N.W., Hodge, R.D., Kalmbach, B., Lee, C., Lee, B.R., Alfiler, L., Baker, K., Barkan, E., Beller, A., Berry, K., Bertagnolli, D., Bickley, K., Bomben, J., Braun, T., Brouner, K., Casper, T., Chong, P., Crichton, K., Dalley, R., de Frates, R., Desta, T., Lee, S.D., D'Orazi, F., Dotson, N., Egdorf, T., Enstrom, R., Farrell, C., Feng, D., Fong, O., Furdan, S., Galakhova, A.A., Gamlin, C., Gary, A., Glandon, A., Goldy, J., Gorham, M., Goriounova, N.A., Gratiy, S., Graybuck, L., Gu, H., Hadley, K., Hansen, N., Heistek, T.S., Henry, A.M., Heyer, D.B., Hill, D., Hill, C., Hupp, M., Jarsky, T., Kebede, S., Keene, L., Kim, L., Kim, M.-H., Kroll, M., Latimer, C., Levi, B.P., Link, K.E., Mallory, M., Mann, R., Marshall, D., Maxwell, M., McGraw, M., McMillen, D., Melief, E., Mertens, E.J., Mezei, L., Mihut, N., Mok, S., Molnar, G., Mukora, A., Ng, L., Ngo, K., Nicovich, P.R., Nyhus, J., Olah, G., Oldre, A., Omstead, V., Ozsvar, A., Park, D., Peng, H., Pham, T., Pom, C.A., Potekhina, L., Rajanbabu, R., Ransford, S., Reid, D., Rimorin, C., Ruiz, A., Sandman, D., Sulc, J., Sunkin, S.M., Szafer, A., Szemenyei, V., Thomsen, E.R., Tieu, M., Torkelson, A., Trinh, J., Tung, H., Wakeman, W., Waleboer, F., Ward, K., Wilbers, R., Williams, G., Yao, Z., Yoon, J.-G., Anastassiou, C., Arkhipov, A., Barzo, P., Bernard, A., Cobbs, C., de Witt Hamer, P.C., Ellenbogen, R.G., Esposito, L., Ferreira, M., Gwinn, R.P., Hawrylycz, M.J., Hof, P.R., Idema, S., Jones, A.R., Keene, C.D., Ko, A.L., Murphy, G.J., Ng, L., Ojemann, J.G., Patel, A.P., Phillips, J.W., Silbergeld, D.L., Smith, K., Tasic, B., Yuste, R., Segev, I., de Kock, C.P.J., Mansvelder, H.D., Tamas, G., Zeng, H., Koch, C. and Lein, E.S. (2021). "Human neocortical expansion involves glutamatergic neuron diversification." Nature **598**(7879): 151-158.

Berning, M., Boergens, K.M. and Helmstaedter, M. (2015). "SegEM: Efficient Image Analysis for High-Resolution Connectomics." Neuron **87**(6): 1193-1206.

Bi, G.-q. and Poo, M.-m. (1998). "Synaptic Modifications in Cultured Hippocampal Neurons: Dependence on Spike Timing, Synaptic Strength, and Postsynaptic Cell Type." The Journal of Neuroscience **18**(24): 10464.

Bienenstock, E. (1995). "A model of neocortex." Network: Computation in Neural Systems **6**(2): 179-224.

Bienenstock, E.L., Cooper, L.N. and Munro, P.W. (1982). "Theory for the development of neuron selectivity: orientation specificity and binocular interaction in visual cortex." J Neurosci **2**(1): 32-48.

Binzegger, T., Douglas, R.J. and Martin, K.A.C. (2004). "A Quantitative Map of the Circuit of Cat Primary Visual Cortex." The Journal of Neuroscience **24**(39): 8441.

Binzegger, T., Douglas, R.J. and Martin, K.A.C. (2005). Cortical Architecture. Brain, Vision, and Artificial Intelligence, Berlin, Heidelberg, Springer Berlin Heidelberg.

Blackstad, T.W. (1975). "Electron microscopy of experimental axonal degeneration in photochemically modified golgi preparations: A procedure for precise mapping of nervous connections." Brain Research **95**(2): 191-210.

Bliss, T.V.P. and Lømo, T. (1973). "Long-lasting potentiation of synaptic transmission in the dentate area of the anaesthetized rabbit following stimulation of the perforant path." The Journal of Physiology **232**(2): 331-356.

Bliss, T.V.P. and Collingridge, G.L. (1993). "A synaptic model of memory: long-term potentiation in the hippocampus." Nature **361**(6407): 31-39.

Bloss, E.B., Cembrowski, M.S., Karsh, B., Colonell, J., Fetter, R.D. and Spruston, N. (2018). "Single excitatory axons form clustered synapses onto CA1 pyramidal cell dendrites." Nature Neuroscience **21**(3): 353-363.

Bock, D.D., Lee, W.-C.A., Kerlin, A.M., Andermann, M.L., Hood, G., Wetzel, A.W., Yurgenson, S., Soucy, E.R., Kim, H.S. and Reid, R.C. (2011). "Network anatomy and in vivo physiology of visual cortical neurons." Nature **471**(7337): 177-182.

Boergens, K.M., Berning, M., Bocklisch, T., Braunlein, D., Drawitsch, F., Frohnhofen, J., Herold, T., Otto, P., Rzepka, N., Werkmeister, T., Werner, D., Wiese, G., Wissler, H. and Helmstaedter, M. (2017). "webKnossos: efficient online 3D data annotation for connectomics." Nat Methods **14**(7): 691-694.

Bohland, J.W., Wu, C., Barbas, H., Bokil, H., Bota, M., Breiter, H.C., Cline, H.T., Doyle, J.C., Freed, P.J., Greenspan, R.J., Haber, S.N., Hawrylycz, M., Herrera, D.G., Hilgetag, C.C., Huang, Z.J., Jones, A., Jones, E.G., Karten, H.J., Kleinfeld, D., Kötter, R., Lester, H.A., Lin, J.M., Mensh, B.D., Mikula, S., Panksepp, J., Price, J.L., Safdieh, J., Saper, C.B., Schiff, N.D., Schmahmann, J.D., Stillman, B.W., Svoboda, K., Swanson, L.W., Toga, A.W., Van Essen, D.C., Watson, J.D. and Mitra, P.P. (2009). "A Proposal for a Coordinated Effort for the Determination of Brainwide Neuroanatomical Connectivity in Model Organisms at a Mesoscopic Scale." PLOS Computational Biology **5**(3): e1000334.

Boldog, E., Bakken, T.E., Hodge, R.D., Novotny, M., Aevermann, B.D., Baka, J., Bordé, S., Close, J.L., Diez-Fuertes, F., Ding, S.-L., Faragó, N., Kocsis, Á.K., Kovács, B., Maltzer, Z., McCorrison, J.M., Miller, J.A., Molnár, G., Oláh, G., Ozsvár, A., Rózsa, M., Shehata, S.I., Smith, K.A., Sunkin, S.M., Tran, D.N., Venepally, P., Wall, A., Puskás, L.G., Barzó, P., Steemers, F.J., Schork, N.J., Scheuermann, R.H., Lasken, R.S., Lein, E.S. and Tamás, G. (2018). "Transcriptomic and morphophysiological evidence for a specialized human cortical GABAergic cell type." Nature Neuroscience **21**(9): 1185-1195.

Bonhoeffer, T. and Grinvald, A. (1991). "Iso-orientation domains in cat visual cortex are arranged in pinwheel-like patterns." Nature **353**(6343): 429-431.

Bopp, R., Holler-Rickauer, S., Martin, K.A.C. and Schuhknecht, G.F.P. (2017). "An Ultrastructural Study of the Thalamic Input to Layer 4 of Primary Motor and Primary Somatosensory Cortex in the Mouse." The Journal of Neuroscience **37**(9): 2435.

Bosch, M., Castro, J., Saneyoshi, T., Matsuno, H., Sur, M. and Hayashi, Y. (2014). "Structural and Molecular Remodeling of Dendritic Spine Substructures during Long-Term Potentiation." Neuron **82**(2): 444-459.

Botvinick, M., Barrett, D.G.T., Battaglia, P., de Freitas, N., Kumaran, D., Leibo, J.Z., Lillicrap, T., Modayil, J., Mohamed, S., Rabinowitz, N.C., Rezende, D.J., Santoro, A., Schaul, T., Summerfield, C., Wayne, G., Weber, T., Wierstra, D., Legg, S. and Hassabis, D. (2017). "Building machines that learn and think for themselves." Behavioral and Brain Sciences **40**: e255.

Bourgeois, J.P. and Rakic, P. (1993). "Changes of synaptic density in the primary visual cortex of the macaque monkey from fetal to adult stage." The Journal of Neuroscience **13**(7): 2801.

Braitenberg, V. and Schüz, A. (1998). Cortex: Statistics and Geometry of Neuronal Connectivity, Springer Berlin, Heidelberg.

Branco, T., Clark Beverley, A. and Häusser, M. (2010). "Dendritic Discrimination of Temporal Input Sequences in Cortical Neurons." Science **329**(5999): 1671-1675.

Brecht, M. and Sakmann, B. (2002). "Dynamic representation of whisker deflection by synaptic potentials in spiny stellate and pyramidal cells in the barrels and septa of layer 4 rat somatosensory cortex." J Physiol **543**(Pt 1): 49-70.

Briggman, K.L. and Denk, W. (2006). "Towards neural circuit reconstruction with volume electron microscopy techniques." Current Opinion in Neurobiology **16**(5): 562-570.

Briggman, K.L., Helmstaedter, M. and Denk, W. (2011). "Wiring specificity in the direction-selectivity circuit of the retina." Nature **471**(7337): 183-188.

Briggman, K.L. and Bock, D.D. (2012). "Volume electron microscopy for neuronal circuit reconstruction." Current Opinion in Neurobiology **22**(1): 154-161.

Broca, P. (1861). "Remarques sur le siège de la faculté du langage articulé, suivies d'une observation d'aphémie (perte de la parole)." Bulletin et Memoires de la Societe anatomique de Paris **6**: 330-357.

Brodmann, K. (1909). Vergleichende Lokalisationslehre der Grosshirnrinde in ihren Prinzipien dargestellt auf Grund des Zellenbaues, Barth.

Bromer, C., Bartol, T.M., Bowden, J.B., Hubbard, D.D., Hanka, D.C., Gonzalez, P.V., Kuwajima, M., Mendenhall, J.M., Parker, P.H., Abraham, W.C., Sejnowski, T.J. and Harris, K.M. (2018). "Long-term potentiation expands information content of hippocampal dentate gyrus synapses." Proceedings of the National Academy of Sciences **115**(10): E2410-E2418.

Bruno, R.M. and Simons, D.J. (2002). "Feedforward Mechanisms of Excitatory and Inhibitory Cortical Receptive Fields." The Journal of Neuroscience **22**(24): 10966.

Buehner, M. and Young, P. (2006). "A tighter bound for the echo state property." IEEE Transactions on Neural Networks **17**: 820–824.

Buonomano, D.V. and Maass, W. (2009). "State-dependent computations: spatiotemporal processing in cortical networks." Nature Reviews Neuroscience **10**: 113-125.

Burkart, J.M., Schubiger, M.N. and van Schaik, C.P. (2017). "The evolution of general intelligence." Behavioral and Brain Sciences **40**: e195.

Buzsáki, G. and Mizuseki, K. (2014). "The log-dynamic brain: how skewed distributions affect network operations." Nature Reviews Neuroscience **15**(4): 264-278.

Cajal, S.R.y. (1899). "Estudios sobre la corteza cerebral humana. II. Estructura de la corteza motriz del hombre y mamíferos superiores." Revista Trimestral Microgáfica **4**: 117-200.

Calì, C., Wawrzyniak, M., Becker, C., Maco, B., Cantoni, M., Jorstad, A., Nigro, B., Grillo, F., De Paola, V., Fua, P. and Knott, G.W. (2018). "The effects of aging on neuropil structure in mouse somatosensory cortex—A 3D electron microscopy analysis of layer 1." PLOS ONE **13**(7): e0198131.

Cano-Astorga, N., DeFelipe, J. and Alonso-Nanclares, L. (2021). "Three-Dimensional Synaptic Organization of Layer III of the Human Temporal Neocortex." Cerebral Cortex **31**(10): 4742-4764.

Carr, C.E. and Konishi, M. (1988). "Axonal delay lines for time measurement in the owl's brainstem." Proceedings of the National Academy of Sciences **85**(21): 8311-8315.

Carr, C.E. and Konishi, M. (1990). "A circuit for detection of interaural time differences in the brain stem of the barn owl." The Journal of Neuroscience **10**(10): 3227.

Carroll, J.B. (1993). Human cognitive abilities: A survey of factor-analytic studies. New York, NY, US, Cambridge University Press.

Carroll, R.C., Lissin, D.V., Zastrow, M.v., Nicoll, R.A. and Malenka, R.C. (1999). "Rapid redistribution of glutamate receptors contributes to long-term depression in hippocampal cultures." Nature Neuroscience **2**(5): 454-460.

Carvell, G.E. and Simons, D.J. (1990). "Biometric analyses of vibrissal tactile discrimination in the rat." J Neurosci **10**(8): 2638-2648.

Cauli, B., Audinat, E., Lambolez, B., Angulo, M.C., Ropert, N., Tsuzuki, K., Hestrin, S. and Rossier, J. (1997). "Molecular and Physiological Diversity of Cortical Nonpyramidal Cells." The Journal of Neuroscience **17**(10): 3894.

Chang, F.-L.F. and Greenough, W.T. (1984). "Transient and enduring morphological correlates of synaptic activity and efficacy change in the rat hippocampal slice." Brain Research **309**(1): 35-46.

Cheetham, C.E.J., Barnes, S.J., Albieri, G., Knott, G.W. and Finnerty, G.T. (2014). "Pansynaptic Enlargement at Adult Cortical Connections Strengthened by Experience." Cerebral Cortex **24**(2): 521-531.

Chhetri, R.K., Amat, F., Wan, Y., Höckendorf, B., Lemon, W.C. and Keller, P.J. (2015). "Whole-animal functional and developmental imaging with isotropic spatial resolution." Nature Methods **12**(12): 1171-1178.

Chiu, C.Q., Lur, G., Morse, T.M., Carnevale, N.T., Ellis-Davies, G.C.R. and Higley, M.J. (2013). "Compartmentalization of GABAergic Inhibition by Dendritic Spines." Science **340**(6133): 759-762.

Ciresan, D.C., Meier, U., Masci, J., Gambardella, L.M. and Schmidhuber, J. (2011). Flexible, high performance convolutional neural networks for image classification. Twenty-second international joint conference on artificial intelligence.

Clack, N.G., O'Connor, D.H., Huber, D., Petreanu, L., Hires, A., Peron, S., Svoboda, K. and Myers, E.W. (2012). "Automated Tracking of Whiskers in Videos of Head Fixed Rodents." PLOS Computational Biology **8**(7): e1002591.

Colonnier, M. (1964). "Experimental degeneration in the cerebral cortex." J Anat **98**(Pt 1): 47-53.

Colonnier, M. (1968). "Synaptic patterns on different cell types in the different laminae of the cat visual cortex. An electron microscope study." Brain Research **9**(2): 268-287.

Cook, S.J., Jarrell, T.A., Brittin, C.A., Wang, Y., Bloniarz, A.E., Yakovlev, M.A., Nguyen, K.C.Q., Tang, L.T.H., Bayer, E.A., Duerr, J.S., Bülow, H.E., Hobert, O., Hall, D.H. and Emmons, S.W. (2019). "Whole-animal connectomes of both Caenorhabditis elegans sexes." Nature **571**(7763): 63-71.

Cooke, S.F. and Bear, M.F. (2010). "Visual Experience Induces Long-Term Potentiation in the Primary Visual Cortex." The Journal of Neuroscience **30**(48): 16304.

Corney, J., Rea, H., Clark, D., Pritchard, J., Breaks, M. and Macleod, R. (2002). "Coarse filters for shape matching." IEEE Computer Graphics and Applications **22**(3): 65-74.

Cragg, B. (1976). "Ultrastructural features of human cerebral cortex." Journal of Anatomy **121**(Pt 2): 331.

Crair, M.C. and Malenka, R.C. (1995). "A critical period for long-term potentiation at thalamocortical synapses." Nature **375**(6529): 325-328.

Curcio, C.A. and Allen, K.A. (1990). "Topography of ganglion cells in human retina." Journal of Comparative Neurology **300**(1): 5-25.

da Costa, N.M. and Martin, K.A.C. (2009). "Selective Targeting of the Dendrites of Corticothalamic Cells by Thalamic Afferents in Area 17 of the Cat." The Journal of Neuroscience **29**(44): 13919.

da Costa, N.M. and Martin, K.A.C. (2013). "Sparse reconstruction of brain circuits: Or, how to survive without a microscopic connectome." NeuroImage **80**: 27-36.

Dale, H. (1935). "Pharmacology and Nerve-endings (Walter Ernest Dixon Memorial Lecture): (Section of Therapeutics and Pharmacology)." Proceedings of the Royal Society of Medicine **28**: 319-332.

Dawson, T.M., Golde, T.E. and Lagier-Tourenne, C. (2018). "Animal models of neurodegenerative diseases." Nature Neuroscience **21**(10): 1370-1379.

De Lima, A.D. and Morrison, J.H. (1989). "Ultrastructural analysis of somatostatin-immunoreactive neurons and synapses in the temporal and occipital cortex of the macaque monkey." Journal of Comparative Neurology **283**(2): 212-227.

de Robertis, E., Arnaiz, G.R.d.L., de Iraldi, L.S.A.P. and Zieher, L.M. (1963). "Isolation of synaptic vesicles and structural organization of the acetylcholine system within brain nerve endings." Journal of Neurochemistry **10**(4): 225-235.

de Robertis, E.D. and Bennett, H.S. (1955). "Some features of the submicroscopic morphology of synapses in frog and earthworm." J Biophys Biochem Cytol **1**(1): 47-58.

de Vivo, L., Bellesi, M., Marshall, W., Bushong Eric, A., Ellisman Mark, H., Tononi, G. and Cirelli, C. (2017). "Ultrastructural evidence for synaptic scaling across the wake/sleep cycle." Science **355**(6324): 507-510.

DeFelipe, J., Hendry, S.H.C. and Jones, E.G. (1989). "Synapses of double bouquet cells in monkey cerebral cortex visualized by calbindin immunoreactivity." Brain Research **503**(1): 49-54.

DeFelipe, J., Hendry, S.H.C., Hashikawa, T., Molinari, M. and Jones, E.G. (1990). "A microcolumnar structure of monkey cerebral cortex revealed by immunocytochemical studies of double bouquet cell axons." Neuroscience **37**(3): 655-673.

DeFelipe, J., Alonso-Nanclares, L. and Arellano, J.I. (2002). "Microstructure of the neocortex: Comparative aspects." Journal of Neurocytology **31**(3): 299-316.

del Río, M.a.R. and DeFelipe, J. (1997). "Double bouquet cell axons in the human temporal neocortex: relationship to bundles of myelinated axons and colocalization of calretinin and calbindin D-28k immunoreactivities." Journal of Chemical Neuroanatomy **13**(4): 243-251.

del Río, M.R. and DeFelipe, J. (1995). "A light and electron microscopic study of calbindin D-28k immunoreactive double bouquet cells in the human temporal cortex." Brain Research **690**(1): 133-140.

del Río, M.R. and DeFelipe, J. (1996). "Colocalization of calbindin D-28k, calretinin, and GABA immunoreactivities in neurons of the human temporal cortex." Journal of Comparative Neurology **369**(3): 472-482.

Denk, W., Strickler, J.H. and Webb, W.W. (1990). "Two-Photon Laser Scanning Fluorescence Microscopy." Science **248**(4951): 73-76.

Denk, W. and Svoboda, K. (1997). "Photon Upmanship: Why Multiphoton Imaging Is More than a Gimmick." Neuron **18**(3): 351-357.

Denk, W. and Horstmann, H. (2004). "Serial block-face scanning electron microscopy to reconstruct three-dimensional tissue nanostructure." PLoS Biol **2**(11): e329.

Denk, W., Briggman, K.L. and Helmstaedter, M. (2012). "Structural neurobiology: missing link to a mechanistic understanding of neural computation." Nature Reviews Neuroscience **13**(5): 351-358.

Desmond, N.L. and Levy, W.B. (1983). "Synaptic correlates of associative potentiation/depression: an ultrastructural study in the hippocampus." Brain Research **265**(1): 21-30.

Desmond, N.L. and Levy, W.B. (1988). "Synaptic interface surface area increases with long-term potentiation in the hippocampal dentate gyrus." Brain Research **453**(1): 308-314.

Desmond, N.L. and Levy, W.B. (1990). "Morphological correlates of long-term potentiation imply the modification of existing synapses, not synaptogenesis, in the hippocampal dentate gyrus." Synapse **5**(2): 139-143.

Diesmann, M., Gewaltig, M.-O. and Aertsen, A. (1999). "Stable propagation of synchronous spiking in cortical neural networks." Nature **402**(6761): 529-533.

Domínguez-Álvaro, M., Montero-Crespo, M., Blazquez-Llorca, L., DeFelipe, J. and Alonso-Nanclares, L. (2019). "3D Electron Microscopy Study of Synaptic Organization of the Normal Human Transentorhinal Cortex and Its Possible Alterations in Alzheimer's Disease." eneuro **6**(4): ENEURO.0140-0119.2019.

Domínguez-Álvaro, M., Montero-Crespo, M., Blazquez-Llorca, L., DeFelipe, J. and Alonso-Nanclares, L. (2021). "3D Ultrastructural Study of Synapses in the Human Entorhinal Cortex." Cerebral Cortex **31**(1): 410-425.

Dorkenwald, S., Schubert, P.J., Killinger, M.F., Urban, G., Mikula, S., Svara, F. and Kornfeld, J. (2017). "Automated synaptic connectivity inference for volume electron microscopy." Nature Methods **14**(4): 435-442.

Dorkenwald, S., Turner, N.L., Macrina, T., Lee, K., Lu, R., Wu, J., Bodor, A.L., Bleckert, A.A., Brittain, D., Kemnitz, N., Silversmith, W.M., Ih, D., Zung, J., Zlateski, A., Tartavull, I., Yu, S.-C., Popovych, S., Wong, W., Castro, M., Jordan, C.S., Wilson, A.M., Froudarakis, E., Buchanan, J., Takeno, M., Torres, R., Mahalingam, G., Collman, F., Schneider-Mizell, C., Bumbarger, D.J., Li, Y., Becker, L., Suckow, S., Reimer, J., Tolias, A.S., Maçarico da Costa, N., Reid, R.C. and Seung, H.S. (2021). "Binary and analog variation of synapses between cortical pyramidal neurons." bioRxiv: 2019.2012.2029.890319.

Dorkenwald, S., McKellar, C.E., Macrina, T., Kemnitz, N., Lee, K., Lu, R., Wu, J., Popovych, S., Mitchell, E., Nehoran, B., Jia, Z., Bae, J.A., Mu, S., Ih, D., Castro, M., Ogedengbe, O., Halageri, A., Kuehner, K., Sterling, A.R., Ashwood, Z., Zung, J., Brittain, D., Collman, F., Schneider-Mizell, C., Jordan, C., Silversmith, W., Baker, C., Deutsch, D., Encarnacion-Rivera, L., Kumar, S., Burke, A., Bland, D., Gager, J., Hebditch, J., Koolman, S., Moore, M., Morejohn, S., Silverman, B., Willie, K., Willie, R., Yu, S.-c., Murthy, M. and Seung, H.S. (2022). "FlyWire: online community for whole-brain connectomics." Nature Methods **19**(1): 119-128.

Doyle, D.A., Cabral, J.M., Pfuetzner, R.A., Kuo, A., Gulbis, J.M., Cohen, S.L., Chait, B.T. and MacKinnon, R. (1998). "The Structure of the Potassium Channel: Molecular Basis of K+ Conduction and Selectivity." Science **280**(5360): 69-77.

Drawitsch, F., Karimi, A., Boergens, K.M. and Helmstaedter, M. (2018). "FluoEM, virtual labeling of axons in three-dimensional electron microscopy data for long-range connectomics." eLife **7**: e38976.

Druckmann, S. and Chklovskii, D.B. (2010). "Over-complete representations on recurrent neural networks can support persistent percepts." Advances in neural information processing systems **23**: 541–549.

Druckmann, S. and Chklovskii, D.B. (2012). "Neuronal circuits underlying persistent representations despite time varying activity." Curr Biol **22**(22): 2095-2103.

Dunn, T.W., Mu, Y., Narayan, S., Randlett, O., Naumann, E.A., Yang, C.-T., Schier, A.F., Freeman, J., Engert, F. and Ahrens, M.B. (2016). "Brain-wide mapping of neural activity controlling zebrafish exploratory locomotion." eLife **5**: e12741.

Durand, G.M., Kovalchuk, Y. and Konnerth, A. (1996). "Long-term potentiation and functional synapse induction in developing hippocampus." Nature **381**(6577): 71-75.

Džaja, D., Hladnik, A., Bičanić, I., Baković, M. and Petanjek, Z. (2014). "Neocortical calretinin neurons in primates: increase in proportion and microcircuitry structure." Frontiers in Neuroanatomy **8**.

Eberle, A.L., Mikula, S., Schalek, R., Lichtman, J., Tate, M.L.K. and Zeidler, D. (2015). "High-resolution, high-throughput imaging with a multibeam scanning electron microscope." Journal of Microscopy **259**(2): 114-120.

Eccles, J.C., Jones, R.V. and Paton, W.D.M. (1976). "From electrical to chemical transmission in the central nervous system: The closing address of the Sir Henry Dale Centennial Symposium Cambridge, 19 September 1975." Notes and Records of the Royal Society of London **30**(2): 219-230.

Efron, B. (1979). "Bootstrap Methods: Another Look at the Jackknife." The Annals of Statistics **7**(1): 1-26.

Egger, R., Dercksen, V.J., Udvary, D., Hege, H.-C. and Oberlaender, M. (2014). "Generation of dense statistical connectomes from sparse morphological data." Frontiers in Neuroanatomy **8**.

Egger, V., Feldmeyer, D. and Sakmann, B. (1999). "Coincidence detection and changes of synaptic efficacy in spiny stellate neurons in rat barrel cortex." Nature Neuroscience **2**(12): 1098-1105.

Eichler, K., Li, F., Litwin-Kumar, A., Park, Y., Andrade, I., Schneider-Mizell, C.M., Saumweber, T., Huser, A., Eschbach, C., Gerber, B., Fetter, R.D., Truman, J.W., Priebe, C.E., Abbott, L.F., Thum, A.S., Zlatic, M. and Cardona, A. (2017). "The complete connectome of a learning and memory centre in an insect brain." Nature **548**(7666): 175-182.

El Hihi, S. and Bengio, Y. (1996). "Hierarchical recurrent neural networks for long-term dependencies." Advances in neural information processing systems **8**.

Elston, G.N., Benavides-Piccione, R. and DeFelipe, J. (2001). "The Pyramidal Cell in Cognition: A Comparative Study in Human and Monkey." The Journal of Neuroscience **21**(17): RC163.

Engert, F. and Bonhoeffer, T. (1999). "Dendritic spine changes associated with hippocampal long-term synaptic plasticity." Nature **399**(6731): 66-70.

Engert, F. (2014). "The Big Data Problem: Turning Maps into Knowledge." Neuron **83**(6): 1246-1248.

Erdős, P. and Rényi, A. (1959). "On Random Graphs." Publicationes Mathematicae **6**: 290-297.

Esteva, A., Kuprel, B., Novoa, R.A., Ko, J., Swetter, S.M., Blau, H.M. and Thrun, S. (2017). "Dermatologist-level classification of skin cancer with deep neural networks." Nature **542**(7639): 115-118.

Eyal, G., Verhoog, M.B., Testa-Silva, G., Deitcher, Y., Lodder, J.C., Benavides-Piccione, R., Morales, J., DeFelipe, J., de Kock, C.P.J., Mansvelder, H.D. and Segev, I. (2016). "Unique membrane properties and enhanced signal processing in human neocortical neurons." eLife **5**: e16553.

Eyal, G., Verhoog, M.B., Testa-Silva, G., Deitcher, Y., Benavides-Piccione, R., DeFelipe, J., de Kock, C.P.J., Mansvelder, H.D. and Segev, I. (2018). "Human Cortical Pyramidal Neurons: From Spines to Spikes via Models." Frontiers in Cellular Neuroscience **12**.

Fairén, A., Peters, A. and Saldanha, J. (1977). "A new procedure for examining Golgi impregnated neurons by light and electron microscopy." Journal of Neurocytology **6**(3): 311-337.

Fatt, P. and Katz, B. (1952). "Spontaneous subthreshold activity at motor nerve endings." J Physiol **117**(1): 109-128.

Fay, D., Moore, A.W., Brown, K., Filosi, M. and Jurman, G. (2015). "Graph metrics as summary statistics for Approximate Bayesian Computation with application to network model parameter estimation." Journal of Complex Networks **3**(1): 52-83.

Feldmeyer, D., Egger, V., Lübke, J. and Sakmann, B. (1999). "Reliable synaptic connections between pairs of excitatory layer 4 neurones within a single 'barrel' of developing rat somatosensory cortex." The Journal of Physiology **521**(1): 169-190.

Feldmeyer, D. and Sakmann, B. (2000). "Synaptic efficacy and reliability of excitatory connections between the principal neurones of the input (layer 4) and output layer (layer 5) of the neocortex." The Journal of Physiology **525**(1): 31-39.

Feldmeyer, D., Roth, A. and Sakmann, B. (2005). "Monosynaptic Connections between Pairs of Spiny Stellate Cells in Layer 4 and Pyramidal Cells in Layer 5A Indicate That Lemniscal and Paralemniscal Afferent Pathways Converge in the Infragranular Somatosensory Cortex." The Journal of Neuroscience **25**(13): 3423.

Feldmeyer, D. (2012). "Excitatory neuronal connectivity in the barrel cortex." Frontiers in Neuroanatomy **6**.

Fiala, J.C. (2005). "Reconstruct: a free editor for serial section microscopy." Journal of Microscopy **218**(1): 52-61.

Field, M., Lukacs, I.P., Hunter, E., Stacey, R., Plaha, P., Livermore, L., Ansorge, O. and Somogyi, P. (2021). "Tonic GABA-A Receptor-Mediated Currents of Human Cortical GABAergic Interneurons Vary Amongst Cell Types." The Journal of Neuroscience **41**(47): 9702.

Fifková, E. and Van Harreveld, A. (1977). "Long-lasting morphological changes in dendritic spines of dentate granular cells following stimulation of the entorhinal area." Journal of Neurocytology **6**(2): 211-230.

Fischler, M.A. and Bolles, R.C. (1981). "Random sample consensus: a paradigm for model fitting with applications to image analysis and automated cartography." Commun. ACM **24**(6): 381–395.

Foster, M. and Sherrington, C.S. (1897). The central nervous system.

Freeman, L.C. (1978). "Centrality in social networks conceptual clarification." Social networks **1**(3): 215-239.

French, R.M. (1999). "Catastrophic forgetting in connectionist networks." Trends in Cognitive Sciences **3**(4): 128-135.

Friedman, J., Hastie, T. and Tibshirani, R. (2000). "Additive logistic regression: a statistical view of boosting (With discussion and a rejoinder by the authors)." The Annals of Statistics **28**(2): 337-407.

Fritsch, G. and Hitzig, E. (1870). "Uber die elektrische Erregbarkeit des Grosshirns." Arch, anat. Physiol. Wiss. Med. **37**: 300-332.

Froemke, R.C., Poo, M.-m. and Dan, Y. (2005). "Spike-timing-dependent synaptic plasticity depends on dendritic location." Nature **434**(7030): 221-225.

Froemke, R.C., Tsay, I.A., Raad, M., Long, J.D. and Dan, Y. (2006). "Contribution of Individual Spikes in Burst-Induced Long-Term Synaptic Modification." Journal of Neurophysiology **95**(3): 1620-1629.

Fu, M., Yu, X., Lu, J. and Zuo, Y. (2012). "Repetitive motor learning induces coordinated formation of clustered dendritic spines in vivo." Nature **483**(7387): 92-95.

Fukushima, K. (1979). "Neural Network Model for a Mechanism of Pattern Recognition Unaffected by Shift in Position- Neocognitron." ELECTRON. & COMMUN. JAPAN **62**: 11–18.

Fukushima, K. (1980). "Neocognitron: A self-organizing neural network model for a mechanism of pattern recognition unaffected by shift in position." Biological Cybernetics **36**(4): 193-202.

Funke, J., Tschopp, F., Grisaitis, W., Sheridan, A., Singh, C., Saalfeld, S. and Turaga, S.C. (2019). "Large Scale Image Segmentation with Structured Loss Based Deep Learning for Connectome Reconstruction." IEEE Transactions on Pattern Analysis and Machine Intelligence **41**(7): 1669-1680.

Gabbott, P.L.A. and Bacon, S.J. (1996). "Local circuit neurons in the medial prefrontal cortex (areas 24a,b,c, 25 and 32) in the monkey: I. Cell morphology and morphometrics." Journal of Comparative Neurology **364**(4): 567-608.

Gallego, G., Delbrück, T., Orchard, G., Bartolozzi, C., Taba, B., Censi, A., Leutenegger, S., Davison, A.J., Conradt, J., Daniilidis, K. and Scaramuzza, D. (2022). "Event-Based Vision: A Survey." IEEE Transactions on Pattern Analysis and Machine Intelligence **44**(1): 154-180.

Galvani, L. (1791). "De viribus electricitatis in motu musculari. Commentarius." De Bonoiensi Scientiarum et Artium Intituo atque Academie Commentarii **7**: 363-418.

Geren, B.B. and McCulloch, D. (1951). "Development and use of the minot rotary microtome for thin sectioning." Experimental Cell Research **2**(1): 97-102.

Gerstner, W., Kempter, R., van Hemmen, J.L. and Wagner, H. (1996). "A neuronal learning rule for sub-millisecond temporal coding." Nature **383**: 76-78.

Gewaltig, M.-O., Diesmann, M. and Aertsen, A. (2001). "Propagation of cortical synfire activity: survival probability in single trials and stability in the mean." Neural Networks **14**: 657-673.

Gibson, J.R., Beierlein, M. and Connors, B.W. (1999). "Two networks of electrically coupled inhibitory neurons in neocortex." Nature **402**(6757): 75-79.

Gibson, J.R., Beierlein, M. and Connors, B.W. (2005). "Functional Properties of Electrical Synapses Between Inhibitory Interneurons of Neocortical Layer 4." Journal of Neurophysiology **93**(1): 467-480.

Gidon, A., Zolnik, T.A., Fidzinski, P., Bolduan, F., Papoutsi, A., Poirazi, P., Holtkamp, M., Vida, I. and Larkum, M.E. (2020). "Dendritic action potentials and computation in human layer 2/3 cortical neurons." Science **367**(6473): 83-87.

Gilbert, C.D. and Wiesel, T.N. (1979). "Morphology and intracortical projections of functionally characterised neurones in the cat visual cortex." Nature **280**(5718): 120-125.

Gilbert, C.D. and Wiesel, T.N. (1983). Functional Organization of the Visual Cortex. Progress in Brain Research. J. P. Changeux, J. Glowinski, M. Imbert and F. E. Bloom, Elsevier. **58:** 209-218.

Gilbert, E.N. (1959). "Random Graphs." The Annals of Mathematical Statistics **30**(4): 1141-1144.

Gilman, J.P., Medalla, M. and Luebke, J.I. (2017). "Area-Specific Features of Pyramidal Neurons—a Comparative Study in Mouse and Rhesus Monkey." Cerebral Cortex **27**(3): 2078-2094.

Glantz, L.A. and Lewis, D.A. (2000). "Decreased Dendritic Spine Density on Prefrontal Cortical Pyramidal Neurons in Schizophrenia." Archives of General Psychiatry **57**(1): 65-73.

Goedeke, S. and Diesmann, M. (2008). "The mechanism of synchronization in feed-forward neuronal networks." New Journal of Physics **10**: 015007.

Golgi, C. (1883). "Recherches sur l'histologie des centres nerveux." Arch Ital Biol **3**: 285–317.

Goodfellow, I., Pouget-Abadie, J., Mirza, M., Xu, B., Warde-Farley, D., Ozair, S., Courville, A. and Bengio, Y. (2014). "Generative adversarial nets." Advances in neural information processing systems **27**.

Goodfellow, I., Bengio, Y. and Courville, A. (2016). Deep learning, MIT press.

Goodfellow, I.J., Mirza, M., Xiao, D., Courville, A. and Bengio, Y. (2013). "An empirical investigation of catastrophic forgetting in gradient-based neural networks." arXiv preprint arXiv:1312.6211.

Goodfellow, I.J., Shlens, J. and Szegedy, C. (2014). "Explaining and harnessing adversarial examples." arXiv preprint arXiv:1412.6572.

Goriounova, N.A. and Mansvelder, H.D. (2019). "Genes, Cells and Brain Areas of Intelligence." Front Hum Neurosci **13**: 44.

Gottfredson, L.S. (1997). "Why g matters: The complexity of everyday life." Intelligence **24**(1): 79-132.

Gour, A., Boergens, K.M., Heike, N., Hua, Y., Laserstein, P., Song, K. and Helmstaedter, M. (2021). "Postnatal connectomic development of inhibition in mouse barrel cortex." Science.

Graham, B.J., Hildebrand, D.G.C., Kuan, A.T., Maniates-Selvin, J.T., Thomas, L.A., Shanny, B.L. and Lee, W.-C.A. (2019). "High-throughput transmission electron microscopy with automated serial sectioning." bioRxiv: 657346.

Granger, A.J., Wallace, M.L. and Sabatini, B.L. (2017). "Multi-transmitter neurons in the mammalian central nervous system." Current Opinion in Neurobiology **45**: 85-91.

Gray, E.G. (1959). "Axo-somatic and axo-dendritic synapses of the cerebral cortex: an electron microscope study." Journal of anatomy **93**(Pt 4): 420.

Griffith, J.S. (1963). "On the Stability of Brain-Like Structures." Biophysical Journal **3**: 299-308.

Grutzendler, J., Kasthuri, N. and Gan, W.-B. (2002). "Long-term dendritic spine stability in the adult cortex." Nature **420**(6917): 812-816.

Guić-Robles, E., Valdivieso, C. and Guajardo, G. (1989). "Rats can learn a roughness discrimination using only their vibrissal system." Behavioural Brain Research **31**: 285-289.

Gustafsson, B., Wigstrom, H., Abraham, W.C. and Huang, Y.Y. (1987). "Long-term potentiation in the hippocampus using depolarizing current pulses as the conditioning stimulus to single volley synaptic potentials." The Journal of Neuroscience **7**(3): 774.

Haier, R.J., Siegel, B.V., Nuechterlein, K.H., Hazlett, E., Wu, J.C., Paek, J., Browning, H.L. and Buchsbaum, M.S. (1988). "Cortical glucose metabolic rate correlates of abstract reasoning and attention studied with positron emission tomography." Intelligence **12**(2): 199-217.

Han, S., Pool, J., Tran, J. and Dally, W. (2015). "Learning both weights and connections for efficient neural network." Advances in neural information processing systems **28**.

Han, Y., Kebschull, J.M., Campbell, R.A.A., Cowan, D., Imhof, F., Zador, A.M. and Mrsic-Flogel, T.D. (2018). "The logic of single-cell projections from visual cortex." Nature **556**(7699): 51-56.

Hansel, D. and van Vreeswijk, C. (2002). "How noise contributes to contrast invariance of orientation tuning in cat visual cortex." Journal of Neuroscience **22**(12): 5118-5128.

Hansen, T. and Neumann, H. (2004). "A simple cell model with dominating opponent inhibition for robust image processing." Neural Networks **17**: 647-662.

Harman, A., Abrahams, B., Moore, S. and Hoskins, R. (2000). "Neuronal density in the human retinal ganglion cell layer from 16–77 years." The Anatomical Record **260**(2): 124-131.

Harris, J.A., Mihalas, S., Hirokawa, K.E., Whitesell, J.D., Choi, H., Bernard, A., Bohn, P., Caldejon, S., Casal, L., Cho, A., Feiner, A., Feng, D., Gaudreault, N., Gerfen, C.R., Graddis, N., Groblewski, P.A., Henry, A.M., Ho, A., Howard, R., Knox, J.E., Kuan, L., Kuang, X., Lecoq, J., Lesnar, P., Li, Y., Luviano, J., McConoughey, S., Mortrud, M.T., Naeemi, M., Ng, L., Oh, S.W., Ouellette, B., Shen, E., Sorensen, S.A., Wakeman, W., Wang, Q., Wang, Y., Williford, A., Phillips, J.W., Jones, A.R., Koch, C. and Zeng, H. (2019). "Hierarchical organization of cortical and thalamic connectivity." Nature **575**(7781): 195-202.

Harris, K.M. and Stevens, J.K. (1989). "Dendritic spines of CA 1 pyramidal cells in the rat hippocampus: serial electron microscopy with reference to their biophysical characteristics." The Journal of Neuroscience **9**(8): 2982.

Harvey, C.D. and Svoboda, K. (2007). "Locally dynamic synaptic learning rules in pyramidal neuron dendrites." Nature **450**(7173): 1195-1200.

Hassabis, D., Kumaran, D., Summerfield, C. and Botvinick, M. (2017). "Neuroscience-Inspired Artificial Intelligence." Neuron **95**(2): 245-258.

Hayashi-Takagi, A., Yagishita, S., Nakamura, M., Shirai, F., Wu, Y.I., Loshbaugh, A.L., Kuhlman, B., Hahn, K.M. and Kasai, H. (2015). "Labelling and optical erasure of synaptic memory traces in the motor cortex." Nature **525**(7569): 333-338.

Hayworth, K.J., Kasthuri, N., Schalek, R. and Lichtman, J.W. (2006). "Automating the Collection of Ultrathin Serial Sections for Large Volume TEM Reconstructions." Microscopy and Microanalysis **12**(S02): 86-87.

Hayworth, K.J., Morgan, J.L., Schalek, R., Berger, D.R., Hildebrand, D.G.C. and Lichtman, J.W. (2014). "Imaging ATUM ultrathin section libraries with WaferMapper: a multi-scale approach to EM reconstruction of neural circuits." Frontiers in Neural Circuits **8**.

Hayworth, K.J., Xu, C.S., Lu, Z., Knott, G.W., Fetter, R.D., Tapia, J.C., Lichtman, J.W. and Hess, H.F. (2015). "Ultrastructurally smooth thick partitioning and volume stitching for large-scale connectomics." Nature Methods **12**(4): 319-322.

Hazan, H. and Manevitz, L.M. (2012). "Topological constraints and robustness in liquid state machines." Expert Systems with Applications **39**: 1597-1606.

He, K. and Sun, J. (2015). Convolutional neural networks at constrained time cost. Proceedings of the IEEE conference on computer vision and pattern recognition.

He, K., Zhang, X., Ren, S. and Sun, J. (2015). Delving Deep into Rectifiers: Surpassing Human-Level Performance on ImageNet Classification. Proceedings of the 2015 IEEE International Conference on Computer Vision (ICCV), IEEE Computer Society**:** 1026–1034.

Hebb, D.O. (1949). The organization of behavior: a neuropsychological theory. New York, Wiley.

Hedges, S.B. and Kumar, S. (2002). "Vertebrate Genomes Compared." Science **297**(5585): 1283-1285.

Hedrick, N.G., Lu, Z., Bushong, E., Singhi, S., Nguyen, P., Magaña, Y., Jilani, S., Lim, B.K., Ellisman, M. and Komiyama, T. (2022). "Learning binds new inputs into functional synaptic clusters via spinogenesis." Nature Neuroscience **25**(6): 726-737.

Heinrich, L., Bennett, D., Ackerman, D., Park, W., Bogovic, J., Eckstein, N., Petruncio, A., Clements, J., Pang, S., Xu, C.S., Funke, J., Korff, W., Hess, H.F., Lippincott-Schwartz, J., Saalfeld, S., Weigel, A.V., Ali, R., Arruda, R., Bahtra, R., Nguyen, D. and Team, C.P. (2021). "Whole-cell organelle segmentation in volume electron microscopy." Nature **599**(7883): 141-146.

Helmstaedter, M., Briggman, K.L. and Denk, W. (2008). "3D structural imaging of the brain with photons and electrons." Current Opinion in Neurobiology **18**(6): 633-641.

Helmstaedter, M., Briggman, K.L. and Denk, W. (2011). "High-accuracy neurite reconstruction for high-throughput neuroanatomy." Nature Neuroscience **14**(8): 1081-1088.

Helmstaedter, M. (2013). "Cellular-resolution connectomics: challenges of dense neural circuit reconstruction." Nature Methods **10**(6): 501-507.

Helmstaedter, M., Briggman, K.L., Turaga, S.C., Jain, V., Seung, H.S. and Denk, W. (2013). "Connectomic reconstruction of the inner plexiform layer in the mouse retina." Nature **500**(7461): 168-174.

Helmstaedter, M. (2015). "The Mutual Inspirations of Machine Learning and Neuroscience." Neuron **86**(1): 25-28.

Herculano-Houzel, S., Mota, B. and Lent, R. (2006). "Cellular scaling rules for rodent brains." Proceedings of the National Academy of Sciences **103**(32): 12138-12143.

Herculano-Houzel, S. (2009). "The human brain in numbers: a linearly scaled-up primate brain." Frontiers in Human Neuroscience **3**.

Herculano-Houzel, S., Watson, C. and Paxinos, G. (2013). "Distribution of neurons in functional areas of the mouse cerebral cortex reveals quantitatively different cortical zones." Frontiers in Neuroanatomy **7**.

Herndon, J.G., Moss, M.B., Rosene, D.L. and Killiany, R.J. (1997). "Patterns of cognitive decline in aged rhesus monkeys." Behavioural Brain Research **87**(1): 25-34.

Herring, B.E. and Nicoll, R.A. (2016). "Long-Term Potentiation: From CaMKII to AMPA Receptor Trafficking." Annual Review of Physiology **78**(1): 351-365.

Herrmann, M., Hertz, J.A. and Prügel-Bennett, A. (1995). "Analysis of synfire chains." Network: Computation in Neural Systems **6**: 403-414.

Hersch, S.M. and White, E.L. (1981). "Quantification of synapses formed with apical dendrites of golgi-impregnated pyramidal cells: Variability in thalamocortical inputs, but consistency in the ratios of asymmetrical to symmetrical synapses." Neuroscience **6**(6): 1043-1051.

Hertz, J. and Prügel-Bennett, A. (1996). "Learning synfire chains: turning noise into signal." International Journal of Neural Systems **7**: 445-450.

Hildebrand, D.G.C., Cicconet, M., Torres, R.M., Choi, W., Quan, T.M., Moon, J., Wetzel, A.W., Scott Champion, A., Graham, B.J., Randlett, O., Plummer, G.S., Portugues, R., Bianco, I.H., Saalfeld, S., Baden, A.D., Lillaney, K., Burns, R., Vogelstein, J.T., Schier, A.F., Lee, W.-C.A., Jeong, W.-K., Lichtman, J.W. and Engert, F. (2017). "Whole-brain serial-section electron microscopy in larval zebrafish." Nature **545**(7654): 345-349.

Hinton, G., Deng, L., Yu, D., Dahl, G.E., Mohamed, A., Jaitly, N., Senior, A., Vanhoucke, V., Nguyen, P., Sainath, T.N. and Kingsbury, B. (2012). "Deep Neural Networks for Acoustic Modeling in Speech Recognition: The Shared Views of Four Research Groups." IEEE Signal Processing Magazine **29**(6): 82-97.

Hinton, G.E., Osindero, S. and Teh, Y.-W. (2006). "A Fast Learning Algorithm for Deep Belief Nets." Neural Computation **18**(7): 1527-1554.

Hodge, R.D., Bakken, T.E., Miller, J.A., Smith, K.A., Barkan, E.R., Graybuck, L.T., Close, J.L., Long, B., Johansen, N., Penn, O., Yao, Z., Eggermont, J., Höllt, T., Levi, B.P., Shehata, S.I., Aevermann, B., Beller, A., Bertagnolli, D., Brouner, K., Casper, T., Cobbs, C., Dalley, R., Dee, N., Ding, S.-L., Ellenbogen, R.G., Fong, O., Garren, E., Goldy, J., Gwinn, R.P., Hirschstein, D., Keene, C.D., Keshk, M., Ko, A.L., Lathia, K., Mahfouz, A., Maltzer, Z., McGraw, M., Nguyen, T.N., Nyhus, J., Ojemann, J.G., Oldre, A., Parry, S., Reynolds, S., Rimorin, C., Shapovalova, N.V., Somasundaram, S., Szafer, A., Thomsen, E.R., Tieu, M., Quon, G., Scheuermann, R.H., Yuste, R., Sunkin, S.M., Lelieveldt, B., Feng, D., Ng, L., Bernard, A., Hawrylycz, M., Phillips, J.W., Tasic, B., Zeng, H., Jones, A.R., Koch, C. and Lein, E.S. (2019). "Conserved cell types with divergent features in human versus mouse cortex." Nature **573**(7772): 61-68.

Hofman, M. (2014). "Evolution of the human brain: when bigger is better." Frontiers in Neuroanatomy **8**.

Holler, S., Kostinger, G., Martin, K.A.C., Schuhknecht, G.F.P. and Stratford, K.J. (2021). "Structure and function of a neocortical synapse." Nature.

Holtmaat, A.J.G.D., Trachtenberg, J.T., Wilbrecht, L., Shepherd, G.M., Zhang, X., Knott, G.W. and Svoboda, K. (2005). "Transient and Persistent Dendritic Spines in the Neocortex In Vivo." Neuron **45**(2): 279-291.

Hornung, J.-P. and De Tribolet, N. (1994). "Distribution of GABA-containing neurons in human frontal cortex: a quantitative immunocytochemical study." Anatomy and Embryology **189**(2): 139-145.

Hsu, A., Luebke, J.I. and Medalla, M. (2017). "Comparative ultrastructural features of excitatory synapses in the visual and frontal cortices of the adult mouse and monkey." Journal of Comparative Neurology **525**(9): 2175-2191.

Hua, Y., Laserstein, P. and Helmstaedter, M. (2015). "Large-volume en-bloc staining for electron microscopy-based connectomics." Nature Communications **6**(1): 7923.

Hua, Y., Loomba, S., Pawlak, V., Laserstein, P., Boergens, K.M., Kerr, J.N.D. and Helmstaedter, M. (2022). "Connectomic analysis of thalamus-driven disinhibition in cortical layer 4." bioRxiv: 2022.2006.2001.494290.

Hubel, D.H. and Wiesel, T.N. (1959). "Receptive fields of single neurones in the cat's striate cortex." The Journal of Physiology **148**(3): 574-591.

Hubel, D.H. and Wiesel, T.N. (1962). "Receptive fields, binocular interaction and functional architecture in the cat's visual cortex." The Journal of Physiology **160**(1): 106-154.

Humphries, M.D. and Gurney, K. (2008). "Network 'Small-World-Ness': A Quantitative Method for Determining Canonical Network Equivalence." PLOS ONE **3**(4): e0002051.

Ikegaya, Y., Aaron, G., Cossart, R., Aronov, D., Lampl, I., Ferster, D. and Yuste, R. (2004). "Synfire Chains and Cortical Songs: Temporal Modules of Cortical Activity." Science **304**(5670): 559-564.

Ivakhnenko, A.G. (1971). "Polynomial Theory of Complex Systems." IEEE Transactions on Systems, Man and Cybernetics **SMC-1**: 364-378.

Ivakhnenko, A.G.e. and Lapa, V.G. (1965). Cybernetic predicting devices., Joint Publications Research Service [available from the Clearinghouse for Federal Scientific and Technical Information].

Jadhav, S.P., Wolfe, J. and Feldman, D.E. (2009). "Sparse temporal coding of elementary tactile features during active whisker sensation." Nature Neuroscience **12**: 792-800.

Jaeger, H. (2001). Short term memory in echo state networks.

Jaeger, H. and Haas, H. (2004). "Harnessing Nonlinearity: Predicting Chaotic Systems and Saving Energy in Wireless Communication." Science **304**(5667): 78-80.

Jaeger, H. (2010). "The "echo state" approach to analysing and training recurrent neural networks-with an erratum note." Bonn, Germany: German National Research Center for Information Technology GMD Technical Report **148**: 34.

Jain, V., Murray, J.F., Roth, F., Turaga, S., Zhigulin, V., Briggman, K.L., Helmstaedter, M.N., Denk, W. and Seung, H.S. (2007). Supervised Learning of Image Restoration with Convolutional Networks. 2007 IEEE 11th International Conference on Computer Vision.

Jain, V., Turaga, S.C., Briggman, K., Helmstaedter, M., Denk, W. and Seung, H. (2011). "Learning to agglomerate superpixel hierarchies." Advances in Neural Information Processing Systems **24**.

Januszewski, M., Kornfeld, J., Li, P.H., Pope, A., Blakely, T., Lindsey, L., Maitin-Shepard, J., Tyka, M., Denk, W. and Jain, V. (2018). "High-precision automated reconstruction of neurons with flood-filling networks." Nat Methods **15**(8): 605-610.

Jenks, K.R., Tsimring, K., Ip, J.P.K., Zepeda, J.C. and Sur, M. (2021). "Heterosynaptic Plasticity and the Experience-Dependent Refinement of Developing Neuronal Circuits." Front Neural Circuits **15**: 803401.

Jia, H., Varga, Z., Sakmann, B. and Konnerth, A. (2014). "Linear integration of spine Ca2+ signals in layer 4 cortical neurons in vivo." Proceedings of the National Academy of Sciences **111**(25): 9277-9282.

Johansen, J.P., Diaz-Mataix, L., Hamanaka, H., Ozawa, T., Ycu, E., Koivumaa, J., Kumar, A., Hou, M., Deisseroth, K., Boyden, E.S. and LeDoux, J.E. (2014). "Hebbian and neuromodulatory mechanisms interact to trigger associative memory formation." Proceedings of the National Academy of Sciences **111**(51): E5584-E5592.

Jonas, E. and Kording, K.P. (2017). "Could a Neuroscientist Understand a Microprocessor?" PLOS Computational Biology **13**(1): e1005268.

Jones, E.G. (1968). "An electron microscopic study of the termination of afferent fiber systems within the somatic sensory cortex of the cat." J Anat **103**(3): 595–597.

Jones, E.G. and Powell, T.P.S. (1969). "Morphological Variations in the Dendritic Spines of the Neocortex." Journal of Cell Science **5**(2): 509-529.

Jones, E.G., Huntley, G.W. and Benson, D.L. (1994). "Alpha calcium/calmodulin-dependent protein kinase II selectively expressed in a subpopulation of excitatory neurons in monkey sensory-motor cortex: comparison with GAD-67 expression." The Journal of Neuroscience **14**(2): 611.

Jumper, J., Evans, R., Pritzel, A., Green, T., Figurnov, M., Ronneberger, O., Tunyasuvunakool, K., Bates, R., Žídek, A., Potapenko, A., Bridgland, A., Meyer, C., Kohl, S.A.A., Ballard, A.J., Cowie, A., Romera-Paredes, B., Nikolov, S., Jain, R., Adler, J., Back, T., Petersen, S., Reiman, D., Clancy, E., Zielinski, M., Steinegger, M., Pacholska, M., Berghammer, T., Bodenstein, S., Silver, D., Vinyals, O., Senior, A.W., Kavukcuoglu, K., Kohli, P. and Hassabis, D. (2021). "Highly accurate protein structure prediction with AlphaFold." Nature **596**(7873): 583-589.

Jun, J.J., Steinmetz, N.A., Siegle, J.H., Denman, D.J., Bauza, M., Barbarits, B., Lee, A.K., Anastassiou, C.A., Andrei, A., Aydın, Ç., Barbic, M., Blanche, T.J., Bonin, V., Couto, J., Dutta, B., Gratiy, S.L., Gutnisky, D.A., Häusser, M., Karsh, B., Ledochowitsch, P., Lopez, C.M., Mitelut, C., Musa, S., Okun, M., Pachitariu, M., Putzeys, J., Rich, P.D., Rossant, C., Sun, W.-l., Svoboda, K., Carandini, M., Harris, K.D., Koch, C., O'Keefe, J. and Harris, T.D. (2017). "Fully integrated silicon probes for high-density recording of neural activity." Nature **551**(7679): 232-236.

Jung, R.E. and Haier, R.J. (2007). "The Parieto-Frontal Integration Theory (P-FIT) of intelligence: Converging neuroimaging evidence." Behavioral and Brain Sciences **30**(2): 135-154.

Karimi, A., Odenthal, J., Drawitsch, F., Boergens, K.M. and Helmstaedter, M. (2020). "Cell-type specific innervation of cortical pyramidal cells at their apical dendrites." Elife **9**.

Kasthuri, N., Hayworth, K.J., Berger, D.R., Schalek, R.L., Conchello, J.A., Knowles-Barley, S., Lee, D., Vazquez-Reina, A., Kaynig, V., Jones, T.R., Roberts, M., Morgan, J.L., Tapia, J.C., Seung, H.S., Roncal, W.G., Vogelstein, J.T., Burns, R., Sussman, D.L., Priebe, C.E., Pfister, H. and Lichtman, J.W. (2015). "Saturated Reconstruction of a Volume of Neocortex." Cell **162**(3): 648-661.

Kauer, J.A., Malenka, R.C. and Nicoll, R.A. (1988). "NMDA application potentiates synaptic transmission in the hippocampus." Nature **334**(6179): 250-252.

Kawaguchi, Y. and Kubota, Y. (1996). "Physiological and morphological identification of somatostatin- or vasoactive intestinal polypeptide-containing cells among GABAergic cell subtypes in rat frontal cortex." The Journal of Neuroscience **16**(8): 2701.

Kawaguchi, Y., Karube, F. and Kubota, Y. (2006). "Dendritic Branch Typing and Spine Expression Patterns in Cortical Nonpyramidal Cells." Cerebral Cortex **16**(5): 696-711.

Kaynig, V., Fuchs, T. and Buhmann, J.M. (2010). Neuron geometry extraction by perceptual grouping in ssTEM images. 2010 IEEE Computer Society Conference on Computer Vision and Pattern Recognition.

Kaynig, V., Vazquez-Reina, A., Knowles-Barley, S., Roberts, M., Jones, T.R., Kasthuri, N., Miller, E., Lichtman, J. and Pfister, H. (2015). "Large-scale automatic reconstruction of neuronal processes from electron microscopy images." Medical Image Analysis **22**(1): 77-88.

Kayser, A.S. and Miller, K.D. (2002). "Opponent Inhibition: A Developmental Model of Layer 4 of the Neocortical Circuit." Neuron **33**: 131-142.

Keller, P.J., Schmidt, A.D., Santella, A., Khairy, K., Bao, Z., Wittbrodt, J. and Stelzer, E.H.K. (2010). "Fast, high-contrast imaging of animal development with scanned light sheet–based structured-illumination microscopy." Nature Methods **7**(8): 637-642.

Kharazia, V.N. and Weinberg, R.J. (1999). "Immunogold localization of AMPA and NMDA receptors in somatic sensory cortex of albino rat." Journal of Comparative Neurology **412**(2): 292-302.

Kim, C.-H. and Lisman, J.E. (1999). "A Role of Actin Filament in Synaptic Transmission and Long-Term Potentiation." The Journal of Neuroscience **19**(11): 4314.

Kim, J.S., Greene, M.J., Zlateski, A., Lee, K., Richardson, M., Turaga, S.C., Purcaro, M., Balkam, M., Robinson, A., Behabadi, B.F., Campos, M., Denk, W., Seung, H.S. and the, E. (2014). "Space–time wiring specificity supports direction selectivity in the retina." Nature **509**(7500): 331-336.

Kim, R. and Sejnowski, T.J. (2021). "Strong inhibitory signaling underlies stable temporal dynamics and working memory in spiking neural networks." Nature Neuroscience **24**(1): 129-139.

Kingma, D.P. and Welling, M. (2013). "Auto-encoding variational bayes." arXiv preprint arXiv:1312.6114.

Kingma, D.P. and Ba, J. (2014). Adam: A Method for Stochastic Optimization.

Kingma, D.P., Mohamed, S., Jimenez Rezende, D. and Welling, M. (2014). "Semi-supervised learning with deep generative models." Advances in neural information processing systems **27**.

Kirov, S.A., Petrak, L.J., Fiala, J.C. and Harris, K.M. (2004). "Dendritic spines disappear with chilling but proliferate excessively upon rewarming of mature hippocampus." Neuroscience **127**(1): 69-80.

Knoll, M. and Ruska, E. (1932). "Das Elektronenmikroskop." Zeitschrift für Physik **78**(5): 318-339.

Knott, G., Marchman, H., Wall, D. and Lich, B. (2008). "Serial Section Scanning Electron Microscopy of Adult Brain Tissue Using Focused Ion Beam Milling." The Journal of Neuroscience **28**(12): 2959.

Knott, G.W., Quairiaux, C., Genoud, C. and Welker, E. (2002). "Formation of Dendritic Spines with GABAergic Synapses Induced by Whisker Stimulation in Adult Mice." Neuron **34**(2): 265-273.

Knott, G.W., Holtmaat, A., Wilbrecht, L., Welker, E. and Svoboda, K. (2006). "Spine growth precedes synapse formation in the adult neocortex in vivo." Nature Neuroscience **9**(9): 1117-1124.

Koch, K., McLean, J., Segev, R., Freed, M.A., Berry, M.J., Balasubramanian, V. and Sterling, P. (2006). "How Much the Eye Tells the Brain." Current Biology **16**(14): 1428-1434.

Koelbl, C., Helmstaedter, M., Lübke, J. and Feldmeyer, D. (2015). "A Barrel-Related Interneuron in Layer 4 of Rat Somatosensory Cortex with a High Intrabarrel Connectivity." Cerebral Cortex **25**(3): 713-725.

Kohda, M., Sogawa, S., Jordan, A.L., Kubo, N., Awata, S., Satoh, S., Kobayashi, T., Fujita, A. and Bshary, R. (2022). "Further evidence for the capacity of mirror self-recognition in cleaner fish and the significance of ecologically relevant marks." PLOS Biology **20**(2): e3001529.

Kooijmans, R.N., Sierhuis, W., Self, M.W. and Roelfsema, P.R. (2020). "A Quantitative Comparison of Inhibitory Interneuron Size and Distribution between Mouse and Macaque V1, Using Calcium-Binding Proteins." Cerebral Cortex Communications **1**(1): tgaa068.

Kornfeld, J., Benezra, S.E., Narayanan, R.T., Svara, F., Egger, R., Oberlaender, M., Denk, W. and Long, M.A. (2017). "EM connectomics reveals axonal target variation in a sequence-generating network." eLife **6**: e24364.

Kornfeld, J. and Denk, W. (2018). "Progress and remaining challenges in high-throughput volume electron microscopy." Current Opinion in Neurobiology **50**: 261-267.

Kornfeld, J., Januszewski, M., Schubert, P., Jain, V., Denk, W. and Fee, M.S. (2020). "An anatomical substrate of credit assignment in reinforcement learning." bioRxiv: 2020.2002.2018.954354.

Korogod, N., Petersen, C.C.H. and Knott, G.W. (2015). "Ultrastructural analysis of adult mouse neocortex comparing aldehyde perfusion with cryo fixation." eLife **4**: e05793.

Kreshuk, A., Straehle, C.N., Sommer, C., Koethe, U., Cantoni, M., Knott, G. and Hamprecht, F.A. (2011). "Automated detection and segmentation of synaptic contacts in nearly isotropic serial electron microscopy images." PLoS One **6**(10): e24899.

Kreshuk, A., Koethe, U., Pax, E., Bock, D.D. and Hamprecht, F.A. (2014). "Automated Detection of Synapses in Serial Section Transmission Electron Microscopy Image Stacks." PLOS ONE **9**(2): e87351.

Kreshuk, A., Funke, J., Cardona, A. and Hamprecht, F.A. (2015). Who Is Talking to Whom: Synaptic Partner Detection in Anisotropic Volumes of Insect Brain. Medical Image Computing and Computer-Assisted Intervention -- MICCAI 2015, Cham, Springer International Publishing.

Krienen, F.M., Goldman, M., Zhang, Q., C. H. del Rosario, R., Florio, M., Machold, R., Saunders, A., Levandowski, K., Zaniewski, H., Schuman, B., Wu, C., Lutservitz, A., Mullally, C.D., Reed, N., Bien, E., Bortolin, L., Fernandez-Otero, M., Lin, J.D., Wysoker, A., Nemesh, J., Kulp, D., Burns, M., Tkachev, V., Smith, R., Walsh, C.A., Dimidschstein, J., Rudy, B., S. Kean, L., Berretta, S., Fishell, G., Feng, G. and McCarroll, S.A. (2020). "Innovations present in the primate interneuron repertoire." Nature **586**(7828): 262-269.

Krizhevsky, A., Sutskever, I. and Hinton, G.E. (2012). "Imagenet classification with deep convolutional neural networks." Advances in neural information processing systems **25**.

Kuan, A.T., Phelps, J.S., Thomas, L.A., Nguyen, T.M., Han, J., Chen, C.-L., Azevedo, A.W., Tuthill, J.C., Funke, J., Cloetens, P., Pacureanu, A. and Lee, W.-C.A. (2020). "Dense neuronal reconstruction through X-ray holographic nano-tomography." Nature Neuroscience **23**(12): 1637-1643.

Kuan, L., Li, Y., Lau, C., Feng, D., Bernard, A., Sunkin, S.M., Zeng, H., Dang, C., Hawrylycz, M. and Ng, L. (2015). "Neuroinformatics of the Allen Mouse Brain Connectivity Atlas." Methods **73**: 4-17.

Kubota, Y., Hatada, S., Kondo, S., Karube, F. and Kawaguchi, Y. (2007). "Neocortical Inhibitory Terminals Innervate Dendritic Spines Targeted by Thalamocortical Afferents." The Journal of Neuroscience **27**(5): 1139.

Kubota, Y., Kondo, S., Nomura, M., Hatada, S., Yamaguchi, N., Mohamed, A.A., Karube, F., Lübke, J. and Kawaguchi, Y. (2015). "Functional effects of distinct innervation styles of pyramidal cells by fast spiking cortical interneurons." eLife **4**: e07919.

Kubota, Y., Karube, F., Nomura, M. and Kawaguchi, Y. (2016). "The Diversity of Cortical Inhibitory Synapses." Front Neural Circuits **10**: 27.

Kubota, Y., Sohn, J., Hatada, S., Schurr, M., Straehle, J., Gour, A., Neujahr, R., Miki, T., Mikula, S. and Kawaguchi, Y. (2018). "A carbon nanotube tape for serial-section electron microscopy of brain ultrastructure." Nature Communications **9**(1): 437.

Kudithipudi, D., Aguilar-Simon, M., Babb, J., Bazhenov, M., Blackiston, D., Bongard, J., Brna, A.P., Chakravarthi Raja, S., Cheney, N., Clune, J., Daram, A., Fusi, S., Helfer, P., Kay, L., Ketz, N., Kira, Z., Kolouri, S., Krichmar, J.L., Kriegman, S., Levin, M., Madireddy, S., Manicka, S., Marjaninejad, A., McNaughton, B., Miikkulainen, R., Navratilova, Z., Pandit, T., Parker, A., Pilly, P.K., Risi, S., Sejnowski, T.J., Soltoggio, A., Soures, N., Tolias, A.S., Urbina-Meléndez, D., Valero-Cuevas, F.J., van de Ven, G.M., Vogelstein, J.T., Wang, F., Weiss, R., Yanguas-Gil, A., Zou, X. and Siegelmann, H. (2022). "Biological underpinnings for lifelong learning machines." Nature Machine Intelligence **4**(3): 196-210.

Kumar, A., Rotter, S. and Aertsen, A. (2008). "Conditions for propagating synchronous spiking and asynchronous firing rates in a cortical network model." J Neurosci **28**(20): 5268-5280.

Kwon, T., Merchán-Pérez, A., Rial Verde, E.M., Rodríguez, J.-R., DeFelipe, J. and Yuste, R. (2019). "Ultrastructural, Molecular and Functional Mapping of GABAergic Synapses on Dendritic Spines and Shafts of Neocortical Pyramidal Neurons." Cerebral Cortex **29**(7): 2771-2781.

Lake, B.M., Ullman, T.D., Tenenbaum, J.B. and Gershman, S.J. (2017). "Ingredients of intelligence: From classic debates to an engineering roadmap." Behavioral and Brain Sciences **40**: e281.

Lake, B.M., Ullman, T.D., Tenenbaum, J.B. and Gershman, S.J. (2017). "Building machines that learn and think like people." Behavioral and Brain Sciences **40**: e253.

Langford, E., Schwertman, N. and Owens, M. (2001). "Is the Property of Being Positively Correlated Transitive?" The American Statistician **55**(4): 322-325.

LaVail, J.H. and LaVail, M.M. (1972). "Retrograde Axonal Transport in the Central Nervous System." Science **176**(4042): 1416-1417.

Lavzin, M., Rapoport, S., Polsky, A., Garion, L. and Schiller, J. (2012). "Nonlinear dendritic processing determines angular tuning of barrel cortex neurons in vivo." Nature **490**(7420): 397-401.

Lawrence, J.D., Gramacy, R.B., Thomas, L. and Buckland, S.T. (2013). "The importance of prior choice in model selection: a density dependence example." Methods in Ecology and Evolution **4**(1): 25-33.

Lazar, A., Pipa, G. and Triesch, J. (2007). "Fading memory and time series prediction in recurrent networks with different forms of plasticity." Neural Networks **20**(3): 312-322.

Lazar, A., Pipa, G. and Triesch, J. (2009). "SORN: a self-organizing recurrent neural network." Frontiers in Computational Neuroscience **3**.

LeCun, Y., Boser, B., Denker, J., Henderson, D., Howard, R., Hubbard, W. and Jackel, L. (1989). "Backpropagation Applied to Handwritten Zip Code Recognition." Neural Computation **1**: 541-551.

LeCun, Y., Bottou, L., Bengio, Y. and Haffner, P. (1998). "Gradient-based learning applied to document recognition." Proceedings of the IEEE **86**(11): 2278-2324.

Lee, K., Zung, J., Li, P., Jain, V. and Seung, H.S. (2017). "Superhuman accuracy on the SNEMI3D connectomics challenge." arXiv preprint arXiv:1706.00120.

Lee, K., Turner, N., Macrina, T., Wu, J., Lu, R. and Seung, H.S. (2019). "Convolutional nets for reconstructing neural circuits from brain images acquired by serial section electron microscopy." Current Opinion in Neurobiology **55**: 188-198.

Lee, K.S., Schottler, F., Oliver, M. and Lynch, G. (1980). "Brief bursts of high-frequency stimulation produce two types of structural change in rat hippocampus." Journal of Neurophysiology **44**(2): 247-258.

Lee, T.J., Kumar, A., Balwani, A.H., Brittain, D., Kinn, S., Tovey, C.A., Dyer, E.L., da Costa, N.M., Reid, R.C., Forest, C.R. and Bumbarger, D.J. (2018). "Large-scale neuroanatomy using LASSO: Loop-based Automated Serial Sectioning Operation." PLOS ONE **13**(10): e0206172.

Lee, W.C., Bonin, V., Reed, M., Graham, B.J., Hood, G., Glattfelder, K. and Reid, R.C. (2016). "Anatomy and function of an excitatory network in the visual cortex." Nature **532**(7599): 370-374.

Lefort, S., Tomm, C., Floyd Sarria, J.C. and Petersen, C.C.H. (2009). "The Excitatory Neuronal Network of the C2 Barrel Column in Mouse Primary Somatosensory Cortex." Neuron **61**(2): 301-316.

Lendvai, B., Stern, E.A., Chen, B. and Svoboda, K. (2000). "Experience-dependent plasticity of dendritic spines in the developing rat barrel cortex in vivo." Nature **404**(6780): 876-881.

Lenz, M., Kruse, P., Eichler, A., Straehle, J., Beck, J., Deller, T. and Vlachos, A. (2021). "All-trans retinoic acid induces synaptic plasticity in human cortical neurons." eLife **10**: e63026.

Letinic, K., Zoncu, R. and Rakic, P. (2002). "Origin of GABAergic neurons in the human neocortex." Nature **417**(6889): 645-649.

Letzkus, J.J., Kampa, B.M. and Stuart, G.J. (2006). "Learning Rules for Spike Timing-Dependent Plasticity Depend on Dendritic Synapse Location." The Journal of Neuroscience **26**(41): 10420.

Letzkus, J.J., Wolff, S.B.E., Meyer, E.M.M., Tovote, P., Courtin, J., Herry, C. and Lüthi, A. (2011). "A disinhibitory microcircuit for associative fear learning in the auditory cortex." Nature **480**(7377): 331-335.

Letzkus, Johannes J., Wolff, Steffen B.E. and Lüthi, A. (2015). "Disinhibition, a Circuit Mechanism for Associative Learning and Memory." Neuron **88**(2): 264-276.

Levinthal, C. and Ware, R. (1972). "Three Dimensional Reconstruction from Serial Sections." Nature **236**(5344): 207-210.

Levy, N., Horn, D., Meilijson, I. and Ruppin, E. (2001). "Distributed synchrony in a cell assembly of spiking neurons." Neural Networks **14**: 815-824.

Levy, W.B. and Steward, O. (1983). "Temporal contiguity requirements for long-term associative potentiation/depression in the hippocampus." Neuroscience **8**(4): 791-797.

Li, H., Fertuzinhos, S., Mohns, E., Hnasko, Thomas S., Verhage, M., Edwards, R., Sestan, N. and Crair, Michael C. (2013). "Laminar and Columnar Development of Barrel Cortex Relies on Thalamocortical Neurotransmission." Neuron **79**(5): 970-986.

Li, H., Januszewski, M., Jain, V. and Li, P.H. (2020). "Neuronal Subcompartment Classification and Merge Error Correction." bioRxiv: 2020.2004.2016.043398.

Li, P.H., Lindsey, L.F., Januszewski, M., Tyka, M., Maitin-Shepard, J., Blakely, T. and Jain, V. (2019). "Automated Reconstruction of a Serial-Section EM Drosophila Brain with Flood-Filling Networks and Local Realignment." Microscopy and Microanalysis **25**(S2): 1364-1365.

Lichtman, J.W., Pfister, H. and Shavit, N. (2014). "The big data challenges of connectomics." Nature Neuroscience **17**(11): 1448-1454.

Lien, A.D. and Scanziani, M. (2013). "Tuned thalamic excitation is amplified by visual cortical circuits." Nature Neuroscience **16**(9): 1315-1323.

Lillicrap, T.P., Santoro, A., Marris, L., Akerman, C.J. and Hinton, G. (2020). "Backpropagation and the brain." Nature Reviews Neuroscience **21**(6): 335-346.

Liu, Z.-W., Faraguna, U., Cirelli, C., Tononi, G. and Gao, X.-B. (2010). "Direct Evidence for Wake-Related Increases and Sleep-Related Decreases in Synaptic Strength in Rodent Cortex." The Journal of Neuroscience **30**(25): 8671.

Liu, Z. and Keller, Philipp J. (2016). "Emerging Imaging and Genomic Tools for Developmental Systems Biology." Developmental Cell **36**(6): 597-610.

Livet, J., Weissman, T.A., Kang, H., Draft, R.W., Lu, J., Bennis, R.A., Sanes, J.R. and Lichtman, J.W. (2007). "Transgenic strategies for combinatorial expression of fluorescent proteins in the nervous system." Nature **450**(7166): 56-62.

Loomba, S., Straehle, J., Gangadharan, V., Heike, N., Khalifa, A., Motta, A., Ju, N., Sievers, M., Gempt, J., Meyer, H.S. and Helmstaedter, M. (2022). "Connectomic comparison of mouse and human cortex." Science **377**(6602): eabo0924.

Lorente de Nó, R. (1922). "La corteza cerebral del ratón." Trab. Lab. Invest. Bio.(Madrid) **20**: 41-78.

Lorente de Nó, R. (1949). Cerebral cortex: architecture, intracortical connections, motor projections. Oxford, Oxford University Press.

Lu, J.-t., Li, C.-y., Zhao, J.-P., Poo, M.-m. and Zhang, X.-h. (2007). "Spike-Timing-Dependent Plasticity of Neocortical Excitatory Synapses on Inhibitory Interneurons Depends on Target Cell Type." The Journal of Neuroscience **27**(36): 9711.

Lübke, J., Egger, V., Sakmann, B. and Feldmeyer, D. (2000). "Columnar Organization of Dendrites and Axons of Single and Synaptically Coupled Excitatory Spiny Neurons in Layer 4 of the Rat Barrel Cortex." The Journal of Neuroscience **20**(14): 5300.

Lübke, J., Roth, A., Feldmeyer, D. and Sakmann, B. (2003). "Morphometric Analysis of the Columnar Innervation Domain of Neurons Connecting Layer 4 and Layer 2/3 of Juvenile Rat Barrel Cortex." Cerebral Cortex **13**(10): 1051-1063.

Lukoševičius, M. and Jaeger, H. (2009). "Reservoir computing approaches to recurrent neural network training." Computer Science Review **3**: 127–149.

Lukoševičius, M., Jaeger, H. and Schrauwen, B. (2012). "Reservoir Computing Trends." KI - Künstliche Intelligenz **26**: 365-371.

Luo, L., Callaway, E.M. and Svoboda, K. (2018). "Genetic Dissection of Neural Circuits: A Decade of Progress." Neuron **98**(2): 256-281.

Lynch, G.S., Dunwiddie, T. and Gribkoff, V. (1977). "Heterosynaptic depression: a postsynaptic correlate of long-term potentiation." Nature **266**(5604): 737-739.

Maass, W., Natschläger, T. and Markram, H. (2002). "Real-Time Computing Without Stable States: A New Framework for Neural Computation Based on Perturbations." Neural Computation **14**(11): 2531-2560.

Maass, W. and Markram, H. (2004). "On the computational power of circuits of spiking neurons." Journal of Computer and System Sciences **69**: 593-616.

Maass, W., Natschläger, T. and Markram, H. (2004). "Computational models for generic cortical microcircuits." Computational neuroscience: A comprehensive approach **18**: 575.

Maass, W., Natschläger, T. and Markram, H. (2004). "Fading memory and kernel properties of generic cortical microcircuit models." Journal of Physiology-Paris **98**: 315-330.

Maass, W., Joshi, P. and Sontag, E.D. (2006). "Principles of real-time computing with feedback applied to cortical microcircuit models." Advances in neural information processing systems **18**: 835.

Macrina, T., Lee, K., Lu, R., Turner, N.L., Wu, J., Popovych, S., Silversmith, W., Kemnitz, N., Bae, J.A., Castro, M.A., Dorkenwald, S., Halageri, A., Jia, Z., Jordan, C., Li, K., Mitchell, E., Mondal, S.S., Mu, S., Nehoran, B., Wong, W., Yu, S.-c., Bodor, A.L., Brittain, D., Buchanan, J., Bumbarger, D.J., Cobos, E., Collman, F., Elabbady, L., Fahey, P.G., Froudarakis, E., Kapner, D., Kinn, S., Mahalingam, G., Papadopoulos, S., Patel, S., Schneider-Mizell, C.M., Sinz, F.H., Takeno, M., Torres, R., Yin, W., Pitkow, X., Reimer, J., Tolias, A.S., Reid, R.C., Costa, N.M.d. and Seung, H.S. (2021). "Petascale neural circuit reconstruction: automated methods." bioRxiv: 2021.2008.2004.455162.

Major, G., Larkum, M.E. and Schiller, J. (2013). "Active Properties of Neocortical Pyramidal Neuron Dendrites." Annual Review of Neuroscience **36**(1): 1-24.

Malenka, R.C. (1994). "Synaptic plasticity in the hippocampus: LTP and LTD." Cell **78**(4): 535-538.

Maletic-Savatic, M., Malinow, R. and Svoboda, K. (1999). "Rapid Dendritic Morphogenesis in CA1 Hippocampal Dendrites Induced by Synaptic Activity." Science **283**(5409): 1923-1927.

Malsburg, C.V.D. (1986). Frank Rosenblatt: Principles of Neurodynamics: Perceptrons and the Theory of Brain Mechanisms. Brain Theory. D. G. Palm and D. A. Aertsen, Springer**:** 245-248.

Manevitz, L. and Hazan, H. (2010). Stability and Topology in Reservoir Computing. Advances in Soft Computing. G. Sidorov, A. H. Aguirre and C. A. R. García, Springer**:** 245-256.

Manjunath, G. and Jaeger, H. (2013). "Echo state property linked to an input: Exploring a fundamental characteristic of recurrent neural networks." Neural computation **25**: 671–696.

Mao, B.-Q., Hamzei-Sichani, F., Aronov, D., Froemke, R.C. and Yuste, R. (2001). "Dynamics of Spontaneous Activity in Neocortical Slices." Neuron **32**(5): 883-898.

Marco, P. and DeFelipe, J. (1997). "Altered synaptic circuitry in the human temporal neocortex removed from epileptic patients." Experimental Brain Research **114**(1): 1-10.

Maret, S., Faraguna, U., Nelson, A.B., Cirelli, C. and Tononi, G. (2011). "Sleep and waking modulate spine turnover in the adolescent mouse cortex." Nature Neuroscience **14**(11): 1418-1420.

Marin, J.-M., Pillai, N.S., Robert, C.P. and Rousseau, J. (2014). "Relevant statistics for Bayesian model choice." Journal of the Royal Statistical Society: Series B (Statistical Methodology) **76**(5): 833-859.

Markram, H., Lübke, J., Frotscher, M., Roth, A. and Sakmann, B. (1997). "Physiology and anatomy of synaptic connections between thick tufted pyramidal neurones in the developing rat neocortex." The Journal of Physiology **500**(2): 409-440.

Markram, H., Lübke, J., Frotscher, M. and Sakmann, B. (1997). "Regulation of Synaptic Efficacy by Coincidence of Postsynaptic APs and EPSPs." Science **275**(5297): 213-215.

Markram, H., Wang, Y. and Tsodyks, M. (1998). "Differential signaling via the same axon of neocortical pyramidal neurons." Proceedings of the National Academy of Sciences **95**(9): 5323-5328.

Markram, H., Gerstner, W. and Sjöström, P.J. (2012). "Spike-Timing-Dependent Plasticity: A Comprehensive Overview." Frontiers in Synaptic Neuroscience **4**.

Markram, H., Muller, E., Ramaswamy, S., Reimann, Michael W., Abdellah, M., Sanchez, Carlos A., Ailamaki, A., Alonso-Nanclares, L., Antille, N., Arsever, S., Kahou, Guy Antoine A., Berger, Thomas K., Bilgili, A., Buncic, N., Chalimourda, A., Chindemi, G., Courcol, J.-D., Delalondre, F., Delattre, V., Druckmann, S., Dumusc, R., Dynes, J., Eilemann, S., Gal, E., Gevaert, Michael E., Ghobril, J.-P., Gidon, A., Graham, Joe W., Gupta, A., Haenel, V., Hay, E., Heinis, T., Hernando, Juan B., Hines, M., Kanari, L., Keller, D., Kenyon, J., Khazen, G., Kim, Y., King, James G., Kisvarday, Z., Kumbhar, P., Lasserre, S., Le Bé, J.-V., Magalhães, Bruno R.C., Merchán-Pérez, A., Meystre, J., Morrice, Benjamin R., Muller, J., Muñoz-Céspedes, A., Muralidhar, S., Muthurasa, K., Nachbaur, D., Newton, Taylor H., Nolte, M., Ovcharenko, A., Palacios, J., Pastor, L., Perin, R., Ranjan, R., Riachi, I., Rodríguez, J.-R., Riquelme, Juan L., Rössert, C., Sfyrakis, K., Shi, Y., Shillcock, Julian C., Silberberg, G., Silva, R., Tauheed, F., Telefont, M., Toledo-Rodriguez, M., Tränkler, T., Van Geit, W., Díaz, Jafet V., Walker, R., Wang, Y., Zaninetta, Stefano M., DeFelipe, J., Hill, Sean L., Segev, I. and Schürmann, F. (2015). "Reconstruction and Simulation of Neocortical Microcircuitry." Cell **163**(2): 456-492.

Mason, A., Nicoll, A. and Stratford, K. (1991). "Synaptic transmission between individual pyramidal neurons of the rat visual cortex in vitro." The Journal of Neuroscience **11**(1): 72.

Matsuzaki, M., Ellis-Davies, G.C.R., Nemoto, T., Miyashita, Y., Iino, M. and Kasai, H. (2001). "Dendritic spine geometry is critical for AMPA receptor expression in hippocampal CA1 pyramidal neurons." Nature Neuroscience **4**(11): 1086-1092.

Matsuzaki, M., Honkura, N., Ellis-Davies, G.C.R. and Kasai, H. (2004). "Structural basis of long-term potentiation in single dendritic spines." Nature **429**(6993): 761-766.

Matzel, L.D., Han, Y.R., Grossman, H., Karnik, M.S., Patel, D., Scott, N., Specht, S.M. and Gandhi, C.C. (2003). "Individual Differences in the Expression of a “General” Learning Ability in Mice." The Journal of Neuroscience **23**(16): 6423.

McGuire, B.A., Hornung, J.P., Gilbert, C.D. and Wiesel, T.N. (1984). "Patterns of synaptic input to layer 4 of cat striate cortex." The Journal of Neuroscience **4**(12): 3021.

Medalla, M., Gilman, J.P., Wang, J.-Y. and Luebke, J.I. (2017). "Strength and Diversity of Inhibitory Signaling Differentiates Primate Anterior Cingulate from Lateral Prefrontal Cortex." The Journal of Neuroscience **37**(18): 4717.

Mehring, C., Hehl, U., Kubo, M., Diesmann, M. and Aertsen, A. (2003). "Activity dynamics and propagation of synchronous spiking in locally connected random networks." Biological Cybernetics **88**: 395-408.

Meirovitch, Y., Matveev, A., Saribekyan, H., Budden, D., Rolnick, D., Odor, G., Knowles-Barley, S., Jones, T.R., Pfister, H. and Lichtman, J.W. (2016). "A multi-pass approach to large-scale connectomics." arXiv preprint arXiv:1612.02120.

Meirovitch, Y., Mi, L., Saribekyan, H., Matveev, A., Rolnick, D. and Shavit, N. (2019). "Cross-Classification Clustering: An Efficient Multi-Object Tracking Technique for 3-D Instance Segmentation in Connectomics."

Melchitzky, D.S., Sesack, S.R. and Lewis, D.A. (1999). "Parvalbumin-immunoreactive axon terminals in macaque monkey and human prefrontal cortex: Laminar, regional, and target specificity of type I and type II synapses." Journal of Comparative Neurology **408**(1): 11-22.

Melchitzky, D.S. and Lewis, D.A. (2008). "Dendritic-targeting GABA neurons in monkey prefrontal cortex: Comparison of somatostatin- and calretinin-immunoreactive axon terminals." Synapse **62**(6): 456-465.

Meyer, D., Bonhoeffer, T. and Scheuss, V. (2014). "Balance and Stability of Synaptic Structures during Synaptic Plasticity." Neuron **82**(2): 430-443.

Meyer, H.S., Wimmer, V.C., Oberlaender, M., de Kock, C.P.J., Sakmann, B. and Helmstaedter, M. (2010). "Number and Laminar Distribution of Neurons in a Thalamocortical Projection Column of Rat Vibrissal Cortex." Cerebral Cortex **20**(10): 2277-2286.

Meyer, H.S., Schwarz, D., Wimmer, V.C., Schmitt, A.C., Kerr, J.N.D., Sakmann, B. and Helmstaedter, M. (2011). "Inhibitory interneurons in a cortical column form hot zones of inhibition in layers 2 and 5A." Proceedings of the National Academy of Sciences **108**(40): 16807-16812.

Micheva, K.D. and Beaulieu, C. (1995). "Postnatal Development of GABA Neurons in the Rat Somatosensory Barrel Cortex: A Quantitative Study." European Journal of Neuroscience **7**(3): 419-430.

Micheva, K.D. and Beaulieu, C. (1996). "Quantitative aspects of synaptogenesis in the rat barrel field cortex with special reference to GABA circuitry." Journal of Comparative Neurology **373**(3): 340-354.

MICrONS consortium, Bae, J.A., Baptiste, M., Bodor, A.L., Brittain, D., Buchanan, J., Bumbarger, D.J., Castro, M.A., Celii, B., Cobos, E., Collman, F., da Costa, N.M., Dorkenwald, S., Elabbady, L., Fahey, P.G., Fliss, T., Froudarakis, E., Gager, J., Gamlin, C., Halageri, A., Hebditch, J., Jia, Z., Jordan, C., Kapner, D., Kemnitz, N., Kinn, S., Koolman, S., Kuehner, K., Lee, K., Li, K., Lu, R., Macrina, T., Mahalingam, G., McReynolds, S., Miranda, E., Mitchell, E., Mondal, S.S., Moore, M., Mu, S., Muhammad, T., Nehoran, B., Ogedengbe, O., Papadopoulos, C., Papadopoulos, S., Patel, S., Pitkow, X., Popovych, S., Ramos, A., Reid, R.C., Reimer, J., Schneider-Mizell, C.M., Seung, H.S., Silverman, B., Silversmith, W., Sterling, A., Sinz, F.H., Smith, C.L., Suckow, S., Takeno, M., Tan, Z.H., Tolias, A.S., Torres, R., Turner, N.L., Walker, E.Y., Wang, T., Williams, G., Williams, S., Willie, K., Willie, R., Wong, W., Wu, J., Xu, C., Yang, R., Yatsenko, D., Ye, F., Yin, W. and Yu, S.-c. (2021). "Functional connectomics spanning multiple areas of mouse visual cortex." bioRxiv: 2021.2007.2028.454025.

Mikula, S. (2016). "Progress Towards Mammalian Whole-Brain Cellular Connectomics." Frontiers in Neuroanatomy **10**.

Miller, K.D., Pinto, D.J. and Simons, D.J. (2001). "Processing in layer 4 of the neocortical circuit: new insights from visual and somatosensory cortex." Current Opinion in Neurobiology **11**(4): 488-497.

Milo, R., Shen-Orr, S., Itzkovitz, S., Kashtan, N., Chklovskii, D. and Alon, U. (2002). "Network Motifs: Simple Building Blocks of Complex Networks." Science **298**(5594): 824-827.

Mishchenko, Y., Hu, T., Spacek, J., Mendenhall, J., Harris, K.M. and Chklovskii, D.B. (2010). "Ultrastructural Analysis of Hippocampal Neuropil from the Connectomics Perspective." Neuron **67**(6): 1009-1020.

Mitra, Partha P. (2014). "The Circuit Architecture of Whole Brains at the Mesoscopic Scale." Neuron **83**(6): 1273-1283.

Mnih, V., Kavukcuoglu, K., Silver, D., Rusu, A.A., Veness, J., Bellemare, M.G., Graves, A., Riedmiller, M., Fidjeland, A.K., Ostrovski, G., Petersen, S., Beattie, C., Sadik, A., Antonoglou, I., King, H., Kumaran, D., Wierstra, D., Legg, S. and Hassabis, D. (2015). "Human-level control through deep reinforcement learning." Nature **518**(7540): 529-533.

Mohan, H., Verhoog, M.B., Doreswamy, K.K., Eyal, G., Aardse, R., Lodder, B.N., Goriounova, N.A., Asamoah, B., B. Brakspear, A.B.C., Groot, C., van der Sluis, S., Testa-Silva, G., Obermayer, J., Boudewijns, Z.S.R.M., Narayanan, R.T., Baayen, J.C., Segev, I., Mansvelder, H.D. and de Kock, C.P.J. (2015). "Dendritic and Axonal Architecture of Individual Pyramidal Neurons across Layers of Adult Human Neocortex." Cerebral Cortex **25**(12): 4839-4853.

Molnár, G., Oláh, S., Komlósi, G., Füle, M., Szabadics, J., Varga, C., Barzó, P. and Tamás, G. (2008). "Complex Events Initiated by Individual Spikes in the Human Cerebral Cortex." PLOS Biology **6**(9): e222.

Morgan, J.L. and Lichtman, J.W. (2013). "Why not connectomics?" Nature Methods **10**(6): 494-500.

Morgan, J.L., Berger, D.R., Wetzel, A.W. and Lichtman, J.W. (2016). "The Fuzzy Logic of Network Connectivity in Mouse Visual Thalamus." Cell **165**(1): 192-206.

Morrison, J.H. and Baxter, M.G. (2012). "The ageing cortical synapse: hallmarks and implications for cognitive decline." Nature Reviews Neuroscience **13**(4): 240-250.

Mortensen, H.S., Pakkenberg, B., Dam, M., Dietz, R., Sonne, C., Mikkelsen, B. and Eriksen, N. (2014). "Quantitative relationships in delphinid neocortex." Front Neuroanat **8**: 132.

Mota, B. and Herculano-Houzel, S. (2015). "Cortical folding scales universally with surface area and thickness, not number of neurons." Science **349**(6243): 74-77.

Motta, A., Berning, M., Boergens, K.M., Staffler, B., Beining, M., Loomba, S., Hennig, P., Wissler, H. and Helmstaedter, M. (2019). "Dense connectomic reconstruction in layer 4 of the somatosensory cortex." Science **366**(6469).

Mountcastle, V.B. (1957). "Modality and topographic properties of single neurons of cat's somatic sensory cortex." Journal of Neurophysiology **20**(4): 408-434.

Mrsic-Flogel, T.D., Hofer, S.B., Ohki, K., Reid, R.C., Bonhoeffer, T. and Hübener, M. (2007). "Homeostatic Regulation of Eye-Specific Responses in Visual Cortex during Ocular Dominance Plasticity." Neuron **54**(6): 961-972.

Nabavi, S., Fox, R., Proulx, C.D., Lin, J.Y., Tsien, R.Y. and Malinow, R. (2014). "Engineering a memory with LTD and LTP." Nature **511**(7509): 348-352.

Nägerl, U.V., Eberhorn, N., Cambridge, S.B. and Bonhoeffer, T. (2004). "Bidirectional Activity-Dependent Morphological Plasticity in Hippocampal Neurons." Neuron **44**(5): 759-767.

Narr, K.L., Woods, R.P., Thompson, P.M., Szeszko, P., Robinson, D., Dimtcheva, T., Gurbani, M., Toga, A.W. and Bilder, R.M. (2007). "Relationships between IQ and Regional Cortical Gray Matter Thickness in Healthy Adults." Cerebral Cortex **17**(9): 2163-2171.

Nass, M.M. and Cooper, L.N. (1975). "A theory for the development of feature detecting cells in visual cortex." Biological Cybernetics **19**(1): 1-18.

Naumann, R.K., Anjum, F., Roth-Alpermann, C. and Brecht, M. (2012). "Cytoarchitecture, areas, and neuron numbers of the Etruscan Shrew cortex." Journal of Comparative Neurology **520**(11): 2512-2530.

Newman, S.B., Borisko, E. and Swerdlow, M. (1943). "Ultra-microtomy by a new method." J Research Nat Bureau Stand **43**.

Nimchinsky, E.A., Gilissen, E., Allman, J.M., Perl, D.P., Erwin, J.M. and Hof, P.R. (1999). "A neuronal morphologic type unique to humans and great apes." Proceedings of the National Academy of Sciences **96**(9): 5268-5273.

Nogales, E. (2016). "The development of cryo-EM into a mainstream structural biology technique." Nature Methods **13**(1): 24-27.

Noguchi, J., Nagaoka, A., Hayama, T., Ucar, H., Yagishita, S., Takahashi, N. and Kasai, H. (2019). "Bidirectional in vivo structural dendritic spine plasticity revealed by two-photon glutamate uncaging in the mouse neocortex." Scientific Reports **9**(1): 13922.

Nunez-Iglesias, J., Kennedy, R., Parag, T., Shi, J. and Chklovskii, D.B. (2013). "Machine Learning of Hierarchical Clustering to Segment 2D and 3D Images." PLOS ONE **8**(8): e71715.

Nusser, Z., Lujan, R., Laube, G., Roberts, J.D.B., Molnar, E. and Somogyi, P. (1998). "Cell Type and Pathway Dependence of Synaptic AMPA Receptor Number and Variability in the Hippocampus." Neuron **21**(3): 545-559.

O'Connor, D.H., Wittenberg, G.M. and Wang, S.S.H. (2005). "Graded bidirectional synaptic plasticity is composed of switch-like unitary events." Proceedings of the National Academy of Sciences **102**(27): 9679-9684.

O'Connor, D.H., Peron, S.P., Huber, D. and Svoboda, K. (2010). "Neural Activity in Barrel Cortex Underlying Vibrissa-Based Object Localization in Mice." Neuron **67**(6): 1048-1061.

Oberlaender, M., Ramirez, A. and Bruno, Randy M. (2012). "Sensory Experience Restructures Thalamocortical Axons during Adulthood." Neuron **74**(4): 648-655.

Oh, S.W., Harris, J.A., Ng, L., Winslow, B., Cain, N., Mihalas, S., Wang, Q., Lau, C., Kuan, L., Henry, A.M., Mortrud, M.T., Ouellette, B., Nguyen, T.N., Sorensen, S.A., Slaughterbeck, C.R., Wakeman, W., Li, Y., Feng, D., Ho, A., Nicholas, E., Hirokawa, K.E., Bohn, P., Joines, K.M., Peng, H., Hawrylycz, M.J., Phillips, J.W., Hohmann, J.G., Wohnoutka, P., Gerfen, C.R., Koch, C., Bernard, A., Dang, C., Jones, A.R. and Zeng, H. (2014). "A mesoscale connectome of the mouse brain." Nature **508**(7495): 207-214.

Oh, W.C., Hill, T.C. and Zito, K. (2013). "Synapse-specific and size-dependent mechanisms of spine structural plasticity accompanying synaptic weakening." Proceedings of the National Academy of Sciences **110**(4): E305-E312.

Ohki, K., Chung, S., Ch'ng, Y.H., Kara, P. and Reid, R.C. (2005). "Functional imaging with cellular resolution reveals precise micro-architecture in visual cortex." Nature **433**(7026): 597-603.

Ohyama, T., Schneider-Mizell, C.M., Fetter, R.D., Aleman, J.V., Franconville, R., Rivera-Alba, M., Mensh, B.D., Branson, K.M., Simpson, J.H., Truman, J.W., Cardona, A. and Zlatic, M. (2015). "A multilevel multimodal circuit enhances action selection in Drosophila." Nature **520**(7549): 633-639.

Okamoto, K.-I., Nagai, T., Miyawaki, A. and Hayashi, Y. (2004). "Rapid and persistent modulation of actin dynamics regulates postsynaptic reorganization underlying bidirectional plasticity." Nature Neuroscience **7**(10): 1104-1112.

Osada, R., Funkhouser, T., Chazelle, B. and Dobkin, D. (2001). Matching 3D models with shape distributions. Proceedings International Conference on Shape Modeling and Applications.

Palade, G. and Palay, S.L. (1954). "Electron microscope observations of interneuronal and neuromuscular synapses." Anat Rec **118**: 335-336.

Palade, G.E. (1952). "A study of fixation for electron microscopy." Journal of Experimental Medicine **95**(3): 285-298.

Palay, S.L. (1956). "Synapses In The Central Nervous System." The Journal of Biophysical and Biochemical Cytology **2**(4): 193-202.

Parag, T., Chakraborty, A., Plaza, S. and Scheffer, L. (2015). "A Context-Aware Delayed Agglomeration Framework for Electron Microscopy Segmentation." PLOS ONE **10**(5): e0125825.

Parag, T., Berger, D., Kamentsky, L., Staffler, B., Wei, D., Helmstaedter, M., Lichtman, J.W. and Pfister, H. (2018). Detecting synapse location and connectivity by signed proximity estimation and pruning with deep nets. Proceedings of the European Conference on Computer Vision (ECCV) Workshops.

Parisi, G.I., Kemker, R., Part, J.L., Kanan, C. and Wermter, S. (2019). "Continual lifelong learning with neural networks: A review." Neural Networks **113**: 54-71.

Pascanu, R. and Jaeger, H. (2011). "A neurodynamical model for working memory." Neural Networks **24**: 199-207.

Pavlov, I.P. (1927). Conditioned reflexes: an investigation of the physiological activity of the cerebral cortex. Oxford, England, Oxford Univ. Press.

Pease, D.C. and Baker, R.F. (1948). "Sectioning Techniques for Electron Microscopy Using a Conventional Microtome." Proceedings of the Society for Experimental Biology and Medicine **67**(4): 470-474.

Peddie, C.J., Genoud, C., Kreshuk, A., Meechan, K., Micheva, K.D., Narayan, K., Pape, C., Parton, R.G., Schieber, N.L., Schwab, Y., Titze, B., Verkade, P., Weigel, A. and Collinson, L.M. (2022). "Volume electron microscopy." Nature Reviews Methods Primers **2**(1): 51.

Pedregosa, F., Varoquaux, G., Gramfort, A., Michel, V., Thirion, B., Grisel, O., Blondel, M., Prettenhofer, P., Weiss, R., Dubourg, V., Vanderplas, J., Passos, A., Cournapeau, D., Brucher, M., Perrot, M. and Duchesnay, É. (2011). "Scikit-learn: Machine Learning in Python." J. Mach. Learn. Res. **12**(null): 2825–2830.

Perin, R., Berger, T.K. and Markram, H. (2011). "A synaptic organizing principle for cortical neuronal groups." Proc Natl Acad Sci U S A **108**(13): 5419-5424.

Peters, A. and Feldman, M.L. (1976). "The projection of the lateral geniculate nucleus to area 17 of the rat cerebral cortex. I. General description." Journal of Neurocytology **5**(1): 63-84.

Peters, A., White, E.L. and Fairén, A. (1977). "Synapses between identified neuronal elements. An electron microscopic demonstration of degenerating axon terminals synapsing with Golgi impregnated neurons." Neuroscience Letters **6**(2): 171-175.

Peters, A. (1979). "Thalamic input to the cerebral cortex." Trends in Neurosciences **2**: 183-185.

Peters, A. (1984). Cerebral Cortex: Cellular Components of the Cerebral Cortex, Springer, New York.

Petersen, C.C.H., Malenka, R.C., Nicoll, R.A. and Hopfield, J.J. (1998). "All-or-none potentiation at CA3-CA1 synapses." Proceedings of the National Academy of Sciences **95**(8): 4732-4737.

Petreanu, L., Huber, D., Sobczyk, A. and Svoboda, K. (2007). "Channelrhodopsin-2–assisted circuit mapping of long-range callosal projections." Nature Neuroscience **10**(5): 663-668.

Pfeffer, C.K., Xue, M., He, M., Huang, Z.J. and Scanziani, M. (2013). "Inhibition of inhibition in visual cortex: the logic of connections between molecularly distinct interneurons." Nature Neuroscience **16**(8): 1068-1076.

Phelps, J.S., Hildebrand, D.G.C., Graham, B.J., Kuan, A.T., Thomas, L.A., Nguyen, T.M., Buhmann, J., Azevedo, A.W., Sustar, A., Agrawal, S., Liu, M., Shanny, B.L., Funke, J., Tuthill, J.C. and Lee, W.-C.A. (2021). "Reconstruction of motor control circuits in adult Drosophila using automated transmission electron microscopy." Cell **184**(3): 759-774.e718.

Pietschnig, J., Penke, L., Wicherts, J.M., Zeiler, M. and Voracek, M. (2015). "Meta-analysis of associations between human brain volume and intelligence differences: How strong are they and what do they mean?" Neuroscience & Biobehavioral Reviews **57**: 411-432.

Platt, J.C. (2000). Probabilities for support-vector machines. Advances in large-margin classifiers. A. J. Smola, P. Bartlett, B. Scholkopf and D. Schuurmans. Cambridge, MA, MIT Press**:** 422.

Plaza, S.M., Scheffer, L.K. and Saunders, M. (2012). "Minimizing Manual Image Segmentation Turn-Around Time for Neuronal Reconstruction by Embracing Uncertainty." PLOS ONE **7**(9): e44448.

Plaza, S.M. (2016). Focused Proofreading to Reconstruct Neural Connectomes from EM Images at Scale. Deep Learning and Data Labeling for Medical Applications, Cham, Springer International Publishing.

Pocock, S.J. and Stone, G.W. (2016). "The Primary Outcome Fails — What Next?" New England Journal of Medicine **375**(9): 861-870.

Porter, J.T., Johnson, C.K. and Agmon, A. (2001). "Diverse Types of Interneurons Generate Thalamus-Evoked Feedforward Inhibition in the Mouse Barrel Cortex." The Journal of Neuroscience **21**(8): 2699.

Prigg, T., Goldreich, D., Carvell, G.E. and Simons, D.J. (2002). "Texture discrimination and unit recordings in the rat whisker/barrel system." Physiology & Behavior **77**(4): 671-675.

Probst, D., Maass, W., Markram, H. and Gewaltig, M.-O. (2012). Liquid Computing in a Simplified Model of Cortical Layer IV: Learning to Balance a Ball. Artificial Neural Networks and Machine Learning – ICANN 2012, Berlin, Heidelberg, Springer Berlin Heidelberg.

Ramocki, M.B. and Zoghbi, H.Y. (2008). "Failure of neuronal homeostasis results in common neuropsychiatric phenotypes." Nature **455**(7215): 912-918.

Ramón y Cajal, S. (1891). "Sur la structure de l'écorce cérébrale de quelques mamifères." La Cellule **7**: 124–176.

Ramón y Cajal, S. (1911). Histologie du système nerveux de l'homme et des vertébrés. Paris, Maloine.

Ramón y Cajal, S. (1923). Recuerdos de mi vida. Madrid, Spain, Imprenta de Juan Pueyo.

Rasmus, A., Berglund, M., Honkala, M., Valpola, H. and Raiko, T. (2015). "Semi-supervised learning with ladder networks." Advances in neural information processing systems **28**.

Rastegari, M., Ordonez, V., Redmon, J. and Farhadi, A. (2016). XNOR-Net: ImageNet Classification Using Binary Convolutional Neural Networks. Computer Vision – ECCV 2016, Cham, Springer International Publishing.

Reimann, M.W., King, J.G., Muller, E.B., Ramaswamy, S. and Markram, H. (2015). "An algorithm to predict the connectome of neural microcircuits." Frontiers in Computational Neuroscience **9**.

Ren, J.Q., Aika, Y., Heizmann, C.W. and Kosaka, T. (1992). "Quantitative analysis of neurons and glial cells in the rat somatosensory cortex, with special reference to GABAergic neurons and parvalbumin-containing neurons." Experimental Brain Research **92**(1): 1-14.

Richards, B.A., Lillicrap, T.P., Beaudoin, P., Bengio, Y., Bogacz, R., Christensen, A., Clopath, C., Costa, R.P., de Berker, A., Ganguli, S., Gillon, C.J., Hafner, D., Kepecs, A., Kriegeskorte, N., Latham, P., Lindsay, G.W., Miller, K.D., Naud, R., Pack, C.C., Poirazi, P., Roelfsema, P., Sacramento, J., Saxe, A., Scellier, B., Schapiro, A.C., Senn, W., Wayne, G., Yamins, D., Zenke, F., Zylberberg, J., Therien, D. and Kording, K.P. (2019). "A deep learning framework for neuroscience." Nature Neuroscience **22**(11): 1761-1770.

Rioult-Pedotti, M.-S., Friedman, D. and Donoghue, J.P. (2000). "Learning-Induced LTP in Neocortex." Science **290**(5491): 533-536.

Robert, C.P., Cornuet, J.-M., Marin, J.-M. and Pillai Natesh, S. (2011). "Lack of confidence in approximate Bayesian computation model choice." Proceedings of the National Academy of Sciences **108**(37): 15112-15117.

Rollenhagen, A., Walkenfort, B., Yakoubi, R., Klauke, S.A., Schmuhl-Giesen, S.F., Heinen-Weiler, J., Voortmann, S., Marshallsay, B., Palaz, T., Holz, U., Hasenberg, M. and Lübke, J.H.R. (2020). "Synaptic Organization of the Human Temporal Lobe Neocortex as Revealed by High-Resolution Transmission, Focused Ion Beam Scanning, and Electron Microscopic Tomography." International Journal of Molecular Sciences **21**(15).

Rolnick, D., Meirovitch, Y., Parag, T., Pfister, H., Jain, V., Lichtman, J.W., Boyden, E.S. and Shavit, N. (2017). "Morphological error detection in 3D segmentations." arXiv preprint arXiv:1705.10882.

Rosenblatt, F. (1962). Principles of Neurodynamics: Perceptrons and the Theory of Brain Mechanisms, Spartan Books.

Rubenstein, J.L.R. and Merzenich, M.M. (2003). "Model of autism: increased ratio of excitation/inhibition in key neural systems." Genes, Brain and Behavior **2**(5): 255-267.

Rubinov, M. and Sporns, O. (2010). "Complex network measures of brain connectivity: Uses and interpretations." NeuroImage **52**(3): 1059-1069.

Ruder, S. (2017). "An overview of multi-task learning in deep neural networks." arXiv preprint arXiv:1706.05098.

Rumelhart, D.E., Hinton, G.E. and Williams, R.J. (1986). "Learning representations by back-propagating errors." Nature **323**(6088): 533-536.

Sáez, I. and Friedlander, M.J. (2009). "Plasticity between Neuronal Pairs in Layer 4 of Visual Cortex Varies with Synapse State." The Journal of Neuroscience **29**(48): 15286.

Sanes, J.R. and Zipursky, S.L. (2020). "Synaptic Specificity, Recognition Molecules, and Assembly of Neural Circuits." Cell **181**(3): 536-556.

Sarko, D.K., Catania, K.C., Leitch, D.B., Kaas, J.H. and Herculano-Houzel, S. (2009). "Cellular scaling rules of insectivore brains." Front Neuroanat **3**: 8.

Savage, J.E., Jansen, P.R., Stringer, S., Watanabe, K., Bryois, J., de Leeuw, C.A., Nagel, M., Awasthi, S., Barr, P.B., Coleman, J.R.I., Grasby, K.L., Hammerschlag, A.R., Kaminski, J.A., Karlsson, R., Krapohl, E., Lam, M., Nygaard, M., Reynolds, C.A., Trampush, J.W., Young, H., Zabaneh, D., Hägg, S., Hansell, N.K., Karlsson, I.K., Linnarsson, S., Montgomery, G.W., Muñoz-Manchado, A.B., Quinlan, E.B., Schumann, G., Skene, N.G., Webb, B.T., White, T., Arking, D.E., Avramopoulos, D., Bilder, R.M., Bitsios, P., Burdick, K.E., Cannon, T.D., Chiba-Falek, O., Christoforou, A., Cirulli, E.T., Congdon, E., Corvin, A., Davies, G., Deary, I.J., DeRosse, P., Dickinson, D., Djurovic, S., Donohoe, G., Conley, E.D., Eriksson, J.G., Espeseth, T., Freimer, N.A., Giakoumaki, S., Giegling, I., Gill, M., Glahn, D.C., Hariri, A.R., Hatzimanolis, A., Keller, M.C., Knowles, E., Koltai, D., Konte, B., Lahti, J., Le Hellard, S., Lencz, T., Liewald, D.C., London, E., Lundervold, A.J., Malhotra, A.K., Melle, I., Morris, D., Need, A.C., Ollier, W., Palotie, A., Payton, A., Pendleton, N., Poldrack, R.A., Räikkönen, K., Reinvang, I., Roussos, P., Rujescu, D., Sabb, F.W., Scult, M.A., Smeland, O.B., Smyrnis, N., Starr, J.M., Steen, V.M., Stefanis, N.C., Straub, R.E., Sundet, K., Tiemeier, H., Voineskos, A.N., Weinberger, D.R., Widen, E., Yu, J., Abecasis, G., Andreassen, O.A., Breen, G., Christiansen, L., Debrabant, B., Dick, D.M., Heinz, A., Hjerling-Leffler, J., Ikram, M.A., Kendler, K.S., Martin, N.G., Medland, S.E., Pedersen, N.L., Plomin, R., Polderman, T.J.C., Ripke, S., van der Sluis, S., Sullivan, P.F., Vrieze, S.I., Wright, M.J. and Posthuma, D. (2018). "Genome-wide association meta-analysis in 269,867 individuals identifies new genetic and functional links to intelligence." Nature Genetics **50**(7): 912-919.

Schalek, R., Kasthuri, N., Hayworth, K., Berger, D., Tapia, J., Morgan, J., Turaga, S., Fagerholm, E., Seung, H. and Lichtman, J. (2011). "Development of High-Throughput, High-Resolution 3D Reconstruction of Large-Volume Biological Tissue Using Automated Tape Collection Ultramicrotomy and Scanning Electron Microscopy." Microscopy and Microanalysis **17**(S2): 966-967.

Scheffer, L.K., Karsh, B. and Vitaladevun, S. (2013). "Automated alignment of imperfect EM images for neural reconstruction." arXiv preprint arXiv:1304.6034.

Scheffer, L.K., Xu, C.S., Januszewski, M., Lu, Z., Takemura, S.-y., Hayworth, K.J., Huang, G.B., Shinomiya, K., Maitlin-Shepard, J., Berg, S., Clements, J., Hubbard, P.M., Katz, W.T., Umayam, L., Zhao, T., Ackerman, D., Blakely, T., Bogovic, J., Dolafi, T., Kainmueller, D., Kawase, T., Khairy, K.A., Leavitt, L., Li, P.H., Lindsey, L., Neubarth, N., Olbris, D.J., Otsuna, H., Trautman, E.T., Ito, M., Bates, A.S., Goldammer, J., Wolff, T., Svirskas, R., Schlegel, P., Neace, E., Knecht, C.J., Alvarado, C.X., Bailey, D.A., Ballinger, S., Borycz, J.A., Canino, B.S., Cheatham, N., Cook, M., Dreher, M., Duclos, O., Eubanks, B., Fairbanks, K., Finley, S., Forknall, N., Francis, A., Hopkins, G.P., Joyce, E.M., Kim, S., Kirk, N.A., Kovalyak, J., Lauchie, S.A., Lohff, A., Maldonado, C., Manley, E.A., McLin, S., Mooney, C., Ndama, M., Ogundeyi, O., Okeoma, N., Ordish, C., Padilla, N., Patrick, C.M., Paterson, T., Phillips, E.E., Phillips, E.M., Rampally, N., Ribeiro, C., Robertson, M.K., Rymer, J.T., Ryan, S.M., Sammons, M., Scott, A.K., Scott, A.L., Shinomiya, A., Smith, C., Smith, K., Smith, N.L., Sobeski, M.A., Suleiman, A., Swift, J., Takemura, S., Talebi, I., Tarnogorska, D., Tenshaw, E., Tokhi, T., Walsh, J.J., Yang, T., Horne, J.A., Li, F., Parekh, R., Rivlin, P.K., Jayaraman, V., Costa, M., Jefferis, G.S.X.E., Ito, K., Saalfeld, S., George, R., Meinertzhagen, I.A., Rubin, G.M., Hess, H.F., Jain, V. and Plaza, S.M. (2020). "A connectome and analysis of the adult Drosophila central brain." eLife **9**: e57443.

Schikorski, T. and Stevens, C.F. (1997). "Quantitative Ultrastructural Analysis of Hippocampal Excitatory Synapses." The Journal of Neuroscience **17**(15): 5858.

Schlegel, P., Costa, M. and Jefferis, G.S.X.E. (2017). "Learning from connectomics on the fly." Current Opinion in Insect Science **24**: 96-105.

Schleiden, M.J. (1838). "Beiträge zur Phztogenesis." Arch, anat. Physiol. Wiss. Med.: 137–176.

Schmidhuber, J. (1992). "Learning Complex, Extended Sequences Using the Principle of History Compression." Neural Computation **4**(2): 234-242.

Schmidhuber, J. (2015). "Deep Learning in Neural Networks: An Overview." Neural Networks **61**: 85-117.

Schmidt, H., Gour, A., Straehle, J., Boergens, K.M., Brecht, M. and Helmstaedter, M. (2017). "Axonal synapse sorting in medial entorhinal cortex." Nature **549**(7673): 469-475.

Schmidt, M., Motta, A., Sievers, M. and Helmstaedter, M. (2022). "RoboEM: automated 3D flight tracing for synaptic-resolution connectomics." bioRxiv.

Schneider-Mizell, C.M., Gerhard, S., Longair, M., Kazimiers, T., Li, F., Zwart, M.F., Champion, A., Midgley, F.M., Fetter, R.D., Saalfeld, S. and Cardona, A. (2016). "Quantitative neuroanatomy for connectomics in Drosophila." eLife **5**: e12059.

Schneider-Mizell, C.M., Bodor, A.L., Collman, F., Brittain, D., Bleckert, A., Dorkenwald, S., Turner, N.L., Macrina, T., Lee, K., Lu, R., Wu, J., Zhuang, J., Nandi, A., Hu, B., Buchanan, J., Takeno, M.M., Torres, R., Mahalingam, G., Bumbarger, D.J., Li, Y., Chartrand, T., Kemnitz, N., Silversmith, W.M., Ih, D., Zung, J., Zlateski, A., Tartavull, I., Popovych, S., Wong, W., Castro, M., Jordan, C.S., Froudarakis, E., Becker, L., Suckow, S., Reimer, J., Tolias, A.S., Anastassiou, C.A., Seung, H.S., Reid, R.C. and Costa, N.M.d. (2021). "Structure and function of axo-axonic inhibition." eLife **10**: e73783.

Scholl, B., Thomas, C.I., Ryan, M.A., Kamasawa, N. and Fitzpatrick, D. (2021). "Cortical response selectivity derives from strength in numbers of synapses." Nature **590**(7844): 111-114.

Schrader, S., Grün, S., Diesmann, M. and Gerstein, G.L. (2008). "Detecting Synfire Chain Activity Using Massively Parallel Spike Train Recording." Journal of Neurophysiology **100**: 2165-2176.

Schubert, D., Kötter, R., Zilles, K., Luhmann, H.J. and Staiger, J.F. (2003). "Cell Type-Specific Circuits of Cortical Layer IV Spiny Neurons." The Journal of Neuroscience **23**(7): 2961.

Schwann, T. (1839). Mikroskopische Untersuchungen über die Uebereinstimmung in der Struktur und dem Wachsthum der Thiere und Pflanzen. Berlin, Verlag der Sander'schen Buchhandlung.

Sejnowski, T.J. and Tesauro, G. (1989). The Hebb Rule for Synaptic Plasticity: Algorithms and Implementations. Neural Models of Plasticity. J. H. Byrne and W. O. Berry, Academic Press: 94-103.

Seung, H.S. (2009). "Reading the Book of Memory: Sparse Sampling versus Dense Mapping of Connectomes." Neuron **62**(1): 17-29.

Shapson-Coe, A., Januszewski, M., Berger, D.R., Pope, A., Wu, Y., Blakely, T., Schalek, R.L., Li, P.H., Wang, S., Maitin-Shepard, J., Karlupia, N., Dorkenwald, S., Sjostedt, E., Leavitt, L., Lee, D., Bailey, L., Fitzmaurice, A., Kar, R., Field, B., Wu, H., Wagner-Carena, J., Aley, D., Lau, J., Lin, Z., Wei, D., Pfister, H., Peleg, A., Jain, V. and Lichtman, J.W. (2021). "A connectomic study of a petascale fragment of human cerebral cortex." bioRxiv: 2021.2005.2029.446289.

Shein-Idelson, M., Pammer, L., Hemberger, M. and Laurent, G. (2017). "Large-scale mapping of cortical synaptic projections with extracellular electrode arrays." Nature Methods **14**(9): 882-890.

Shepherd, G.M.G., Stepanyants, A., Bureau, I., Chklovskii, D. and Svoboda, K. (2005). "Geometric and functional organization of cortical circuits." Nature Neuroscience **8**(6): 782-790.

Sheridan, A., Nguyen, T., Deb, D., Lee, W.-C.A., Saalfeld, S., Turaga, S., Manor, U. and Funke, J. (2022). "Local Shape Descriptors for Neuron Segmentation." bioRxiv: 2021.2001.2018.427039.

Shi, S.-H., Hayashi, Y., Petralia, R.S., Zaman, S.H., Wenthold, R.J., Svoboda, K. and Malinow, R. (1999). "Rapid Spine Delivery and Redistribution of AMPA Receptors After Synaptic NMDA Receptor Activation." Science **284**(5421): 1811-1816.

Shimizu, G., Yoshida, K., Kasai, H. and Toyoizumi, T. (2021). "Computational roles of intrinsic synaptic dynamics." Current Opinion in Neurobiology **70**: 34-42.

Sievers, M. (unpublished).

Silver, D., Huang, A., Maddison, C.J., Guez, A., Sifre, L., van den Driessche, G., Schrittwieser, J., Antonoglou, I., Panneershelvam, V., Lanctot, M., Dieleman, S., Grewe, D., Nham, J., Kalchbrenner, N., Sutskever, I., Lillicrap, T., Leach, M., Kavukcuoglu, K., Graepel, T. and Hassabis, D. (2016). "Mastering the game of Go with deep neural networks and tree search." Nature **529**(7587): 484-489.

Silver, D., Schrittwieser, J., Simonyan, K., Antonoglou, I., Huang, A., Guez, A., Hubert, T., Baker, L., Lai, M., Bolton, A., Chen, Y., Lillicrap, T., Hui, F., Sifre, L., van den Driessche, G., Graepel, T. and Hassabis, D. (2017). "Mastering the game of Go without human knowledge." Nature **550**(7676): 354-359.

Sisson, S.A., Fan, Y. and Tanaka Mark, M. (2007). "Sequential Monte Carlo without likelihoods." Proceedings of the National Academy of Sciences **104**(6): 1760-1765.

Sjöström, P.J. and Häusser, M. (2006). "A Cooperative Switch Determines the Sign of Synaptic Plasticity in Distal Dendrites of Neocortical Pyramidal Neurons." Neuron **51**(2): 227-238.

Skinner, B.F. (1938). The behavior of organisms: an experimental analysis. Oxford, England, Appleton-Century.

Somogyi, P., Hodgson, A.J. and Smith, A.D. (1979). "An approach to tracing neuron networks in the cerebral cortex and basal ganglia. Combination of golgi staining, retrograde transport of horseradish peroxidase and anterograde degeneration of synaptic boutons in the same material." Neuroscience **4**(12): 1805-1852.

Somogyi, P. and Cowey, A. (1981). "Combined golgi and electron microscopic study on the synapses formed by double bouquet cells in the visual cortex of the cat and monkey." Journal of Comparative Neurology **195**(4): 547-566.

Somogyi, P., Freund, T.F. and Cowey, A. (1982). "The axo-axonic interneuron in the cerebral cortex of the rat, cat and monkey." Neuroscience **7**(11): 2577-2607.

Song, S., Sjostrom, P.J., Reigl, M., Nelson, S. and Chklovskii, D.B. (2005). "Highly nonrandom features of synaptic connectivity in local cortical circuits." PLoS Biol **3**(3): e68.

Sorra, K.E. and Harris, K.M. (1993). "Occurrence and three-dimensional structure of multiple synapses between individual radiatum axons and their target pyramidal cells in hippocampal area CA1." The Journal of Neuroscience **13**(9): 3736.

Sorra, K.E. and Harris, K.M. (1998). "Stability in Synapse Number and Size at 2 Hr after Long-Term Potentiation in Hippocampal Area CA1." The Journal of Neuroscience **18**(2): 658.

Sousa André, M.M., Zhu, Y., Raghanti Mary, A., Kitchen Robert, R., Onorati, M., Tebbenkamp Andrew, T.N., Stutz, B., Meyer Kyle, A., Li, M., Kawasawa Yuka, I., Liu, F., Perez Raquel, G., Mele, M., Carvalho, T., Skarica, M., Gulden Forrest, O., Pletikos, M., Shibata, A., Stephenson Alexa, R., Edler Melissa, K., Ely John, J., Elsworth John, D., Horvath Tamas, L., Hof Patrick, R., Hyde Thomas, M., Kleinman Joel, E., Weinberger Daniel, R., Reimers, M., Lifton Richard, P., Mane Shrikant, M., Noonan James, P., State Matthew, W., Lein Ed, S., Knowles James, A., Marques-Bonet, T., Sherwood Chet, C., Gerstein Mark, B. and Sestan, N. (2017). "Molecular and cellular reorganization of neural circuits in the human lineage." Science **358**(6366): 1027-1032.

Spano, G.M., Banningh, S.W., Marshall, W., de Vivo, L., Bellesi, M., Loschky, S.S., Tononi, G. and Cirelli, C. (2019). "Sleep Deprivation by Exposure to Novel Objects Increases Synapse Density and Axon–Spine Interface in the Hippocampal CA1 Region of Adolescent Mice." The Journal of Neuroscience **39**(34): 6613.

Spearman, C. (1927). The abilities of man. Oxford, England, Macmillan.

Sporns, O., Tononi, G. and Kötter, R. (2005). "The Human Connectome: A Structural Description of the Human Brain." PLOS Computational Biology **1**(4): e42.

Squire, L.R. and Zola-Morgan, S. (1991). "The Medial Temporal Lobe Memory System." Science **253**(5026): 1380-1386.

Staffler, B., Berning, M., Boergens, K.M., Gour, A., Smagt, P.v.d. and Helmstaedter, M. (2017). "SynEM, automated synapse detection for connectomics." eLife **6**: e26414.

Stegmaier, J., Amat, F., Lemon, William C., McDole, K., Wan, Y., Teodoro, G., Mikut, R. and Keller, Philipp J. (2016). "Real-Time Three-Dimensional Cell Segmentation in Large-Scale Microscopy Data of Developing Embryos." Developmental Cell **36**(2): 225-240.

Stephens, Z.D., Lee, S.Y., Faghri, F., Campbell, R.H., Zhai, C., Efron, M.J., Iyer, R., Schatz, M.C., Sinha, S. and Robinson, G.E. (2015). "Big Data: Astronomical or Genomical?" PLOS Biology **13**(7): e1002195.

Storey, J.D. and Tibshirani, R. (2003). "Statistical significance for genomewide studies." Proceedings of the National Academy of Sciences **100**(16): 9440-9445.

Strata, P. and Harvey, R. (1999). "Dale's principle." Brain Research Bulletin **50**(5): 349-350.

Striedter, G.F., Srinivasan, S. and Monuki, E.S. (2015). "Cortical Folding: When, Where, How, and Why?" Annual Review of Neuroscience **38**(1): 291-307.

Sussillo, D. and Abbott, L.F. (2009). "Generating Coherent Patterns of Activity from Chaotic Neural Networks." Neuron **63**: 544-557.

Sussillo, D. and Barak, O. (2012). "Opening the Black Box: Low-Dimensional Dynamics in High-Dimensional Recurrent Neural Networks." Neural Computation **25**: 626-649.

Svara, F.N., Kornfeld, J., Denk, W. and Bollmann, J.H. (2018). "Volume EM Reconstruction of Spinal Cord Reveals Wiring Specificity in Speed-Related Motor Circuits." Cell Reports **23**(10): 2942-2954.

Szegedi, V., Paizs, M., Csakvari, E., Molnar, G., Barzo, P., Tamas, G. and Lamsa, K. (2016). "Plasticity in Single Axon Glutamatergic Connection to GABAergic Interneurons Regulates Complex Events in the Human Neocortex." PLOS Biology **14**(11): e2000237.

Szegedi, V., Paizs, M., Baka, J., Barzó, P., Molnár, G., Tamas, G. and Lamsa, K. (2020). "Robust perisomatic GABAergic self-innervation inhibits basket cells in the human and mouse supragranular neocortex." eLife **9**: e51691.

Szegedy, C., Zaremba, W., Sutskever, I., Bruna, J., Erhan, D., Goodfellow, I. and Fergus, R. (2013). "Intriguing properties of neural networks." arXiv preprint arXiv:1312.6199.

Szegedy, C., Liu, W., Jia, Y., Sermanet, P., Reed, S., Anguelov, D., Erhan, D., Vanhoucke, V. and Rabinovich, A. (2015). Going deeper with convolutions. Proceedings of the IEEE conference on computer vision and pattern recognition.

Takahashi, N., Kitamura, K., Matsuo, N., Mayford, M., Kano, M., Matsuki, N. and Ikegaya, Y. (2012). "Locally Synchronized Synaptic Inputs." Science **335**(6066): 353-356.

Takemura, S.-y., Xu, C.S., Lu, Z., Rivlin, P.K., Parag, T., Olbris, D.J., Plaza, S., Zhao, T., Katz, W.T., Umayam, L., Weaver, C., Hess, H.F., Horne, J.A., Nunez-Iglesias, J., Aniceto, R., Chang, L.-A., Lauchie, S., Nasca, A., Ogundeyi, O., Sigmund, C., Takemura, S., Tran, J., Langille, C., Le Lacheur, K., McLin, S., Shinomiya, A., Chklovskii, D.B., Meinertzhagen, I.A. and Scheffer, L.K. (2015). "Synaptic circuits and their variations within different columns in the visual system of Drosophila." Proceedings of the National Academy of Sciences **112**(44): 13711-13716.

Takemura, S.-y., Aso, Y., Hige, T., Wong, A., Lu, Z., Xu, C.S., Rivlin, P.K., Hess, H., Zhao, T., Parag, T., Berg, S., Huang, G., Katz, W., Olbris, D.J., Plaza, S., Umayam, L., Aniceto, R., Chang, L.-A., Lauchie, S., Ogundeyi, O., Ordish, C., Shinomiya, A., Sigmund, C., Takemura, S., Tran, J., Turner, G.C., Rubin, G.M. and Scheffer, L.K. (2017). "A connectome of a learning and memory center in the adult Drosophila brain." eLife **6**: e26975.

Takemura, S.Y., Bharioke, A., Lu, Z., Nern, A., Vitaladevuni, S., Rivlin, P.K., Katz, W.T., Olbris, D.J., Plaza, S.M., Winston, P., Zhao, T., Horne, J.A., Fetter, R.D., Takemura, S., Blazek, K., Chang, L.A., Ogundeyi, O., Saunders, M.A., Shapiro, V., Sigmund, C., Rubin, G.M., Scheffer, L.K., Meinertzhagen, I.A. and Chklovskii, D.B. (2013). "A visual motion detection circuit suggested by Drosophila connectomics." Nature **500**(7461): 175-181.

Takumi, Y., Ramírez-León, V., Laake, P., Rinvik, E. and Ottersen, O.P. (1999). "Different modes of expression of AMPA and NMDA receptors in hippocampal synapses." Nature Neuroscience **2**(7): 618-624.

Tang, S., Zhang, Y., Li, Z., Li, M., Liu, F., Jiang, H. and Lee, T.S. (2018). "Large-scale two-photon imaging revealed super-sparse population codes in the V1 superficial layer of awake monkeys." eLife **7**: e33370.

Taniguchi, H., Lu, J. and Huang, Z.J. (2013). "The Spatial and Temporal Origin of Chandelier Cells in Mouse Neocortex." Science **339**(6115): 70-74.

Tasic, B., Yao, Z., Graybuck, L.T., Smith, K.A., Nguyen, T.N., Bertagnolli, D., Goldy, J., Garren, E., Economo, M.N., Viswanathan, S., Penn, O., Bakken, T., Menon, V., Miller, J., Fong, O., Hirokawa, K.E., Lathia, K., Rimorin, C., Tieu, M., Larsen, R., Casper, T., Barkan, E., Kroll, M., Parry, S., Shapovalova, N.V., Hirschstein, D., Pendergraft, J., Sullivan, H.A., Kim, T.K., Szafer, A., Dee, N., Groblewski, P., Wickersham, I., Cetin, A., Harris, J.A., Levi, B.P., Sunkin, S.M., Madisen, L., Daigle, T.L., Looger, L., Bernard, A., Phillips, J., Lein, E., Hawrylycz, M., Svoboda, K., Jones, A.R., Koch, C. and Zeng, H. (2018). "Shared and distinct transcriptomic cell types across neocortical areas." Nature **563**(7729): 72-78.

Tavanaei, A., Ghodrati, M., Kheradpisheh, S.R., Masquelier, T. and Maida, A. (2019). "Deep learning in spiking neural networks." Neural Networks **111**: 47-63.

Templier, T. (2019). "MagC, magnetic collection of ultrathin sections for volumetric correlative light and electron microscopy." eLife **8**: e45696.

Thomson, A.M., West, D.C., Wang, Y. and Bannister, A.P. (2002). "Synaptic Connections and Small Circuits Involving Excitatory and Inhibitory Neurons in Layers 2–5 of Adult Rat and Cat Neocortex: Triple Intracellular Recordings and Biocytin Labelling In Vitro." Cerebral Cortex **12**(9): 936-953.

Thorndike, E.L. (1911). Animal intelligence: Experimental studies. Lewiston, NY, US, Macmillan Press.

Toni, N., Buchs, P.A., Nikonenko, I., Bron, C.R. and Muller, D. (1999). "LTP promotes formation of multiple spine synapses between a single axon terminal and a dendrite." Nature **402**(6760): 421-425.

Toni, T., Welch, D., Strelkowa, N., Ipsen, A. and Stumpf, M.P.H. (2009). "Approximate Bayesian computation scheme for parameter inference and model selection in dynamical systems." Journal of The Royal Society Interface **6**(31): 187-202.

Toni, T. and Stumpf, M.P.H. (2010). "Simulation-based model selection for dynamical systems in systems and population biology." Bioinformatics **26**(1): 104-110.

Tononi, G. and Cirelli, C. (2014). "Sleep and the Price of Plasticity: From Synaptic and Cellular Homeostasis to Memory Consolidation and Integration." Neuron **81**(1): 12-34.

Toyoizumi, T., Pfister, J., Aihara, K. and Gerstner, W. (2007). "Optimality Model of Unsupervised Spike-Timing-Dependent Plasticity: Synaptic Memory and Weight Distribution." Neural Computation **19**(3): 639-671.

Trachtenberg, J.T., Chen, B.E., Knott, G.W., Feng, G., Sanes, J.R., Welker, E. and Svoboda, K. (2002). "Long-term in vivo imaging of experience-dependent synaptic plasticity in adult cortex." Nature **420**(6917): 788-794.

Trengove, C., van Leeuwen, C. and Diesmann, M. (2013). "High-capacity embedding of synfire chains in a cortical network model." Journal of Computational Neuroscience **34**(2): 185-209.

Triki, Z. and Bshary, R. (2018). "Cleaner fish Labroides dimidiatus discriminate numbers but fail a mental number line test." Animal Cognition **21**(1): 99-107.

Trommald, M., Hulleberg, G. and Andersen, P. (1996). "Long-term potentiation is associated with new excitatory spine synapses on rat dentate granule cells." Learning & Memory **3**(2-3): 218-228.

Troyer, T.W., Krukowski, A.E., Priebe, N.J. and Miller, K.D. (1998). "Contrast-Invariant Orientation Tuning in Cat Visual Cortex: Thalamocortical Input Tuning and Correlation-Based Intracortical Connectivity." The Journal of Neuroscience **18**(15): 5908.

Turaga, S.C., Murray, J.F., Jain, V., Roth, F., Helmstaedter, M., Briggman, K., Denk, W. and Seung, H.S. (2009). "Convolutional Networks Can Learn to Generate Affinity Graphs for Image Segmentation." Neural Computation **22**(2): 511-538.

Turner, N.L., Macrina, T., Bae, J.A., Yang, R., Wilson, A.M., Schneider-Mizell, C., Lee, K., Lu, R., Wu, J., Bodor, A.L., Bleckert, A.A., Brittain, D., Froudarakis, E., Dorkenwald, S., Collman, F., Kemnitz, N., Ih, D., Silversmith, W.M., Zung, J., Zlateski, A., Tartavull, I., Yu, S.-c., Popovych, S., Mu, S., Wong, W., Jordan, C.S., Castro, M., Buchanan, J., Bumbarger, D.J., Takeno, M., Torres, R., Mahalingam, G., Elabbady, L., Li, Y., Cobos, E., Zhou, P., Suckow, S., Becker, L., Paninski, L., Polleux, F., Reimer, J., Tolias, A.S., Reid, R.C., da Costa, N.M. and Seung, H.S. (2020). "Multiscale and multimodal reconstruction of cortical structure and function." bioRxiv: 2020.2010.2014.338681.

Turrigiano, G.G., Leslie, K.R., Desai, N.S., Rutherford, L.C. and Nelson, S.B. (1998). "Activity-dependent scaling of quantal amplitude in neocortical neurons." Nature **391**(6670): 892-896.

Turrigiano, G.G. and Nelson, S.B. (2004). "Homeostatic plasticity in the developing nervous system." Nature Reviews Neuroscience **5**(2): 97-107.

Uchizono, K. (1965). "Characteristics of Excitatory and Inhibitory Synapses in the Central Nervous System of the Cat." Nature **207**(4997): 642-643.

van den Heuvel, M.P., Bullmore, E.T. and Sporns, O. (2016). "Comparative Connectomics." Trends in Cognitive Sciences **20**(5): 345-361.

Van der Maaten, L. and Hinton, G. (2008). "Visualizing data using t-SNE." Journal of machine learning research **9**(11).

Van Essen, D.C., Smith, S.M., Barch, D.M., Behrens, T.E.J., Yacoub, E. and Ugurbil, K. (2013). "The WU-Minn Human Connectome Project: An overview." NeuroImage **80**: 62-79.

Van Harreveld, A. and Fifková, E. (1975). "Swelling of dendritic spines in the fascia dentata after stimulation of the perforant fibers as a mechanism of post-tetanic potentiation." Experimental Neurology **49**(3): 736-749.

Varshney, L.R., Chen, B.L., Paniagua, E., Hall, D.H. and Chklovskii, D.B. (2011). "Structural Properties of the Caenorhabditis elegans Neuronal Network." PLOS Computational Biology **7**(2): e1001066.

Vogelstein, J.T., Conroy, J.M., Lyzinski, V., Podrazik, L.J., Kratzer, S.G., Harley, E.T., Fishkind, D.E., Vogelstein, R.J. and Priebe, C.E. (2015). "Fast Approximate Quadratic Programming for Graph Matching." PLOS ONE **10**(4): e0121002.

Vogelstein, J.T. and Priebe, C.E. (2015). "Shuffled Graph Classification: Theory and Connectome Applications." Journal of Classification **32**(1): 3-20.

von Bartheld, C.S., Bahney, J. and Herculano-Houzel, S. (2016). "The search for true numbers of neurons and glial cells in the human brain: A review of 150 years of cell counting." Journal of Comparative Neurology **524**(18): 3865-3895.

von der Malsburg, C. (1973). "Self-organization of orientation sensitive cells in the striate cortex." Kybernetik **14**(2): 85-100.

von Heimendahl, M., Itskov, P.M., Arabzadeh, E. and Diamond, M.E. (2007). "Neuronal activity in rat barrel cortex underlying texture discrimination." PLoS Biol **5**(11): e305.

Waldeyer-Hartz, H.W.G. (1891). "Über einige neuere Forschungen im Gebiete der Anatomie des Centralnervenszstems." Deutsch Med Wchnschr **17**.

Wang, B., Yin, L., Zou, X., Ye, M., Liu, Y., He, T., Deng, S., Jiang, Y., Zheng, R., Wang, Y., Yang, M., Lu, H., Wu, S. and Shu, Y. (2015). "A Subtype of Inhibitory Interneuron with Intrinsic Persistent Activity in Human and Monkey Neocortex." Cell Reports **10**(9): 1450-1458.

Wanner, A.A., Genoud, C. and Friedrich, R.W. (2016). "3-dimensional electron microscopic imaging of the zebrafish olfactory bulb and dense reconstruction of neurons." Scientific Data **3**(1): 160100.

Wanner, A.A., Genoud, C., Masudi, T., Siksou, L. and Friedrich, R.W. (2016). "Dense EM-based reconstruction of the interglomerular projectome in the zebrafish olfactory bulb." Nature Neuroscience **19**(6): 816-825.

Watson, J.B. (1913). "Psychology as the behaviorist views it." Psychological Review **20**(2): 158-177.

Watts, D.J. and Strogatz, S.H. (1998). "Collective dynamics of 'small-world' networks." Nature **393**(6684): 440-442.

Weber, J.P., Andrásfalvy, B.K., Polito, M., Magó, Á., Ujfalussy, B.B. and Makara, J.K. (2016). "Location-dependent synaptic plasticity rules by dendritic spine cooperativity." Nature Communications **7**(1): 11380.

Wernicke, C. (1874). Der aphasische Symptomencomplex: eine psychologische Studie auf anatomischer Basis, Cohn.

White, E.L. (1978). "Identified neurons in mouse SmI cortex which are postsynaptic to thalamocortical axon terminals: a combined Golgi-electron microscopic and degeneration study." Journal of Comparative Neurology **181**(3): 627-661.

White, E.L. and Hersch, S.M. (1981). "Thalamocortical synapses of pyramidal cells which project from SmI to MsI cortex in the mouse." Journal of Comparative Neurology **198**(1): 167-181.

White, E.L. and Rock, M.P. (1981). "A comparison of thalamocortical and other synaptic inputs to dendrites of two non-spiny neurons in a single barrel of mouse SmI cortex." Journal of Comparative Neurology **195**(2): 265-277.

White, E.L., Benshalom, G. and Hersch, S.M. (1984). "Thalamocortical and other synapses involving nonspiny multipolar cells of mouse SmI cortex." Journal of Comparative Neurology **229**(3): 311-320.

White, E.L. and Keller, A. (1989). Cortical Circuits: Synaptic Organization of the Cerebral Cortex: Structure, Function, and Theory. Boston, MA, USA, Birkhäuser.

White, J.G. (1974). Computer Aided Reconstruction of the Nervous System of Caenorhabditis Elegans. PhD, University of Cambridge

White, J.G., Southgate, E., Thomson, J.N. and Brenner, S. (1986). "The structure of the nervous system of the nematode Caenorhabditis elegans." Philosophical Transactions of the Royal Society of London. B, Biological Sciences **314**(1165): 1-340.

Whittaker, V.P., Michaelson, I.A. and Kirkland, R.J. (1963). "The separation of synaptic vesicles from disrupted nerve-ending particles." Biochemical Pharmacology **12**(3): 300-302.

Wickersham, I.R., Lyon, D.C., Barnard, R.J.O., Mori, T., Finke, S., Conzelmann, K.-K., Young, J.A.T. and Callaway, E.M. (2007). "Monosynaptic Restriction of Transsynaptic Tracing from Single, Genetically Targeted Neurons." Neuron **53**(5): 639-647.

Wildenberg, G.A., Rosen, M.R., Lundell, J., Paukner, D., Freedman, D.J. and Kasthuri, N. (2021). "Primate neuronal connections are sparse in cortex as compared to mouse." Cell Reports **36**(11): 109709.

Wilson, A.M., Schalek, R., Suissa-Peleg, A., Jones, T.R., Knowles-Barley, S., Pfister, H. and Lichtman, J.W. (2019). "Developmental Rewiring between Cerebellar Climbing Fibers and Purkinje Cells Begins with Positive Feedback Synapse Addition." Cell Rep **29**(9): 2849-2861 e2846.

Wilson, D.E., Whitney, D.E., Scholl, B. and Fitzpatrick, D. (2016). "Orientation selectivity and the functional clustering of synaptic inputs in primary visual cortex." Nature Neuroscience **19**(8): 1003-1009.

Wilson, M.K., Karakasis, K. and Oza, A.M. (2015). "Outcomes and endpoints in trials of cancer treatment: the past, present, and future." The Lancet Oncology **16**(1): e32-e42.

Wolfe, J., Hill, D.N., Pahlavan, S., Drew, P.J., Kleinfeld, D. and Feldman, D.E. (2008). "Texture coding in the rat whisker system: slip-stick versus differential resonance." PLoS Biol **6**(8): e215.

Wouters, J., Kloosterman, F. and Bertrand, A. (2018). "Towards online spike sorting for high-density neural probes using discriminative template matching with suppression of interfering spikes." Journal of Neural Engineering **15**(5): 056005.

Wu, Y., Wawrzusin, P., Senseney, J., Fischer, R.S., Christensen, R., Santella, A., York, A.G., Winter, P.W., Waterman, C.M., Bao, Z., Colón-Ramos, D.A., McAuliffe, M. and Shroff, H. (2013). "Spatially isotropic four-dimensional imaging with dual-view plane illumination microscopy." Nature Biotechnology **31**(11): 1032-1038.

Xu, C., Liu, H.-J., Qi, L., Tao, C.-L., Wang, Y.-J., Shen, Z., Tian, C.-L., Lau, P.-M. and Bi, G.-Q. (2020). "Structure and plasticity of silent synapses in developing hippocampal neurons visualized by super-resolution imaging." Cell Discovery **6**(1): 8.

Xu, C.S., Hayworth, K.J., Lu, Z., Grob, P., Hassan, A.M., García-Cerdán, J.G., Niyogi, K.K., Nogales, E., Weinberg, R.J. and Hess, H.F. (2017). "Enhanced FIB-SEM systems for large-volume 3D imaging." eLife **6**: e25916.

Xu, T., Yu, X., Perlik, A.J., Tobin, W.F., Zweig, J.A., Tennant, K., Jones, T. and Zuo, Y. (2009). "Rapid formation and selective stabilization of synapses for enduring motor memories." Nature **462**(7275): 915-919.

Xue, Y., Yang, L. and Haykin, S. (2007). "Decoupled echo state networks with lateral inhibition." Neural Networks **20**: 365-376.

Yamins, D.L.K., Hong, H., Cadieu, C.F., Solomon, E.A., Seibert, D. and DiCarlo, J.J. (2014). "Performance-optimized hierarchical models predict neural responses in higher visual cortex." Proceedings of the National Academy of Sciences **111**(23): 8619-8624.

Yamins, D.L.K. and DiCarlo, J.J. (2016). "Using goal-driven deep learning models to understand sensory cortex." Nature Neuroscience **19**(3): 356-365.

Yáñez, I.B., Muñoz, A., Contreras, J., Gonzalez, J., Rodriguez-Veiga, E. and DeFelipe, J. (2005). "Double bouquet cell in the human cerebral cortex and a comparison with other mammals." Journal of Comparative Neurology **486**(4): 344-360.

Yang, G., Pan, F. and Gan, W.-B. (2009). "Stably maintained dendritic spines are associated with lifelong memories." Nature **462**(7275): 920-924.

Yi, L., Jiantao, P., Hongbin, Z., Liu, W. and Uehara, Y. (2004). Thickness histogram and statistical harmonic representation for 3D model retrieval. Proceedings. 2nd International Symposium on 3D Data Processing, Visualization and Transmission, 2004. 3DPVT 2004.

Yildiz, I.B., Jaeger, H. and Kiebel, S.J. (2012). "Re-visiting the echo state property." Neural Networks **35**: 1-9.

Yin, W., Brittain, D., Borseth, J., Scott, M.E., Williams, D., Perkins, J., Own, C.S., Murfitt, M., Torres, R.M., Kapner, D., Mahalingam, G., Bleckert, A., Castelli, D., Reid, D., Lee, W.-C.A., Graham, B.J., Takeno, M., Bumbarger, D.J., Farrell, C., Reid, R.C. and da Costa, N.M. (2020). "A petascale automated imaging pipeline for mapping neuronal circuits with high-throughput transmission electron microscopy." Nature Communications **11**(1): 4949.

Yu, J., Hu, H., Agmon, A. and Svoboda, K. (2019). "Recruitment of GABAergic Interneurons in the Barrel Cortex during Active Tactile Behavior." Neuron **104**(2): 412-427.e414.

Yuste, R. and Bonhoeffer, T. (2001). "Morphological Changes in Dendritic Spines Associated with Long-Term Synaptic Plasticity." Annual Review of Neuroscience **24**(1): 1071-1089.

Yuste, R., Hawrylycz, M., Aalling, N., Aguilar-Valles, A., Arendt, D., Armañanzas, R., Ascoli, G.A., Bielza, C., Bokharaie, V., Bergmann, T.B., Bystron, I., Capogna, M., Chang, Y., Clemens, A., de Kock, C.P.J., DeFelipe, J., Dos Santos, S.E., Dunville, K., Feldmeyer, D., Fiáth, R., Fishell, G.J., Foggetti, A., Gao, X., Ghaderi, P., Goriounova, N.A., Güntürkün, O., Hagihara, K., Hall, V.J., Helmstaedter, M., Herculano-Houzel, S., Hilscher, M.M., Hirase, H., Hjerling-Leffler, J., Hodge, R., Huang, J., Huda, R., Khodosevich, K., Kiehn, O., Koch, H., Kuebler, E.S., Kühnemund, M., Larrañaga, P., Lelieveldt, B., Louth, E.L., Lui, J.H., Mansvelder, H.D., Marin, O., Martinez-Trujillo, J., Chameh, H.M., Mohapatra, A.N., Munguba, H., Nedergaard, M., Němec, P., Ofer, N., Pfisterer, U.G., Pontes, S., Redmond, W., Rossier, J., Sanes, J.R., Scheuermann, R.H., Serrano-Saiz, E., Staiger, J.F., Somogyi, P., Tamás, G., Tolias, A.S., Tosches, M.A., García, M.T., Wozny, C., Wuttke, T.V., Liu, Y., Yuan, J., Zeng, H. and Lein, E. (2020). "A community-based transcriptomics classification and nomenclature of neocortical cell types." Nature Neuroscience **23**(12): 1456-1468.

Zador, A.M. (2019). "A critique of pure learning and what artificial neural networks can learn from animal brains." Nature Communications **10**(1): 3770.

Zhang, W., Gao, B., Tang, J., Yao, P., Yu, S., Chang, M.-F., Yoo, H.-J., Qian, H. and Wu, H. (2020). "Neuro-inspired computing chips." Nature Electronics **3**(7): 371-382.

Zhang, X., Zou, J., He, K. and Sun, J. (2016). "Accelerating Very Deep Convolutional Networks for Classification and Detection." IEEE Transactions on Pattern Analysis and Machine Intelligence **38**(10): 1943-1955.

Zheng, P., Dimitrakakis, C. and Triesch, J. (2013). "Network Self-Organization Explains the Statistics and Dynamics of Synaptic Connection Strengths in Cortex." PLOS Computational Biology **9**(1): e1002848.

Zheng, P. and Triesch, J. (2014). "Robust development of synfire chains from multiple plasticity mechanisms." Frontiers in Computational Neuroscience **8**: 66.

Zheng, Z., Lauritzen, J.S., Perlman, E., Robinson, C.G., Nichols, M., Milkie, D., Torrens, O., Price, J., Fisher, C.B., Sharifi, N., Calle-Schuler, S.A., Kmecova, L., Ali, I.J., Karsh, B., Trautman, E.T., Bogovic, J.A., Hanslovsky, P., Jefferis, G.S.X.E., Kazhdan, M., Khairy, K., Saalfeld, S., Fetter, R.D. and Bock, D.D. (2018). "A Complete Electron Microscopy Volume of the Brain of Adult Drosophila melanogaster." Cell **174**(3): 730-743.e722.

Zhou, Q., Homma, K.J. and Poo, M.-m. (2004). "Shrinkage of Dendritic Spines Associated with Long-Term Depression of Hippocampal Synapses." Neuron **44**(5): 749-757.

Zung, J., Tartavull, I., Lee, K. and Seung, H.S. (2017). "An error detection and correction framework for connectomics." Advances in neural information processing systems **30**.